

AD-A144 144

UNITED STATES AIR FORCE GEOPHYSICS SCHOLAR PROGRAM

1982-1983(U) SOUTHEASTERN CENTER FOR ELECTRICAL

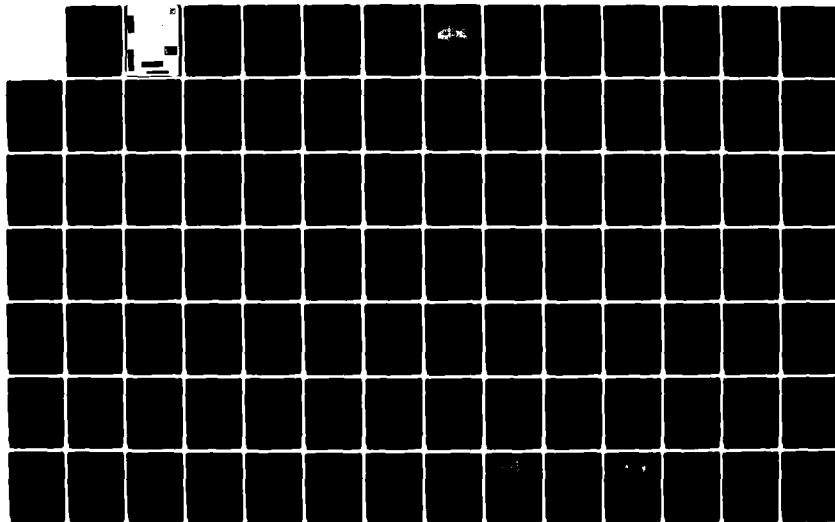
ENGINEERING EDUCATION INC S. W D PEELE ET AL. MAR 84

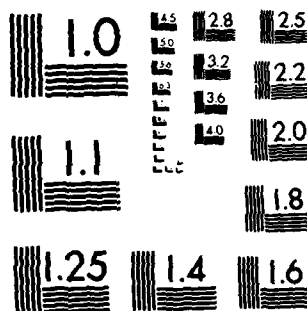
UNCLASSIFIED AFOSR-TR-84-0622 F49620-82-C-0035

F/G 5/1

NL

1/3





MICROCOPY RESOLUTION TEST CHART
NATIONAL BUREAU OF STANDARDS-1963-A

1982-1983 USAF/SCEEE
AIR FORCE GEOPHYSICS SCHOLAR PROGRAM

conducted by

Southeastern Center for
Electrical Engineering Education

under

USAF Contract Number F49620-82-C-0035

MANAGEMENT AND TECHNICAL REPORT

submitted to

Air Force Office of Scientific Research

Bolling Air Force Base

Washington D.C.

by

Southeastern Center for
Electrical Engineering Education

March 1984

UNCLASSIFIED

SECURITY CLASSIFICATION OF THIS PAGE

REPORT DOCUMENTATION PAGE

1a. REPORT SECURITY CLASSIFICATION UNCLASSIFIED			1b. RESTRICTIVE MARKINGS		
2a. SECURITY CLASSIFICATION AUTHORITY			3. DISTRIBUTION/AVAILABILITY OF REPORT APPROVED FOR PUBLIC RELEASE; DISTRIBUTION UNLIMITED		
2b. DECLASSIFICATION/DOWNGRADING SCHEDULE					
4. PERFORMING ORGANIZATION REPORT NUMBER(S)			5. MONITORING ORGANIZATION REPORT NUMBER(S) AFOSR-TR- 84 . 0 6 2 2		
6a. NAME OF PERFORMING ORGANIZATION Southeastern Center for Electrical Engineering Education		6b. OFFICE SYMBOL (if applicable)	7a. NAME OF MONITORING ORGANIZATION AFOSR/XO		
6c. ADDRESS (City, State, and ZIP Code) 11th & Massachusetts Ave. St. Cloud, Florida 32769			7b. ADDRESS (City, State, and ZIP Code) Building 410 Bolling AFB, DC 20332		
8a. NAME OF FUNDING/SPONSORING ORGANIZATION AFOSR		8b. OFFICE SYMBOL (if applicable) XO	9. PROCUREMENT INSTRUMENT IDENTIFICATION NUMBER F49620-82-C-0035		
8c. ADDRESS (City, State, and ZIP Code) Building 410 Bolling AFB, DC 20332			10. SOURCE OF FUNDING NUMBERS		
			PROGRAM ELEMENT NO. 61102F	PROJECT NO. 2301	TASK NO. D5
11. TITLE (Include Security Classification) UNITED STATES AIR FORCE GEOPHYSICS SCHOLAR PROGRAM - 1982-1983					
12. PERSONAL AUTHOR(S) Warren D. Peele, Earl L. Steele, Dr A.T. Stair					
13a. TYPE OF REPORT Technical		13b. TIME COVERED FROM TO		14. DATE OF REPORT (Year, Month, Day) 1982-1983	
15. PAGE COUNT					
16. SUPPLEMENTARY NOTATION					
17. COSATI CODES			18. SUBJECT TERMS (Continue on reverse if necessary and identify by block number)		
FIELD	GROUP	SUB-GROUP			
19. ABSTRACT (Continue on reverse if necessary and identify by block number) <p>The Geophysics Scholar Program was initiated as a pilot program to provide new Research Scholars with one year appointments to the Air Force Geophysics Laboratory.</p> <p>Extensive mailings were made to technical departments at universities around the United States where programs of prime interest to the Geophysics Laboratory were established. These included Atmospheric Studies, Geophysics, Meteorology and related applied sciences.</p> <p>Ten Scholars were appointed beginning in September 1982 and extending through December 1982, for 12 months duration. Six of these were subsequently continued in the Geophysics Scholar Program under another contract for a second year.</p> <p>Five technical papers were presented by the Scholars during the year. The final technical reports on the Scholar's work are included in this report. →</p> <p style="text-align: right;">(OVER)</p>					
20. DISTRIBUTION/AVAILABILITY OF ABSTRACT <input checked="" type="checkbox"/> UNCLASSIFIED/UNLIMITED <input type="checkbox"/> SAME AS RPT. <input type="checkbox"/> DTIC USERS			21. ABSTRACT SECURITY CLASSIFICATION UNCLASSIFIED		
22a. NAME OF RESPONSIBLE INDIVIDUAL MAJOR AMOS OTIS			22b. TELEPHONE (Include Area Code) (202) 767-4971		22c. OFFICE SYMBOL AFOSR/XO

DD FORM 1473, 84 MAR

83 APR edition may be used until exhausted
All other editions are obsolete.

SECURITY CLASSIFICATION OF THIS PAGE

19. (Continued)

→ This pilot program was judged a success by both the Scholars and their Laboratory Associates. Their comments were solicited by questionnaire and are included. The Scholars were judged to be beneficial to the Laboratory. The opportunity of having new Research people on a short term basis was felt to be very stimulating and worth while. Their interaction with the Laboratory was very positive.

At the initiation of this program, travel funds were provided only for travel to the Laboratory site at the start of the appointment and return funds at the end. Some difficulties were subsequently encountered in transferring funds and authorizing travel to technical meetings. This caused some distress among the Scholars.

However, overall, the Scholars felt their experiences at the Laboratory were constructive steps in their professional development.

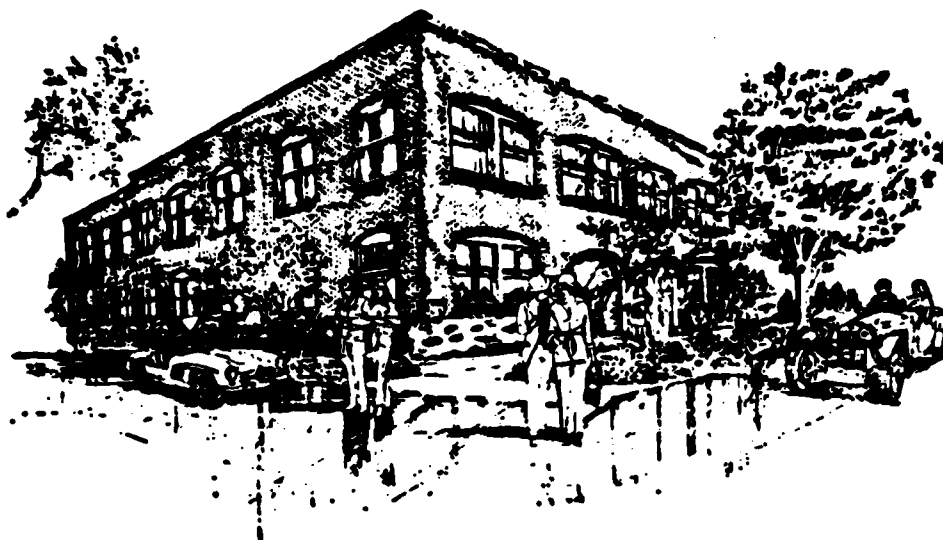
Accession For	
NTIS GRA&I	<input checked="checked" type="checkbox"/>
DTIC TAB	<input type="checkbox"/>
Unannounced	<input type="checkbox"/>
Justification	
By _____	
Distribution/	
Availability Codes	
Dist	Avail and/or Special
A/1	



UNCLASSIFIED

SECURITY CLASSIFICATION OF THIS PAGE

UNITED STATES AIR FORCE
AIR FORCE GEOPHYSICS SCHOLAR PROGRAM
1982-1983
PROGRAM MANAGEMENT AND TECHNICAL REPORT
SOUTHEASTERN CENTER FOR ELECTRICAL ENGINEERING EDUCATION



SCEEE
©
1984

TABLE OF CONTENTS

<u>Section</u>	<u>Page</u>
I. Summary.....	5
II. Introduction.....	6
III. Application Information.....	6
IV. Information Brochure for Geophysics Scholars.....	8
V. Questionnaires and Responses.....	22

APPENDIX I

Program Statistics.....	I.2
List of 1982-83 Geophysics Scholars.....	I.5

APPENDIX II

Scholars Statements of Goals & Objectives.....	II.2
Listing of Research Reports.....	II.14
Abstracts of Geophysics Scholar Research Reports.....	II.15

APPENDIX III

1982-83 AF Geophysics Scholar Final Reports.....	III.1
--------------------------------------------------	-------

1982-1983 AIR FORCE GEOPHYSICS SCHOLAR PROGRAM

I. SUMMARY

The Geophysics Scholar Program was initiated as a pilot program to provide new Research Scholars with one year appointments to the Air Force Geophysics Laboratory.

Extensive mailings were made to technical departments at universities around the United States where programs of prime interest to the Geophysics Laboratory were established. These included Atmospheric Studies, Geophysics, Meteorology and related applied sciences.

Ten Scholars were appointed beginning in September 1982 and extending through December 1982, for 12 months duration. Six of these were subsequently continued in the Geophysics Scholar Program under another contract for a second year.

Five technical papers were presented by the Scholars during the year. The final technical reports on the Scholar's work are included in this report.

This pilot program was judged a success by both the Scholars and their Laboratory Associates. Their comments were solicited by questionnaire and are included. The Scholars were judged to be beneficial to the Laboratory. The opportunity of having new Research people on a short term basis was felt to be very stimulating and worth while. Their interaction with the Laboratory was very positive.

At the initiation of this program, travel funds were provided only for travel to the Laboratory site at the start of the appointment and return funds at the end. Some difficulties were subsequently encountered in transferring funds and authorizing travel to technical meetings. This caused some distress among the Scholars.

However, overall, the Scholars felt their experiences at the Laboratory were constructive steps in their professional development.

1982-1983 AIR FORCE GEOPHYSICS SCHOLAR PROGRAM

II. INTRODUCTION

The Air Force Office of Scientific Research, the Air Force Geophysics Laboratory, and the Southeastern Center for Electrical Engineering Education initiated a pilot Air Force Geophysics Scholar Research Program beginning in the fall of 1982. This new program was an adjunct effort to the U.S. Air Force Summer Faculty Research Program (SFRP) established by contract modification dated June 1982 under a special studies clause. This pilot program provided research opportunities for selected Engineers and Scientists holding a doctoral degree to work in residence at the Air Force Geophysics Laboratory for a one year research period.

To be eligible, all candidates must have had a Ph.D. or equivalent in an appropriate technical field. The Scholars were selected primarily from such basic and applied science fields as Physics, particularly Geophysics and Atmospheric Physics, Meteorology, and Chemistry, and also from Mathematics, Computer Science, and Engineering. The scholars must be U.S. citizens, holding an appropriate advanced graduate research degree.

The Air Force Geophysics Scholar in this program had the following specific obligations:

- 1) To participate in advanced research programs at the Air Force Geophysics Laboratory;
- 2) To prepare a report at the end of the one year appointment describing their research accomplishments. This report will be approved by the Air Force Geophysics Laboratory.
- 3) To complete an evaluation questionnaire on the Air Force Geophysics Scholar Research Program.

III. APPLICATION INFORMATION

Qualified technical people who were interested in an appointment under this program were asked to file a formal application and supporting materials with the program director at SCEEE. Formal application forms and program announcements were widely distributed and also available from the SCEEE programs office. In this program SCEEE supports equal opportunity/affirmative action so that all qualified applicants received consideration without regard to race, color, religion, sex, or national origin.

The application deadline was August 1, 1982.

THE AIR FORCE GEOPHYSICS SCHOLAR PROGRAM OBJECTIVES WERE:

- (1) to provide a productive means for Scientist and Engineers holding Ph.D. degrees to participate in research at the Air Force Geophysics Laboratory;
- (2) to stimulate continuing professional association among the Scholars and their professional peers in the Air Force;
- (3) to further the research objectives of the United States Air Force; and
- (4) to enhance the research productivity and capabilities of Scientists and Engineers especially as these relate to Air Force technical interests.

PREREQUISITES FOR APPOINTMENTS: To be qualified for consideration as a Geophysics Scholar in the fall 1982 program, the applicant must:

- (1) be a U.S. Citizen;
- (2) be the holder of a Ph.D. degree, or equivalent, in an appropriate technical specialty; and
- (3) be willing to pursue research work of limited time duration at the Air Force Geophysics Laboratory.

Although it was anticipated that the research itself might be unclassified, the Scholar should hold or be eligible for a Department of Defense SECRET clearance in order to insure access to work areas.

RESEARCH PERIOD: The period of this appointment was for one year at the Air Force Geophysics Laboratory research site, Hanscom AFB, Mass. It was planned initially that all appointments would begin in September 1982 and end during September 1983. However, some appointments were delayed in starting, so the ending date was extended through December 1983.

FINANCIAL TERMS: The stipend for the Air Force Geophysics Scholar in this program was as follows:

\$80.00 per day for a maximum of 260 days

Travel expenses were to be reimbursed for one trip from the Scholar's normal location to the Air Force facility at the start of the appointment; and one return trip from the Laboratory to the Scholar's normal home base at the end of the appointment period. This travel would be reimbursed in accordance with SCEE travel policy.

An expense allowance of \$25.00 per day will be reimbursed for each day the Scholar spends at the Air Force Geophysics Laboratory location during the research year.

III. INFORMATION BROCHURE FOR GEOPHYSICS SCHOLARS

The information brochure was furnished to all appointed Scholars. The purpose was to inform them of their responsibilities and obligations under the program and to furnish guidance in properly completing their invoices for compensation and reimbursement of expenses.

Also appended to this Brochure is a copy of the Budget Memorandum to be completed by the Scholar. This established the program budget against which the individual Scholars could bill SCEEE for their services.

**SOUTHEASTERN
CENTER FOR
ELECTRICAL
ENGINEERING
EDUCATION (SCEEE)**

Management Office
Central Florida Facility
11th & Massachusetts Avenue
St. Cloud, FL 32769
(305) 892-6146

Please reply to:

**INFORMATION BROCHURE
for
AIR FORCE GEOPHYSICS SCHOLARS
on the
1982-1983 AIR FORCE GEOPHYSICS SCHOLAR PROGRAM**

August 1, 1982

INFORMATION BROCHURE
for
AIR FORCE GEOPHYSICS SCHOLARS

Table of Contents

	Page
I. Air Force Geophysics Scholar Obligations.	2
1. Research Goals & Objectives	
2. Final Report	
3. Program Critique	
4. US Air Force-SCEEE Geophysics Scholar Relationship	3
II. Allowable Travel Expenses.	4
III. Instructions for Invoicing for Compensation and Reimbursement.	5
A. Preparation of Brief Report of Effort.	5
B. Preparation of Invoice Format.	6
(1) Dates	
(2) Compensation	
(3) Travel	
(4) Expense Allowance	
IV. Invoice Format	9

I. AIR FORCE GEOPHYSICS SCHOLAR OBLIGATIONS

SCEEE is required by contract to impose certain obligations on you in your status as an AF Geophysics Scholar. This section outlines those obligations, and you should read them thoroughly. You are required to sign and return the statement of understanding before the final processing of your appointment can be completed. The following is a list of these obligations:

1. Research Goals and Objectives: A statement of research objectives must be provided to SCEEE near the beginning of the Research period. It should outline your goals and the approach you intend to follow in researching these goals. It should be submitted with your first invoice for payment. Neither travel expenses nor expense allowances will be reimbursed until after receipt of your statement of research objectives. The report should also clearly indicate the date of your first working day of the research period.
2. Final Report: At the end of your research effort, you are required to submit to SCEEE a completed, typewritten scientific report stating the objective of the research effort, the approach taken, results, and recommendations. Information on the required format is included in a "FINAL REPORT INFORMATION BULLETIN" which will be furnished to you at a later time. However, the final report must be approved by the AF Geophysics Laboratory and then transmitted so as to reach SCEEE by Monday October 10, 1983. Payment of "Compensation" for the final four weeks of your research period cannot be made until SCEEE has received and approved this report in the required format.
3. Program Critique: You will be asked to complete a critique form at the end of your research period regarding your impressions of the program. This critique form should be completed and returned to SCEEE no later than Friday October 14, 1983. Return of this form is a program requirement.

4. U.S. Air Force-SCEEE Geophysics Scholar Relationship:

The U.S. Air Force and SCEEE understand and agree that the services to be delivered by the Air Force Geophysics Scholar under this contract will be non-personal services and the parties recognize and agree that no employer-employee or master-servant relationships will exist between the U.S. Air Force and the Air Force Geophysics Scholar. Non-personal services are defined as work performed by an individual who is responsible for an end item (such as a report), free of supervision of the U.S. Air Force and free of an employer-employee relationship.

As an Air Force Geophysics Scholar, you will not:

- (a) be placed in a position where you are appointed or employed by a Federal Officer or are under the supervision, direction, or evaluation of a Federal Officer, military or civilian.
- (b) be placed in a staff or policy-making position.
- (c) be placed in a position of command, supervision, administration, or control over Air Force military or civilian personnel or personnel of other contractors or become a part of the U. S. Air Force organization.

The services to be performed under the Air Force Geophysics Scholar Program do not require SCEEE or the Geophysics Scholar to exercise personal judgement and discretion on behalf of the U.S. Air Force; rather, the Geophysics Scholar will act and exercise personal judgement and discretion in coordination with the Air Force Geophysics Laboratory Technical Focal Point.

The Air Force will have unrestricted use of and access to all data developed during the period of this appointment.

II. ALLOWABLE TRAVEL EXPENSES

The Geophysics Scholar Program provides potential funding for one round trip between your home and your assigned research location. As soon as you have signed and returned your appointment letter along with the budget sheet, you will be authorized to receive reimbursement for travel expenses as described below.

As outlined in the SCEEE-Air Force Geophysics Scholar Obligations section in this brochure, you are authorized reimbursement for travel to your assigned research location at the start of your research effort and a return trip at the end of the research period. You are expected to make your own arrangements for this travel; after each trip you may invoice SCEEE for reimbursement of allowable expenses in the format described in the Instructions for Invoicing for Compensation and Reimbursement section of this brochure. Closely coordinate your travel plans with your TECHNICAL EFFORT FOCAL POINT AT THE LABORATORY. Your Technical Effort Focal Point is an individual at your research location who will be identified prior to your effort start date.

All travel reimbursements under SCEEE-AF Geophysics Scholar appointments are made according to current SCEEE policy, and deviations from the approved budget are not authorized and will not be reimbursed. In light of these restrictions, you may choose either to travel by commercial airline at coach rates or less, by bus, by driving your private auto, or by a combination. (Please note that funding for rental cars is not allowed; SCEEE will not reimburse this expense. With any of these choices you may claim reimbursement up to the amount for the most direct routing, taking into the account the desirability of routing on interstate highways if you drive your private auto.

Reimbursement for direct route travel by commercial airline will thus be paid on your submission of an invoice to SCEEE following the invoicing instructions referenced above. In the view of the convenience of having a car at the research location, SCEEE strongly recommends that a private auto be used for travel when practical. Reimbursement for mileage when you drive your private auto is at the rate of 20¢ per mile within the routing restrictions mentioned above and will likewise be paid on submission of an invoice prepared according to the referenced instructions.

These items above are the only reimbursable travel allowances authorized for the GEOPHYSICS SCHOLAR appointment. Please be advised that any additional travel expenses incurred during the appointment period will be your personal responsibility. However, travel expenses incurred at the request of the Laboratory should be arranged through your Laboratory Technical Focal Point and will be covered by other travel budgets. This other travel is not covered by the Geophysics Scholar Program.

During the Research period, you will be authorized to receive an expense allowance in lieu of a per diem payment. The rate of this allowance is \$25 per day for a maximum of 365 days. To receive this allowance, you are required to invoice for it as described in the invoicing reference above.

III. INSTRUCTIONS FOR INVOICING FOR COMPENSATION AND REIMBURSEMENT

Attached is a copy of the Invoice Format that you are required to use to obtain compensation or other reimbursement from SCEEE. Note that all disbursements by SCEEE for compensation, travel, and/or other expenses are subject to audit approval, so you must submit receipts substantiating charges invoiced.

In addition, you must prepare and attached to each completed invoice a Brief Report of Effort.

A. PREPARATION OF BRIEF REPORT OF EFFORT

Whenever you submit an Invoice for reimbursement to SCEEE you must also include a brief report describing your activities for the invoice period. To meet this obligation, you must prepare, date, sign, and attach to your completed invoice a Brief Report of Effort describing the research accomplished on the appointment and explain any travel during the invoice period.

This report should include innovative techniques and designs or discoveries which may be disclosed as patents. Rights to any inventions or discoveries shall reside with SCEEE unless determined otherwise by the contracting agency.

The Brief report should never exceed one typewritten page and most often should be considerably shorter than one page.

The following is an example of such a report:

BRIEF REPORT OF EFFORT

Effort has been initiated on pole extraction methods. The modified ordinary least squares technique has been giving fair results. Work is presently being done on finding a better matrix inversion technique for the case when the coefficient matrix is ill-conditioned. Some problems have been encountered with conditioning when the data is filtered.

Travel invoice is for the trip to my research location.

November 19, 1982

B. PREPARATION OF INVOICE FORMAT

Detailed instructions on properly completing your Invoice Format for reimbursement are provided below. Review them carefully.

- (1) In the opening statement of the claim for remuneration on the invoice format, two dates are required. They are the date of your appointment letter from SCEE (in the first blank) and the date you signed that letter accepting your appointment (in the second blank).

Other financial items required on the Invoice Format are for COMPENSATION, TRAVEL, EXPENSE ALLOWANCE. These are now explained individually with examples.

(2) COMPENSATION

- (a) In the first blank to the right of COMPENSATION indicate the number of days you are claiming for compensation in this particular invoice.
- (b) In the next blank enter your SCEE-AF GEOPHYSICS SCHOLAR daily appointment rate as noted in your appointment letter.
- (c) Multiply the number of days times your appointment rate and enter the total dollar amount in the blank at the far right side. Note that the accumulated total number of days you claim on this appointment may not exceed the number authorized in your appointment letter. Some specific details on the compensation days must be provided in the next space.
- (d) Under the heading Date, list the date of each of the days you are claiming for compensation, and opposite each date under the heading Place of Activity indicate where you worked on that date.

A sample entry of a correctly completed COMPENSATION item is shown below:

SAMPLE COMPENSATION ENTRY ON INVOICE

COMPENSATION: (12 days @ \$80.00 per day)..... \$ 960.00 (II)

Date (Specify exact dates)

Place of Activity

Nov. 4-5, 1982

AF Geophysics Laboratory

Nov. 8-12, 1982 (inclusive)

Hanscom AFB, Mass.

Nov. 15, 16, 17, 18, 19, 1982

(3) TRAVEL

- (a) Under the heading Date indicate the date you departed on your trip and the date you arrived at your destination.
- (b) Under the heading Departure/Arrival Time list the departure and arrival times for the corresponding days you listed under Date.
- (c) List your destination under the heading Destination.
- (d) Under the heading Mode, indicate your principal means of conveyance; i.e., commercial air, private auto, etc.
- (e) Under the heading Amount, itemize these expenditures for travel reimbursement.
- (f) Total these travel items and enter the total dollar amount to be reimbursed for travel in this particular submission on the line to the right of Total Travel Expense.

An example of a correctly completed TRAVEL entry is shown below.

TRAVEL EXAMPLE: TRAVEL TO RESEARCH LOCATION BY PRIVATE AUTO

TRAVEL: (Attach receipts for all Airline or Bus charges. Payment cannot be made without receipts attached to invoice.)

<u>Date</u>	<u>Departure/Arrival Time</u>	<u>Destination</u>	<u>Mode</u>	<u>Amount</u>
9/27-10/2/82	0630/1530	AF Geophysics Lab Hanscom AFB, Mass.	Private Auto	\$620.00

One-way trip from home in Eugene, Oregon to Hanscom AFB Mass.
(3100 mi x 20¢/mi = \$620.00)
(mileage at start: 24162; at end: 27262)

Total Travel Expense \$ 620.00 (III)

Please note the following comments about the TRAVEL EXAMPLE:

- i) Travel by your private auto in lieu of a commercial airline is authorized as a convenience to the traveler.
- ii) Travel with use of a privately-owned vehicle will be reimbursed at the rate of 20¢ per mile provided mileage is listed with the start and end mileage on each separate use for all distances over 100 miles.

(4) EXPENSE ALLOWANCE

This item on the invoice will be used to claim the \$25 per day for reimbursement of costs incurred at your assigned research location.

- (a) In the first blank to the right of EXPENSE ALLOWANCE enter the number of days for which you are claiming reimbursement of the expense allowance for costs incurred at your assigned research location.
- (b) Multiply this number by the daily allowance rate of \$25.00 and enter this total dollar amount in the blank at the far right.
- (c) Itemize the specific days for which you are claiming the Expense Allowance reimbursement. It can include weekend days and holidays as well as regular work days.

The following is a sample of a correctly completed EXPENSE ALLOWANCE item.

<u>SAMPLE</u>
<u>EXPENSE ALLOWANCE:</u> (<u>16</u> days @ \$25.00/day)..... \$ <u>400.00</u> (IV)
Specific dates covered: 11/4/82 - 11/19/82 (inclusive)

- (5) You may combine reimbursement requests for compensation, travel, and expense allowance in the same invoice. The total for all items invoiced should be indicated on the blank labeled "GRAND TOTAL FOR INVOICE" in the lower right hand side of line 5.
- (6) **IMPORTANT:** Indicate in the space provided on each invoice the address to which you want the check mailed.
- (7) You must sign and date your invoice in the lower right hand corner as "VENDOR" before it is submitted; you **MUST** also have your Laboratory Technical Focal Point countersign the invoice before it is mailed to SCEEE.

Invoices should be mailed to:

AIR FORCE GEOPHYSICS SCHOLAR PROGRAM OFFICE
SCEEE Central Florida Facility
1101 Massachusetts Avenue
St. Cloud, Florida 32769

AIR FORCE GEOPHYSICS SCHOLAR PROGRAM
INVOICE FORMAT

(Brief Report of Effort Attached)

1. I claim remuneration from SCEEE, Inc. via the terms and conditions of the agreement dated _____ and accepted _____ as follows:

2. COMPENSATION: (_____ days @ \$ _____ per day).....\$ _____ (II)

Date (Specify exact dates)

Place of Activity

3. TRAVEL: (Attach receipts for all Airline or Bus charges. Payment cannot be made without receipts attached to invoice.)

Date

Departure/Arrival Time

Destination

Mode

Amount

Total Travel Expense \$ _____ (III)

4. EXPENSE ALLOWANCE: (_____ days @ \$25.00/day)..... \$ _____ (IV)

Specific dates covered:

5. GRAND TOTAL FOR INVOICE (Sum of II, III, IV above)..... \$ _____ (V)

6. Please send check to following address:

7. I certify that compensation invoice is not concurrent with compensation received from other Federal government projects, grants, contracts, or employment.

X

LAB. TECHNICAL FOCAL POINT SIGNATURE

Location of Faculty _____

Telephone _____

Date _____

X

VENDOR SIGNATURE

Social Sec. No. _____

Telephone _____

Date _____

**SOUTHEASTERN
CENTER FOR
ELECTRICAL
ENGINEERING
EDUCATION (SCEEE)**

Management Office
Central Florida Facility
11th & Massachusetts Avenue
St. Cloud, FL 32769
(305) 892-6146

Please reply to: Dr. Steele
/vi/

BUDGET MEMORANDUM

TO: ALL AIR FORCE GEOPHYSICS SCHOLARS
FROM: AF Geophysics Scholar Program Director
DATE: September 1, 1982
SUBJECT: 1982-1983 Geophysics Scholar Budget

Attached is a partially completed budget for your GEOPHYSICS SCHOLAR Program appointment which we ask you to complete according to the following instructions and return to SCEEE. Note that the budget requires you to complete the travel item.

The travel budget has not been completed for you because you have two options on how you may complete this travel: (1) by way of commercial airline, bus or train or (2) by way of your private auto. The private auto mode of travel is strongly recommended due to the convenience of having an auto at your research location. You may request funding for one round trip between your home and your assigned research location.

The Travel item authorizes reimbursement for either travel by your private auto @ 20¢/mile or travel by commercial airline (coach), bus or train. If you choose to drive your own vehicle on this trip, estimate the total round-trip mileage you will drive and enter that figure in the appropriate blank under "Travel by Private Auto". Then multiply that figure by \$0.20 and enter the dollar amount in the appropriate space at the right under "Travel by Private Auto".

If you choose to travel by way of commercial airline, bus or train call your selected carrier and request the rate for round trip coach fare between your home and your assigned research location. Itemize the rate and write the total in the appropriate space beside "Travel by Common Carrier".

If your travel will be a mixture of common carrier and private auto, enter the estimated figures as described in both of the above cases.

Rental cars are not authorized for the research period and will not be reimbursed by SCEEE unless specific approval has been obtained from SCEEE for exceptional circumstances. Except for the mileage or travel fare, expenses incurred enroute to the research location and return for the research period are not reimbursable.

DO NOT TOTAL THE BUDGET.

After completing the above steps, please enter your name and address in the space provided in the upper left corner of the sheet, enter your research period starting date, sign and enter your social security number on the indicated blank at the bottom right corner, and return the budget sheet to SCEEE with your appointment letter.

TENTATIVE APPOINTMENT BUDGET

AIR FORCE GEOPHYSICS SCHOLAR

Name

Research Period Starting Date

Address

BUDGET ITEM

- | | |
|---------------------------------------------------------------|--------------|
| 1. Time compensation: [260 days @ \$ 80.00 per day] | \$ 20,800.00 |
| 2. Travel | |
| Travel by Common Carrier: [Coach Fare or less] | _____ |
| Travel by Private Auto: [_____ miles @ 20¢ per mile] | _____ |
| 3. Other Expenses: | |
| Expense Allowance: [365 days @ \$25 per day] | 9,125.00 |
| 4. TOTAL | _____ |
| 5. SCEE G&A @ 9.5% | _____ |
| 6. Total from Federal Agency | _____ |
| 7. Total invoicing under your appointment may not exceed: | _____ |

Signature

Social Security Number

IV. QUESTIONNAIRES AND RESPONSES

Questionnaires were sent to the Geophysics Scholars and their technical associates at the Laboratory to obtain their evaluation of the program. The sample questionnaires used are furnished here along with some tabulated summaries of the responses.

1982 - 83 GEOPHYSICS SCHOLAR PROGRAM
EVALUATION QUESTIONNAIRE
(TO BE COMPLETED BY PARTICIPANT)

Name _____
Department (at home) _____
Home Institution _____
Research Colleague: _____
Laboratory Division of Colleague: _____
Brief Title of Research Topic: _____

A. TECHNICAL ASPECTS

1. Was your research assignment within your field of competency and/or interest?
YES ____ NO ____.

2. Did you have a reasonable choice of research assignment? YES ____ NO ____.
If no, why? _____

3. Was the work challenging? YES ____ NO ____.
If no, what would have made it so? _____

4. Would you classify your year activity as research? YES ____ NO ____.
Comment: _____

5. Were your relations with your research colleagues satisfactory from a
technical point of view? YES ____ NO ____.
If no, why? _____

6. Suggestions for improvement of relationship. _____

7. Were you afforded adequate facilities and support? YES ____ NO ____.
If no, what did you need and why was it not provided? _____

PARTICIPANT QUESTIONNAIRE (Page 2 of 4)

8. During this program calendar period of one year: Did you accomplish: more than____, less than____, about what you expected____?

9. Were you asked to present seminars on your work and/or your basic expertise? YES____NO____.

Please list number, dates, approximate attendance, length of seminars, title of presentations (use reverse side if necessary.)

10. Were you asked to participate in regular meetings in your laboratory? YES____NO____.

If yes, approximately how often?_____

11. Did you perform travel on behalf of the laboratory? YES____NO____.

Where to?_____

_____Purpose?_____

12. Give a list of any "special" meetings you may have attended or participated in, such as conferences, visiting lectures, etc.

13. Other comments concerning any "extra" activities._____

14. On a scale of A to D, how would you rate this program? (A high, D low)

Technically challenging	A	B	C	D
Future research opportunity	A	B	C	D
Professional association	A	B	C	D
Enhancement of my academic qualifications	A	B	C	D
Enhancement of my research qualifications	A	B	C	D
Overall value	A	B	C	D

PARTICIPANT QUESTIONNAIRE (Page 3 of 4)

B. ADMINISTRATIVE ASPECTS

1. How did you first hear of this program? _____

2.. What aspect of the program was the most decisive in causing you to apply? _____

3. Considering the time of year that you were required to accept or reject the offer, did this cause you any problems of commitment? YES ___ NO ____.
How could it be improved? _____

4. After your acceptance, was information (housing, location, directions, etc.) supplied to you prior to the research period satisfactory? YES ___ NO ____.
How could it be improved? _____

5. Did you have any difficulty in any domestic aspects (i.e., locate suitable housing, acceptance in community, social life, any other "off-duty" aspects)? YES ___ NO ____.
If yes, please explain. _____

6. How do you rate the stipend level? Meager ___ Adequate ___ Generous ____.

7. Would an expense-paid pre-program visit to the work site have been helpful? Not worth expense ___ Convenient ___ Essential ____.
Please add any other comments you may have. _____

8. Please suggest names (and give source) of organization, mailing lists, or other information you think would be helpful in advertising a continuing program.

PARTICIPANT QUESTIONNAIRE (Page 4 of 4)

9. Considering the many-faceted aspects of administration of a program, how do you rate the overall conduct of this program?

Poor ___ Fair ___ Good ___ Excellent _____. Please add any additional comments.

10. Please comment on what, in your opinion, are:

a. Strong points of the program: _____

b. Weak points of the program: _____

11. On balance, do you feel this has been a fruitful, worthwhile, constructive experience? YES ___ NO ____.

12. Other remarks: _____

THANK YOU

1982-83 GEOPHYSICS SCHOLAR PROGRAM
EVALUATION QUESTIONNAIRE
(TO BE COMPLETED BY PARTICIPANT'S RESEARCH COLLEAGUE)

Name _____ Title _____

Division/Group _____ Geophysics Laboratory

Name of Participant _____

A. TECHNICAL ASPECTS

1. Did you have personal knowledge of the Geophysics Scholar's capabilities prior to arrival at work site? YES ____ NO ____ If yes, where/how/what? _____

2. Was the Geophysics Scholar prepared for his project? YES ____ NO ____

3. Please comment on his preparedness/competency/scope/depth of knowledge of subject area: _____

4. Please comment on the Scholar's cooperativeness, diligence, interest, etc. _____

5. Did work performed by the Geophysics Scholar contribute to the overall mission/program of your laboratory? YES ____ NO ____ If yes, how? _____

6. Would you classify the summer effort under the Geophysics Scholar Program as research? YES ____ NO ____.

Comment: _____

COLLEAGUE QUESTIONNAIRE (Page 2 of 3)

7. Were your relations with the Geophysics Scholar satisfactory from a technical point of view? YES ____ NO ____.

Suggestions as to how they might be improved: _____

8. Do you think that by having this Geophysics Scholar working with your group, others in the group benefited and/or were stimulated by his presence?

YES ____ NO ____ . Comments: _____

9. Do you feel that the introduction to each other, together with the Scholar's work experience and performance could form a sound basis for continuation of effort by the Scholar at his resident institute? YES ____ NO ____.

If yes, how? _____

If no, why not? _____

10. One of the objectives of this program is to identify sources of basic research capability and availability to the USAF. On a scale of A to D, how effective to you think this program will be in that respect? (A high, D low):

A B C D

11. Also, please evaluate (A high, D low):

Opportunity to stimulate group activity	A	B	C	D
Professional association	A	B	C	D
Program administration	A	B	C	D

COLLEAGUE QUESTIONNAIRE (Page 3 of 3)

B. ADMINISTRATIVE ASPECTS

1. When did you first hear of this program? _____

2. Were you involved in the screening and prioritizing of the faculty applicants for your lab? YES _____ NO _____.

If yes, do you have any suggestions for improvement of the procedures used? _____

3. Would an expense-paid pre-program visit to the work site be advisable?

Not worth expense _____ Convenient _____ Essential _____.

Please add any comments: _____

4. Please comment on the program length. Were you as a team able to accomplish more than _____, less than _____, about what you expected _____?

Comments: _____

5. Would you desire another Geophysics Scholar to be assigned to you and/or your group/division? YES _____ NO _____.

If no, why not? _____

6. Other remarks: _____

THANK YOU

SCHOLAR RESPONSES TO QUESTIONNAIRE

The Scholars who responded to our questionnaire indicated they had a reasonable choice of research assignments, were challenged, were afforded adequate facilities and support and enjoyed a satisfactory experience. They endorsed the idea of an early pre-appointment visit before the research period actually started.

Some problems were encountered relative to travel authorizations and procedures in this first pilot year. The questions which received the most extensive comments are noted below. The comments are attached verbatim with only slight editing. These were in regard to the administrative aspects of the program.

ADMINISTRATIVE ASPECTS

QUESTION 9: Considering the many-faceted aspects of administration of a program, how do you rate the overall conduct of this program? The response was fair.

Please add any additional comments.

The people with whom I interacted at SCEEE were friendly and helpful, although there were times when they did not know or had not determined policy matters. There were also some conflicting responses to requests for travel funds; apparently the two chief administrators had not been in communication concerning these requests.

QUESTION 10: Please comment on what, in your opinion, are:

a. Strong points of the program:

The research opportunity is excellent, and the stipend generous; The facilities are of high quality.

The facilities provided the flexibility allowed in one's research project, the stipend was adequate, and the proximity to other scientific institutions (e.g. M.I.T.) was of considerable advantage.

b. Weak points of the program:

There was a noticeable lack of fringe benefits and no concern for remedying this. There were clearly some aspects of policy which had not been well-planned or even planned at all.

The lack of travel money, the lack of publication funds, the invoicing procedure were problems.

QUESTION 12: Other remarks:

The mix up concerning travel was serious. Travel to conferences is necessary to professional growth for a young scientist and is useful to the affiliated institution by associating the institution's name with active research. I strongly encourage SCEEE and the Air Force to devise and follow a clear procedure for this kind of travel.

The program is quite obviously managed in the same way as the 3 month Summer Faculty Program, which leads to some inadequacies in this program. Some are specifically noted below:

a.) The money allotted for travel to the appointment is based on airplane fare when, in general, most people will move their families and belongings when faced with a 12 month stay. It is probably too costly to move all scholars, and certainly impossible to budget in advance. but there are some solutions. For instance, an amount of money could be set aside for moving expenses and then distributed among the scholars in such a way that all received the same fraction of their total moving expenses.

b.) The lack of any health insurance coverage is a problem. Individual health insurance is quite expensive. Some scholars may have suitable arrangements such as coverage on their spouse's policy, but many will not. A simple solution to this is to inform the Scholars, before the appointment starts, of a local agent who could form a group from those Scholars who need insurance. This would relieve SCEEE of the burden of providing insurance while giving the Scholars an easy means of obtaining it at reduced rates.

c.) The invoicing procedure for payment is far from ideal, mainly because of the uncertainty of the time between invoice and payment. The time between mailing the invoice and receiving payment took as little as 6 days and as long as 22 days. This was especially a concern at the beginning of the appointment when the cash flow situation was not as good.

QUESTION 12(c): (continued).

Budgeting properly for essentials such as rent was nearly impossible. One possible solution would be to mail checks on a regular schedule (say bi-weekly) and require invoices on a regular schedule (say monthly). If the invoiced compensation was different than the regular compensation, an adjustment would be made on the following check. If the invoice was not received on time, the following check would be held until it was received. After the first pay period, this essentially reduces to the system used now but delaying the invoice by one pay period. The difference being that all checks would be sent on a regular basis with everyone on the same schedule. The last check should still be held until the final invoice was received in order to settle up the difference.

d.) The method of payment puts the Scholar in an interesting tax situation. Since no withholding is done by SCEEE, the Scholar must file quarterly estimated tax to both Massachusetts and the Federal Government. My failure to realize this in time for the first quarter of the appointment led to my owing a penalty to Massachusetts. It would be helpful to alert Scholars to this so that they can send for the proper information and forms early in the appointment.

e.) Some form of I.D. would have been helpful for use in the evenings and on weekends so as to provide access to the Laboratory at off hours when the Scholars may want to work.

QUESTIONNAIRE RESPONSES FROM SCHOLAR'S RESEARCH COLLEAGUES

The attached responses were abstracted from comments furnished SCEEE by technical personnel at the Geophysics Laboratory who were directly associated with the Geophysics Scholars. Their responses have been slightly edited to put them in a generalized format. /

A. TECHNICAL ASPECTS

1. Did you have personal knowledge of the Geophysics Scholar's capabilities prior to arrival at work site? Yes-5
No--1

Comments:

By reviewing application prior to Scholar's acceptance into the program; Scholar was known by another member of Branch who was a Fellow Graduate Student; from mutual colleagues and published papers; as Ph.D. candidate, Scholar did research with AFGL sponsorship. Scholar visited AFGL prior to selection and gave a seminar on research studies; we had met and talked at a NATO conference.

2. Was the Geophysics Scholar prepared for his project? Yes-5
No--1
3. Please comment on preparedness/competency/scope/depth of knowledge of subject area:

After acceptance, Scholar contacted us to assure the projected goals for this research were in line with and supplemented on-going efforts within the Task.

Excellent in all areas related to geodetic science.

Scholar was well prepared in the technical area. The Scholar mastered the required experimental techniques at AFGL; the project involved an extension of Scholar's Ph.D. work.

Scholar had done graduate work with a most outstanding group in the field. The qualifications in all these respects were superb.

It was a new field for the Scholar who was very highly recommended for intelligence, diligence and hard work.

4. Please comment on the Scholar's cooperativeness, diligence, interest, etc.

Scholar was enthusiastic in his work and interacted very well with other members of our Branch; Outstanding scientist; Scholar worked hard on his project and was cooperative.

In addition to completing an ambitious extension of the Ph.D. studies, Scholar contributed papers to two AMS Conferences, presented a seminar on Scholar studies at AFGL and prepared a report on the studies which is being published in the AFGL Technical Report series.

Unexcelled; Scholar did very well on all counts.

5. Did work performed by the Geophysics Scholar contribute to the overall mission/program of your laboratory? Yes-6

No—0

How?

By completing a very comprehensive literature search and by testing a boundary layer inversion model; Published important contributions by Mites system—one of our most important programs; Scholar brought a new point of view to the project. Scholar's numerical investigation into the decoupling of gust fronts from parent thunderstorms contributed understanding and new data which can be applied in other modeling efforts. Scholar's studies on atmospheric ion chemistry have provided rate coefficients of immediate usefulness in the computer models of the normal and perturbed stratosphere and of re-entry phenomena. Scholar did research that was valuable to us.

6. Would you classify the summer effort under the Geophysics Scholar Program as research? Yes-6

No—0

Comments:

One Scholar presented the results at the 13th Conference on Severe Local Storms, Tulsa, OK, Oct. 1983. The focus of Scholar's work was to develop a improved fundamental understanding of the dynamics and kinematics of gust fronts.

7. Were your relations with the Geophysics Scholar satisfactory from a technical point of view? Yes-6

No—0

8. Do you think that by having this Geophysics Scholar working with your group, others in the group benefited and/or were stimulated by his presence? Yes-6

No—0

Comments:

Scholar brought a new perspective to LSI.

9. Do you feel that the introduction to each other, together with the Scholar's work experience and performance could form a sound basis for continuation of effort by the Scholar at his resident institute?

Yes-4

No--1

If yes, how?

Through contractual effort; Possible contract for further research.

One Scholar is now on the faculty at the University of Lowell. We are seeking his participation in the Summer Faculty Program in 1984 and he is formulating unsolicited proposals to submit to AFGL and AFOSR.

The Scholar has no resident institute; We hope he will stay at AFGL.

Scholar is still doing some work and finishing up the program.

If no, why not?

One project required unique apparatus not available elsewhere.

10. One of the objectives of this program is to identify sources of basic research capability and availability to USAF. On a scale of A to D, how effective do you think this program will be in that respect?

(A high, D low):

A-6

B-0

C-0

D-0

11. Also, please evaluate.

A(HIGH).....D(LOW)

Opportunity to Stimulate Group activity	A-5	B-1	C-0	D-0
Professional association	A-6	B-0	C-0	D-0
Program administration	A-3	B-2	C-0	D-0

B. ADMINISTRATIVE ASPECTS

1. When did you first hear of this program?

About 2 years ago; at the beginning; in Spring 82; from the beginning stages; fall of 1981; from an advertisement.

2. Were you involved in the screening and prioritizing of the faculty applicants for your lab? Yes-2

No--4

If yes, do you have any suggestions for improvement of the procedures used?

Greater publicity at Universities.

3. Would an expense-paid pre-program visit to the work site be advisable?

Not worth expense-0

Convenient-3

Essential-3

Comments:

It is very helpful to establish common goals for the Scholar's research and to recommend slight changes in suggested approaches prior to arrival for work.

A visit is required to properly evaluate candidate.

We should encourage potential applicants to visit AFGL prior to selection period to present seminar.

4. Please comment on the program length. Were you as a team able to accomplish:

more than-2

less than-0

about what you expected-4

Comments:

Quite honestly much was accomplished because of Scholar's productivity and initiative which included doing all his own programming and analysis.

5. Would you desire another Geophysics Scholar to be assigned to you and/or your group/division? Yes-6

No--0

6. Other remarks:

It is a very useful program and introduces people to the basic research needs of Air Force.

Program seems to work very smoothly with a minimum of administrative effort.

More travel money for the Scholars may need to be provided.

APPENDIX I

In this appendix we have listed some program statistics, a list of the meetings Scholars attended or had co-authored presented papers, and a list of the participating Scholars with some background information. The three categories within this appendix are:

- A. Program Statistics
- B. Technical meetings or conferences attended
and bibliography of papers presented or
published while in residence
- C. List of 1982-1983 Geophysics Scholars

A. PROGRAM STATISTICS

A.1 Applications Received (First choice as follows)-----19

Aeronomy (AERO)	3
Meteorology (MET)	5
Optical Physics (OPTICS)	3
Space Physics (SPACE)	7
Terrestrial Sciences (TERR)	1

A.2 Number of Scholars Appointed-----10

Highest Degrees Awarded:	
Number holding Doctorate Degree	9
Number holding Masters Degree	1

A.3 Average Age of Participating Scholars-----30

A.4 The Following nine (9) Technical Disciplines were represented by the 10 initial appointments.

	Number of Scholars
Astrogeophysics	1
Astrophysics	1
Atmospheric Science	1
Chemical Physics	1
Geodetic Science	1
Meteorology	2
Physical Chemistry	2
Space Physics	1

A.5 The Seven (7) Universities from which Scholars received their Graduate Degrees are as follows:

	Number of Scholars
University of Colorado Boulder, Colorado	2
University of Chicago Chicago, Illinois	1
University of Michigan Ann Arbor, Michigan	1
Massachusetts Institute of Technology Cambridge, Massachusetts	3
University of Southern California Los Angeles, California	1
Utah State University Logan, Utah	1
Ohio State University Columbus, Ohio	1

A.6 The Scholars were chosen from a wide variety of geographical locations. The locations of their primary residences are:

West Germany	1
Chicago, Illinois	1
Cambridge, Massachusetts	2
Wellesley, Massachusetts	1
Los Angeles, California	1
Logan, Utah	1
Columbus, Ohio	1
Boulder, Colorado	1
Boston, Massachusetts	1

A.7 Division Assignment of Scholars within the Geophysics Laboratory

	Number of Scholars
Aeronomy Division	2
Meteorology Division	3
Optical Physics Division	2
Space Physics Division	2
Terrestrial Division	1

B. Technical Meetings or conferences attended and Bibliography of papers presented or published while in residence.

B.1 Technical Meetings: Attendees....8

Northeast Computer Show, Boston, Massachusetts
AGU Meeting, San Francisco, California (2 attendees)
AIAA Shuttle Environment Conference, Washington, DC
IAMAP 5th International Symposium, Oxford, England
AGU Conference, Hamburg, Germany (2 attendees)
Conference on Dynamics of Molecular Collisions,
Gull Lake, Minnesota

B.2 Bibliography: Papers....5

Anderson, G.P.
Hall, L.A.
"Attenuation of Solar Irradiance in the
Stratosphere: Spectrometer Measurements between 191 and
207 nm.
Journal of Geophysical Research, 88, 6801-6806 (Aug. 20, 1983)

Lee, Yean
Barnes, Arnold A. Jr.
"An Evaluation of Scavenging of Rocket Effluents"
Proceedings of AIAA Shuttle Environment and
Operations Conference, Washington, DC. (Oct. 31-Nov. 2, 1983)

Seitter, Keith L.
"The Effect of Arc Cloud Generation on Thunderstorm Gust Front
Motion".
Preprint from 13th conference on Severe Local Storms, American
Meteorological Society. (Oct. 17-20, 1983)

Seitter, Keith, L.
Kuo, H.L.
"Instability of Shearing Geostrophic Currents in Neutral and
Partly Unstable Atmospheres"
Fourth Conference on Atmospheric and Oceanic Waves and
Stability, Boston, Mass. (March 23, 1983)

Viggiano, A.A.
Paulson, John F.
"Temperature Dependence of Associative Detachment Reactions"
J. Chemical Physics, 79, 2241-2245 (Sept. 1, 1983)

C. List of 1982-1983 Geophysics Scholars

NAME/ADDRESS

DEGREE/SPECIALTY

Ms. Gail P. Anderson
AF Geophysical Laboratory/LKD
AFGL/LKD
Hanscom AFB, MA 01731
(617) 861-3091

Degree: M.S., Astrogeophysics, 1969
Specialty: Determination of
Stratospheric Ozone Profiles
from Satellite UV
Spectroscopy

Dr. Yehuda Bock
Ohio State University
Geodetic Science and Surveying
404 Cockins Hall
1958 Neil Avenue
Columbus, OH 43210
(614) 457-5599

Degree: M.S., Geodetic Science, 1980
Specialty: Geodetic Space Techniques

Dr. Marion K. Bullitt
Boston College
Dept. of Chemistry
Chestnut Hill, MA 02167
(617) 969-0100

Degree: Ph.D., Physical Chemistry,
1973
Specialty: Physical Chemistry

Dr. Frank P. Colby, Jr.
Mass. Inst. of Technology
Meteorology and Physical
Oceanography
Room 54-1616
Cambridge, MA 02139
(617) 648-3974

Degree: M.S., Meteorology, 1979
Specialty: Pre-storm Boundry Layer,
Severe Storms

Dr. William Denig
Utah State University
Physics Department
UMC-34 Cass
Logan, UT 84322
(801) 750-2357

Degree: Ph.D. Space Physics, 1982
Specialty: Space Physics

Dr. Kenneth G. Kosnik
University of Southern Calif.
Dept. of Chemistry
University Park
Los Angeles, CA 90007
(213)846-5641

Degree: Ph.D. Physical Chemistry,
1982
Specialty: Laser Induced
Photodecomposition,
Laser Development

Dr. Yean Lee
12 Patton Rd.
Wellesley, MA 02181
(617) 235-5834

Degree: Ph.D., Atmospheric Sciences,
1974
Specialty: Cloud Physics and Air
Pollution

C. (continued)

NAME/ADDRESS

DEGREE/SPECIALTY

Dr. Frederic J. Marshall
Mass. Inst. of Technology
Center for Space Research
77 Mass. Avenue
Cambridge, MA 02139
(617) 661-7752

Degree: Ph.D. Astrophysics, 1982
Specialty: Astrophysics

Dr. Keith L. Seitter
University of Chicago
Dept. of Geophysical Sciences
5734 S. Ellis Avenue
Chicago, IL 60637
(312) 962-7326

Degree: Ph.D. Meteorology, 1982
Specialty: Dynamic Meteorology

Dr. Albert A. Viggiano
Max Planck Institut for
Kernphysik
Postfach 103980
D-6900 Heidelberg W. Germany
(6221) 5161

Degree: Ph.D., Chemical Physics,
1980
Specialty: Chemical Kinetics

APPENDIX II

1982-1983 Geophysics Scholar Final Reports

In this appendix we have collected the Statements of Goals and Objectives provided by the Scholars after their consultation with Geophysics Laboratory Technical personnel. A list of their Research Report titles and a compilation of report abstracts are also included.

- A. Goals and Objectives
- B. List of Research Reports
- C. Abstracts of Research Reports.

II.A RESEARCH GOALS AND OBJECTIVES

II.A GOALS & OBJECTIVES

RESEARCH GOALS AND OBJECTIVES

Gail P. Anderson

Air Force Geophysics Scholar

Appointment starting date: 30 September 1982

The importance of the near ultraviolet (UV) solar irradiance to the chemistry and dynamics of the stratosphere is well established. The photodissociation of O_2 in the Schumann Runge bands and Herzberg continuum is the primary source of odd oxygen, which leads to the formation and maintenance of the ozone shield. The photodissociation of ozone, in turn, is responsible for the differential heating of the stratosphere.

Through a combination of balloon, satellite, and rocket measurements of stratospheric ozone, temperature, and solar irradiance, it should be possible to study the photochemical response of ozone near the stratosopause to varying solar, thermal and/or diurnal conditions. The steps in this effort will be to:

- (1) determine the O_2 absorption cross section between 190 and 240 nm and calculate the photodissociation rates of O_2 in the stratosphere, as derived from in-situ balloon measurements;
- (2) analyze the diurnal and thermal response of ozone at the stratosopause, (solar zenith angles from 40-120°) using infrared satellite and rocket measurements;
- (3) establish the differential O_3 column density for the four balloon flights by normalizing the spectral shapes to each other and to a top of the atmosphere standard flux. An estimate of the total O_3 column and the solar flux absolute intensity for a five year period will then provide a base from which to compare solar cycle variability for wavelengths between 191 and 310 nm.

Such a composite picture of the variability of the solar UV flux, the O_2 and O_3 photodissociations rates, and the O_3 diurnal behavior should aid in understanding the dominant photochemical controls of the stratosphere.

RESEARCH GOALS AND OBJECTIVES

Yehuda Bock

Air Force Geophysics Scholar

Appointment starting date: 1 December 1982

In my dissertation research I have investigated algorithms for the establishment and maintenance of a new Conventional Terrestrial System (CTS) based on a network of Very Long Baseline Interferometry and satellite and lunar laser ranging stations. The difference between the new CTS and the present one is that the stations defining the CTS frame can no longer be assumed to be motionless with respect to each other, i.e., they are situated on a deformable earth. These motions are expected to be secular so that if not analyzed they will soon render the CTS frame inconsistent. This will bias estimation of the variations in the earth's rotation rate and polar motion.

The algorithms outlined in my dissertation are general enough to incorporate geophysical evidence of deformations. I have mainly considered, though, deformations of interplate type to be monitored by periodic re-observation of the interstation baseline lengths. Another aspect to be considered is the site stability problem. Local effects need also be modeled on the basis of on-site observations such as gravity surveys and local geodetic nets. I propose to investigate the optimal way to incorporate these observations and their corresponding frames of reference into CTS operations. This has significance for determining and compensating for earth-motion effects on Air Force ground facilities.

In the modeling of local effects and their relation to areal motions, prediction techniques may be necessary. I also propose to investigate this aspect and possibly apply relevant software.

RESEARCH GOALS AND OBJECTIVES

Marion K. Bullitt

Air Force Geophysics Scholar

Appointment starting date: 15 November 1982

Measurements of infrared radiance in the upper atmosphere offer the potential to give information on a variety of quantities and processes such as excited state populations and the energy budget. These measurements are however frequently difficult to interpret at higher altitudes (above 65-70 km) where molecules are not in local thermodynamic equilibrium, i.e. a vibrational population distribution is not necessarily represented by the same temperature as that which represents the translational or rotational population distribution. The difficulty is particularly acute at altitudes where the atmosphere is not optically thin, so that emissions from one region of the atmosphere are self-absorbed in other regions (characterized by different sets of vibrational and kinetic temperatures than the region(s) giving rise to the emissions).

Our work involves developing an approach which was initiated in this research group, as well as evaluating other current approaches. The approach currently taken in this group involves first computing a vibrational temperature profile for the molecule responsible for the emission of interest. This involves identification of processes which excite or deexcite this vibrational mode, such as earthshine, sunshine, and collisional and chemical processes. The vibrational temperature profile is calculated by following the absorption of the infrared source by a specific rotational line: this is done through successive atmospheric layers, until convergence is achieved.

The vibrational temperature profile is then used in a line-by-line calculation of emission from and absorption by successive atmospheric layers, to arrive at a net radiance as viewed by a detector, to compare to experiment.

The initial focus of this work is a continuation of work begun earlier in this group on the CO_2 15 micron radiance. This work is confirming an earlier result, that excitation by O atoms contributes significantly to the excited state populations and hence to the radiance.

Another spectral region to be modelled will be that around 2.9 microns, due to the OH Meinel bands. This may elucidate the role of various chemical and physical processes thought to affect the population of OH emitters. In addition, the fact that the OH density peaks in a relatively thin layer around 75 km offers the opportunity to incorporate possible fluctuations due to gravity waves in the model.

RESEARCH GOALS AND OBJECTIVES

Frank P. Colby, Jr.

Air Force Geophysics Scholar

Appointment starting date: 21 October 1982

GOALS:

1. Develop new/improved theory of inversion layer dynamics in real topography.
2. Develop simple modeling techniques for prediction of inversion layer properties—height, thickness, strength.
3. Develop measurement strategies necessary to operationally measure and forecast inversion behavior.

INITIAL OBJECTIVES:

1. Simple analytic Models
 - A. Literature review—see if any are available
 - B. Develop some of our own
 1. Barotropic 3 or 4 layer model
 2. Baroclinic model (simple form for shear flow)
 3. Parameterization of turbulence (mechanical/buoyant)
2. Models and Parameterizations Available for Inversion Dynamics
 - A. Literature review
Examples: McNider and Pielke, 1981, JAS v.38, 2198-2212.
Deardorff, 1979, JAS v.36, 424-436.

Are any of these useful for real-time forecasting of multipath?

After 1 and 2, examine the feasibility of completing the following:

3. Use 1,2 to develop useful schemes for use on local link and/or at Vandenberg—Make measurements on link and/or use data from Vandenberg for development and verification.
4. Make suggestions for measurement strategies for Vandenberg
 - A. Necessary parameters for operational use
 - B. Case study data needed for model verification

Last month of tenure:

5. Final report to fulfill contract—theory and model experience concerning inversion layer dynamics.

RESEARCH GOALS AND OBJECTIVES

William F. Denig

Air Force Geophysics Scholar

Appointment starting date: 25 October 1982

During my period of study at the USAF Geophysics Laboratory I propose to study the dynamics of the coupled Ionosphere-Magnetosphere system using the data sets available through the Laboratory. These data sets include particle measurements of both thermal and energetic plasma from satellites such as DMSP/F2, DMSP/F4, SCATHA (P78-2), S3-2, and S3-3. Instrumentation includes Langmuir probes and electrostatic analyzers from which the distribution function of the charged particles can be derived. These distributions then help our understanding of the physics of the upper atmosphere and auroral regions by classifying energy sources in relation to geomagnetic field morphology. The above is a fairly broad description and it is my desire to use the expertise of the scientists at AFGL to narrow down my specific topic in accordance with the available data.

My background is in Space Physics specifically related to the observation of plasma instabilities in a space simulation chamber. I have used a variety of wave and particle detectors similar to those used on spacecraft to classify the interaction of an electron beam with a neutral plasma. An application is to the problem of spacecraft charging and neutralization. I have also been involved in several rocket experiments designed to study the vehicle charging problem in the less controlled but more realistic space environment.

My eventual goal is to be deeply involved in the experimental end of Space Physics. During my post-doctoral studies I would like to emphasize data analysis to strengthen my understanding of the physics involved in the upper atmosphere.

RESEARCH GOALS AND OBJECTIVES

Yean Lee

Air Force Geophysics Scholar

Appointment starting date: 13 September 1982

A: Research Objectives

An analysis of the deposition of the exhaust products from clouds formed by space shuttle launch.

B: Approach

It is known that a large amount of water is used for cooling the space shuttle during the firing stage. This large amount of water is vaporized by the exhaust heat and then recondenses to form rainclouds (if meteorological conditions are favorable). Through many different micro-physical processes, the exhaust products may become attached to the cloud and precipitation elements, and then fall out from the cloud together with the raindrops and deposit on the ground.

In the case there are independently generated rainclouds, the removal of exhaust products would be accelerated, because of additional raindrops falling through the exhaust clouds. On the other hand, in the absence of rain, dry deposition is the primary mechanism for removal of exhaust products from the clouds.

The purpose of this study is to construct a mathematical model investigating the fate of airborne contaminants associated with the exhaust clouds. The model will incorporate the physical processes of diffusive attachment, impact collection, accretion, phoretic and electrical influences, and includes consideration of particle and cloud droplet size spectra.

RESEARCH GOALS AND OBJECTIVES

Frederic J. Marshall

Air Force Geophysics Scholar

Appointment starting date: 27 September 1982

As an AF Geophysics Scholar I intend to pursue the following line of research. I will assist the staff at AFGL in the design and testing of flight quality instruments capable of measuring space plasma characteristics. To this end I am presently working on the design of a low energy (approximately 10 eV) electron beam facility to be used in calibration tests of new designs of instruments such as electrostatic analyzers and Faraday cups.

Concurrent with the instrumental work, I will be analyzing results of past space experiments in order to:

a) Interpret these results so as to better the understanding of conditions and processes present in the earth's magnetosphere.

b) Use this knowledge to help determine which plasma characteristics might be measured by future experiments and how best to measure them. One project I am presently considering is analyzing measurements of the flux of precipitating electrons at high altitudes in the F region. This would be accomplished using data from the electrostatic analyzers on the DMSP satellites. Such measurements may be useful in predicting the existence of plasma density enhancements which cause scintillations in satellite radio communications.

I will also continue to investigate the phenomena of particle "burst" seen by the SAS-3 satellite, (as I mentioned in my original proposal) in hopes of determining their origin.

RESEARCH GOALS AND OBJECTIVES

Keith L. Seitter

Air Force Geophysics Scholar

Appointment starting date: 4 October 1982

Gust Front Dynamics

A prominent feature of thunderstorm circulations is the gust front formed by the surface outflow of cool downdraft air. The leading edge of the gust front acts as a wedge to lift potentially buoyant air and release the instability. This may serve to initiate new cells on one flank of the storm or maintain existing ones. A necessary condition for the maintenance of the thunderstorm is that the gust front does not propagate too far ahead of the storm and cut off the inflow of potentially buoyant air. The gust front is often observed to propagate ahead of the storm and cut off the inflow of potentially buoyant air. The gust front is often observed to propagate ahead of the storm during the storm's decaying stage (Wakimoto, 1982), but it is not clear whether this causes the decay of the storm or is a result of it. A better understanding of the coupling between a thunderstorm and its gust front should lead to an improved ability to determine which storms will decay quickly and which will remain vigorous for long periods of time.

This research effort will concentrate on determining the factors governing the coupling of the gust front with the parent thunderstorm. In order for the gust front to remain at the base of the thunderstorm, its propagation speed must not be greater than that of the thunderstorm. It has been shown that once decoupled from the storm, the gust front moves as a density current (Wakimoto, 1982). Its speed is then governed by

$$V = k \left[g d \frac{p' - p}{p} \right]^{\frac{1}{2}}, \quad (1)$$

where d is the depth of the outflow, p' and p are the densities of the cold and warm air, respectively, and k is the internal Froude number. The speed of the thunderstorm, on the other hand, is determined by the wind profile in the depth of the troposphere and the convective available potential energy (Moncrieff and Green, 1972). Observations have not determined if (1) may be applied while the gust front is still coupled to the thunderstorm. If it can, then the gust front will remain coupled provided v given by (1) is less than or equal to the propagation speed of the storm.

A two-dimensional model capable of reproducing the structure of squall-line type thunderstorms has already been developed (Seitter, 1982). This model has simulated the decoupling of the gust front and it is felt that relatively minor improvements in the microphysics of the model will allow the simulated storm to remain vigorous for a longer period of time. This will allow a more complete study of the coupling and decoupling of the gust front.

After rewriting the model code to make more efficient use of the local computer facility and including the microphysical improvements, pure density current motion will be simulated. This will test the model's ability to satisfy (1). A moisture profile can be included in some of these runs to test the model's ability to generate an arc cloud at the leading edge of the density current.

For a prototype experiment, environmental temperature, moisture and wind profiles will be constructed which yield a simulated storm in which the gust front does not decouple from the thunderstorm. In this simulation, the speed predicted by (1) will be compared with the thunderstorm speed to determine if the thunderstorm speed is, in fact, greater than the density current speed. Comparative runs, in which the wind profile is adjusted to yield thunderstorm speeds less than the appropriate density current speed, will be made to test the hypothesis that the gust front will decouple in this situation.

This research should lead to a greater understanding of the gust front decoupling process and possible causes for decoupling. It should also shed light on whether the decoupling of the gust front is a result of the decay of the thunderstorm or a cause of it.

References

- Moncrief, M.W., and J.S.A. Green, 1972: The propagation and transfer properties of steady convective overturning in shear. Quart. J. Roy. Met. Soc. 98, 336-353.
- Seitter, K.L., 1982: The Dynamical Structure of Squall-Line Type Thunderstorms. Ph.D. Thesis, Univ. of Chicago, 141 pp.
- Wakimoto, R.M., 1982: The life cycle of thunderstorm gust fronts as viewed with Doppler radar and rawinsonde data. Mon. Wea. Rev., 110, 1060-1082.

II.B LIST OF RESEARCH REPORTS
1982-83 USAF-SCEEE GEOPHYSICS SCHOLAR PROGRAM

<u>TITLE</u>	<u>RESEARCH ASSOCIATE</u>
1. Stratospheric Determination of Effective Photodissociation Cross Sections for Molecular Oxygen: 191:204 nm	Ms. Gail Anderson
2. Geodetic Accuracy of the Macrometer Model V-1000	Dr. Yehuda Bock
3. Not available	Dr. Marion K. Bullitt
4. A Simple One-Dimensional Boundary Layer Model for both Stable and Unstable Conditions	Dr. Frank P. Colby, Jr.
5. Measurement of a Narrow Latitudinal Region of Intense Antisunward Convective Flow in the Late Morning Time Sector	Dr. William Denig
6. Quenching of Vibrationally Excited NH by N ₂ and H ₂	Dr. Kenneth G. Kosnik
7. An Analysis of Particulate Removal from the Titan Rocket Exhaust Cloud	Dr. Yean Lee
8. An Experimental Method for Calibrating Electron Detectors	Dr. Frederic J. Marshall
9. Numerical Simulation of Thunderstorm Gust Fronts Including Ambient Shear and Arc Cloud Generation	Dr. Keith L. Seitter
10. Reactions of Negative Ions	Dr. Albert A. Viggiano

II.C ABSTRACTS OF GEOPHYSICS SCHOLAR RESEARCH REPORTS

Stratospheric Determination of Effective Photodissociation Cross

Sections for Molecular Oxygen: 191-204 nm

G.P. Anderson

Abstract

Balloon-borne spectrometer measurements of solar ultraviolet irradiance have been used to provide direct estimates of effective photodissociation cross sections (σ_i^e , $i = \Delta\lambda$ interval) for molecular oxygen appropriate for altitudes between 30 and 40 km. The calculations from which σ_i^e can be determined are based on an internally consistent, two-part analysis of ascent spectra. The fine resolution O_2 absorption cross section derived from the fractional transmission between two altitudes is convolved with the calibrated insitu irradiances and then integrated over wavelength, yielding photodissociation rate coefficients (J-values) for the conditions of the flight: 22 April 1981 at 33°N latitude and ~ 50° solar zenith angle. The J-values are then decomposed into the σ_i^e and average attenuated irradiances for the selected wavelength intervals. Photochemical models which incorporate these altitude-dependent O_2 cross sections will reasonably approximate both the local optical attenuation and the photodissociation rate coefficients, since the σ_i^e have been calculated by a simultaneous solution of both the attenuation and the photodissociation equations.

The spectral data used in this study had sufficient resolution to record details in the rotational structure of the Schumann-Runge bands. The effective cross sections, however, are independent of the instrument resolution and agree well with other published theoretical and experimental values.

Geodetic Accuracy of the MacrometerTM Model V-1000

by

Dr. Yehuda Bock

ABSTRACT

The Macrometer model V-1000 is a geodetic positioning instrument that uses the radio signals broadcast by the GPS satellites. The Macrometer is the only GPS user equipment commercially available that does not require any of the GPS codes. The Model V-1000 receives only the 19-cm wavelength signals from GPS although similar instruments, built recently for the U.S. Air Force Geophysics Laboratory, receive both the 19- and the 24-cm wavelengths. In this paper we summarize the results of 18 months of field testing of the V-1000. This instrument, observing four or five satellites for a few hours, yields a point position accurate within several meters in each coordinate: latitude, longitude and ellipsoidal height. All three components of the relative position vector between a pair of points can be determined within 2 parts per million of the distance, given a similar schedule of observations. This accuracy has been obtained for intersite distances from one kilometer to several thousand kilometers.

TMMacrometer is a trademark of Macrometrics, Inc., 185 New Boston St., Woburn, Massachusetts 01801.

A SIMPLE 1-DIMENSIONAL BOUNDARY-LAYER MODEL
FOR BOTH STABLE AND UNSTABLE CONDITIONS

by

Frank P. Colby, Jr.

ABSTRACT

There were two objectives to be accomplished while a Geophysics Scholar at AFGL/LYT: 1) conduct a literature search to determine the state of the art in simple boundary layer models, especially those able to handle steep terrain; 2) encode and test a model which would be capable of simulating dynamic and thermodynamic changes in the atmospheric boundary layer in irregular terrain.

The first objective resulted in the conclusion that models which were available in the literature were either very complex and required much computer space and time, or were so simplified that they omitted important physics.

The second objective proved beyond the reach of a one year appointment. A model was developed which could predict thermodynamic changes during both day and night and which used only the resources of a micro-computer. This model incorporates all the important physics, runs quickly, and furthermore, has the potential to be the backbone for a model which could handle the diurnal variation in mountain/valley or seabreeze wind systems.

MEASUREMENT OF A NARROW LATITUDINAL REGION
OF INTENSE ANTISUNWARD CONVECTIVE FLOW IN
THE LATE MORNING TIME SECTOR

by

William F. Denig

ABSTRACT

A case study is presented of the morphology of the winter polar cap and auroral regions during the recovery phase of a substorm shortly after the start of a geomagnetic storm on June 24, 1976. Measurements of the field-aligned currents, the convective electric field and the distribution of precipitating electrons were made as the S3-2 satellite traversed the southern high latitude region on the dawn-dusk meridian at an altitude of 1400 km. These data show that the antisunward convective flow was very intense and mostly confined to a narrow region of approximately 3 degrees in latitude and immediately poleward of the morningside auroral zone (0900 MLT). Bordering this region of antisunward flow were two balanced large-scale current sheets with the outward flowing current sheet poleward of the inward flowing current. Precipitating magnetosheath electrons detected within the poleward sheet suggest that they have been thermalized to more than 1 keV.

QUENCHING OF VIBRATIONALLY EXCITED NH BY N₂ AND H₂

by

Kenneth G. Kosnik

ABSTRACT

The collisional quenching of electron beam produced vibrationally excited NH($v \leq 3$) by N₂ and H₂ was investigated. The quenching rate of vibrationally excited NH by N₂ and H₂ was determined by time resolved Fourier Transform Spectroscopy. In a preliminary curve fit the NH($v=1$) to NH($v=0$) quenching rate constants for N₂ and H₂ were found to be approximately $10^{-13.7 \pm 0.3}$ cm³/sec. The theoretical kinetic model accurately predicts the time resolved behavior of the experimental NH system at both moderate pressure (15.0 torr N₂) and low pressure (5.0 torr N₂) with varying amounts of H₂ (4.0 torr to 0.1 torr).

Experimental data was taken from nitrogen pressures of 5.0 torr to 50.0 torr; however, the rates for the 50.0 torr runs need to be corrected for the detection system time constant (approximately 50 μ sec) which is determined by the observed low signal to noise ratio. The effect of varying the hydrogen pressure seems to be more pronounced at the high nitrogen pressure (50.0 torr) experiments.

AN ANALYSIS OF PARTICULATE REMOVAL FROM THE TITAN ROCKET EXHAUST CLOUD

by

Yean Lee

ABSTRACT

A simplified analytical model is developed to analyze the removal of particles from the Titan rocket exhaust cloud. The model incorporates the physical process of deposition, impact collection, and includes consideration of particle size spectra. Results of calculations are in good agreement with the measurements and shows that sedimentation plays the most important role in the substantial removal of the mass of material in the elevated ground cloud within the first hour after launch of the rocket. The model allows for easy estimates of the consequences when relevant input data are available.

AN EXPERIMENTAL METHOD FOR CALIBRATING
ELECTRON DETECTORS

by

Frederic J. Marshall

ABSTRACT

A method for calibrating the absolute detection efficiency of electrostatic analyzers is herein described. This experiment is designed specifically to measure the response of electrostatic analyzers to a uniform beam of electrons with known flux density. The experiment consists of a vacuum chamber in which is housed a gold coated quartz window. The window is back illuminated with 2537 Å ultraviolet light which is of sufficient energy to produce photoelectrons in the gold coating. The photoelectrons are accelerated by a selected negative high voltage applied to the gold layer. An electron detector is then placed in the beam where its response versus energy and angle are measured. The geometric factor versus energy for the detector can then be computed from the observed response. The results of using this method to calibrate the DMSP F8 electrostatic analyzers are presented in this report.

Parameters of the experiment are: a 30 cm diameter 1.9 cm thick gold coated quartz window which is used to generate a parallel electron beam of flux density up to 10^6 electrons $\text{cm}^{-2} \text{ s}^{-1}$ with selected energy in the range 10 eV to 50 keV. A monoenergetic beam, $E/\Delta E > 100$, will be maintained even at low energies since the photoelectrons will be ejected from the gold surface with < 0.1 eV of kinetic energy. The beam direction will be maintained at low energies by using a set of Helmholtz coils surrounding the apparatus which will cancel the ambient magnetic field.

NUMERICAL SIMULATION OF THUNDERSTORM GUST FRONTS
INCLUDING AMBIENT SHEAR AND ARC CLOUD GENERATION

by

Keith L. Seitter

ABSTRACT

The thunderstorm gust front is an important feature for both the initiation and maintenance of storms. The gust front can be treated to a good approximation as the leading edge of an atmospheric density current. It is shown that an equation based on the surface pressure rise associated with gust front passage is a much better predictor of gust front speed than the commonly used equations. A two-dimensional numerical model is used to investigate the effects of environmental stability, ambient wind, and arc cloud generation on the gust front motion. It is found that the outflow depth decreases with increasing stability, but increases slightly when propagating through a sheared environment. The production of an arc cloud results in a slower gust front compared to a similar outflow which did not produce a cloud.

Reactions of Negative Ions

by

Albert A. Viggiano

Abstract

The reactions of negative ions are discussed in two parts. In the first part, temperature dependences of the rate coefficients for associative detachment reactions are reported. For the reactions, $O^- + NO$, $S^- + CO$ and $S^- + O_2$ a $T^{-0.74 \pm 0.1}$ variation was found. In addition, the rate coefficients for the reactions of $O^- + C_2H_2$ and $O^- + C_2H_4$ were studied over the temperature range 140-494 K. Both reactions showed appreciable associative detachment channels over the entire temperature range and the rate coefficients for these channels were found to vary as $T^{-0.4 \pm 0.1}$. The second part of this report is a review of all the experiments relating to negative ion-molecule reactions performed in swarm apparatus in the last five years. The topics covered include reactions of atmospheric species, electron affinity determinations, associative detachment reactions and proton transfer reactions.

APPENDIX III

1982-1983 Geophysics Scholar Final Reports

In this appendix are the completed final reports prepared and submitted by the Geophysics Scholars. These reports have been accepted by the Geophysics Laboratory and approved for inclusion in this Program Technical Report.

1982-83 AIR FORCE GEOPHYSICS SCHOLAR PROGRAM

Sponsored by the

AIR FORCE OFFICE OF SCIENTIFIC RESEARCH

Conducted by the

SOUTHEASTERN CENTER FOR ELECTRICAL ENGINEERING EDUCATION

FINAL REPORT

STRATOSPHERIC DETERMINATION OF EFFECTIVE PHOTODISSOCIATION CROSS SECTIONS

FOR MOLECULAR OXYGEN: 191-204 nm

Prepared by:	Ms. Gail P. Anderson
Research Location:	Air Force Geophysics Laboratory Aeronomy Division, Composition Branch
USAF Research:	Dr. R. Earl Good Dr. L. Alton Hall
Date:	September 30, 1983
Contract No:	F49620-82-C-0035

Acknowledgement

The author would like to thank the Air Force Systems Command, the Air Force Office of Scientific Research, the Air Force Geophysics Laboratory, and the Southeastern Center for Electrical Engineering Education for presenting the opportunity to pursue this research avenue.

The support of the Aeronomy Division, AFGL has been critical to the completion of this report. In particular, Dr. L. Alton Hall generously provided both data and expertise throughout the investigation. The general support of the Composition Branch, especially by Dr. R. Earl Good and Mrs. Pauline Beardsley, is also acknowledged. Finally, the additional scientific, logistic, and travel commitments made by Drs. Christos G. Stergis and Rocco S. Narcisi is appreciated.

I. Introduction:

The photochemical behavior of the stratosphere relies strongly on the depth of penetration of solar ultraviolet irradiance, especially over the wavelength intervals in which the dissociation of molecular oxygen occurs. The band structure and magnitude of the O_2 absorption cross section between 190 and 240 nm, coupled with attenuation by O_3 , governs the transmission and deposition of energy to altitudes as low as 20 km.¹ Balloon-borne experiments, including photometer measurements by Brewer and Wilson² and more recent data from spectrometers^{3,4,5}, (Anderson & Hall, 1983, ref. 5, will subsequently be referred to as [A-H]), suggest that the transmission in this wavelength range, particularly near 200 nm, is greater than expected, indicating that the recommended⁶ O_2 Herzberg continuum cross sections may be too large. Photochemical models which incorporate the smaller O_2 cross sections derived from stratospheric balloon data predict significantly different vertical profiles for ozone and several catalytic species.^{1,7}

The accuracy of any balloon derivation of an O_2 cross section is predicated upon the reliability of previously measured O_3 cross sections⁸ plus the correct in-flight detection of pressure and differential O_3 column amounts. Even with the sometimes large error estimates (10-30%) associated with the stratospheric data and analyses, the greater atmospheric transparency at 200 nm has been persistently observed.

These cross sections for absorption by molecular oxygen also enter directly into the calculation of photodissociation rate coefficients (J-values) which describe the efficiency of odd oxygen production at any altitude. In general,

$$J(z) = \int_{\lambda_1}^{\lambda_2} \sigma(\lambda) I(\lambda, z) d\lambda \quad (1a)$$

where: $\sigma(\lambda)$ = photodissociation cross section of species being considered (O_2)

$$I(\lambda, z) = I_0(\lambda) \exp(-\int \tau(\lambda, z)) = \quad (1b)$$

attenuated solar irradiance available at altitude z

$I_0(\lambda)$ = unattenuated solar irradiance

$\int \tau(\lambda, z)$ = total optical depth of intervening atmosphere, (1c)

including nonvertical path length factor

λ, λ_2 = wavelength limits for the dissociation process or interval being considered,

Because of the complexity of the O_2 Schumann-Runge band system, whose cross section varies by orders of magnitude within .1 nm, the wavelength resolution required for this numerical integration is smaller than .01 nm. Excessive computer resources are required to incorporate such repetitive calculations, including the temperature dependencies and slant path variables, into stratospheric photochemical models. This realization has led to the development of various parameterizing schemes which approximate the integral with broad resolution solar irradiance measurements $[\bar{I}_0(\Delta\lambda)]$ convolved with altitude-dependent effective absorption cross sections, $\sigma_{eff}(Z, \Delta\lambda)$,^{9,10} (Allen & Frederick, 1982, ref. 10, will subsequently be referred to as [A-F].)

II. Objectives:

To the extent that balloon-borne spectrometers give both a direct measure of the attenuated local irradiance (equation 1b) and an in-situ derivation of the observed O_2 cross section at the instrument resolution, they can verify the predicted variations of the theoretically-based effective cross sections. In addition, within the error estimates of both the instrument calibration and the atmospherically derived cross sections, the balloon data can also provide an estimate of (1) photodissociation rate coefficients (equation 1a) for the particular flight conditions, (2) the unattenuated solar irradiance, ($I_0(\lambda)$), and (3) the more general J-values corrected to overhead sun conditions, for comparison with the theoretical estimates necessary in modelling efforts.

III. Experiment:

The present analysis is based primarily on the ascent data from the April 1981 flight of a single-dispersion, half-meter Ebert-Fastie spectrometer at Holloman Air Force Base, N.M. The instrument and flight characteristics for the experiment have been described in previous publications.^{5,11} The two detectors, each with its own exit slit, optical path, and resolution, make simultaneous measurements over the wavelength range 191-310 nm. The wide and narrow slit resolutions are 0.1 and .012 nm respectively.

An O_2 absorption cross section has been extracted from the differential transmission between 33 and 39 km.⁵ Because of dual contamination from the instrument (stray light) and the atmosphere (ozone), the absolute error estimates for that derived cross section were large ($\sim 30\%$). However, the relative errors were small, resulting in a cross section which exhibited feature-for-feature replication of much of the theoretically expected, pressure-broadened, Schumann-Runge band structure.

This relative accuracy provides a realistic opportunity to explore the implications of using "effective" cross sections as an approximation in atmospheric models.

On April 20, 1983, the same spectrometer was flown with a broad band filter modification which virtually eliminated instrumental scattered light for the narrow resolution detector. The preliminary data from that flight will be used to augment this study and tighten the error estimates.

IV. Theory:

As Allen and Frederick¹⁰ point out, the detailed O_2 cross section, satisfies two simultaneous relationships. The first governs the attenuation of energy within a layer (Z_1 - Z_2) such that at any wavelength:

$$I(Z_2) = I(Z_1) \cdot \exp(-\sigma(O_2) \cdot \Delta N(O_2)) \cdot \exp(-\Delta\tau(\text{other})) \quad (2)$$

where: $I(Z)$ = measured irradiance at altitude Z

$\Delta N(O_2)$ = incremental increase in column density of O_2 between Z_1 and Z_2 , including slant path factor

$\Delta\tau(\text{other})$ = incremental increase in optical depth due to non- O_2 processes, (O_3 and Rayleigh scattering), also including slant path factor.

The second relationship is the integral equation which defines the photodissociation rate coefficient for O_2 at altitude Z :

$$J(O_2, Z) = \int_{\lambda} \sigma(O_2) I(Z) d\lambda \quad (3)$$

Using "standard atmosphere" approximations for ozone, pressure, and temperature profiles, plus the compilation of $\sigma(O_2)$ by Frederick & Hudson¹³ at better than .004 nm resolution, [A-F] evaluate the exact $J_i(Z)$ over broad wavelength intervals and parameterize a set of effective cross sections, $\sigma_1^e(Z)$ which fit the altitude behavior of the exact solutions

and satisfy the criteria of equations 2 and 3, rewritten as:

$$I_1(Z_2) = I_1(Z_1) \cdot \exp(-\sigma_1^e(Z') \cdot \Delta N(O_2)) \cdot \exp(-\Delta \tau_1(\text{other})) \quad (4a)$$

$$J_1(Z_2) = \sigma_1^e(Z_2) \cdot I_1(Z_2) \cdot \Delta \lambda_1 \quad (4b)$$

where: I_1 = average solar irradiance over the λ_1 interval and

$$\sigma_1^e(Z') = \frac{1}{2} (\sigma_1^e(Z_1) + \sigma_1^e(Z_2)) \sim \sigma_1^e(Z_1)$$

The appearance of the same $\sigma_1^e(Z)$ in both the exponential term of equation 4a and the linear term of equation 4b is based on the assumption that the O_2 optical depth over the selected wavelength interval and within the altitude layer is small ($\ll 1$). Of course, the strong band excursions in the detailed O_2 cross section cause complete extinction to occur unevenly over the spectral and altitude intervals. The accuracy and altitude dependence of the effective cross sections rests then mostly on the choice of relatively small ΔZ increments. [A-F] could formulate almost continuous altitude profiles so this was not a problem. However, even with finite altitude intervals, the restriction is minimized because once the solar irradiance has been extinguished by a strong band within a wavelength interval, that band can make no further contribution to the local J-values or subsequent attenuation.

This same system of non-linear equations (2 & 3), involving $\sigma(O_2)$, can be explicitly evaluated using only the atmospheric balloon data. At high resolution the derived cross section encompasses the detail necessary for accurate integration of equation 3 to yield $J(O_2, Z)$. The integration limits are chosen to coincide with the wavelength intervals of the [A-F] effective cross sections. Substituting equation 4a into equation 4b gives:

$$\sigma_1^e(Z_2) \cdot \exp(-\sigma_1^e(Z_2) \cdot \Delta N(O_2)) \quad (5)$$

$$= \left[J_1(Z_2) / (I_1(Z_1)) \right] \cdot e^{-\Delta \tau(\text{other})} \cdot \Delta \lambda_1$$

All the terms on the right hand side of equation 5 are readily determined from the measurements. The atmospherically derived $\sigma_1^e(Z_1)$ that can satisfy the non-linearities of equation 5 are the values to be compared to the published [A-F] results. Again, the accuracy of these experimentally derived $\sigma_1^e(Z)$'s is dependent on the thickness of the altitude layer and the strength of the incurred attenuation. For $\lambda > 196$ nm, the differential O_2 optical depth is generally less than 2 for the imposed ΔZ of ~ 3 km. At shorter wavelengths where the Schumann-Runge bands become very strong, the accuracy falls accordingly.

To the extent that the atmospherically derived detailed cross section is measurable (usually within the dynamic range of 6×10^{-23} and 4×10^{-24} cm^2 ; see [A-H] for discussion), the total optical depth of the atmosphere can be estimated. Equation 1b can then be used to determine an $I_0(\lambda)$, the unattenuated solar irradiance, for any spectral scan. The repeatability of the spectral detail observed in these "top of the atmosphere" extrapolations lends credibility to the analysis scheme. At those wavelengths where it is possible to obtain an extrapolated $I_0(\lambda)$, more fundamental photodissociation rate coefficients can be formulated that describe the Schumann-Runge and Herzberg continuum behavior appropriate in the stratosphere under arbitrary atmospheric conditions, not just those of the flight.

V. Preliminary Results:

The wavelength intervals over which the effective cross section analysis has been attempted are those of Allen & Frederick¹⁰ (Table I).

TABLE I

Interval	Range	
	cm ⁻¹	nm
1	48600 - 49000	204.1 - 205.8
2	49000 - 49500	202.0 - 204.1
3	49500 - 50000	200.0 - 202.0
4	50000 - 50500	198.0 - 200.0
5	50500 - 51000	196.1 - 198.0
6	51000 - 51500	194.2 - 196.1
7	51500 - 52000	192.3 - 194.2

The first step in the procedure requires the derivation of $\sigma(O_2)$ at fine resolution, as described in [A-H]. The detailed cross section is then convolved pointwise with the measured calibrated irradiances at each wavelength (500 points/nm at .012 nm resolution) and integrated over the selected intervals (eq. 3). This yields the photodissociation rate of O_2 over that interval for the atmospheric conditions of the particular spectral measurement. The inability to determine values of $\sigma(O_2)$ greater than $1 \times 10^{-22} \text{ cm}^2$ (see [A-H] and previous discussion) is generally not important in that the coupled local irradiance measurement should be zero within a strong band. If, because of the instrumental scattering characteristics and noise, a true zero was not recorded by the spectrometer, a zero-fill value for that $I(\lambda, Z)$ was assigned [$I(\lambda, Z) \equiv 0$ if $\sigma(\lambda) > 1 \times 10^{-22} \text{ cm}^2$]. Such an approximation worked well for Schumann-Runge intervals 3, 4, and 5. It was unnecessary for Herzberg continuum intervals 1 and 2 because at those wavelengths the atmosphere is optically

thin. However, for intervals 6 and 7, $J_1(Z)$ was significantly underestimated because of the coupled strong attenuation and relatively low signal-to-noise ratio.

For demonstration purposes the photodissociation rate coefficient for flight conditions over the wavelength interval 191-205 nm has been calculated and appears in figure 1a (heavy line). The error bars are $\sim 30\%$ at 3.2 mb.; the largest individual error source comes directly from the errors in the derived cross section. This particular curve results from the convolution of the detailed spectral measurements with the [A-H] cross section. However, if the instrument resolution had been coarser, the results would have been the same; that is, the data analysis, including the $\sigma(O_2)$ derivation, is internally consistent, relying only on the measured irradiances and the self-determined, instrumentally appropriate $\sigma(O_2)$.

The fine-line curve in figure 1a is an approximation of the photodissociation rate coefficients that would have been inferred from the spectral measurements if the sun had been overhead. This requires extrapolating back to the irradiance at the top of the atmosphere, $I_0(\lambda)$. The accuracy of $J(\theta=0)$ depends on the degree to which that inference is appropriate, which is, of course, only at those wavelengths where $\Delta\tau(O_2)$ does not lead to complete attenuation. Figure 2 shows a portion of the solar irradiance in the optically thin Herzberg continuum region for two independent extrapolations, one from a scan at 39 km, the other from a scan at 37 km. The agreement is excellent; the features are repeatable Fraunhofer solar structure at $\sim .02$ nm resolution. The circles plotted for comparison, are sample .2 nm resolution values from Mount & Rottman¹⁴ [M-R]. The straightline segments are 1 nm averages from [M-R] and this analysis. The $I_0(\lambda)$ values for this experiment average 10-15% higher

than the [M-R] values, but that difference is within the current large error estimates. In other wavelength intervals, where strong O₂ band structure occurs, the extrapolation is imprecise and may even be impossible.

As described in the theory section, the information contained in the vertical behavior of the irradiance depletion relative to the float measurements over broad wavelength intervals can be used to derive effective cross sections. Figure 1b (heavy line) shows $\sigma^e(Z)$ appropriate to flight conditions for the complete 191-205 nm interval. These altitude dependent values were calculated from equation 5 and satisfy equations 4a & b for that wavelength interval. The fine-line curve again is appropriate for overhead-sun conditions and at 3.2 mb (39 km) is normalized to the slant path value because of the lack of any additional information at higher altitudes. The differences between the $\Theta=0$ extrapolation and the $\Theta > 45^\circ$ measurements are real only at and below 33 km.

The arbitrary wavelength interval 191-205 nm demonstrates the basic vertical behavior of both the effective cross sections and related photodissociation rate coefficients. The $\sigma^e(Z)$ and $J(Z)$ will be the same within the instrumental error estimates, independent of instrument resolution. However, photochemical models need to accommodate smaller wavelength intervals because of possible solar variability, minor constituent absorption properties, etc. that may vary as a function of wavelength. Figure 3 (heavy lines) shows the results for wavelength intervals 2 through 6 (from Table 1) as derived from the atmospheric data. For comparison, the approximate [A-F] results (for overhead sun conditions) that encompass the altitude range of the measurements are also included. The curves for

σ_1^e ($i = 2$) (~ 202 - 204 nm) exhibit a similar lack of response to altitude changes in both the experimental and theoretical analysis, but the magnitudes differ by 40%. This behavior is attributable to the difference between the laboratory determinations of the Herzberg continuum used by [A-F], (see their discussion), and the atmospherically determined values. The new laboratory estimates of Yoshino et al.¹⁵ are much closer to the low [A-H] values ($\sim 8.5 \times 10^{-24} \text{ cm}^2$ at 200 nm and $\sim 7.0 \times 10^{-24} \text{ cm}^2$ at 203 nm, respectively).

In general, the vertical behavior for each interval approximates the theoretical predictions. Interval 3 includes most of the Schumann-Runge 1-0 band which is not considered to be predissociative in the [F-H] O_2 cross section compilation and is not incorporated in the [A-F] computations. If the measured band structure were removed and only the underlying continuum included in this analysis, the discrepancy would be slightly ($< 10\%$) larger. Again, the fine-line curves denote the effective cross section for overhead sun, $\sigma_1^e(\theta=0)$, and are most accurate at 33 km and underestimated at 39 km [especially for the strong band intervals 5 (the 2-0 band) and 6 (the 3-0 band)]. The 4-0 and part of the 5-0 bands (intervals 7 & 8 respectively) are so optically thick that the results are not included in the figure, although they give reasonable results at 37 and 33 km (within 30% of the [A-F] values).

Because of the internal consistency of the data set, the general applicability of these derived effective cross sections can be tested directly against the measurements of the solar irradiance as it is attenuated within the atmosphere. Intervals 2 and 3 are sufficiently optically thin that $\sigma_1^e(i=2,3)$ can replace the exact cross sections in either equation 2 (as an exponential term) or equation 3 (as a linear term) with no dis-

cernible errors. Because intervals 4 and 5 center on portions of the relatively strong 2-0 Schumann-Runge band, the thickness of the altitude layers imposed by the experiment force those attenuation terms to become unevenly opaque. A comparison between the measured average irradiance at 33 km and the value predicted from equation 2, with σ_i^e ($i=4,5$) in the attenuation term and $I_1(Z=39 \text{ km})$ as the unattenuated average irradiance, leads to an error of 4% for interval 4 and 8% for interval 5. At 37 km, the errors are 2 & 4% respectively. In each case the effective cross section accounted for too little attenuation. These differences, though small, would be significant in a modelling effort. The potential errors emanating from using σ_i^e ($i=4,5$) in equation 3 are small, leading to less than 4% differences in predicted vs. measured photodissociation rate coefficients, independent of altitude.

VI. Conclusions:

Effective cross sections appropriate for O_2 photodissociation rate calculations have been derived solely from in-situ measurements of stratospheric irradiance. The results agree well with the predicted vertical and zenith angle behavior suggested by Allen and Frederick¹⁰; the absolute magnitude differences, where they exceed the 30% experimental errors, can be attributed to differences in the adopted Herzberg continuum cross sections (relatively large laboratory values [A-F] vs. the relatively small values derived from the balloon data). In addition to the $\sigma_i^e(Z)$'s, this analysis also provides extrapolated estimates of $I_0(\lambda)$ whenever the optical depth at 39 km is < 1.0 . Such extrapolations are, on average, 10-20% higher than the Mount and Rottman (1983) values, but still within the error estimates. The resultant photodissociation rates also agree with theoretical work¹² to within the error estimates, with a persistent tendency to be slightly higher.

VI. Recommendations:

This study was based primarily on data from the 1981 balloon flight which exhibited considerable optical contamination near 200 nm. The instrument has been reflown (4/20/83) with design modifications which significantly improved the signal-to-noise ratio. Figure 4 shows three spectral segments; 4a is a 1981 scan initiated at 33 km, 4b is a 1983 scan at the same approximate altitude, and 4c is a 1983 scan measured at float altitude (39 km). In the wavelength range 192.3 to 192.8 nm the atmosphere is optically thick because of the strong 4-0 bandhead and all three scans should measure zero (0) solar irradiance. In the 1981 analysis, the observed stray light background was estimated over that interval (and others) and removed (see [A-H]); this process is primarily responsible for introducing the large error estimates in the derived quantities. The full analysis described here, when applied to the 1983 data set, should yield more accurate results. A preliminary study has already shown that the low Herzberg continuum estimates will be reproduced.

In addition, solar variability in the critical ultraviolet window region has yet to be established. The 1983 flight, coupled with a reanalysis of the '77, '78, '80 and '81 flights, may lead to a definitive understanding of the natural oscillations of odd oxygen in general and some catalytic species in particular. This may shed additional light on the recuperative properties of the stratosphere.

Finally, recent theoretical work by Blake et al.¹⁶ on the isotopic O₂ absorption properties, ($\sigma(\text{O}_{16}\text{O}_{18})$), may be experimentally verified by a careful analysis of the '83 flight data. If this can be done, the importance of heavy O₂ and O₃ to the stratospheric chemical balance may be ascertained.

References

1. Brasseur, G., A. De Rudder and P.C. Simon, Implication for stratospheric composition of a reduced absorption cross section in the Herzberg continuum of molecular oxygen, Geophys. Res. Lett., 10, 20-23, 1983.
2. Brewer, A.W. and A.W. Wilson, Measurements of solar ultraviolet radiation in the stratosphere, Quart. J. Roy. Meteorol. Soc., 91, 452-461, 1965.
3. Frederick, J.E. and J.E. Mentall, Solar Irradiance in the Stratosphere: Implications for the Herzberg continuum absorption of O₂, Geophys. Res. Lett., 9, 461-464, 1982.
4. Herman, J.R. and J.E. Mentall, O₂ absorption cross sections (187-225 nm) from stratospheric solar flux measurements, J. Geophys. Res., 87, 8967-8975, 1982.
5. Anderson, G.P. and L.A. Hall, Attenuation of solar irradiance in the stratosphere: spectrometer measurements between 191 and 207 nm, J. Geophys. Res., in press, 1983.
6. World Meteorological Organization, The Stratosphere 1981: Theory and measurements, Rep. II, WMO Global Ozone Res. Monit. Proj., NASA/GSFC, Greenbelt, MD, 1982.
7. Froidevaux, L. and Y.L. Yung, Radiation and chemistry in the stratosphere: sensitivity to O₂ absorption cross sections in the Herzberg continuum, Geophys. Res. Lett., 9, 854-857, 1982.
8. Inn, E.C.Y. and Y. Tanaka, Absorption coefficient of ozone in the ultraviolet and visible regions, J. Opt. Soc. Am., 43, 870-873, 1953.

9. Park, J.H., The equivalent mean absorption cross sections for the O₂ Schumann-Runge bands: Application to the H₂O and NO Photodissociation Rates, J. Atmos. Sci., 31, 1893-1997, 1974.
10. Allen, M. and J.E. Frederick, Effective photodissociation cross sections for molecular oxygen and nitric oxide in the Schumann-Runge bands, J. Atmos. Sci., 39, 2066-2075, 1982.
11. Hall, L.A., Solar ultraviolet irradiance at 40 kilometers in the stratosphere, J. Geophys. Res., 86, 555-560, 1981.
12. Frederick, J.E. and R.D. Hudson, Predissociation line widths and oscillator strengths for the 2-0 to 13-0 Schumann-Runge bands of O₂, J. Molec. Spectrosc., 74, 247-256, 1979.
13. Frederick, J.E. and R.D. Hudson, Dissociation of molecular oxygen in the Schumann-Runge bands, J. Atmos. Sci., 37, 1099-1106, 1980.
14. Mount, G.H. and G.J. Rottman, The solar absolute spectral irradiance 11503173A: 17 May 1982, in press, J. Geophys. Res., 1983.
15. Yoshino, K., D.E. Freeman, J.R. Esmond and W.H. Parkinson, High resolution absorption cross section measurements and band oscillator strengths of the (1,0) (12,0) Schumann-Runge bands of O₂, Planet. Space Sci., 31, 33935, 1983.
16. Blake, A.J., D.G. McCoy, S.T. Gibson, Modelling atmospheric absorption in the Schumann-Runge region, Abstract, IAGA/IAMAP Joint Symposium on Middle Atmospheric Sciences, Hamburg, Germany, pg 187, 193.

Figure Captions

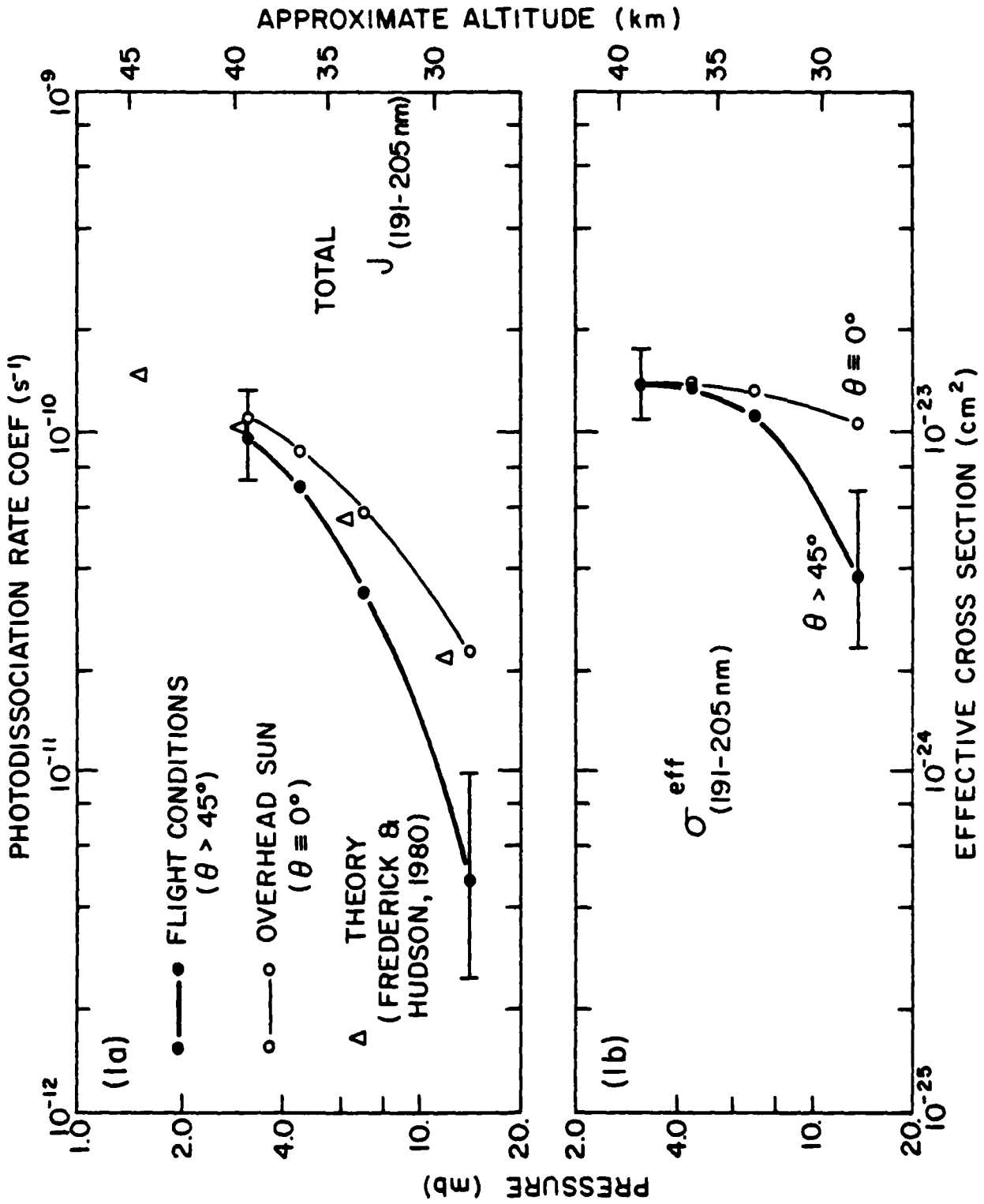
Figure 1a: Experimentally derived photodissociation rate coefficients for the full wavelength interval 191-205 nm.

Figure 1b: Experimentally derived effective cross sections for the same wavelength interval, appropriate for calculating both attenuation and photodissociation within the stratosphere.

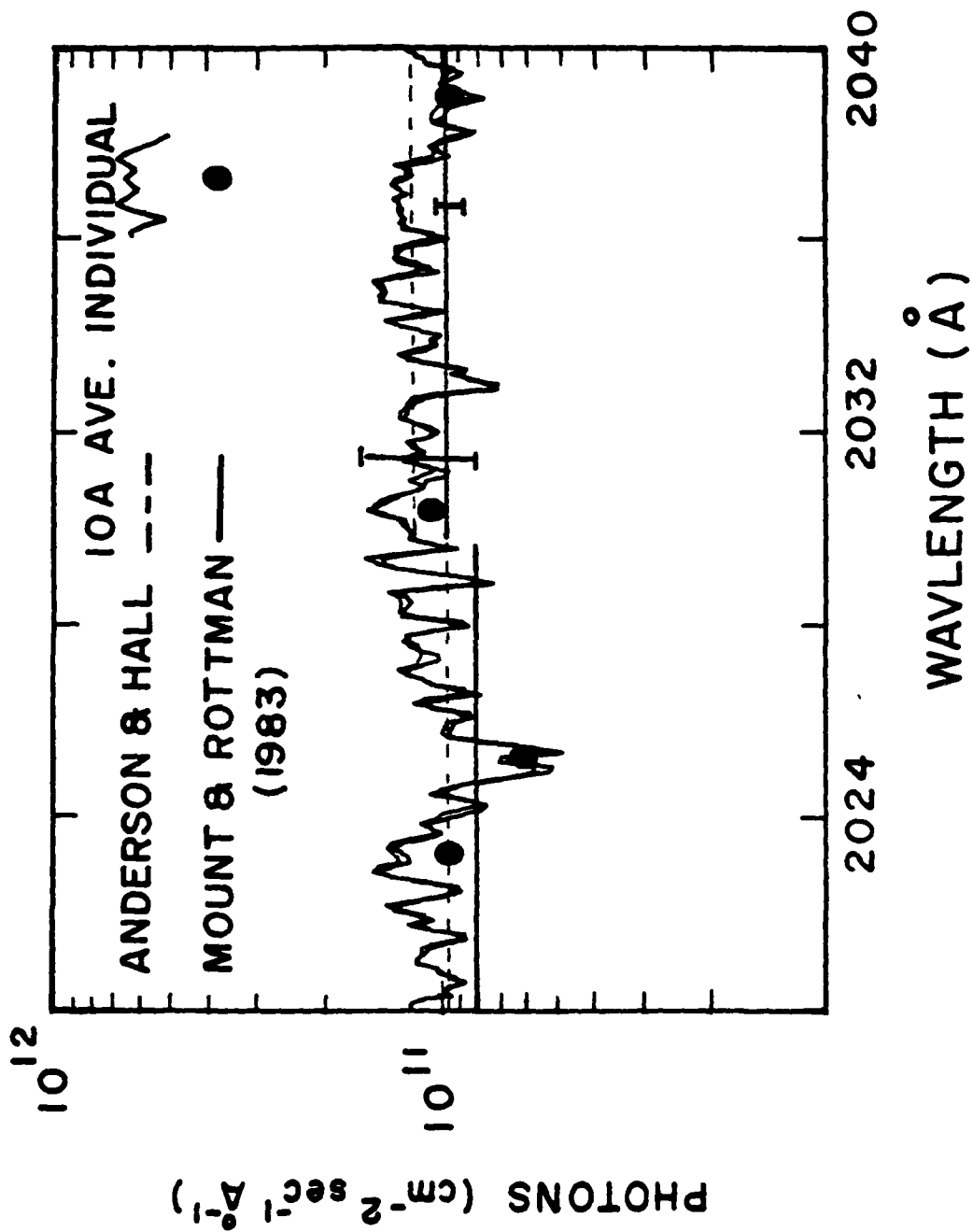
Figure 2: Two independent measures of extrapolated solar irradiance (I_0) for the wavelength interval 2020-2040Å. The repeatability of both the Fraunhofer structure and the absolute magnitude is excellent. For comparison the results of Mount & Rottman (1983) are also presented.

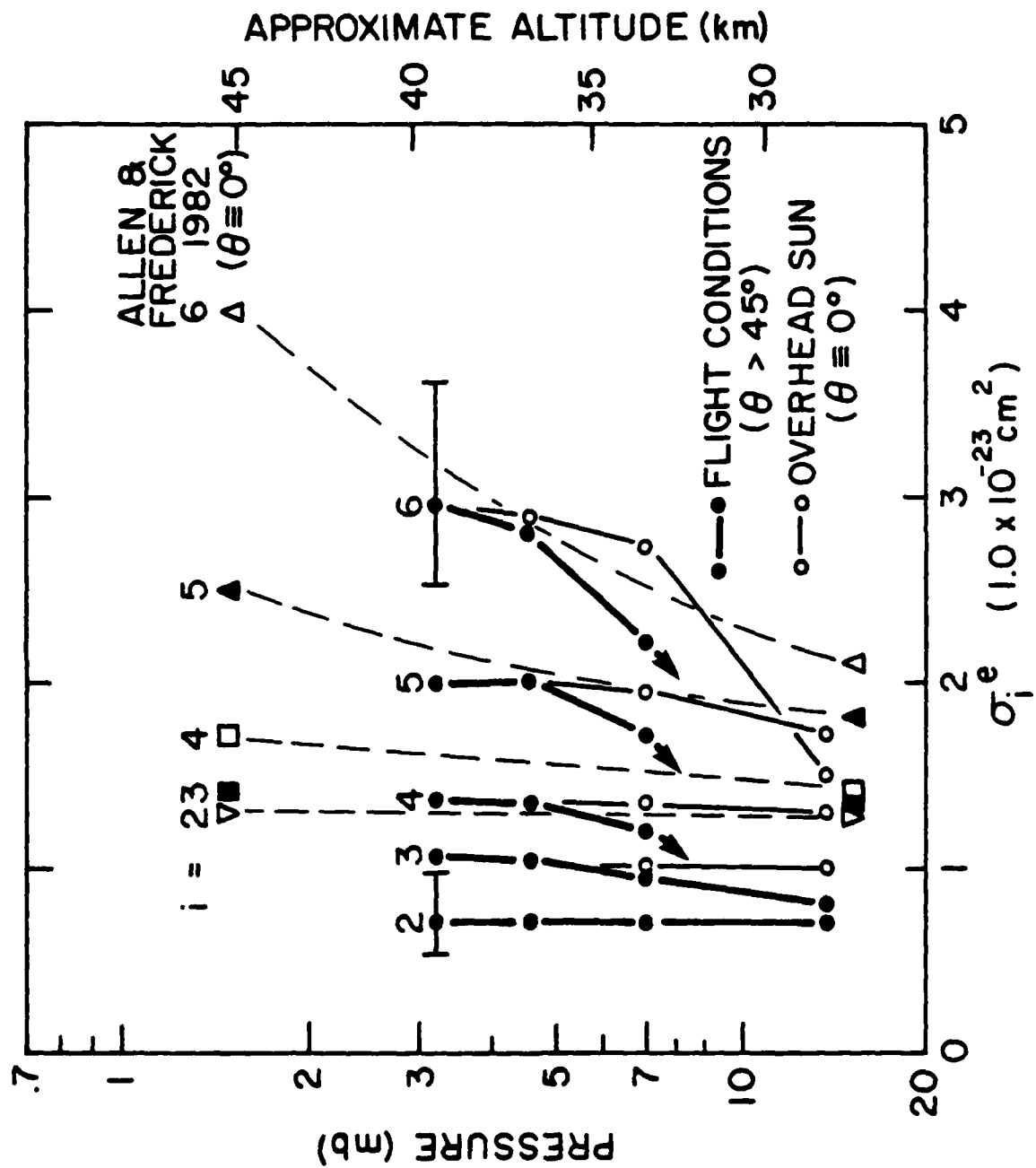
Figure 3: Experimentally derived effective cross sections for the wavelength intervals selected by Allen and Frederick (1982). See Table 1 for wavelength identifications. Because intervals 2 and 3 are located in the region of the Herzberg continuum, the lack of agreement with the theoretical work is expected (see text). The results for the other intervals all fall within the error estimates.

Figure 4: Comparison of solar irradiance spectral data from the 1981 and 1983 flights. The top (1981) and middle (1983) spectra were both measured near 33 km and have undergone similar atmospheric attenuation. However, the addition of a broad band filter to the spectrometer in the 1983 flight removed a significant noise source (as described in the text).

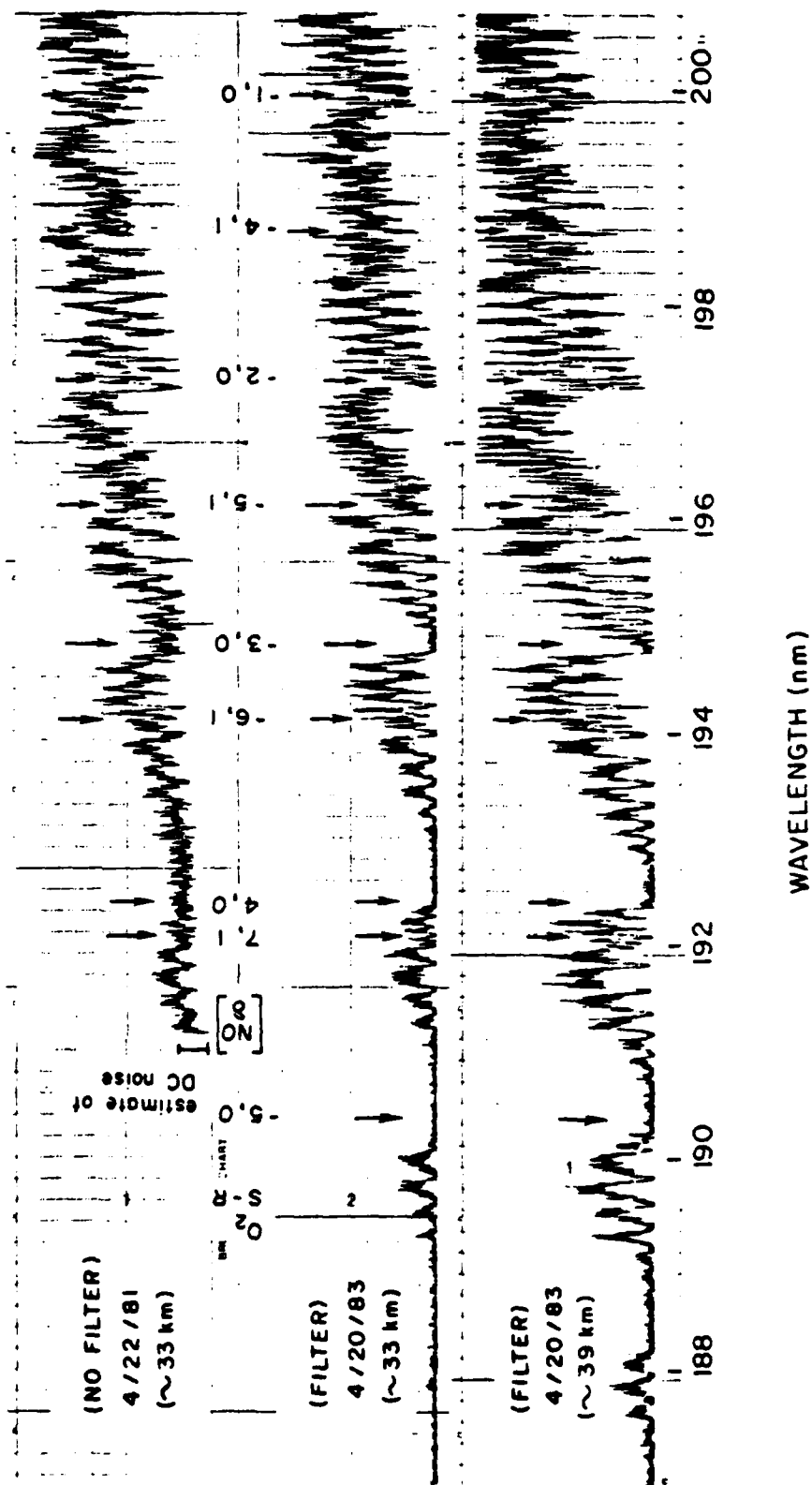


EXTRAPOLATED SOLAR IRRADIANCE





STRATOSPHERIC SOLAR IRRADIANCE (AFGL, HOLLOMAN AFB, N.M.)



Attenuation of Solar Irradiance in the Stratosphere: Spectrometer Measurements Between 191 and 207 nm

G. P. ANDERSON AND L. A. HALL

Air Force Geophysics Laboratory

Measurements made by a balloon-borne, single dispersion spectrometer have been used to investigate the attenuation of solar irradiance in the wavelength region of the O₂ Schumann-Runge bands and the Herzberg continuum. The data cover the altitude range from 28 to 39 km. The fine spectral resolution (0.012 nm) allows transmittance windows in the Schumann-Runge system to be resolved, facilitating the comparison of their characteristic absorption to model calculations. An atmospherically derived O₂ cross section developed in this analysis is significantly lower than the Herzberg continuum values most used in photochemical models.

INTRODUCTION

The importance of the near-ultraviolet irradiance to the chemistry and dynamics of the stratosphere is well established. The photodissociation of O₂ in the Schumann-Runge bands and Herzberg continuum is the primary source of odd oxygen, which leads to the formation and maintenance of the ozone shield. The photodissociation of ozone, in turn, is responsible for the differential heating of the stratosphere.

The optical depths for stratospheric absorption by O₂ and O₃ are of comparable magnitudes in the wavelength range from 195–210 nm. The total O₂ cross section has decreased sharply with increasing wavelength, culminating in the weak continuum absorption, while the Hartley cross section of O₃ is at a broad minimum. This combination of cross-section magnitude and wavelength variability allows the solar irradiance to penetrate deeper into the stratosphere at 200 nm than at surrounding wavelengths. The energy in this ultraviolet window is critical to the chemistry of the stratosphere.

Papers by Brewer and Wilson [1965], Frederick and Mentall [1982], and Herman and Mentall [1982] have suggested that the recommended values [World Meteorological Organization, 1982] for the O₂ continuum cross section are too large. The most recent studies use data from the Solar Absorption Balloon Experiments (SABE 1 and 3). If the smaller values are correct, the chemistry of the stratosphere must be reanalyzed in terms of greater deposition of energy at lower altitudes. These changes would be significant to the photodissociation rates of not only O₂ and O₃ but also minor catalytic reactants [Froidevaux and Yung, 1982; Brasseur *et al.*, 1983].

The analysis presented here is based on observations of the changes in local irradiance as a function of altitude in the window region (191–207 nm) that were made by a balloon-borne, single dispersion spectrometer launched at Holloman Air Force Base, N. Mex., in April 1981. The relatively fine spectral resolution of the instrument (0.012 nm) allows the reconstruction of an approximate ($\pm 30\%$) O₂ cross section with detailed rotational structure. As in the other experiments, the atmosphere has been used as an absorption chamber maintained at both low pressure and long path length. Unfortunately, the large error bars prevent direct

numerical corroboration of the Herzberg continuum values suggested by Herman and Mentall [1982]. However, these results do not conflict with that analysis and do tend to support the adoption of at least the lowest laboratory cross sections for modeling efforts.

EXPERIMENT DESCRIPTION

The instrument used for these measurements is a half-meter Ebert-Fastie spectrometer with a 3600 lines/mm grating used in first order. It was launched on three previous occasions spaced throughout the solar cycle (April 1977, 1978, 1980; see Hall [1981] for instrument description). Figure 1, curve A, shows a typical uncalibrated spectrum (degraded to 0.1-nm resolution) recorded while the balloon was at float altitude (3.2 mbar, ~ 39 km). An entrance slit height change of 50 creates the discontinuity at 275 nm; this served to protect the detectors from the exceedingly bright solar irradiance longward of 280 nm.

Each such scan takes 10 min, and almost all of the small-scale structure is of solar origin. Exceptions to the solar identifications occur between 190 and 200 nm, where the strong O₂ Schumann-Runge 4-0 and 3-0 band heads dominate (192 and 195 nm, respectively). The large atmospheric ozone absorption signature is apparent in the symmetric region of depleted signal centered at 255 nm and extending ± 50 nm. The 'window region' encompasses the entire wavelength span of minimal absorption (191–230 nm). The selected upper wavelength limit for this investigation is 207 nm because the attenuation at longer wavelengths begins to be dominated by ozone.

Curve B in Figure 1 is a scan measured near 7.6 mbar (~ 33 km). Between 235 and 260 nm ozone absorption had totally extinguished the observed solar irradiance; the remaining signal is due to off-axis instrumental scattering from surrounding wavelengths. The 'roughness' of this scattered light is comparable to the random noise of the data and significantly affects the subsequent analysis. The irradiance in the window is only partially depleted, providing energy for the local photodissociation of O₂, O₃, and minor constituents.

ERROR SOURCES

The off-axis scattered-light component of the measured intensity at any wavelength proved to be a major error source. In order to calculate and remove this contribution, a laboratory determination of the spectrometer's scattering

This paper is not subject to U. S. copyright. Published in 1983 by the American Geophysical Union.

Paper number 3C0345.

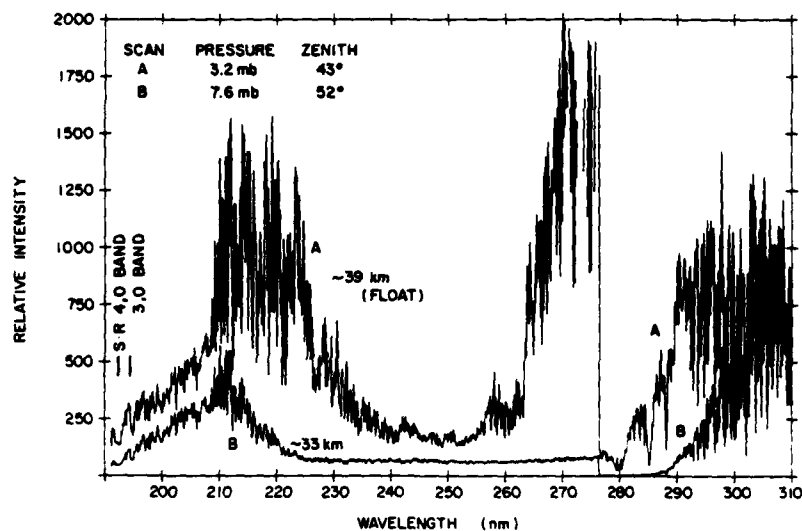


Fig. 1. Uncalibrated spectra at 0.1-nm resolution from the April 22, 1981, balloon flight. The discontinuity near 275 nm is artificially imposed to protect the detectors. The solar irradiance in both scans is severely attenuated by atmospheric ozone, and in scan B it is totally extinguished between 230 and 270 nm. Molecular oxygen absorption (both band and continuum) occurs between 191 and 240 nm.

characteristics distant from line center was convolved with both the measured spectrum and an estimated solar irradiance longward of 310 nm to which the detectors were sensitive ($\lambda < 365$ nm). A self-consistent, analytical formulation was developed that best fit all the known measurements of the true scatter (observed at those wavelengths where the solar irradiance was totally extinguished, such as at the center of the Hartley absorption and at the band heads of the Schumann-Runge system). The actual scattered light exhibits the previously mentioned 'roughness,' which the analytic formulation cannot replicate. Such unremoved structure, which is relatively invariant with altitude, accounts for approximately half of the error in the inferred O_2 cross sections and ultimately limits its dynamic range to between 5×10^{-24} and $5 \times 10^{-23} \text{ cm}^2$.

The other primary error source arises from an instrumental temperature sensitivity. This was recognized in the laboratory and confirmed in the flight data by comparison with a second detector which measured the irradiance at 0.1-nm resolution. (The spectrometer has two optical paths, see Hall [1981].) However, since the laboratory calibration of this sensitivity was not determined over the same range of temperatures as the stratospheric measurements, the correction may introduce an unknown bias. The continuum cross sections presented here are within 10% of those derived from a similar analysis of the broader resolution, temperature-insensitive data.

Finally, since this cross-section derivation is predicated on ratios of intensities observed at different altitudes by the same instrument, no net source of error arises from the laboratory absolute calibration. Therefore, the spectral scans are presented in arbitrary units of counts, with no loss in physical understanding.

DATA ANALYSIS/THEORY

Solar irradiance, as attenuated by atmospheric absorbing species, can be written:

$$I_m(\lambda) = I_0(\lambda) \exp(-\sec \theta \cdot \sum \tau_i(\lambda)) \quad (1)$$

where

- $I_m(\lambda)$ measured irradiance;
- $I_0(\lambda)$ unattenuated irradiance;
- θ solar zenith angle;
- $\tau_i(\lambda)$ $\sigma_i(\lambda)N_i$ = vertical optical depth of i th species;
- $\sigma_i(\lambda)$ absorption cross section of i th species;
- N_i vertical column amount of i th species.

Given a second spectral scan recorded at a different altitude, it is possible to formulate a ratio involving the absorption cross sections, independent of the unknown I_0 .

Dropping the λ notation, the ratio becomes

$$R = I_1/I_2 = \exp(-\sec \theta_1 \cdot \sum \tau_{i,1}) / \exp(-\sec \theta_2 \cdot \sum \tau_{i,2}) \quad (2)$$

where the subscripts 1 and 2 now refer to each scan. For the case of a single absorber ($i = 1$), the inferred cross section would be

$$\sigma = \frac{\ln(R)}{\Delta S} = \frac{\ln R}{(\sec \theta_1 \cdot N_1 - \sec \theta_2 \cdot N_2)} \quad (3)$$

where ΔS is the slant column of absorber in the intervening atmospheric layer. However, in the ultraviolet window region, three major sources of attenuation exist as a result of O_2 , O_3 , and Rayleigh scattering. For purposes of this discussion, ozone and Rayleigh optical depths are assumed to be well known. In particular, the Rayleigh scattering cross section has been approximated (from Goody [1964]) as

$$\beta = 3.55 \times 10^{-25} \cdot \left[\frac{200(\text{nm})}{\lambda(\text{nm})} \right]^4 \text{ cm}^2$$

In the stratosphere it can account for ~10% of the total optical depth, depending on altitude and wavelength. The column amount of scatterers is derived directly from the onboard pressure sensors.

The attenuation caused by ozone absorption can be determined by using the cross section values of Inn and Tanaka

[1953]. (Griggs [1968] measured cross sections within a few percent of the Inn and Tanaka values near 200 nm, but the subtle wavelength dependence has not been redetermined.) The differential ozone profile, $\Delta S(O_3)$, is derived from the long-wavelength region of the spectra, between 294 and 297 nm, where (2) is valid for a single absorbing species. The errors resulting from this column calculation can be significant (5–10%) and are attributed mostly to the pressure interpolation required to accommodate the long scan time during balloon ascent. Errors in the O_3 determination arising from an incorrect calculation of the off-axis instrumental scatter at 295 nm are nil. (The off-axis scatter component contributes approximately 30% to the measured signal at 205 nm but less than 0.5% at 295 nm.) The combined errors (both relative and absolute) in the ozone optical depth could be as large as 15% and would propagate directly into comparable inverse errors in the inferred O_2 optical depth. Thus ozone serves as the primary atmospheric contaminant in this O_2 analysis.

The total optical depth, $\Sigma \tau_i$, in (1) is, then,

$$\Sigma \tau_i = \sigma(O_2) \cdot N(O_2) + \sigma(O_3) \cdot N(O_3) + \beta \cdot N(\text{atm}) \quad (4)$$

Substituting (4) into (2) and solving for $\sigma(O_2)$, yields:

$$\sigma(O_2) = \frac{\ln R - \sigma(O_3) \cdot \Delta S(O_3) - \beta \cdot \Delta S(\text{atm})}{\Delta S(O_2)} \quad (5)$$

This cross section has been derived for wavelengths between 191 and 207 nm. Because a number of independent scans exist over the altitude range of interest, the repeatability of the wavelength behavior of $\sigma(O_2)$ from each pair can be

established. The relative magnitude, however, is best determined from pairs with the optimal path length of O_2 , such that $\tau(O_2) \approx 1$. If the differential column amount is too small, producing insufficient additional absorption, the derived cross section is subject to the errors inherent when working with small differences in large numbers. If the path length is too large, there is insufficient information at the lower altitude. Segments of four scans taken at various altitudes (Figure 2) demonstrate these effects. The strong absorption features beginning at 197 and 200 nm mark the onset of the 2-0 and 1-0 bands of atmospheric O_2 . The weaker features are of solar origin, with some small-scale, repeatable background structure. The scan at 37 km shows only minimally more attenuation than the float scan (at 39 km), while the one at 29 km is almost totally extinguished. Portions of the O_2 cross sections derived from these data by using (5) appear in Figure 3. Cross section 3B, calculated by using $R = I(33 \text{ km})/I(39 \text{ km})$, is the least noisy; the differential column amount of O_2 for this scan pair is $\sim 3 \times 10^{22} \text{ cm}^{-2}$, and the cross sections are of order $1\text{--}3 \times 10^{-23} \text{ cm}^2$, making the optical depth differential approximately unity.

Because of the accurate and repeatable wavelength resolution of the spectrometer, this derived cross section can be used to identify most of the $v'' = 0$ and 1 bands of the Schumann-Runge system longward of 191 nm. However, at some wavelengths the instrumental noise is significant and the atmospheric absorption is virtually complete, resulting in the calculation of erroneous cross-section magnitudes. Whenever the measured irradiance indicates that the atmosphere has become opaque to the spectrometer (i.e., $S_i N \leq 1$), the derived O_2 cross section has been artificially defined as $1 \times 10^{-22} \text{ cm}^2$. The onset of such instrumental opacity

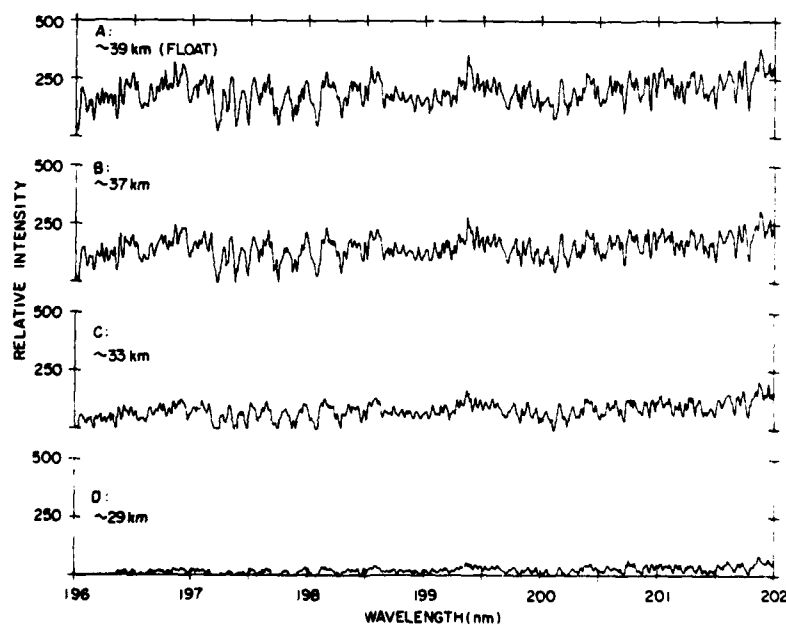


Fig. 2. Portions of four spectra at 0.012-nm resolution with the estimated off-axis scattered light removed. The wider, deeper features (between 197 and 199 nm and, again, near 200 nm) result from band absorption by atmospheric O_2 . The smaller, sharper features are of solar origin. The gradual attenuation with increasing atmospheric penetration at all wavelengths is caused by the continuum absorption of both O_2 and O_3 with a small Rayleigh contribution.

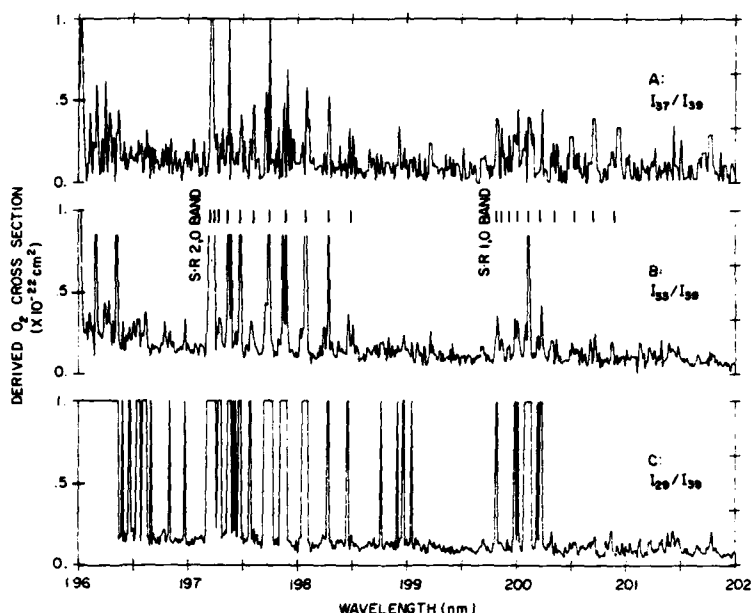


Fig. 3. Stratospherically derived O_2 absorption cross sections determined from the ratios of the spectra in Figure 2. Values of $1 \times 10^{-22} \text{ cm}^2$ indicate those wavelengths where the measured irradiance is insufficient for the derivation. Curve B most clearly resolves the rotational lines of the 2.0 and 1.0 bands. The line identifications are approximate, based on the vibrational doublet tabulations of Ackerman and Biaueme [1970].

varies with the total optical depth and, therefore, altitude and wavelength (see, for instance, Figure 3 near 197 nm). Subsequently, the maximum detectable O_2 cross section for this experiment also varies with altitude and wavelength and can be calculated from (4), assuming appropriate values for $\pi(O_3)$ and τ (Rayleigh). At 200 nm, $\sigma(O_2)_{\text{max}}$ is $\sim 8 \times 10^{-23} \text{ cm}^2$ at 37 km, $\sim 5 \times 10^{-23} \text{ cm}^2$ at 33 km, and $\sim 3 \times 10^{-23} \text{ cm}^2$ at 29 km. At 192 nm the detectability limit falls appreciably ($\sim 1/2$ the 200-nm levels) because the irradiance decreases with wavelength while the noise remains constant. Because of this opacity, the stratospherically derived cross section is only valid between the weaker rotational lines of the Schumann-Runge bands; the individual lines (both widths and amplitudes) cannot be defined, and the values assigned are not intended to replace the carefully measured laboratory results.

RESULTS

The theoretically expected O_2 absorption cross section varies over 3 orders of magnitude between 191 and 210 nm. The cross section presented in Figure 4 (subsequently referred to as F-H) combines the Schumann-Runge band calculations of Frederick and Hudson [1979] for 250 K with a representative Herzberg continuum based on the values of Shardanand and Prasad Rao [1977]. The wavelength resolution has been smoothed to 0.025 nm to improve visual comparison with the results of this study.

A truncated section of the F-H cross section has been expanded in Figure 5 as the shaded area. The overplotted curve is the cross section derived from the balloon-borne spectrometer data with the resolution also degraded to 0.025 nm. The relative agreement between model and measurement in the wavelength regions between the individual

rotation lines is excellent. However, as previously discussed, the maxima of the stronger rotational lines are usually indeterminate in that the measured residual irradiance at 33 km falls within the noise over these wavelength intervals (predictable whenever $\sigma_{\text{FH}} > \sim 5 \times 10^{-23} \text{ cm}^2$). All such instrumentally opaque, indeterminate values are assigned artificial cross sections of $1 \times 10^{-22} \text{ cm}^2$. However, the noise contribution occasionally precludes facile recognition of opacity; see, for instance, the relatively low and equally artificial maximum of the rotational line at 197.6 nm.

Otherwise the locations of almost all the features in the derived cross section correspond to those in the theoretical curve. A major exception is the clearly recognizable 1-0 band beginning at 199.8 nm. It, along with the 0-0 band, is excluded from the F-H cross section, which was compiled for photodissociation calculations only [see Frederick and Hudson, 1980, for details]. Laboratory studies on the predissociation properties of these bands are currently being done by Yoshino *et al.* [1983] and Imre *et al.* [1982]. Whether or not they need to be incorporated into the chemistry of the stratosphere, the 1-0 and 0-0 bands are certainly part of the characteristic O_2 absorption spectrum, and the 1-0 is readily detected with the stratospheric balloon technique.

The lack of relative agreement near 192 nm has two possible explanations. The predicted values are very close to the maximum limit of detectability at this wavelength (see previous discussion), suggesting that the transmittance at 33 km is lost against the background noise (probably the reason for the missing feature at 191.25 nm). However, this particular gap also coincides with the onset of the 7-1 band. A similar cross section derivation, using a scan pair higher in the atmosphere (37 and 39 km) with a correspondingly increased sensitivity to large cross sections, suggests that

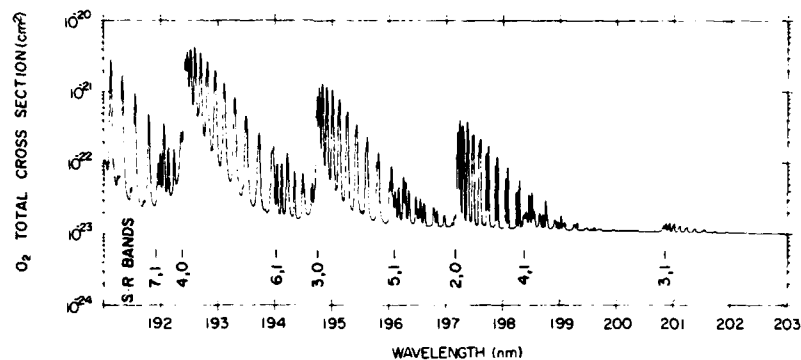


Fig. 4. Theoretical photodissociative O_2 cross section compiled from the Frederick and Hudson [1979] Schumann-Runge values and a representative Herzberg continuum based on Shardanand and Prasad Rao [1977].

the absorption within the 7-1 system might, in fact, be relatively stronger than predicted.

The overall disagreement in magnitude, especially between 193 and 196 nm, is an artifact of the large absolute error bars for the derived values and should not be construed as a suggestion that the Schumann-Runge cross sections be changed. Rather, it offers strong evidence that the experimental errors are of order 30%. (A reasonable change in the off-axis light calculation or the temperature sensitivity could have brought the values into closer agreement, but such a normalization was not justified.) The relative errors (caused by inaccuracies in the wavelength resolution and repeatability) are, of course, very small (<0.005 nm), as evidenced by the feature-for-feature replication between the F-H and

derived cross sections, even so far as to occasionally resolve the splitting of the P and R branches (197.9 nm, for instance).

These results have been plotted on a linear rather than a logarithmic scale in order to emphasize the difficulty of determining an accurate value for the Herzberg continuum. Longward of 200 nm, the average balloon values are less than the theoretical cross section (usually within the $\pm 30\%$ error limits), again in general agreement with the lower values suggested by the SAGE experiments. The potential errors in the derived cross section brought about by both instrumental and atmospheric contamination do not warrant a more detailed comparison at this wavelength resolution.

An average value of the Herzberg continuum cross section for the full wavelength interval 203 to 207 nm is approximate-

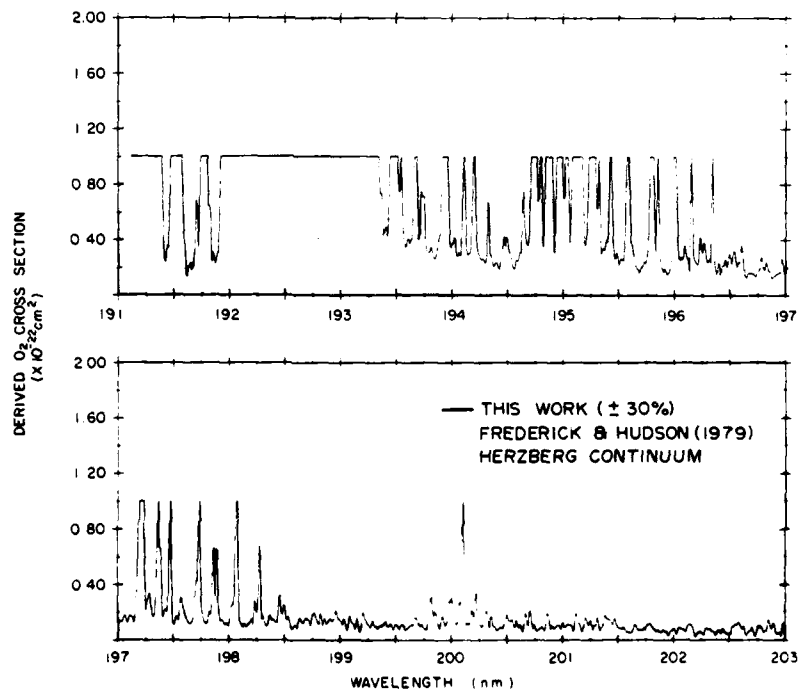


Fig. 5. An overplot of the derived O_2 cross section (solid line) and a truncated cross section from Figure 4 (grey area). Because of stratospheric and instrumental limitations, the dynamic range of sensitivity is from 0.05 to 0.5×10^{-22} cm^2 . Values of 1×10^{-22} cm^2 are artificially assigned to wavelengths for which the derivation is indeterminate. Absolute error bars are $\pm 30\%$ in magnitude, ± 0.005 nm in wavelength.

AD-A144 144

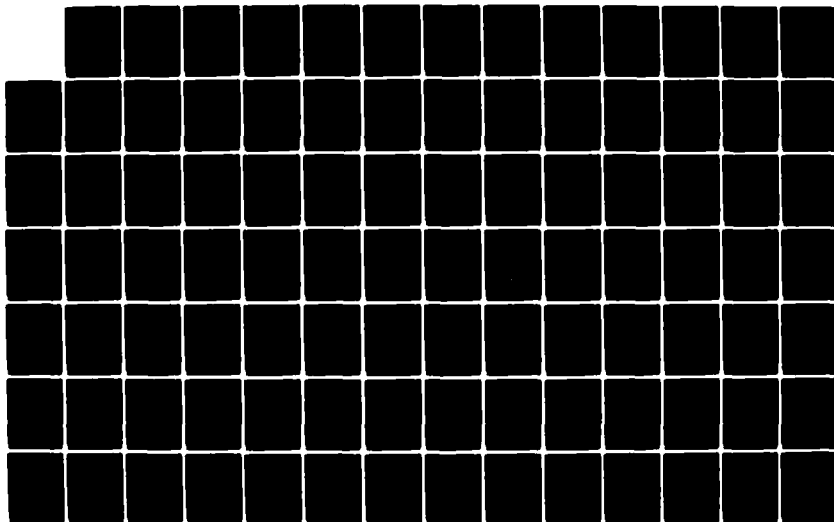
UNITED STATES AIR FORCE GEOPHYSICS SCHOLAR PROGRAM
1982-1983(U) SOUTHEASTERN CENTER FOR ELECTRICAL
ENGINEERING EDUCATION INC S... W D PEELE ET AL. MAR 84
AFOSR-TR-84-0622 F49620-82-C-0035

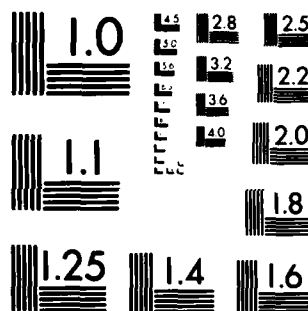
2/3

UNCLASSIFIED

F/G 5/1

NL





MICROCOPY RESOLUTION TEST CHART
NATIONAL BUREAU OF STANDARDS-1963-A

ly $7 \times 10^{-24} \text{ cm}^2 (\pm 30\%)$. (Figure 5 does not include these wavelengths because of the lack of recognizable O_2 band structure.) A similarly derived estimate based on the broader resolution, temperature-insensitive data is also $7 \times 10^{-24} \text{ cm}^2$, while the *Herman and Mentall* [1982] suggested values for that wavelength interval average $6.6 \times 10^{-24} \text{ cm}^2 (\pm 10\%)$. (In their recently published laboratory studies of O_2 cross sections, *Yoshino et al.* [1983] have employed an underlying Herzberg continuum value of $8.5 \times 10^{-24} \text{ cm}^2$ at 200 nm. This is in good agreement with the stratospheric determinations.) The small features in the derived cross section longward of 201.5 nm are caused by residual noise arising from subtraction of the approximation to the off-axis scattered light and tend to replicate solar irradiance variations. This mirroring effect was also seen by *Herman and Mentall* [1982].

CONCLUSIONS

A relative absorption cross section for molecular oxygen has been derived from fine-resolution spectral scans (191–203 nm) measured by a balloon-borne, single dispersion spectrometer. Because of instrumental effects, it is not currently possible to determine a Herzberg continuum cross section ($\lambda \leq 207 \text{ nm}$) to better than 30%; however, even with this large error source, the results support adoption of at least the lowest laboratory values in photochemical models, as previously suggested by *Frederick and Mentall* [1982], and tend to support the values of *Herman and Mentall* [1982].

Because the O_2 rotational structure is so clearly defined, even with ozone contamination and instrumental noise, the technique might be useful for detecting other atmospheric absorbers within the Schumann-Runge bands. *Frederick et al.* [1983] have suggested the importance of NO δ bands in absorption; the strongest would be the 0-0 at $\sim 191 \text{ nm}$, just beyond the wavelength range of this experiment. The instrument will be reflown with a shifted wavelength scale and a long wavelength filter to minimize the off-axis scattering (the primary noise source). In addition to facilitating such a search, these new data should provide both an improved O_2 cross-section determination and a base for comparing the stratospheric attenuation in the ultraviolet window observed in the data from the previous balloon flights.

Acknowledgments. This research was partially sponsored by the Air Force Office of Scientific Research/AFSC, United States Air Force, under contract F49620-82-C-0035.

REFERENCES

- Ackerman, M., and F. Biau. Structure of the Schumann-Runge bands from the 0-0 to the 13-0 band. *J. Mol. Spectrosc.*, **35**, 73–82, 1970.
- Brasseur, G., A. De Rudder, and P. C. Simon. Implication for stratospheric composition of a reduced absorption cross section in the Herzberg continuum of molecular oxygen. *Geophys. Res. Lett.*, **10**, 20–23, 1983.
- Brewer, A. W., and A. W. Wilson. Measurements of solar ultraviolet radiation in the stratosphere. *Q. J. R. Meteorol. Soc.*, **91**, 452–461, 1976.
- Frederick, J. E., and R. D. Hudson. Predissociation line widths and oscillator strengths for the 2-0 to 13-0 Schumann-Runge bands of O_2 . *J. Mol. Spectrosc.*, **74**, 247–256, 1979.
- Frederick, J. E., and J. E. Mentall. Solar irradiance in the stratosphere: Implications for the Herzberg continuum absorption of O_2 . *Geophys. Res. Lett.*, **9**, 461–464, 1982.
- Frederick, J. E., R. B. Abrams, and P. J. Crutzen. The delta band dissociation of nitric oxide: A potential mechanism for coupling thermospheric variations to the mesosphere and stratosphere. *J. Geophys. Res.*, **86**, 3829–3835, 1983.
- Froidevaux, L., and Y. L. Yung. Radiation and chemistry in the stratosphere: Sensitivity to O_2 absorption cross sections in the Herzberg continuum. *Geophys. Res. Lett.*, **9**, 854–857, 1982.
- Goody, R. M., *Atmospheric Radiation: Theoretical Basis*. Appendix 12, Oxford University Press, New York, 1964.
- Griggs, M., Absorption coefficients of ozone in the ultraviolet and visible regions. *J. Chem. Phys.*, **49**, 857–859, 1968.
- Hall, L. A., Solar ultraviolet irradiance at 40 kilometers in the stratosphere. *J. Geophys. Res.*, **86**, 555–560, 1981.
- Herman, J. R., and J. E. Mentall. O_2 absorption cross sections (187–225 nm) from stratospheric solar flux measurements. *J. Geophys. Res.*, **87**, 8967–8975, 1982.
- Imre, D., D. H. Katayama, J. L. Kinesey, and R. W. Field. Laser excitation spectrum of the Schumann-Runge (0, 12) band of oxygen, paper presented at Molecular Spectroscopy Symposium, Dep. Army and Ohio State Univ., Columbus, Ohio, 1982.
- Inn, E. C. Y., and Y. Tanaka. Absorption coefficient of ozone in the ultraviolet and visible regions. *J. Opt. Soc. Am.*, **43**, 870–873, 1953.
- Shardanand, and A. D. Prasad Rao. Collision-induced absorption of O_2 in the Herzberg continuum. *J. Quant. Spectrosc. Radiat. Transfer*, **17**, 433–439, 1977.
- World Meteorological Organization. The Stratosphere 1981: Theory and Measurements. *Rep. 11*, WMO Global Ozone Res. Monit. Proj., NASA/GSFC, Greenbelt, Md., 1982.
- Yoshino, K., D. E. Freeman, J. R. Esmond, and W. H. Parkinson. High resolution absorption cross-section measurements and band oscillator strengths of the (1, 0)–(12, 0) Schumann-Runge bands of O_2 . *Planet. Space Sci.*, **31**, 339–353, 1983.
- G. P. Anderson and L. A. Hall. Air Force Geophysics Laboratory, Bedford, MA 01731.

(Received December 7, 1982;
revised February 22, 1983;
accepted February 24, 1983.)

1982-1983 AFGL-SCEEE GEOPHYSICS SCHOLAR PROGRAM

Sponsored by the

AIR FORCE OFFICE OF SCIENTIFIC RESEARCH

Conducted by the

SOUTHEASTERN CENTER FOR ELECTRICAL ENGINEERING EDUCATION

FINAL REPORT

GEODETIC ACCURACY OF THE MACROMETER MODEL V-1000

Prepared by:	Dr. Yehuda Bock
Research Location:	Air Force Geophysics Laboratory (Geodesy and Gravity Branch)
AFGL Research Contact:	Dr. Thomas P. Rooney
Date:	December 26, 1983
Contract Number:	F49620-82-C-0035

Acknowledgements

The author would like to thank the Air Force Systems Command, the Air Force Office of Scientific Research and the Southeastern Center for Electrical Engineering for providing him with the opportunity to spend the last year at the Air Force Geophysics Laboratory, Hanscom Air Force Base, MA.

The author wishes to thank Dr. Donald H. Eckhardt and Dr. Thomas P. Rooney of AFGL for their support. He is also grateful to Prof. Charles C. Counselman III, Dr. Sergei A. Gourevitch, Dr. Robert W. King Dr. Rick I. Abbot and Mr. A.R. Paradis of MIT for their help. The author would like to express his appreciation to the U.S. National Geodetic Survey, Geo/Hydro, Inc., and Macrometrics, Inc. for providing field data.

Introduction

Dramatic improvements in the accuracy, the efficiency, and the range of geodetic control applications through the use of various NAVSTAR Global Positioning techniques have been anticipated in several articles published in the past few years (e.g., Counselman and Shapiro, 1979; MacDoran, 1979; Fell, 1980; Bossler et. al., 1980; Counselman and Gourevitch, 1981). The introduction, in 1982, of the Macrometer Interferometric Surveyor (Counselman and Steinbrecher, 1982) has proven that the advantages of the Global Positioning System (GPS) are indeed major. With one to three hours in the field and one-half hour of data processing, Macrometer Model V-1000 field units and the P-1000 processor have been yielding first-order baseline determinations on a routine operational basis. Baseline vectors between pairs of points have been estimated to an accuracy of 1:200,000-1:500,000 in all three components for lengths ranging from one to sixty kilometers (Counselman, 1982; Counselman, et. al., 1983). This performance has been independently verified by the Federal Geodetic Control Committee (FGCC) using terrestrial surveys as standards of comparison (Hothem and Fronzcek, 1983).

Published reports have not, however, included any results from measurements of baselines longer than 60 kilometers. Neither have any point-positioning results been published. Thus, two misconceptions have become widely held: first, that the length of the baseline that can be measured accurately with the Macrometer is somehow limited to about 60 kilometers; and second, that the potential applications of the Macrometer are limited to relative positioning; in other words, that "point" positioning cannot be done with the Macrometer.

The emphasis on short-baseline relative positioning results in publications to date has reflected the importance of such measurements both in commercial surveying and in crustal-motion monitoring in the neighborhoods of active faults. However, the potential application of GPS for the establishment of geodetic control on larger scales, up to the global scale, is also important. The latter application is a particular concern of the International Association of Geodesy. We take this occasion, therefore, to report on our use of the Macrometer Model V-1000 to measure several baselines with lengths up to 3600 kilometers, and to determine the "geocentric" positions (for example, with respect to WGS 72) of single points. Our results indicate that the Macrometer Model V-1000 can perform all the geodetic functions of Navy Navigation Satellite System (NNSS) Doppler receivers (see, e.g., Kouba, 1983), but more accurately and efficiently.

We also describe a more advanced version of the Macrometer receiver which has been built for the U.S. Air Force Geophysics Laboratory, and which promises to yield better accuracy than the V-1000.

The Global Positioning System

The GPS offers several advantages over the NNSS for geodetic positioning applications. These include better satellite oscillator stability, reduced ionospheric refraction effects due to the higher frequencies of the signals, and reduced uncertainty in the gravity field and atmospheric drag because of the higher orbits. Most important, though, is that with the planned 18-satellite configuration, at least four satellites will always be visible with 20° or higher elevation angles from any point on the earth's surface. This fact makes it possible to point-position with GPS to the same accuracy as with NNSS but with a shorter observing time. The simultaneous visibility of multiple satellites also allows greater accuracy and efficiency in relative positioning through the use of differenced observables.

The higher and different orbits of the GPS satellites also offer several disadvantages relative to NNSS. The GPS satellites move more slowly, so that the Doppler shifts of the received signals are smaller. Also, the same viewing geometry is repeated pass after pass. With the higher orbits, the effects of solar radiation pressure on the satellites are more serious. A further disadvantage of the GPS concept is that a user requires knowledge of the precise P code in order to navigate accurately in real time. Lack of access to this code would seem to preclude accurate geodetic results, too.

The Macrometer System

The Macrometer system has been designed to exploit the advantages of GPS while minimizing as much as possible the disadvantages. The ability of the model V-1000 to track the phases of the signals from up to six satellites simultaneously is crucial. To use the model V-1000 no knowledge of any GPS code is required, but satellite ephemerides and UTC synchronization must be obtained from external sources. (Satellite orbits may, however, be determined from Macrometer observations, as we discuss below.) Because the Macrometer system cannot obtain ephemerides in real time from the satellite signals, it cannot be used for real-time accurate navigation. A description of the Macrometer system can be found elsewhere (Counselman, 1982; Counselman and Steinbrecher, 1982; Counselman et al., 1983; Bock, 1983; Macrometrics, Inc., 1983) and will not be repeated here.

The Model V-1000 is primarily designed for rapid first-order "short" baseline surveying and uses only the 19-cm-wavelength ("L₁") signals transmitted by the GPS satellites. Thus, the positioning accuracy with this equipment can be limited by ionospheric refraction effects. Still, it is anticipated that with the present equipment and enhanced data processing, 1 ppm accuracy can be achieved routinely. Precision of 1 ppm was demonstrated in the FGCC tests.

Two-frequency instruments similar to the V-1000 but that also receive the 24-cm-wavelength ("L₂") GPS signals have been built for the U.S. Air Force Geophysics Laboratory. With these instruments an ionospheric refraction correction can be made. However, the geodetic positioning accuracy will still be limited by the accuracy of the GPS satellite ephemerides. With orbit determination by dual-frequency instrumentation at VLBI stations, relative positioning accuracy should improve by an order of magnitude, i.e., to 0.1 ppm ($1:10^7$). This accuracy is needed for some applications such as the monitoring of crustal deformations and the maintenance of a conventional terrestrial reference frame (Bender, 1981; Bock, 1982). The ultimate limit on accuracy will probably be set by the variability of the wet component of the troposphere.

The dual-frequency equipment has been used at two VLBI stations (the Haystack Observatory in Westford, Massachusetts and the United States Naval Observatory Timing Station in Richmond, Florida) 2045 km apart. Preliminary results from this baseline indicate that the observations with this equipment do enable the effects of ionospheric refraction to be eliminated at the about the centimeter level. However, all of the results presented here were obtained with the single-frequency model V-1000.

The Macrometer Phase Observables

The output of each of the six channels of a Macrometer receiver is a precise measurement of the difference between the phase of the carrier signal received from a GPS satellite, and the phase of a reference signal generated within the receiver, at a series of epochs determined by a clock in the receiver. We shall refer to this observable as a "oneway phase" measurement. All six channels are sampled simultaneously, usually at 60 epochs equally spaced throughout a user-specified time span.

The received signal phase differs from the satellite transmitted phase by an amount that varies due to the relative motion of the satellite and the receiver, and also to tropospheric and ionospheric refraction. Phase can only be measured modulo one cycle, so the measurements are biased by an unknown integral number of cycles. Added to this integer-cycle bias is the phase difference between the satellite and receiver oscillators. Thus, instabilities in the relative phases of the satellite and the receiver oscillators also affect the measured phase. Phase errors equivalent to propagation-path changes of a few millimeters, at most, are caused by reflections of the satellite signals from objects near the Macrometer antenna. A trivial amount of random noise, equivalent to about 1 mm, is introduced as the signal passes through the receiver.

Differencing of the measured phases of two satellites observed simultaneously by one receiver cancels the effect of instability of the receiver's reference oscillator. Differencing of the phase measured

simultaneously by two receivers observing the same satellite cancels the effect of instability of the satellite's oscillator. The doubly-differenced observable obtained by differencing both between satellites and between receivers is essentially free of any oscillator instability effects, and contains only an integer-cycle bias in addition to refraction errors. Because refraction effects tend to cancel when the difference between closely spaced receivers is taken, the doubly-differenced observable is the most valuable type for the determination of a short baseline (between two receivers) with extreme accuracy. For point positioning with a single receiver, a singly-differenced, between-satellites observable is valuable. For satellite orbit determination with multiple receivers, the singly-differenced, between-receivers observable is valuable. Because this last observable is sensitive to any receiver oscillator instability, receivers to be used for orbit determination should be equipped with atomic frequency standards. Otherwise, for either relative positioning or single-point positioning, the built-in quartz crystal oscillator of the V-1000 may serve as the frequency standard.

Methods of Analysis

Several methods of analyzing phase data have been advanced (e.g., by Bossler, et al., 1980, by Counselman and Gourevitch, 1981, and by Goad and Remondi at this symposium). The results that we present here were obtained by a conventional weighted least squares algorithm in which all of the relevant parameters, e.g. geodetic coordinates and phase biases, are adjusted simultaneously to fit the phase observations, whether one-way, singly-, or doubly-differenced. The space available here does not permit detailed descriptions of the various mathematical models employed. These descriptions will be given in a journal article, now in preparation.

Point Positioning Results

In order to test the accuracy of point positioning, we have analyzed Macrometer data from several sites for which accurate (submeter) WGS 72 coordinates were available. At the times of these observations only five NAVSTAR satellites were operating (at some times only four). The unstable, crystal clock of NAVSTAR 1 always made observations of this satellite useless for point positioning. NAVSTARs 3 and 4 had rubidium frequency standards while NAVSTARs 5 and 6 had cesiums, although the clock on NAVSTAR 5 was "noisy" so observations of NAVSTAR 5 carried considerably less weight in the least squares solutions. The final GPS configuration should consist of 18 satellites, configured in six planes, each containing three satellites (Senus, 1983), and all with very stable cesium standards. Our four useable satellites are in only two planes and have only one good cesium standard among them. It is clear, then, that the conditions for these experiments are sub-optimal with regard to both geometry and instrumentation. The accuracies of the determinations of some of the satellites' orbits are also degraded significantly by the satellite frequency instabilities.

In the future the GPS orbits are expected to be known more accurately. However, if at some time in the future the carrier frequencies of the satellites are deliberately dithered as has been proposed, then the ability to do accurate point positioning (as opposed to relative positioning) will depend on whether the dither pattern is known. Presumably, for security reasons, knowledge of the pattern will not be generally available in advance except to "cleared" users, but it should be possible to obtain the information after the fact, along with accurate orbital ephemerides.

The WGS 72 coordinates of a site at the Haystack observatory in Westford, Mass. had been estimated by Hothem (1979) using about 400 passes of NNSS Doppler observations collected over a two month period, and from later less extensive campaigns. From these observations, all three coordinates are known to sub-meter accuracy (Hothem, private communication). We positioned the same site using four seven-hour sessions during one week in October, 1982, and two ten-hour sessions on April 27 and 28, 1983. The number of observations ranged from 100 to 120 per session. The Macrometer was connected to a hydrogen maser frequency standard though our results from analyses of other observations in which no such stable standard was used suggest that the effect of having used a hydrogen maser standard in this case was not great. (Since none of the satellites has a maser standard, one would not expect the use of one in the receiver to help much.) Results of other observations also suggest that the time spans of the observations, up to 10 hours, could have been shortened appreciably without ill effect.

If we accept the NNSS determination of the Haystack position as correct, then the root mean square error (rmse) of our six daily determinations by GPS was 2.2 m in latitude, 1.6 m in longitude, and 4.6 m in radius. The breakdown of the rmse into bias (mean) and standard deviation about the mean is shown table 1. The rms radial error is largely due to bias. On the last two days that we observed at Haystack, we also observed from several other widely scattered sites in the U.S. (See the next section.) For each of these sites, there was a similar 6-meter bias of the radial coordinate as determined by the Macrometer observations, relative to the NNSS determination. The similarity of the biases at these widely scattered sites suggests that the bias is due mainly to satellite ephemeris error and not to ionospheric refraction.

Another set of observations was performed at a site in Woburn, Mass., in this case with a cesium standard. For reference, NNSS-derived WGS 72 coordinates for this site were obtained from those of the Haystack site by means of a short-baseline (30 km) Macrometer survey. This survey used double-differences and should have been accurate within several centimeters. For point positioning, we took data from nine sessions, each 10 hours long, distributed over 5 weeks in April through June of 1983. The rmse's of the nine GPS results with respect to the "true" NNSS position were 3.6 m in latitude and in longitude, and 4.8 m in radius. These rmse's are primarily due to variance and not bias, as can be seen in table 1.

We believe that the standard deviations of the Woburn coordinates are greater than those of the Haystack coordinates primarily because the Woburn observations spanned more weeks so that a wider range of satellite ephemeris errors was sampled. The use of a cesium instead of a hydrogen maser frequency standard did not significantly increase the rms of the postfit phase residuals.

In order to test how well the Macrometer would perform with only its internal crystal oscillator as a frequency standard, one of the sites used in the FGCC tests was point-positioned. This site is near the Gaithersburg latitude observatory in Maryland. Observations were available from a total of five days. Four sessions, each between 2 and 3 hours long, were during the FGCC tests in January; there was one 10-hour session on April 27, 1983. To suppress the effects of crystal oscillator instability, we analyzed only satellite-difference observables. Since NAVSTAR 1 was not used, we had at most three satellite differences per epoch. The number of observations for the 2-3 hour sessions ranged from 90 to 120. We had only 43 observations from the 10-hour session since for four hours only one satellite was being observed and no satellite differences could be formed. The WGS 72 coordinates of the site are believed to be known at the sub-meter level from NNSS observations. With respect to NNSS, the GPS rmse's were 1.9 m in latitude, 8.2 m in longitude and 3.4 m in radius. The use of satellite differencing coupled with the short time spans of the observing sessions (or the smaller number of observations on April 27) seems to have yielded a significantly poorer determination of longitude than the previous experiments in which oneway phases and more stable, external, frequency standards were used.

Although we have presented a limited number of point positioning results, and although the schedules of observations were far from optimal for point positioning (since all the data were drawn from relative positioning experiments), it can safely be concluded that the Macrometer V-1000 can point-position a site to the several-meter level in all three coordinates using only several hours of observation, regardless of the station frequency standard used, and with the presently available, sub-optimal, constellation of satellites.

Our point positioning results are certainly as good as can be achieved with NNSS Doppler under similar conditions. With better determined orbits, an expanded satellite constellation equipped with good cesium standards, two-frequency observations, longer data spans, and optimal data sampling intervals, point positioning with the Macrometer could be much more time and cost efficient than NNSS Doppler.

Fell (1980) predicted that meter-level accuracy could be obtained with GPS in twenty-four hours, and half-meter accuracy in five days, using either pseudo-range or integrated Doppler observations. However, he assumed that the receiver could track only one GPS satellite at a time. The times required to achieve the same accuracy should be greatly reduced with multi-channel oneway phase and satellite difference

observables. Point-positioning accuracies of between 5 and 10 meters with one-channel GPS receivers have been reported by Lachapelle et al. (1982), Perault(1983), and Carr and O'Toole (1982).

Relative Positioning Results

Relative positioning results with the Macrometer V-1000 on "short" baselines have been reported previously (Counselman, 1982; Counselman, et al., 1983; Hothem and Fronczek, 1983; see also the paper of Goad and Remondi presented at this Symposium) so we give only a brief summary here. In table 2 we summarize the surveys performed with the Macrometer through April 1983. [Since April, hundreds of baselines have been measured by commercial surveyors using Macrometer equipment, and results similar to those shown here have reportedly been obtained (J. Ladd, personal communication).] Items 1-9 of table 2 are "short baseline" results using 2-3 hour observing sessions and doubly-differenced observables. Items 10-11 are "long" baseline results involving 10 hour sessions and single difference observables. For all these relative-positioning results, it was possible to use observations of NAVSTAR 1 (except in April when it was non-functional) since the effects of the satellite oscillator instability were removed by differencing between sites.

The most extensive test of the geodetic accuracy of the Macrometer to date (item 2 in table 2) was performed by the United States Federal Geodetic Control Commission (FGCC) in January, 1983 (Hothem and Fronczek, 1983). According to terrestrial standards, the Macrometer yielded several millimeter-level accuracy in all three vector components for baselines shorter than 1 km. For longer baseline lengths (up to 42 km were included in the test network), accuracies of about 2 ppm (1:500,000) were achieved. Baseline lengths were consistent at about the 1 ppm level and the orientations of the baselines were consistent with the terrestrial network at the 0.1 arcsecond level.

The Macrometer has been used successfully in many surveying projects carried out during the last seven months by Geo/Hydro, Inc. (including table 2 items 3-8). These include, for example, geodetic control for power transmission lines and highway extensions. Since for these surveys there are no other standards with which to compare the Macrometer results, we computed the polygon misclosures for each survey. These ranged from 1:200,000-1:700,000, which meets first-order specifications for traverses (FGCC, 1980). The 5 ppm results were obtained when two lines per day were measured (items 3 and 7) though the misclosures were sometimes as good as those obtained from measuring only one line per day (items 4 and 8). If the survey stations are close enough, it is possible to observe on one baseline in 2 or 3 hours, travel and set up in 1/2 hour, and then spend 2 to 3 hours measuring a second baseline. Obviously, when the full satellite constellation is available, the efficiency of surveying operations will increase significantly because very many lines can be measured in one day.

It is clear from the "short" baselines measured to date that the Model V-1000 is already a powerful surveying tool. For more demanding "short" baseline applications such as the monitoring of local crustal deformations, a two-frequency receiver is desired. Field tests of the two-frequency units are now being conducted.

As can be seen in table 2 (items 10,11), we have also measured "long" baselines. For up to 10 hours on April 27 and again on April 28, 1983, we had observations from a widely distributed set of sites. The stations participating (and their frequency standards) were at Haystack, Mass. (hydrogen maser), Woburn, Mass. (cesium), Greenbank, W. Va. (hydrogen maser), Phoenix, Arizona (cesium) and three FGCC sites in Maryland (crystals). All the baselines except for Haystack-Woburn and those of the FGCC network were determined by analysis of single differences, because the limited satellite inter-visibility over the 10 hour observing spans reduced the number of possible satellite-difference pairs and because the availability of atomic frequency standards made it possible to use single differences instead of double differences. For the Haystack-Woburn and the FGCC baselines we used double differences. The misclosures were all within 2 ppm. The Haystack-Greenbank baseline is known independently with sub-meter uncertainty from NNSS Doppler measurements. Our estimate of the baseline length agreed with the NNSS determination to within 0.25 ppm (20 cm). The Woburn-Greenbank distance agreed to about 1 ppm. See also the paper of Hothem et. al., presented at this symposium, for a detailed comparison of our long baseline results with other measurement techniques.

Conclusions

A commercially available GPS receiver that utilizes no knowledge of the GPS codes and that observes only the L_1 band of GPS signals can perform all the functions of a NNSS Doppler receiver but more accurately and efficiently. This is true even under the present sub-optimal conditions. With the availability of the full GPS constellation, and with two-frequency instruments to monitor the satellite orbits from well-known VLBI sites, better than 0.1 ppm relative positioning and sub-meter point-positioning should be possible.

Table 1: Point Positioning Experiments

Frequency Standard (Location)	Dates	Time Span (Hours)	No. of Sessions	Observations/ Session
1) Hydrogen Maser (Westford, Mass.)	10/20-10/24/82	7	4	120
	4/27-4/28/83	10	2	100
2) Cesium (Woburn, Mass.)	4/27-4/28/83	10	2	100
	6/1-6/22/83	10	7	100
3) Crystal (Gaithersberg, Maryland)	1/17-1/21/83	2 1/4 - 3	4	90-120
	4/27	6	1	43

Geocentric Coordinate Differences (GPS-NNSS)

Observa- tion Type	<u>Latitude</u>			<u>Longitude</u>			<u>Radius</u>			Rms of Postfit Residuals
	std*	bias	rmse	std*	bias	rmse	std*	bias	rmse	
	(m)	(m)	(m)	(m)	(m)	(m)	(m)	(m)	(m)	(cm)
1) Oneway Phase	2.0	1.0	2.2	1.6	-0.4	1.6	2.6	-3.8	4.6	25-40
2) Oneway Phase	3.5	0.7	3.6	3.5	0.7	3.6	4.8	-0.1	4.8	25-55
3) Satellite Differences	0.9	-1.7	1.9	7.4	-3.5	8.2	1.9	-2.8	3.4	15-20

* Root Mean Square Error (rmse) =

$$[[\text{Standard Deviation about the Mean (std)}]^2 + [\text{Mean (bias)}]^2]^{1/2}$$

Table 2: Surveys with the Macrometer Model V-1000

<u>Item</u>	<u>Date</u>	<u>Place</u>	<u>Average Distance</u>	<u>No. of Lines/ Lines/Day</u>	<u>Worst Coord. Error</u>	<u>Notes</u>
1	12/82	Mass.	30 km	5 / 1	1:500,000	(1)
2	1/83	FGCC (2)	<1 km	4 / 1	several mm	Blind (3)
	"	"	20 km	5 / 1	1:500,000	Blind (3)
3	2/83	Florida	12 km	8 / 2	1:200,000	(1)
4	"	Alabama	11 km	3 / 2	1:700,000	(1)
5	3/83	Texas	24 km	5 / 1	1:285,000	Blind (3)
6	"	Germany	11 km	2 / 1	1:230,000	Blind (3,4)
7	4/83	Ohio	5 km	4 / 1	1:450,000	(1)
	"	"	793 m	18 / 2	1:275,000	(1)
8	"	Colorado	5 km	12 / 2	1:500,000	(1)
9	"	Maryland	748 m	1 / 1	1 mm	(5)
	"	"	32 km	3 / 1	1:500,000	(3,5)
10	"	Mass.- W. Va.	845 km	1 / 1	1:500,000	(3)
11	"	Mass.- W. Va.- Arizona	2400 km	3 / 1	1:500,000	(1)

Notes:

1. Misclosure of polygon whose sides were measured at different times.
2. Federal Geodetic Control Committee test network near Washington, D.C.
3. Accuracy tested by comparison with independent survey by other methods. Table shows the (algebraic) sum of the error of the Macrometer survey and the error of the independent survey. Usually the Macrometer survey is the more accurate.
4. Accurate independent information on ellipsoidal height not available.
5. Difference from previous measurement by different V-1000's and operators is shown.

References

- Bender, P.L., 1981, "Establishment of Terrestrial Reference Frames by New Observation Techniques (review)," Reference Coordinate Systems for Earth Dynamics, E.M. Gaposchkin and B. Kolaczek, eds., D.Reidel Publ. Co., Dordrecht, Holland, 23-36.
- Bock, Y., 1982, "The Use of Baseline Measurements and Geophysical Models for the Estimation of Crustal Deformations and the Terrestrial Reference Frame," Dept. of Geodetic Science and Surveying Report 337, The Ohio State Univ., Columbus.
- Bock, Y., "Centimeter-Level Baseline Estimation with GPS Interferometry," accepted for publication in Marine Geodesy, 1983.
- Bossler, J.D., C.C. Goad and P.L. Bender, 1980, "Using the Global Positioning System for Geodetic Positioning," Bulletin Geodesique 54, 553-563.
- Carr, J.T. and J.W. O'Toole, 1982, "Point Positioning with the NAVSTAR Global Positioning System," in Proc. IEEE Symposium on Position, Location, and Navigation, Atlantic City, N.J., 166-170.
- Counselman III, C.C., 1982, "The MacrometerTM Interferometric Surveyor," in Proc. Int. Symposium on Land Information at the Local Level, Univ. of Maine, Orono, 233-241.
- Counselman III, C.C. and I.I. Shapiro, 1979, "Miniature Interferometer Terminals for Earth Surveying," Bulletin Geodesique, 53, 139-164.
- Counselman III, C.C. and S.A. Gourevitch, 1981, "Miniature Interferometer Terminals for Earth Surveying: Ambiguity and Multipath with Global Positioning System," IEEE Transactions Geoscience and Remote Sensing, GE-19, 244-252.
- Counselman III, C.C. and D.H. Steinbrecher, 1982, "The MACROMETER: A Compact Radio Interferometry Terminal for Geodesy with GPS," in Proc. Third International Geodetic Symposium on Satellite Doppler Positioning, Vol. 2, Physical Sciences Laboratory, New Mexico State Univ., 1165-1172.
- Counselman III, C.C., R.A. Abbot, S.A. Gourevitch, R.W. King and A.R. Paradis, 1983, "Centimeter-Level Relative Positioning with GPS," Journal of Surveying Engineering, 109 (ASCE), 81-89.
- Fell, P.J., 1980, "Geodetic Positioning using a Global Positioning System of Satellites," Dept. of Geodetic Science Report 299, The Ohio State Univ., Columbus.
- Federal Geodetic Control Committee (FGCC), 1980, Classifications, Standards of Accuracy, and General Specifications of Geodetic Control Surveys, Rockville, Maryland.
- Goad, C.C. and W. Remondi, 1983, "Initial Relative Positioning Results Using the Global Positioning System," presented at the XVIII General Assembly of the IUGG, IAG Symposium d, Hamburg, FRG, August 15-27, 1983.
- Hothem, L.D., 1979, "Determination of Accuracy, Orientation and Scale of Satellite Doppler Point-Positioning Coordinates," in Proc. Second International Symposium on Satellite Doppler Positioning, Vol. 3, The University of Texas at Austin, 609-630.
- Hothem, L.D. and C.J. Fronczek, 1983, "Report on Test and Demonstration of MACROMETERTM Model V-1000 Interferometric Surveyor," Federal Geodetic Control Committee: FGCCIS-83-2, Rockville, Maryland.

- Hothem, L.D., T. Vincenty and D.B. Hoyle, "Analyses of Doppler, Satellite Laser, VLBI and Terrestrial Coordinate Systems," presented at the XVIII General Assembly of the IUGG, IAG symposium d, Hamburg, FRG, August 15-27, 1983.
- Kouba, J., 1983, "A review of Geodetic and Geodynamic Satellite Doppler Positioning," Reviews of Geophysics and Space Physics, 21, 27-40.
- Lachapelle G., N. Beck and P. Heroux, 1982, "NAVSTAR Single Point Positioning Using Pseudo-Range and Doppler Observations," Proc. of Third InterNational Geodetic Symposium on Satellite Doppler Positioning, Vol. 2, Physical Sciences Laboratory, New Mexico State Univ., pp. 1079-1091.
- MacDoran, P.F., 1979, "Satellite Emission Radio Interferometric Earth Surveying: SERIES - GPS Geodetic System," Bulletin Geodesique, 53, 117-138.
- Macrometrics, Inc., 1983, Macrometer Interferometric Surveyor, 1000 Series Field Manual, 185 New Boston St., Woburn, Massachusetts 01801.
- Perrault, P.D., 1983, "STI GPS Receivers," in CSTG Bulletin No. 5, Technology and Mission Developments, Dept. of Geodetic Science and Surveying, Columbus, Ohio.
- Senus, W.J., 1983, "NAVSTAR Global Positioning System Status," presented at the XVIII General Assembly of IUGG, IAG Symposium d, Hamburg, FRG, August 15-27, 1983.

1982-1983 AFGL-SCEEE GEOPHYSICS SCHOLAR PROGRAM

Sponsored by the

AIR FORCE OFFICE OF SCIENTIFIC RESEARCH

Conducted by the

SOUTHEASTERN CENTER FOR ELECTRICAL ENGINEERING EDUCATION

FINAL REPORT

A SIMPLE 1-DIMENSIONAL BOUNDARY LAYER MODEL

FOR BOTH STABLE AND UNSTABLE CONDITIONS

Prepared by:	Frank P. Colby, Jr.
Research Location:	Air Force Geophysics Laboratory Meteorology Division
AFGL Research Contact:	Donald D. Grantham
Date:	September 1, 1983
Contract Number:	F49620-82-C-0035

Acknowledgements

I am very thankful to the LYT branch and its chief, Don Grantham, for the opportunity to conduct the work outlined in this report. They provided an atmosphere of flexibility and resources of high quality, allowing me to carry out high quality work.

I must also thank the Air Force Systems Command, the Air Force Office of Scientific Research, and the Geophysics Laboratory for sponsoring this worthwhile program. I appreciated and used the excellent facilities, especially the AFGL library which has a wealth of information available to the AFGL community.

Finally, I thank the personnel at the Southeastern Center for Electrical Engineering Education (SCEEE) for their friendly and competent administrative support.

I. INTRODUCTION:

The area of meteorology which has the most immediate impact on the Air Force is that of forecasting short-term weather conditions for various operations. Although computer models have helped make large-scale forecasts more accurate, many Air Force installations have weather which is determined by more local factors such as seabreeze circulations, urban heat island heating patterns, and mountain/valley wind regimes.

One excellent example is the launch site for the Space Shuttle at Vandenberg AFB in California. The Vandenberg site is strongly affected by both seabreeze circulations off the Pacific Ocean and mountain/valley wind regimes in the Coastal range. There is a direct impact of these local circulations on the actual launch itself (i.e., wind shear and fog) and also an indirect impact (i.e., dispersion of toxic exhaust cloud).

To forecast these impacts requires detailed prediction of the local wind regimes responsible for the local variations. Unfortunately, the ability to model these circulations presently resides in complicated models which require heavy computer use and much set-up time.

There is plenty of room for advances in this area of meteorology. Conceivably, a simple model which could handle these local circulations could have applicability far beyond the needs of the Air Force, providing new and useful capabilities to daily forecasters.

II. OBJECTIVES

The research I pursued was aimed at filling this gap in predictive ability. The research was divided into two major areas. The first involved an extensive literature search to determine what kinds of models had been or were presently available, and to delineate the important physics in the problem.

The second part was the development of a simple model to forecast these local circulations. It was hoped that a one-dimensional model previously developed by the author¹ could be modified to serve as the

backbone of a hydrostatic, mass conservation model in three dimensions. It was further hoped that the model could be tested and used operationally with data from past tracer experiments at Vandenberg AFB and with data from current radio communications studies conducted by AFGL/LYT in New England.

III. LITERATURE SEARCH

The literature search was both rewarding and tedious. The subject area of the search was determined by two needs. The first was a desire to find a complete set of references on air flow in complex terrain. The second need was a requirement to modify the author's model¹ to include a real inversion structure above a well-mixed boundary layer. This was needed to make the model useful for radio communications studies.

The primary source for references was the Meteorological and Geostrophysical Abstracts (MGA) published by the American Meteorological Society. This included not only references for the past twenty-five years but also historical reviews which had been conducted to find all early references on specific subjects. Since the subject area was broad, a computerized literature search was impossible, hence the work was done off-line.

To cover the subject areas, references were searched under a number of subject headings including: inversions, mountain/valley winds, topographical flows, drainage flows, slope winds, etc. A total of fifteen categories were included.

One major difficulty with MGA emerged during this search. The subject headings in current use changed over the years, some being effectively dropped entirely and some new ones added without any notations or warnings. Several times a new subject heading was discovered by accident thus requiring previous volumes to be re-checked for the new headings.

A second difficulty with using MGA was the capriciousness in assigning subject headings to individual citations. Several references, some of which were quite valuable, were found by chance, listed under

a particular geographical location or a general subject heading like 'wind'. There is little doubt that many relevant references were missed due to this problem.

Despite the above-mentioned problems, a large number of citations were found and reviewed. The Air Force Geophysics Library has a very complete collection of meteorological journals published throughout the world. As a result, many obscure references could be obtained. Nearly 75% of the citations taken from the abstract journal proved to be of little value. Some were in a foreign language which I could not read (i.e., Japanese or German). Others were large-scale in nature (i.e., lee cyclogenesis), or so theoretical as to be useless for the present study.

Those articles which were of direct relevance were photo-copied and read. This included over 100 articles from journals. The complete bibliography is available on request from AFGL/LYT through the Focal Point, Don Grantham.

The main results of the search were negative, although not unexpected. Simple models including the important physics for the problem have not been developed. Parts of the problem have been parameterized, but the complete problem has not been worked in entirety. For instance, the physics of the nocturnal surface inversion are well known, and rate equations governing the height of the nocturnal inversion have been developed.² However, these equations require as input other physical quantities which are specified or ignored in these studies.

The delineation of the important physics was made clear by the search. Both the mountain/valley and the seabreeze circulations result primarily from differential surface heating, and a hydrostatic response to the heating.^{3,4,5} The depth of the well-mixed boundary layer is governed by the turbulent heat flux at the surface and the entrainment of stable air from the inversion above into the mixed-layer.^{6,7} The stable or nocturnal boundary layer is governed by the downward sensible heat flux and the longwave radiative flux

from the surface layer.^{2,8} The temperature of the soil surface is determined by the net solar heat flux into the soil and the flux of heat out of the soil (surface energy balance).^{9,10} This information provided enough guidance to modify the author's previous model to incorporate all of these effects.

IV. MODEL

The model development was itself in two parts. First, the author's present model needed modifications, and second, a way of linking a number of one-dimensional models through hydrostatic mass conservation was required. Due to time limitations and the discovery that the modifications needed were extensive, the second part was not done during this research period.

The author's model was used in his doctoral research to investigate the behavior of a well-mixed atmospheric boundary layer (ABL). Consequently, routines for a nocturnal ABL had to be developed and included. Additionally, the author's model used a parameterization for mixed-layer height which assumed a jump discontinuity at the inversion instead of a stable layer of finite depth as required for LYT's use.

The general structure is shown in Fig. 1. For the stable ABL, a quadratic form is assumed for the potential temperature in the surface layer. For the unstable ABL, the surface layer is linear and superadiabatic, and the layer above that is assumed well-mixed (constant potential temperature). The structure between all other levels is treated linearly except for the moisture in the radiation routine. The unstable ABL is also assumed to have a 5mb deep surface layer. This assumption is not crucial for modeling the structure of the ABL as a whole or for handling the inversion which caps the well-mixed ABL.

The model includes radiation, a surface energy balance, and entrainment of the inversion by the turbulent ABL. The radiation parameterization is taken from Katayama¹¹ and is a routine originally designed for use in the UCLA general circulation model. The inci-

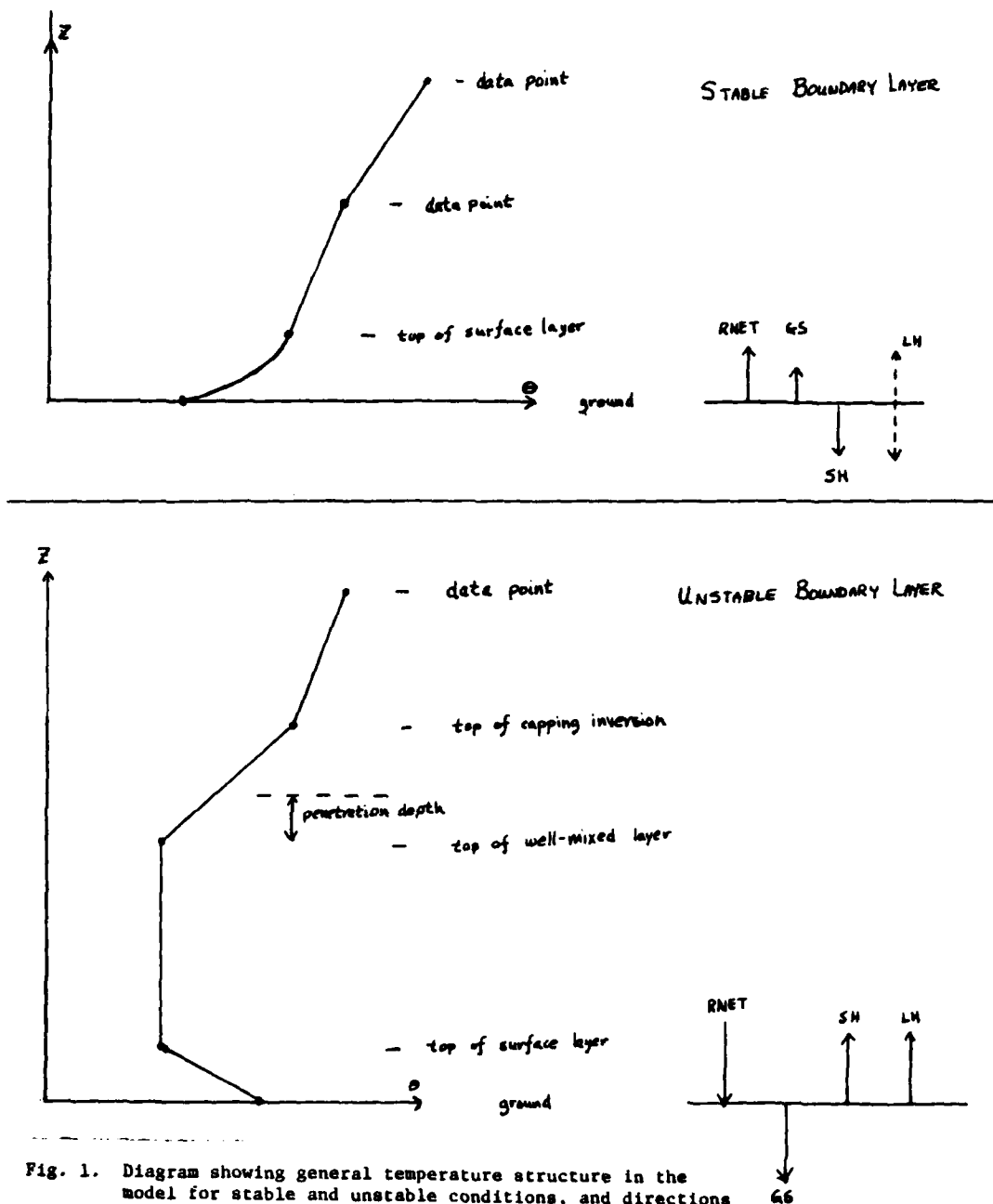


Fig. 1. Diagram showing general temperature structure in the model for stable and unstable conditions, and directions of fluxes at the ground surface. θ is potential temperature, z height above ground. Fluxes are identified in the text.

dent radiation and IR emission are calculated separately. The radiation calculation is only made for the ground level (both long and short wave) and the top of the surface layer (long wave only). The radiative heating during the day is important only at the ground, and IR cooling is significant at the ground during the day and at both top and bottom (ground) of the surface layer in stable conditions. The model incorporates an exponential fit to the data for specific humidity to allow simple integration of water content. CO_2 is included in a fixed form based on experimental data, and its contribution is then fixed for each layer. Clouds may be added in the form of a "grey-ness" coefficient at each level which ranges from 0 for a complete cover to 1 for clear conditions.

The surface energy balance at the surface has the form:

$$NR = SH + LH + GS \quad (1)$$

where NR is the net radiation incident on the surface, SH is the sensible heat flux upward from the surface, LH is the latent heat flux upward from the surface, and GS is the soil heat flux downward into the ground which heats the soil. Fig. 1 illustrates the various fluxes and their directions.

The sensible heat flux and latent heat flux are parameterized using Monin-Obukhov similarity theory for the ABL. The fluxes depend upon the gradients in the surface layer, the depth of the boundary layer, and the incident radiation. The theory assumes that the vertical structure of temperature and moisture in the ABL have forms which can be described by universal structure functions when scaled equations are used. Mixed-layer formulations are obtained by matching solutions for the mixed layer and surface layer at their common boundary.

$$SH = f\left(\frac{\partial \theta}{\partial z}\right) = F(L, z_0) \quad (2)$$

$$LH = f\left(\frac{\partial q}{\partial z}\right) = F(L, z_0) \quad (3)$$

for the unstable ABL

where L is the Monin/Obukhov length, z_0 is the roughness length, θ is potential temperature and q is mixing ratio of water vapor.

$$SH = f\left(\frac{\partial \theta}{\partial z}\right) = G(L, F_c, z_0) \quad (4)$$

$$LH = f\left(\frac{\partial q}{\partial z}\right) = G(L, F_c, z_0) \quad (5)$$

for the stable ABL

where F_c is the Coriolis parameter, and F , G are the structure functions. The stable ABL uses surface layer formulations. The form of the temperature structure function is taken from Arya¹² and the moisture function is assumed to have the same form.

The soil heat flux is given as a residual from the surface energy balance. This flux is then used to drive the thermodynamics of the soil. The vertical temperature profile in the soil is assumed to be cubic, with constant temperature TBAR at the base of the daily heating bulge. The initial profile is assumed to be constant. The profile is:

$$T(z) = TBAR + Bz^2 - Az^3 \quad (6)$$

where A and B are constants and z is height above the TBAR level. The heat balance in the soil and the heat conduction equation are used to determine the coefficients of the cubic profile and the height of the soil surface above the TBAR level. During the heating cycle, this depth is below the second inflection point in the profile. As the soil begins to cool, this depth moves above the second inflection point allowing the surface temperatures to drop, but allowing the heated soil below the surface to stay warmer. During the cooling, the size of the heating bulge is assumed to be constant at the last

value it had during the heating cycle. Heat conduction:

$$C_s \frac{\partial T}{\partial t} = K \frac{\partial^2 T}{\partial z^2} \quad (7)$$

where K is soil thermal conductivity and C_s is soil heat capacity.

$$\text{Total heating} = Q \Delta t = C_s \int (T(z) - T_{BAR}) dz \quad (8)$$

Using these equations, the system reduces to an algebraic equation for the height of the soil surface (S). The ground temperature becomes:

$$T_G \triangleq T(z) = T(S) = T_{BAR} + BS^2 - AS^3 \quad (9)$$

The soil moisture is found by assuming that surface soil moisture responds to three main processes: precipitation, evaporation, and flux from below. The bulk soil moisture is assumed to be constant over the period. According to Deardorff¹³ the bulk soil moisture changes over a time scale of a few weeks, so it can be assumed constant for a twelve hour period with little loss of accuracy. The surface soil moisture is changed according to:

$$\frac{\partial GW}{\partial t} = \frac{-c_1 LH/\lambda}{\rho_w d_1 WMAX} + \frac{-c_2 (GW - GWB)}{\tau} \quad (10)$$

where GWB is percent bulk soil saturation (top 50 cm), GW is percent surface soil saturation, d_1 is depth of diurnal cycle (≈ 10 cm), λ is latent heat of evaporation, ρ_w is density of H_2O (≈ 1 gm/cc), $WMAX$ is field capacity soil moisture, τ is period of cycle, and c_1 , c_2 are non-dimensional constants. Deardorff's values for c_1 and c_2 were computed from data for Jackson¹⁴ taken over bare soil near Phoenix, Arizona in March.

1. Stable ABL

The depth of the stable ABL is computed by using a heat balance for the surface layer as a whole. The major components of this balance are assumed to be radiational cooling and cooling due to sensible heat flux into the cooler ground surface. The vertical profile of potential temperature in the surface layer is assumed to be quadratic⁸ so the change in ABL mean potential temperature can easily be translated into a new ABL height and surface layer top pressure (by hydrostatics).

$$\frac{\partial \theta(g)}{\partial t} = \int_t^{t+ET} SH \cdot dt + \int_t^{t+ET} IR \cdot dt \quad (11)$$

where ET is the model timestep, IR is net infrared flux out of surface layer, and $\theta(g)$ is potential temperature of ground surface.

$$\theta(z) = \theta(g) + Bz^2 \quad (12)$$

is assumed form. The moisture is found using a budget for mixing ratio in the surface layer, and the new values for temperature, pressure, and mixing ratio are then inserted into the sounding.

2. Unstable ABL

For the unstable ABL, the routine from Zeman and Tennekes⁶ used in the old model was discarded. They assumed a jump discontinuity at the inversion capping the ABL. This is an unrealistic structure, and therefore the model was modified to include the real thickness of the inversion. Using the work of Stull⁷ as a guide, a new parameterization for the growth of the mixed layer with time was derived. It is based on a heat budget for the mixed layer, with the sensible heat flux at the bottom of the mixed layer and the entrainment of inversion air into the ABL as the main components. The amount of entrainment is found by assuming that the mixing at the inversion takes place due to the motion of thermals which rise from the surface layer up to

the top of the mixed layer. Using an energy balance for the thermals, and allowing them to entrain ambient ABL air as they rise, the penetration depth into the inversion can be found. Assuming that over a given area the penetration is balanced by entrainment gives the entrainment as a function of the surface layer variables, the depth of the mixed layer, and the stability of the inversion.

$$L \propto \left(\frac{g \cdot DIF}{\theta(h) \cdot h} \right)^{1/2} \quad (13)$$

where L is entrainment rate, g is gravity, DIF is initial potential temperature excess, $\theta(h)$ is potential temperature of mixed layer, and h is height of mixed layer. The mixing ratio in the mixed layer is found using a budget calculation, and the temperatures and pressures of the penetration level and the mixed layer are found using hydrostatics and the assumed structure.

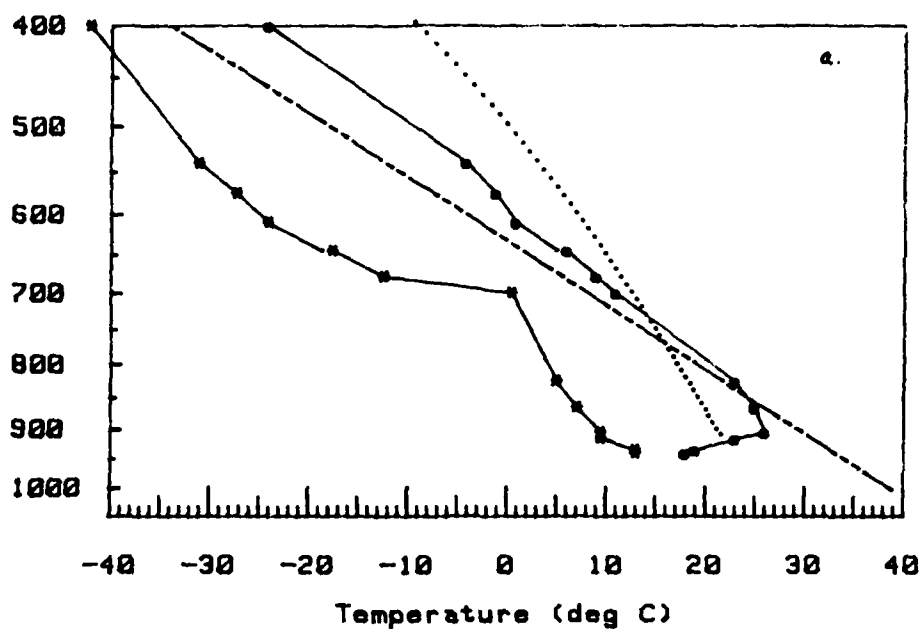
The initial sounding is input as available from 400 mb to near the surface. The surface observation is used to determine initial values of temperature and mixing ratio in the model. These values are set at the top of the surface layer, initially 5 mb above the ground. The ground temperature is initialized to be equal to $TBAR$. The mixing ratio for the ground level (Q_0) is a function of ground wetness and surface layer value (Q_s).

$$Q_0 = Q_s + (.5 \cdot QW^2) \cdot (SATQ - Q_s) \quad (14)$$

where $SATQ$ is saturation mixing ratio at ground.

The program is written in BASIC on a Hewlett Packard 9826 machine with augmented memory. The program takes up about 40K of (RAM) memory. Output consists of both line printer data on the fluxes and the temperatures at specific times and X-Y plots of the sounding at user-selected times on a pseudoadiabatic background. The program is stored on a floppy disk at AFGL/LYT. A typical example of the output at AFGL/LYT is shown in Fig. 2.

Pressure (mb)



Pressure (mb)

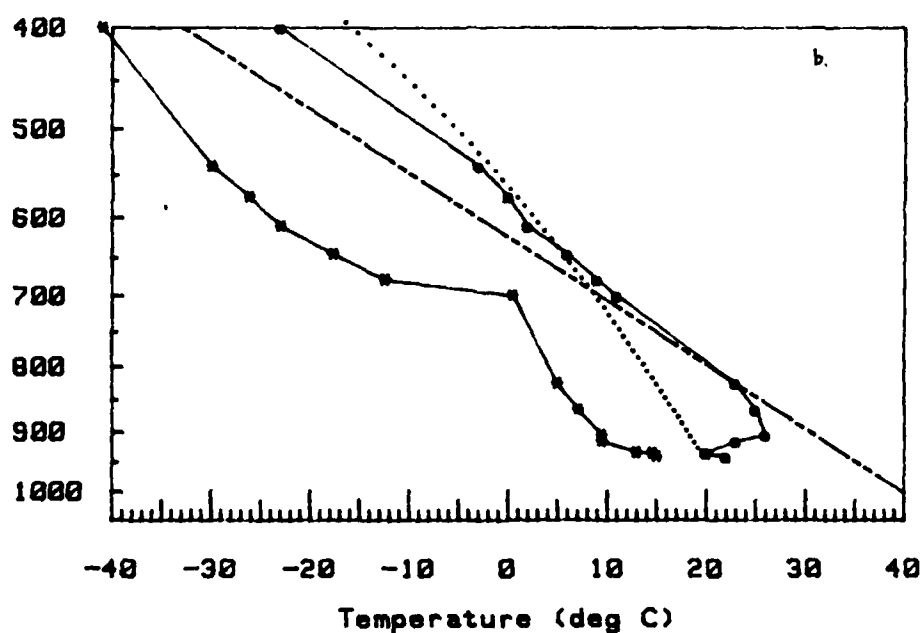


Fig. 2. Plots from model shows a) initial sounding b) results after one hour of integration. Solid line connecting open dots is temperature, * for dewpoint. Dash-dotted line is 313 K isentrope and dotted line is a selected pseudoadiabatic.

time is 6.0833333333

P(mb)	T(deg C)	Q(g/kg)	clouds
400	-23	.2	1
540	-2.2	.5	1
575	.8	1	1
610	2.8	1	1
645	6.8	1.5	1
678	9.5	2.2	1
700	11.3	5.7	1
825	23.7	6.7	1
865	25.8	7.4	1
905	26.2	8.3	1
915	23.6	8.1	1
934	19.7	10.1	1
940	18.8	10.7	1

time is 7.0833333333

P(mb)	T(deg C)	q(g/kg)	clouds
400	-23	.2	1
540	-2.2	.5	1
575	.8	1	1
610	2.8	1	1
645	6.8	1.5	1
678	9.5	2.2	1
700	11.3	5.7	1
825	23.7	6.7	1
905	26.2	8.3	1
915	23.6	8.1	1
933	20	10.1	1
935	20.2	11.3	1
940	22.9	12.3	1

Fig 2c. Line printer output of soundings shown in Figs. 2a and 2b. P is pressure, T is temperature, Q is mixing ratio.

V. RECOMMENDATIONS

There are two immediate tasks still to be completed: 1) testing of the model in its 1-D form, and 2) linking a number of 1-D forms into a hydrostatic mass conservation model. The first task is important to be sure that the various parameterizations are working correctly together. Currently, there is an instability in the model which causes an oscillation in the soil heat flux. This arises only in the final version of the model -- when the routines are run separately, they work well and compare well with data.

The second task is the accomplishment of the goal set forth at the beginning of this research period -- namely to develop a simple model capable of predicting local wind regimes in complex terrain. This important goal is closer to realization, but not yet accomplished.

After the model is fully developed, it should be carefully tested with data from field studies. Many such studies are available, and this testing would demonstrate the usefulness of the model as well as its limitations.

REFERENCES

1. F.P. Colby, Jr., "The Development of Convective Instability During SESAME, 1979" Ph.D. Thesis, Dept. of Meteor. and Phys. Oceanog. Massachusetts Institute of Technology, 312 pp., 1983.
2. T. Yamada, "Prediction of the Nocturnal Surface Inversion Height," J. Appl. Meteor., Vol. 18, pp. 526-531, 1979.
3. N.H. Thyer, "A Theoretical Explanation of Mountain and Valley Winds by a Numerical Method." Archiv. Met. Geoph. Biokl., Vol. 15, pp. 318-348, 1966.
4. M.A. Fosberg, "Numerical Analysis of Convective Motions over a Mountain Ridge," J. Appl. Meteor., Vol. 6, pp. 889-904, 1967.
5. C.D. Whiteman and T.B. McKee, "Breakup of Temperature Inversions in Deep Mountain Valleys: Part II. Thermodynamic Model," J. Appl. Meteor., Vol. 21, pp. 290-302, 1982.
6. O. Zeman and H. Tennekes, "Parameterization of the Turbulent Energy Budget at the Top of the Daytime Boundary Layer," J. Atmos. Sci., Vol. 30, pp. 111-123, 1977.
7. R. Stull, "Inversion Rise Model Based on Penetrative Convection," J. Atmos. Sci., Vol. 30, pp. 1092-1099, 1973.
8. F.T.M. Nieuwstadt, "A Rate Equation for the Inversion Height in a Nocturnal Boundary Layer," J. Appl. Meteor., Vol. 19, pp. 1445-1447, 1980.
9. C.M. Bhumralkar, "Numerical Experiments on the Computation of Ground Surface Temperature in an Atmospheric General Circulation Model," J. Appl. Meteor., Vol. 14, pp. 1246-1258, 1975.
10. J.W. Deardorff, "Parameterization of the Planetary Boundary Layer for use in GCMs," Mon. Wea. Rev., Vol. 100, pp. 93-106, 1972.
11. A. Katayama, "A Simplified Scheme for Computing Radiative Transfer in the Troposphere," Tech. Rep. #6, Dept. Met., UCLA, 77 pp., 1972.
12. S.P.S. Arya, "Geostrophic Drag and Heat Transfer Relations for the Atmospheric Boundary Layer," Quart. J. Roy. Meteor. Soc., Vol. 101, pp. 147-161, 1975.
13. J.W. Deardorff, "A Parameterization of Ground Surface Moisture Content for use in Atmospheric Prediction Models," J. Appl. Meteor., Vol. 16, pp. 1182-1185, 1977.
14. R.D. Jackson, "Diurnal Changes in Soil Water Content During Drying," Field Soil Water Regime, pp. 37-55, 1973.

1982-83 AFGL-SCEEE GEOPHYSICS SCHOLAR PROGRAM

Sponsored by the

AIR FORCE OFFICE OF SCIENTIFIC RESEARCH

Conducted by the

SOUTHEASTERN CENTER FOR ELECTRICAL ENGINEERING EDUCATION

FINAL REPORT

MEASUREMENT OF A NARROW LATITUDINAL REGION

OF INTENSE ANTISUNWARD CONVECTIVE FLOW IN

THE LATE MORNING TIME SECTOR

Prepared by:	Dr. William F. Denig
Research Location:	The Air Force Geophysics Laboratory Space Physics Division Plasmas, Particles, and Fields Branch
AFGL Research Contact:	Dr. Fredrick J. Rich
Date:	November 23, 1983
Contract No.	F49620-82-C-0035

Acknowledgement

I would like to thank the Southeastern Center for Electrical Engineering Education and the Air Force Geophysics Laboratory for providing me with the opportunity to participate in the 1982-83 AFGL-SCEEE Geophysics Scholar Program. Also, I appreciate the guidance from Dr. Fredrick J. Rich during the course of this work. Finally I acknowledge useful discussions with Drs. W. J. Burke, David Hardy, Susan Gussenhoven, and (Sister) Marianne Doyle. The Geophysics Scholar Program is funded by the Air Force Office of Scientific Research under contract #F49620-82-C-0035.

This report is a case study of the southern auroral zones and polar cap morphology as measured by the S3-2 satellite during a geomagnetic substorm of moderate intensity. Measurements of the plasma convective flow pattern and field-aligned currents were made as the satellite traversed the polar region near the dawn-dusk meridian at 18:20 UT on June 24, 1976. Of particular interest is the identification of a region of intense antisunward convective flow on the dawnside (near 0900 MLT) of the polar cap just poleward of the region 1 FAC system. Poleward of this region of intense flow is a FAC of opposite polarity to the region 1 current sheet suggesting that the midday cusp has wrapped around to the late morning time sector.

The format of this report is divided into four sections. Section 1 is an overview of high-latitude auroral phenomena with particular emphasis placed on the ionospheric consequences and morphology. A brief description of the S3-2 satellite and techniques used in the analysis are contained in section 2 while section 3 is the actual presentation of the data. Finally, section 4 is a conclusion and recommendations for future work.

Section 1. The Polar Ionosphere

The high-latitude terrestrial ionosphere is the region above 100 km altitude and above $\sim 50^\circ$ invariant latitude where the interaction of the interplanetary magnetic field (IMF) and the geomagnetic field allow for a strong coupling of the sun, the magnetosphere and the ionosphere. Solar wind interaction with the magnetosphere can drive field-aligned currents and support large-scale electric fields across the high-latitude ionosphere. Implicit in such a description is the assumption that the geomagnetic field and the IMF merge at high altitudes, i.e. an open magnetosphere. Since the magnetic field lines are equipotentials - in the first approximation - solar wind particles entering the merging region or high-altitude cleft have direct access to the midday ionosphere. The solar wind also exerts pressure on the closed field lines of the magnetosphere compressing

the day side magnetosphere while stretching out the field lines at night. The elongated field lines within the magnetotail participate in a dynamo process involving the charged particles of the solar wind which results in a net dawn-to-dusk electric field that maps down into the region of the polar cap. Within the central portion the tail magnetosphere there exists a region of hot plasma called the plasma sheet. The auroral zones are annular regions surrounding the geomagnetic poles equatorward of the polar cap which are the ionospheric projections of the plasma sheet. Within the auroral zones precipitating electrons from the plasma sheet are responsible for the diffuse aurora. Also, the magnetotail dynamo is partly responsible for field-aligned currents in the auroral oval and, perhaps, the polar cap. The distinct patterns of field-aligned currents and electric fields that are present in the morning and evening auroral zones overlap each other in the premidnight sector at the Harang discontinuity. As might be expected, high-latitude geomagnetic activity is dependent upon the dynamic pressure of the solar wind and upon the orientation and strength of the IMF. The statistical pattern of field-aligned currents and high-latitude electric fields are governed by the IMF B_y and B_z components (for a description of Geocentric Solar Magnetospheric coordinates see Russell, 1972). The response of the polar cap potential and of the field-aligned currents to varying IMF conditions is discussed below.

1.1 Polar Cap Potential

Since the open magnetic field lines of the polar cap map into the tail roughly as equipotentials, the cross tail electric field is reflected in a dawn-dusk electric field across the cap. This electric field has been measured by low-altitude, polar-orbiting satellites (Cauffman and Gurnett, 1972; Heppner, 1972; Smiddy et al., 1980) and the electric field integrated over the satellite path has been used to calculate the polar cap potential distribution (Heppner, 1972; Doyle and Burke, 1983). Values as high as 170 kV have been measured although more typical values range from 20 kV to 100 kV depending upon the geomagnetic activity level, i.e. K_p (Heppner, 1972; Hardy et al.,

1981; Doyle and Burke, 1983).

The polar cap potential is a measure of the interaction of the solar wind and the IMF on the magnetosphere and, indeed, the potential distribution or electric field has been found to be quite sensitive to the orientation of the IMF (Heppner, 1972; Burke et al., 1979b; Reiff et al., 1981). For example, when the IMF has a southward component ($B_z < 0$) the motion of plasma within the polar ionosphere at high altitudes ($h > 300$ km) generally follows a two-cell convection pattern driven anti-sunward in the polar cap in response to a dawn-to-dusk electric field (Cauffman and Gurnett, 1972; Heelis et al., 1976). Plasma within the auroral zones convects sunward and the high-latitude electric field reversal is often used as the polar cap boundary (Heelis et al., 1976). Keeping the same $B_z < 0$, the polar cap potential distribution has a statistical response to the sign of the IMF B_y component (Heppner, 1972; Mozer et al., 1974; Fairfield, 1977). This B_y dependence has an asymmetric pattern for the north and south poles where the southern hemisphere has its maximum antisunward flow in the morning for $B_y < 0$ when the maximum flow is in the evening for the north. These patterns are reversed for $B_y > 0$. Under conditions of a strong northward IMF, i.e. $B_z > 0.7 \gamma$, it has been observed (Maezawa et al., 1976; Burke et al., 1979b) that there may exist regions of sunward convecting plasma within the polar cap suggesting the existence of additional convection cells (Burke et al., 1979b; Crooker, 1979). The two outer cells, called viscous cells, have the same pattern as the two cells driven by merging for $B_z < 0$ described above. The vortex motion in these viscous cells is driven by the interaction of the solar wind and the tail magnetosphere. The inner cells, called merging cells, are contained entirely within the polar cap and are believed to be due to dayside merging of the polar cap and solar wind magnetic fields (Crooker, 1979).

The physics of high-latitude phenomena are reflected in the polar cap potential distribution. The interplanetary magnetic field configuration and the velocity of the solar wind interact with the magnetosphere and govern the convective flow patterns within the ionosphere. Knowledge of the high-latitude electric fields, then, is vital to a proper understanding of the coupling between solar parameters and the earth.

1.2 Field-aligned Currents

Field-aligned currents (FAC), also called Birkeland currents, provide a mechanism for the coupling of the ionosphere to the magnetosphere and the solar wind through the transport of charged particles along magnetic field lines. FAC are a permanent feature of the high-latitude auroral zones which respond to the level of geomagnetic activity (Iijima and Potemra, 1976a; Sugiura and Potemra, 1976). The statistical diurnal pattern of FAC have been deduced from an analysis of magnetic perturbations along a satellite path (Zmuda and Armstrong, 1974; Potemra et al., 1975). On the dawn-dusk meridian the basic pattern consists of two regions or sheets of field-aligned currents lying within or bordering the auroral zones - a region 1 current system poleward of a region 2 system where the currents for the morning side are directed "in" towards lower altitudes in region 1 and are directed "out" towards higher altitudes in region 2. The current directions are reversed in the evening sector. Typical values for the current densities range from $0.03 \mu\text{amp m}^{-2}$ to $4 \mu\text{amp m}^{-2}$ although more intense FAC have been noted especially during magnetospheric storm conditions (Shuman et al., 1981). The ionospheric closure for the steady-state FAC is presumably through Pedersen currents (also Hall currents) primarily in the auroral regions although the magnitudes of the dawn and dusk current systems are such that, on the average, there is a net current flowing across the polar cap (Sugiura and Potemra, 1976; Iijima and Potemra, 1976a).

Whereas the FAC patterns in the dawn and dusk time sectors are fairly regular, the patterns within the noon and midnight sectors are more complex. Iijima and Potemra (1976b) detected an "extra" FAC in the vicinity of the midday cleft lying poleward of region 1 and having a statistical pattern of current into the ionosphere in the post-noon sector and out of the ionosphere in pre-noon. Subsequent measurements (McDiarmid et al., 1978; Doyle et al., 1981) of the FAC pattern indicate that the cusp FAC is actually an extension of the morning or evening region 1 FAC across noon which depends upon the sign of the IMF B_y .

component. For $B_y < 0$ the "extra" FAC appears in the pre-noon (post-noon) sector within the southern (northern) hemisphere with a reverse geometry occurring for $B_y > 0$. Doyle et al. (1981) also provide evidence suggesting that, in addition to the region 1 current crossing noon, the associated region 2 FAC also crosses noon where it appears equatorward of the normal region 1 and region 2 systems on the opposite side of noon. An overlap of the FAC patterns also exists within the pre-midnight Harang discontinuity (Potemra et al., 1975) where the morning side region 1 FAC appears poleward of an ambiguous morning region 2/evening region 1 demarcation.

The varying responses of the different FAC regions within the auroral oval suggests that there are several sources that drive the FAC (Iijima and Potemra, 1976a; Saflekos et al., 1982). Two possible mechanisms, for example, are the dynamo at the solar wind - magnetosphere interface and the charge separation from gradient and curvature drifting plasma in the magnetosphere (Stern, 1983).

Section 2. Techniques of Data Analysis

The data presented here was obtained primarily from the S3-2 satellite although ancillary data from other sources has been used to characterize geophysical conditions. The S3-2 satellite was placed into a 96.3° inclination elliptic orbit in December 1975 with an initial apogee and perigee of 1557 km and 240 km, respectively. The attitude of the satellite was spin stabilized with a nominal spin period of 20 seconds and a spin vector perpendicular to the velocity vector (Smiddy et al., 1980). The orbital plane was such that the satellite's ascending node regressed in local time at $\sim 0.25^\circ$ per day. The geophysical parameters measured included the local DC electric and magnetic fields at 32 samples per second, the electron distribution perpendicular to the satellite spin axis and covering the range from 80 eV to 17 keV at one spectrum per second, and a thermal electron probe with a sample rate of 32 samples per second. The magnetic and electric fields are used here to deduce

the FAC pattern and the potential distribution across the polar cap and auroral zones. Only brief mention is made of data from the electron spectrometer although these results are useful in identifying regions of the high-latitude ionosphere. A more complete description of the satellite instrumentation has been given by Burke et al. (1979a).

The component of the local electric field along the satellite velocity vector allows an estimate to be made of the polar cap potential and the convective drift of plasma within the cap. The average component of the geophysical electric field in the direction of satellite motion is calculated from the instantaneous potential between two boom-mounted spheres and the potential distribution is an integration of this local electric field along the satellite path. In addition, the plasma convection drift perpendicular to the velocity vector is determined using this average electric field and a model magnetic field (Olson and Pfitzer, 1974). Since only a single component of the electric field is used to determine the polar cap potential and convective drift velocities it is likely that these quantities are underestimated in the present analysis. No attempt has been made here to correct the data for an orbit at some angle to the dawn-dusk meridian, i.e. the direction of the prevailing electric field.

The local magnetic field on S3-2 was measured with a 3-axis fluxgate magnetometer and field-aligned currents are deduced from spatial fluctuations in the net magnetic field along the satellite path. The net field is the measured vector minus the baseline geomagnetic field from the International Geomagnetic Reference Field (IGRF, 1975). The infinite current sheet approximation is used here where a FAC is assumed to be aligned with the auroral oval, i.e. at a constant invariant latitude but extending in magnetic local time. An application of Ampere's law for such a geometry yields,

$$J_{\parallel} = 2 \Delta B / \mu_0 \xi \quad (1)$$

for the current density in MKS units. ΔB is the change in the eastwest component of the net field and ξ is the latitudinal extent

of the change. Fortunately, the x-component in magnetometer coordinates was closely aligned to the east-west direction so that a change in this component of the net magnetic field could be interpreted as being due to a FAC and the current density calculated from the slope of the deflection.

Estimates of the height-integrated Pedersen conductivity, Σ_p , are obtained using Maxwell's equations within the infinite sheet approximation from,

$$J_{\parallel} = \Sigma_p \Delta E_f / \xi \quad (2)$$

(Shuman et al., 1981) where $\Delta E_f / \xi$ is the change in the electric field component along the satellite velocity. Again, it is assumed here that the satellite crosses the auroral zone transversely and that this is the primary direction of the electric field.

The electron spectrometer on S3-2 had a small geometric factor ($g = 4.68 \times 10^{-5} \text{ cm}^2 \text{ ster}$) allowing only relatively intense fluxes, i.e. above diffuse aurora levels, to be measured. Also, the slow sample time and location of the aperture in the rotation plane combined to allow spatial and angular biasing of the data. In spite of these limitations, we present sample spectra obtained during key times when the location and attitude of the satellite were favorable. These data are presented as total electron flux ($80 \text{ eV} < E < 17 \text{ keV}$) versus time and as distribution versus energy plots.

Section 3. Data Presentation

The data presented here involves the identification on a region of intense antisunward convective flow located between the region 1 FAC and an oppositely directed FAC near 0900 MLT in the southern hemisphere on 24-June-1976 while the magnetosphere was in the recovery phase of a moderately intense substorm. The interest in this event is that the entire polar cap potential appears to be confined to this narrow region.

Indices reflecting the geomagnetic conditions for the period 24-25, June 1976 are shown in figure 1 as 3-hour K_p averages and as 1-hour Dst averages (Mayaud, 1980; Lincoln, 1976; Sugiura and Poros, 1976). The sudden commencement of the magnetospheric storm period was initiated near 1630 UT (Gaum magnetometer record, June 24, 1976) and a substorm of moderate to strong intensity ($K_p \approx 5$) occurred near 1800 UT with the recovery lasting until 0200 UT of the next day. Magnetograms from two stations either side of midnight in the northern hemisphere (Dixon Island and Tixie) recorded the enhancement of the auroral electrojets during the substorm. The strengthening of the electrojets is due to plasma injection near midnight by the substorm mechanism. Interplanetary magnetic field data is not available during this period (King, 1979) but, as best we can tell, the IMF maintained a "towards" structure during the entire storm period (Lincoln, 1976). From the latter fact we deduce that the IMF B_y was negative for the data presented here.

Included in figure 1 are the times during which data was collected by the S3-2 satellite as it traversed the northern and southern polar regions. This report will concentrate on the southern polar crossing labeled "2846S" which occurred during the recovery phase of the substorm. Figure 2 is a plot of the satellite trajectory in invariant latitude and magnetic local time where the satellite crossed the morning auroral zone near 0900 MLT and the evening auroral zone near 2000 MLT. Also shown are the approximate locations of the 100 km and 300 km terminators separating the sunlit portion of the pole from the dark section. The perpendicular convective flow of plasma along the satellite trajectory as deduced from the 5-second averages of the measured electric field is shown in figure 3 where geographic coordinates are used to more easily represent the satellite path. The main feature to note is the intense antisunward convective drift ($\approx 7 \text{ km sec}^{-1}$) present in the midmorning time sector corresponding to a local electric field of 240 mV m^{-1} . An analysis of this rather extreme event will occupy the remainder of this report.

The electric potential, the east-west component of the net magnetic field and the total electron flux as measured during the south polar

pass are plotted versus time in figure 4. The morning and evening auroral zones are apparent as the regions of enhanced electron precipitation centered, respectively, near 65870 UT and 66600 UT. The evening auroral zone, located between about 71° and 63.5° of invariant latitude, has a more or less standard FAC pattern that can be deduced from the net magnetic field. This pattern consists of an outward directed region 1 current sheet of density $1.59 \mu \text{ amp m}^{-2}$ (1.03 amp m^{-1}) poleward of an inward region 2 current of $1.18 \mu \text{ amp m}^{-2}$ (0.65 amp m^{-1}). The potential distribution in the evening pass is consistent with FAC closure through ionospheric Pedersen currents. Rough estimates of the perpendicular conductivity yield 5 mhos presumably due to the diffuse electron precipitation - reaching levels as high as 33 mhos in regions of enhanced precipitation. A more complex FAC pattern is present in the morning time sector where multiple large-scale reversals in the current direction are observed. Currents measured between 73.2° (18:17.21 UT) and 75.4° (18:18.12 UT) are consistent with the "traditional" region 1 (into) and region 2 (out of) configuration having densities of $5.96 \mu \text{ amp m}^{-2}$ (1.75 amp m^{-1}) and $8.18 \mu \text{ amp m}^{-2}$ (0.786 amp m^{-1}), respectively. Both poleward and equatorward of these two FAC are additional current sheets of opposite polarity and having respective densities of $6.97 \mu \text{ amp m}^{-2}$ (0.90 amp m^{-1}) and $4.82 \mu \text{ amp m}^{-2}$ (0.52 amp m^{-1}). The electric fields patterns throughout this region suggest FAC closure via Pedersen currents. The average Pedersen conductivity in the volume connecting region 1 to region 2 and region 2 to the equatorward current sheet are on the order of 4 to 7 mhos while in the space connecting region 1 to the poleward FAC the conductivity is less than 1 mho. The implication here is that diffuse electron precipitation occurs in the former regions whereas the latter region is poleward of the diffuse auroral zone. It is also within this later region where the high-latitude ionospheric plasma undergoes intense antisunward flow in response to a large dawn-to-dusk electric field. The latitudinal extent of this drift region is about

2.7° and the potential difference across the intense drift region is 52.8 kV - comparable to the expected polar cap potential.

Figure 5 is a plot of the electron distribution function obtained while the satellite was at the poleward edge of the region of antisunward flow and embedded within an intense upward current sheet ($38 \mu\text{amp m}^{-2}$) of the poleward FAC indicative, perhaps, of an arc. The spectrometer's entrance aperture at this time was nearly field-aligned ($\approx 10^\circ$) to precipitating electrons. Two populations of electrons are observed - cold and hot components of 97.4 eV and 1.61 keV, respectively. Generally speaking, the hot population is more field-aligned than the cold component which is present in the adjacent sweep when the pitch angle was between 30° and 10° . Although this data should be viewed with caution, the distributions may help to identify the source region of the poleward FAC.

Section 4. Discussion and Conclusions

The data presented in section 3 indicates the presence of an intense antisunward convective drift in the latitudinal zone separating a cusp current from the dawnside region 1 FAC. This drift is due to a large electric field representing the gradient of the polar cap potential that has been compressed to only several degrees of latitude. The overall configuration of field-aligned currents and electric fields, as presented here, is consistent with statistical patterns for $\text{IMF } B_y < 0$ conditions. This extreme case, however, details more information regarding the morphology of the polar cap when the cusp or "extra" current sheet is present.

The cusp current is, presumably, an extension of the post-noon region 1 FAC that has crossed the noon meridian poleward of the morning region 1. The electric field within the cusp/region 1 transition drives a Pedersen current and also drives a Hall current which can be detected as an extra electrojet. Such DPY (Disturbance Polar related to the IMF B_y) currents have been measured by ground-based

magnetometers in the northern hemisphere (Wilhelm et al., 1978) and the response of these currents to the IMF B_y is consistent with the electric field direction presented here for the southern hemisphere. Although the potential distribution is strongly skewed towards the morning hemisphere, this too is consistent with the statistical potential distributions presented by Heppner (1972) for IMF $B_y < 0$. It appears here that the entire polar cap potential drop of 52.8 kV, i.e. the dawn-to-dusk electric field, is limited to 2.7° in latitude. The general morphology, then, is consistent with previous work yet this data characterizes an extreme case of the potential cap structure.

The "extra" current exists poleward of both the convection reversal and the diffuse aurora, i.e. the projection of the central plasma sheet. Thus, this FAC may be within a region of open field lines however we can not be sure of this because of the lack of information regarding the trapping boundary. A cold magnetosheath-like electron population ($T_e < 100$ eV) poleward of region 1 does suggest, however, that the field lines are either within the polar cap or associated with the cusp. The presence of the "extra" FAC which has wrapped around noon into the morning time sector lends support to the latter choice. The question to be addressed is why the entire polar cap potential drops across the interface from the region 1 to the cusp FAC.

The underlying physics involved in this situation is only beginning to be understood by the author. The problem is to define the relationship between the intense antisunward convective flow and the cusp current during the geomagnetic storm. The cusp current is presumably driven by the magnetic field merging on the magnetopause whereas the substorm is primarily a tail event. Although the magnitude of field-aligned currents and ionospheric electric fields are affected by the level of geomagnetic activity, a mechanism that causes the entire polar cap potential to appear over a small latitudinal regime is

not known. Perhaps the ionospheric conductivity seriously alters the potential distribution especially on account of the 100 km and 300 km terminators which intersect the auroral zone and the cusp FAC.

In order to continue in the analysis of this phenomena it will be necessary to analyze the other satellite passes before the substorm and during its various stages. This may allow us to segregate those effects that are purely substorm related from other sources.

REFERENCES

- Burke, W. J., D. A. Hardy, F. J. Rich, M. C. Kelley, M. Smiddy, B. Shuman, R. C. Sagalyn, R. P. Vancour, P. J. L. Wildman, S. T. Lai, and J. Bass, A case study of S3-2 Observations in the late evening auroral oval, AFGL-TR-79-0011, Air Force Geophysics Laboratory, Massachusetts, 1979a.
- Burke, W. J., M. C. Kelley, R. C. Sagalyn, M. Smiddy, and S. T. Lai, Polar cap electric structures with a northward interplanetary magnetic field, Geophys. Res. Lett., 6, 21-24, 1979b.
- Cauffman, D. P. and D. A. Gurnett, Satellite measurements of high latitude convection electric fields, Space Sci. Rev., 13, 369-410, 1972.
- Crooker, N. U., Antisunward merging, the half-wave rectifier response of the magnetosphere, and convection, in Proceedings of the Chapman Conference on Magnetospheric Boundary Layers, ESA Space Publ., SP-148, edited by Bruce Battrock, pp. 343-348, Eur. Space Agency, Neuilly, France, 1979.
- Doyle, M. A. and W. J. Burke, S3-2 measurements of the Polar cap potential, J. Geophys. Res., 88, 9125-9133, 1983.
- Doyle, M. A., F. J. Rich, W. J. Burke, and M. Smiddy, Field-aligned currents and electric fields observed in the region of the dayside cusp, J. Geophys. Res., 86, 5656-5664, 1981.
- Fairfield, D. H., Electric and magnetic fields in the high-latitude magnetosphere, Rev. Geophys. Space Phys., 15, 285-298, 1977.
- Heelis, R. A., W. R. Hanson, and J. L. Burch, Ion convection velocity reversals in the dayside cleft, J. Geophys. Res., 81, 3803-3809, 1976.
- Heppner, J. P., Polar-cap electric field distribution related to the interplanetary magnetic field direction, J. Geophys. Res., 77, 4877-4887, 1972.
- Iijima, T. and T. A. Potemra, The amplitude distribution of field-aligned currents at northern high latitudes observed by Triad, J. Geophys. Res., 81, 2165-2165, 1976a.
- Iijima, T. and T. A. Potemra, Field-aligned currents in the dayside cusp observed by Triad, J. Geophys. Res., 81, 5971-5979, 1976b.
- King, Joseph H., Interplanetary Medium Data Book-Supplement 1, NSSNC/WDC-A-R&S 79-08, NASA, Maryland, 1979.
- Lincoln, J. Virginia, Geomagnetic and solar data, J. Geophys. Res., 81, 5220, 1976.
- Maezawa, K., Magnetic convection induced by the positive and negative Z components of the interplanetary magnetic fields: Quantitative analysis using polar cap magnetic records, J. Geophys. Res., 81, 2289-2303, 1976.
- Mayaud, P. N., Derivation, Meaning, and Use of Geomagnetic Indices, 154 pp., American Geophysical Union, Washington, D. C., 1980.

- McDiarmid, I. B., J. R. Burrows, and M. D. Wilson, Comparison of magnetic field perturbations at high latitudes with charged particle and IMF measurements., J. Geophys. Res., 83, 681-688, 1978.
- Mozer, F. S., W. D. Gonzalez, F. Roqott, M. C. Kelley, and S. Schultz, High-latitude electric fields and the three dimensional interaction between the interplanetary and terrestrial magnetic fields, J. Geophys. Res., 79, 56-63, 1974.
- Nelson, W. P. and K. A. Pfitzer, A quantitative model of the magnetospheric field, J. Geophys. Res., 79, 3739-3748, 1974.
- Potemra, T. A., T. Iijima, and S. Favin, Field-aligned currents in the north and south auroral regions measured with Triad, EOS Trans. AGU, 56, 617-618, 1975.
- Reiff, P. H., R. W. Spiro, and T. W. Hill, Dependence of the polar cap potential drop on the interplanetary parameters, J. Geophys. Res., 86, 7639-7648, 1981.
- Russell, C. T., The configuration of the magnetosphere, in Critical Problems of Magnetospheric Physics, edited by E. R. Dyer, pg 1-16, InterUnion Committee on Solar-Terrestrial Physics, National Academy of Sciences, Washington, D.C., 1972.
- Saflekos, N. A., R. E. Sheenan, and R. L. Carovillano, Global nature of field-aligned currents and their relation to auroral phenomena, Rev. Geophys. Space Phys., 20, 709-734, 1982.
- Shuman, B. M., R. P. Vancour, M. Smiddy, N. A. Saflekos, and F. J. Rich, Field-aligned current, convective electric field and auroral particle measurements during a major magnetic storm, J. Geophys. Res., 86, 5561-5575, 1981.
- Smiddy, M., W. J. Burke, M. C. Kelley, N. A. Saflekos, M. S. Gussenhoven, D. A. Hardy, and F. J. Rich, Effects of high-latitude conductivity on observed convection electric fields and Birkeland currents, J. Geophys. Res., 85, 6811-6818, 1980.
- Stern, D. P., The origins of Birkeland currents, Rev. Geophys. and Space Phys., 21, 125-138, 1983.
- Sugiura, M and D. J. Poros, Hourly equatorial Dst Values (Provisional) - June 1976, World Data Center A for Rockets and Satellites, NASA, Maryland, 1976.
- Sugiura, M. and T. A. Potemra, Net field-aligned currents observed by Triad, J. Geophys. Res., 81, 2155-2164, 1976.
- Wilhelm, J., E. Friis-Christensen, and T. A. Potemra, The relationship between ionospheric and field-aligned currents in the dayside cusp, J. Geophys. Res., 83, 5586-5594, 1978.
- Zmuda, A. J. and James C. Armstrong, The diurnal flow pattern of field-aligned currents, J. Geophys. Res., 79, 4611-4619, 1974.

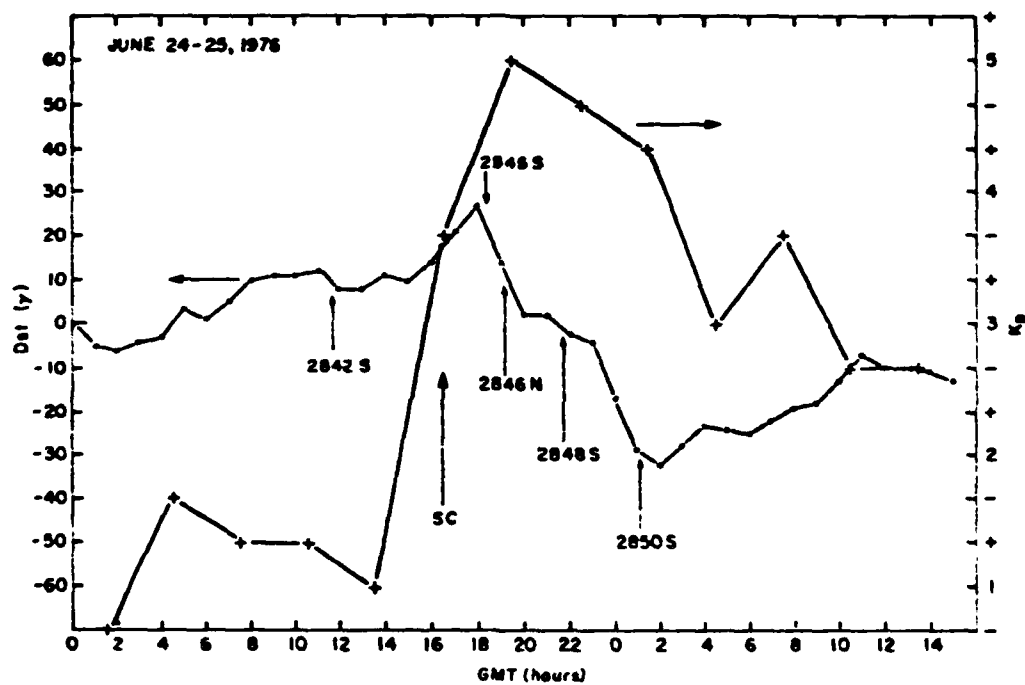


Figure 1. Geomagnetic conditions as reflected in 3-hour K_p averages and 1-hour D_{st} averages for the substorm period on June 24, 1976 through June 25. The time of the sudden commencement was near 1630 UT and the times of S3-2 polar orbits are indicated.

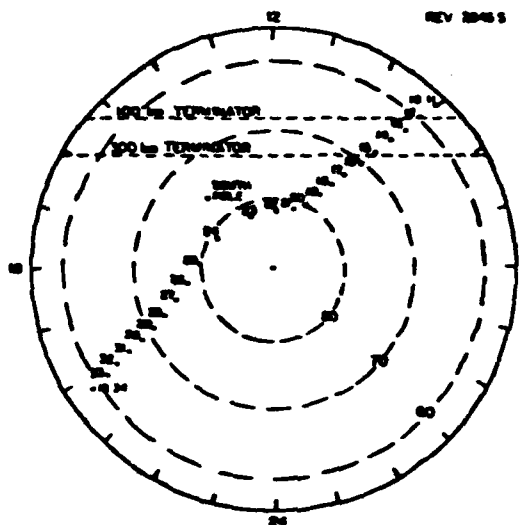


Figure 2. Orbital track of the S3-2 satellite in invariant latitude and magnetic local time coordinates for Rev. 2046S. Approximate locations of the 100 km and 300 km terminators are indicated.

S3-2 Rev. 2046S

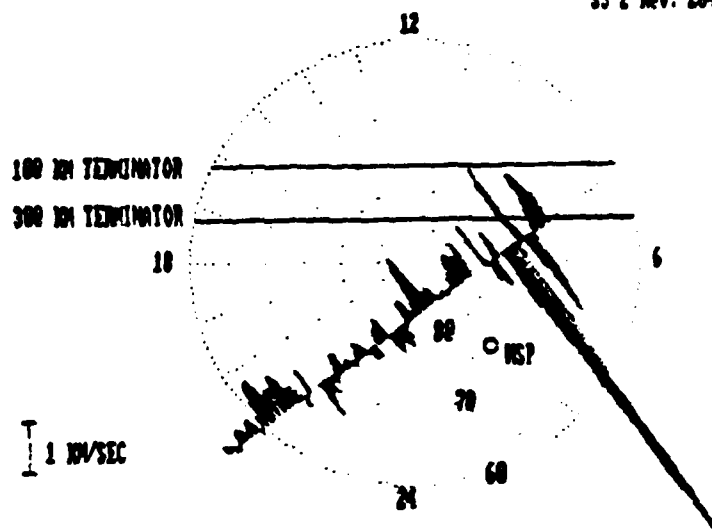


Figure 3. Plasma convective drift perpendicular to the satellite trajectory as deduced from the forward component of the electric field. Geographic coordinates are used here to represent the satellite path.

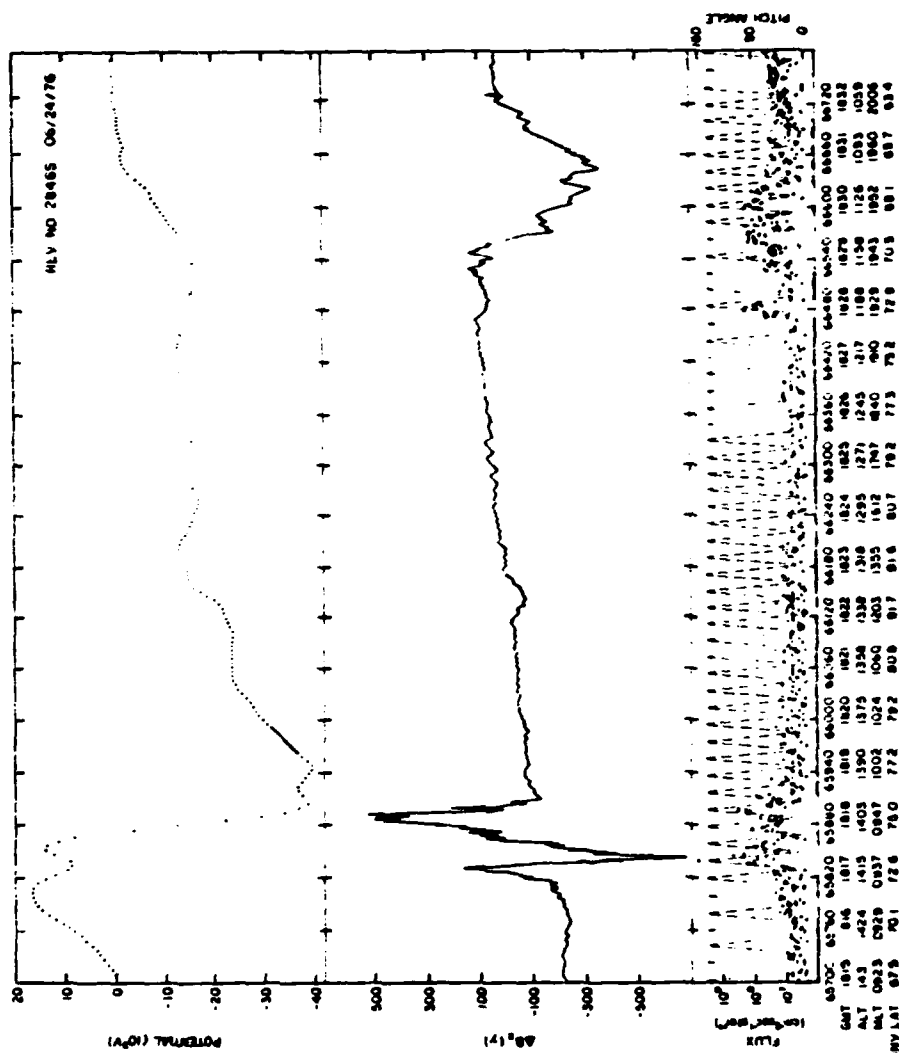


Figure 4. Plots of the polar cap potential, the net magnetic field, and the electron flux versus time (i.e. position) as measured by the H-2 satellite.

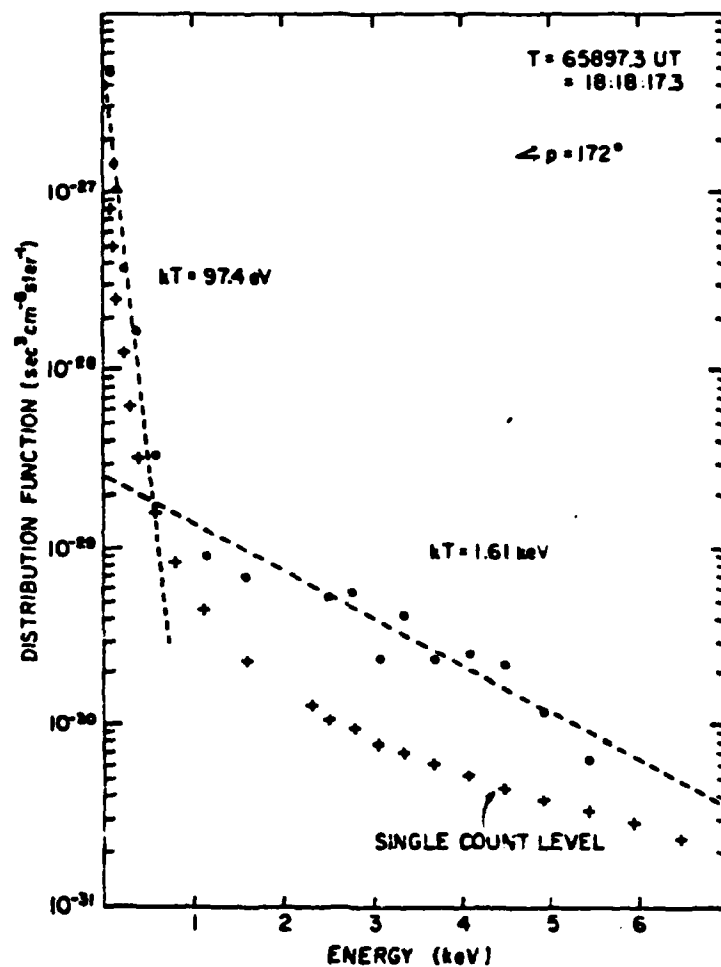


Figure 5. Electron distribution function versus energy for a pitch angle of 172° . The electrostatic analyzer measures precipitating electrons within the region of the cusp current.

1982-1983 AFGL-SCEEE GEOPHYSICS SCHOLAR PROGRAM

Sponsored by the

AIR FORCE OFFICE OF SCIENTIFIC RESEARCH

Conducted by the

SOUTHEASTERN CENTER FOR ELECTRICAL ENGINEERING EDUCATION

FINAL REPORT

QUENCHING OF VIBRATIONALLY EXCITED NH BY N₂ and H₂

Prepared by:	Dr. Kenneth G. Kosnik
Academic Department:	Physical Chemistry, Chemical Kinetics
University:	University of Southern California
Research Location:	Air Force Geophysics Laboratory Optical Physics Division
AFGL Research Contact:	Dr. William A. M. Blumberg
Date:	September 19, 1983
Contract Number:	F49620-82-C-0035

Acknowledgement

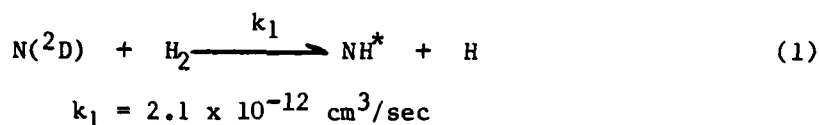
The author would like to thank the Air Force Office of Scientific Research and the Southeastern Center for Electrical Engineering Education for providing him with the opportunity to spend a very worthwhile and interesting year at the Air Force Geophysics Laboratory, Hanscom AFB, MA. He would like to acknowledge the laboratory, in particular the Optical Physics Division, for its hospitality and excellent working conditions.

Finally, he would like to thank Dr. William A. M. Blumberg for suggesting this area of research and for his collaboration and guidance, and Stan Wolnik for many illuminating discussions and his scientific and technical assistance.

I. INTRODUCTION

The accurate kinetic modeling of the atmosphere is essential for understanding optical atmospheric backgrounds and disturbed atmospheres (including natural phenomenon).² The key to atmospheric modeling is the experimental determination of the relevant processes and rate constants.³

The metathesis reaction of $N(^2D)$ and H_2 is mechanistically very similar to the important atmospheric reaction of $N(^2D)$ and O_2 . This reaction is important in the combustion of rocket fuels and also the potential surfaces can be readily calculated. In the past the main kinetic emphasis was on the reactions between metastable $N(^2D)$ and diatomic molecules and many of these rate constants were measured. Of particular interest in this study of vibrationally excited NH in the present report is the reaction of $N(^2D)$ and H_2 .⁵



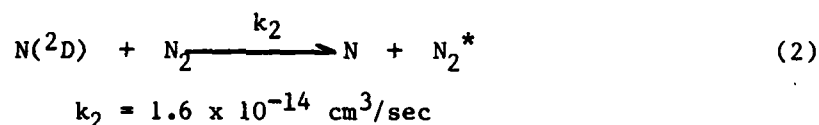
This is the main NH^* formation reaction when $[N_2] \gg [H_2]$. Reaction (1) is exothermic by about 1.4 ev.⁵

The $N(^2D)$ is produced by the electron bombardment of molecular nitrogen with 40 kev electrons. Ground state $N(^4S)$ and electronically excited $N(^2P)$ are also produced by the electron beam; however, the reaction of $N(^4S)$ and H_2 is endothermic by about 1.0 ev, and the reaction of $N(^2P)$ and H_2 has a high activation energy.⁵ Ground state hydrogen atoms also do not appreciably react with N_2 .⁵ The $N(^2D)$ is primarily destroyed by the reaction with H_2 forming NH^* and quenching with N_2 .

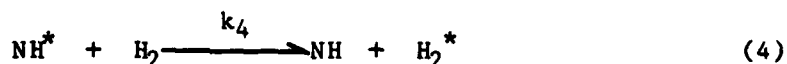
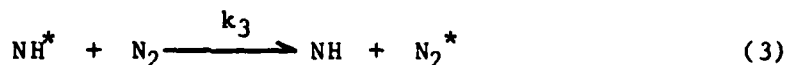
Air leaks are particularly troublesome because O_2 can compete for the available $N(^2D)$ by forming vibrationally excited NO. Molecular hydrogen can react with O_2 forming OH and HO_2 with O-H stretching frequencies at 3000 cm^{-1} , thus potentially providing a considerable background for the NH bands (also approximately 3000 cm^{-1}). Electron beam produced atomic oxygen can react exothermically with H_2 forming OH.² The fate of the vibrationally excited NH and the undesirable vibrationally excited OH and HO_2 are quenched by N_2 and/or H_2 .

This report directs attention to the quenching of the vibrationally excited $NH(v \leq 3)$ by N_2 and H_2 . In electron beam irradiated mixtures of N_2 (in excess) and H_2 reaction (1) was found to be the predominant formation mechanism.⁵

Another reaction that is very important in the NH system is the quenching of $N(^2D)$ with N_2 .⁹



The predominant collisional quenching mechanisms due to the rather large partial pressures of N_2 and H_2 are as follows:



It should be noted that the reaction exothermicity may appear as translational energy and not necessarily in the internal modes of N_2 or H_2 .

II. OBJECTIVES

The main objective of this project was a quantitative measurement and detailed kinetic study of the collisional quenching of electron beam produced vibrationally excited $\text{NH}(v \leq 3)$ by nitrogen and hydrogen.

Our specific objectives were:

- (1) To determine the predominant quenchant species.
- (2) To experimentally measure the relevant quenching rate constants k_3 and k_4 .
- (3) To obtain an accurate theoretical kinetic model to precisely describe the time resolved behavior of the experimental NH system.

III. EXPERIMENTAL MEASUREMENT OF THE QUENCHING RATE CONSTANTS (k_3 & k_4)

An electron beam experiment employing a Michelson interferometer and InSb detector interfaced to a PDP 11/40 computer was used to measure the infrared fluorescence of a mixture of nitrogen (in excess) and hydrogen. Subsequent time dependent Fourier spectroscopy allowed the determination of the quenching rate constants.

The detector signal, after processing by computer, can be used to obtain both spectral and temporal resolution. The signal from the biased detector is band pass amplified and then the amplified signal is fed into a sample and hold network, which samples the detector signal at times determined by a digital delay network. The sampled signal is converted to a digital form by an A/D converter and then stored on a magnetic disk. The digital delay network timing is referenced just prior to the onset of the electron beam. The additional details of this facility have been previously described and will not be discussed further here.¹⁰

Relative intensities were obtained by integration over the R

branch of $v=1$ of the vibrationally excited NH^* because the P branch of $v=1$ was effectively overlapped by the bands $v=2$ and $v=3$.

Much of my initial time on this research project was spent improving the 0.1 milliamps of beam current in the target chamber to approximately 2.0 milliamps to insure adequate signal to noise for the experiment. This involved the very careful aligning of the filament with the non-adjustable baffle in the electron gun assembly and a brace to support the drooping plexiglass column that contained the accelerating electrodes.

By removing all three baffles, and inserting thin aluminum foils at the positions of the 1st (non-adjustable) and 3rd (circular plate in the target chamber) baffles the path of the electron beam through the apparatus could be determined. When the electron beam was then turned on, small holes were burned in the two foils. The non-adjustable 1st baffle was then aligned on the electron beam path described by the tip of the filament and the burned holes in the foils.

Many troublesome air leaks had to be sealed and several improvements had to be made in the vacuum system before the experiment could be performed. These included repairing a very large leak in the booster pump and replacing the heating coils, replacement of much of the polyethylene and rubber tubing in the gas handling system, and the installation of high vacuum ball valves.

Experimental measurements were made using nitrogen pressures from 5.0, 10.0, 15.0, 30.0, and 50.0 torr. Hydrogen pressures were varied from 0.1, 0.2, 0.4, 0.6, 1.0, 2.0, and 4.0 torr.

By curve fitting the experimental ratio $[NH^*]/[NH^*]_0$ to the

theoretically predicted (based on the kinetic model) ratio $[\text{NH}^*]/[\text{NH}^*]_0$, the values of k_3 and k_4 can be estimated. In a preliminary curve fit the quenching rate constants for N_2 (k_3) and H_2 (k_4) were found to be approximately $10^{-13.7}$ $0.3 \text{ cm}^3/\text{sec}$. A curve fitting program is currently being written to determine these quenching rate constants more accurately.

The experimental quantities $[\text{NH}^*]$ and $[\text{NH}^*]_0$ were determined from the integrals of the R branch of $v=1$ as a function of time (interferogram number). The value of the background that was subtracted to determine $[\text{NH}^*]$ and $[\text{NH}^*]_0$ was very important. When the NH^* signal was quenched out to a straight line (slightly negative slope) on a logarithm plot, then this straight line was extrapolated back to obtain the very important backgrounds. Following are a few examples comparing the experimental $[\text{NH}^*]/[\text{NH}^*]_0$ ratio and the theoretical (see theoretical kinetic reaction model) $[\text{NH}^*]/[\text{NH}^*]_0$ ratio at various pressures. The theoretical curve fit is much more sensitive to k_3 than k_4 estimates.

(1) Run #2 on 24 JUN 83; 5.0 torr N_2 , 1.0 torr H_2

t (μsec)	0	100	200	300	400	
Interferogram	63	67	71	75	79	
Experimental $[\text{NH}^*]/[\text{NH}^*]_0$	1.000	0.657	0.503	0.331	0.213	
Theoretical $[\text{NH}^*]/[\text{NH}^*]_0$	1.000	0.848	0.699	0.576	0.475	$k_3=k_4=1.0 \times 10^{-14}$
	1.000	0.719	0.489	0.332	0.226	$k_3=k_4=2.0 \times 10^{-14}$
	1.000	0.611	0.342	0.192	0.107	$k_3=k_4=3.0 \times 10^{-14}$

(2) Run #3 on 27 JUN 83; 10.0 torr N₂, 0.6 torr H₂

t (μsec)	0	50	100	150	200	
Interferogram	62	64	66	68	70	
Experimental [NH*]/[NH*] ₀	1.000	0.853	0.774	0.350	0.299	
Theoretical [NH*]/[NH*] ₀	1.000	0.903	0.767	0.648	0.546	k ₃ =k ₄ =1.0x10 ⁻¹⁴
	1.000	0.818	0.592	0.422	0.300	k ₃ =k ₄ =2.0x10 ⁻¹⁴
	1.000	0.743	0.460	0.277	0.166	k ₃ =k ₄ =3.0x10 ⁻¹⁴

(3) Run #1 on 28 JUN 83; 15.0 torr N₂, 2.0 torr H₂

t (μsec)	0	25	75	125	175	
Interferogram	62	63	65	67	69	
Experimental [NH*]/[NH*] ₀	1.000	0.803	0.634	0.327	0.156	
Theoretical [NH*]/[NH*] ₀	1.000	0.906	0.690	0.525	0.399	k ₃ =k ₄ =1.0x10 ⁻¹⁴
	1.000	0.821	0.477	0.276	0.160	k ₃ =k ₄ =2.0x10 ⁻¹⁴
	1.000	0.746	0.330	0.145	0.064	k ₃ =k ₄ =3.0x10 ⁻¹⁴

(4) Run #4 on 5 MAY 83; 50.0 torr N₂, 4.0 torr H₂

t (μsec)	0	25	50	75	
Interferogram	64	65	66	67	
Experimental [NH*]/[NH*] ₀	1.000	0.588	0.308	0.162	
Theoretical [NH*]/[NH*] ₀	1.000	0.688	0.445	0.288	k ₃ =k ₄ =1.0x10 ⁻¹⁴
	1.000	0.475	0.199	0.083	k ₃ =k ₄ =2.0x10 ⁻¹⁴
	1.000	0.329	0.089	0.024	k ₃ =k ₄ =3.0x10 ⁻¹⁴

It appears that a value of $k_3 = k_4 = 2.0 \times 10^{-14} \text{ cm}^3/\text{sec}$ is a good preliminary curve fit for the runs using 5.0, 10.0, and 15.0 torr of nitrogen. The best fit for the 50.0 torr of N_2 runs appear to be closer to $1.0 \times 10^{-14} \text{ cm}^3/\text{sec}$ but this data has not been corrected for the detection system constant (approximately $50 \mu\text{sec}$).

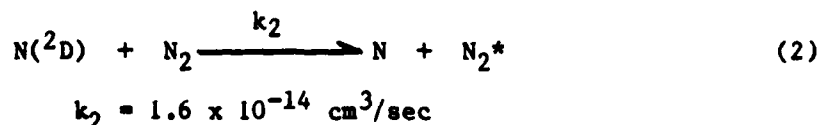
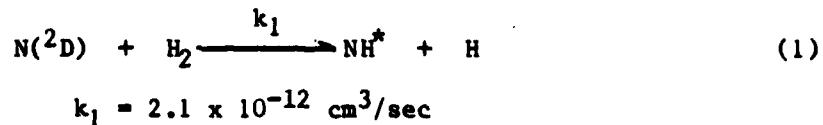
IV. THEORETICAL KINETIC REACTION MODEL

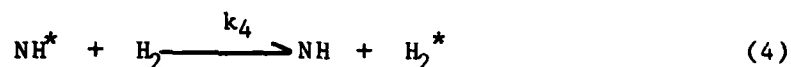
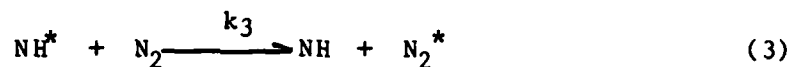
A useful theoretical reaction model must precisely predict the overall behavior of the experimental system. When this condition is met then all of the relevant chemical and physical processes have been appropriately considered.^{2,3}

The three main assumptions in the vibrationally excited NH^* quenching are as follows:

- (1) After the electron beam has been turned off, the production of $\text{N}(^2\text{D})$ stops. This assumption has also been verified experimentally by the reaction of nitrogen ions with O_2 .⁵
- (2) Before the electron beam has been turned off, the $\text{N}(^2\text{D})$ is in steady state with the vibrationally excited NH^* .
- (3) The excited NH^* transfers vibrational energy to the vibrational and/or translational energy of the quenchant molecules.

The system of equations that describe the experimental system after the electron beam has been turned off are the following:





Again it should be noted that the reaction exothermicity may appear as translational energy and not necessarily in the internal modes of N_2 or H_2 .

This system of equations can be solved by the differential operator method to give:⁴

$$\frac{[\text{NH}^*]}{[\text{NH}^*]_0} = e^{-(k_3[\text{N}_2] + k_4[\text{H}_2])t} + \left(\frac{k_3[\text{N}_2] + k_4[\text{H}_2]}{k_3[\text{N}_2] + k_4[\text{H}_2] - k_1[\text{H}_2] - k_2[\text{N}_2]} \right) \times \left(e^{-(k_1[\text{H}_2] + k_2[\text{N}_2])t} - e^{-(k_3[\text{N}_2] + k_4[\text{H}_2])t} \right) \quad (5)$$

Since k_1 , k_2 , $[\text{N}_2]$, and $[\text{H}_2]$ are known and the time resolved ratio $[\text{NH}^*]/[\text{NH}^*]_0$ has been experimentally measured the values of k_3 and k_4 can be obtained by curve fitting. This theoretical kinetic model accurately describes the time resolved behavior of the experimental system at both moderate (15.0 torr) and low (5.0 torr) nitrogen pressures, with varying amounts of hydrogen (4.0 to 0.1 torr).

V. RECOMMENDATIONS

The vibrational temperature of the formed NH^* is about 3000 °K but there is probably not enough resolution to be able to describe the time resolved behavior of $\text{NH}(v=2)$, and $\text{NH}(v=3)$. The equations

previously described appear to represent the quenching of $\text{NH}(v=1)$. Portions of the band system that contains both $\text{NH}(v=1)$ and $\text{NH}(v=2)$ can have relative intensities also determined by integration. If the time resolved behavior of $\text{NH}(v=1)$ and portions of $\text{NH}(v=1)$ and $\text{NH}(v=2)$ are the same then the quenching process would be predominantly vibration to translation. The time resolved history of $\text{NH}(v=0)$, $\text{NH}(v=1)$, $\text{NH}(v=2)$, and $\text{NH}(v=3)$ could be experimentally obtained in the laboratory by a laser absorption technique if an appropriate tunable semiconductor diode laser was available.

The high nitrogen pressure (50.0 torr) experimental runs will have to be repeated to verify reproducibility. An additional reproducible experimental run at an intermediate nitrogen pressure (30.0 torr) would be very helpful.

It is necessary to have an accurate and reproducible curve fitting technique to accurately determine the quenching rate constants k_3 and k_4 .

In summary, more laboratory data has to be taken. If it is possible, a complete analysis of the other vibrational levels ($v=2$ and $v=3$) with the curve fitting technique would be very helpful. A semiconductor laser can be used to obtain the time resolved history of $v=0$.

REFERENCES

1. Jeffrey Steinfeld, Molecules and Radiation, New York, New York, Harper and Row, (1974).
2. Sidney W. Benson, Thermochemical Kinetics, New York, New York, John Wiley Interscience, (1976).
3. Sidney W. Benson, The Foundations of Chemical Kinetics, New York, New York, McGraw-Hill, (1960).
4. Earl Rainville, Elementary Differential Equations, London, England, Macmillan, (1964).
5. B. D. Green, and G. E. Caledonia, J. Chem. Phys., vol. 77, 3821 (1982).
6. R. E. Murphy, F. H. Cook, and H. Sakai, J. Opt. Am., vol. 65, 600 (1975).
7. P. Hansen, H. Sakai, and M. Espling, Proc. Soc. Photo. Opt. Instrum. Eng., vol. 191, 15 (1979).
8. G. Gas, A. C. Wahl, and W. J. Stevens, J. Chem. Phys., vol. 61, 433 (1974).
9. D. Husain, S. K. Mitra, and A. N. Young, J. Chem. Soc. Faraday Trans. 2, vol. 70, 1721 (1974).
10. G. E. Caledonia, B. D. Green, and R. E. Murphy, J. Chem. Phys., vol. 71, 4369 (1979).

1982-1983 AFGL-SCEEE GEOPHYSICS SCHOLAR PROGRAM

Sponsored by the

AIR FORCE OFFICE OF SCIENTIFIC RESEARCH

Conducted by the

SOUTHEASTERN CENTER FOR ELECTRICAL ENGINEERING EDUCATION

FINAL REPORT

AN ANALYSIS OF PARTICULATE REMOVAL

FROM THE TITAN ROCKET EXHAUST CLOUD

Prepared by: Dr. Yean Lee

Research Location: Air Force Geophysics Laboratory
Cloud Physics Branch
Meteorology Division

AFGL Research Contact: Dr. Arnold A. Barnes, Jr.

Date: September 12, 1983

Contract No: F49620-82-C-0035

ACKNOWLEDGEMENT

The author would like to thank the Air Force Systems Command, the Air Force Office of Scientific Research and the Southeastern Center for Electrical Engineering Education for providing him with the opportunity to spend a very worthwhile and interesting year at the Air Force Geophysics Laboratory, Hanscom AFB, MA. He would like to acknowledge the laboratory, in particular Meteorology Division, Cloud Physics Branch, for its hospitality and excellent working conditions.

Finally, he would like to thank Dr. Arnold A. Barnes, Jr. for suggesting this area of research and for his collaboration and guidance, and he would like to thank Mrs. Carolyn Fadden for typing the manuscript.

I. INTRODUCTION

In any Titan launch the solid-fueled rocket engines emit large quantities of effluent into the atmosphere to form a visible, stabilized, elevated, ground cloud. The major component of the rocket exhaust is Al_2O_3 , along with HCl , CO_2 , NO_x , and H_2O gases. The cloud can exist in the atmosphere for periods of several hours. Because the highly polluted cloud has the potential of affecting the environment, many investigators have studied and researched this subject.

In a recent paper, Radke et al¹ presented much valuable information on the nature of the ground clouds produced by the launch of a Titan rocket from the Kennedy Space Flight Center, Cape Canaveral, Florida at 1940 EST on 13 December 1978. They reported that about 10^4 kg of Al_2O_3 is released by a Titan launch. About an hour after launch of the rocket (T+59 min), from the measurements of volume of the ground cloud and the (dried) aerosol volume concentration within the cloud, they estimated that the particulate mass remaining in the cloud was only about 5-10 kg. This result leads to the question, where did all the Al_2O_3 go? While their measurements did not provide a definitive answer to this question, we have taken a theoretical approach by developing a simplified model predicting the depletion of Al_2O_3 within the cloud. By comparing the model results with the measurements, we can examine whether or not the suggested mechanism can account for the depletion of Al_2O_3 .

II. OBJECTIVES

The main objective of this study was to investigate what process is most likely to play the principal role in removing Al_2O_3 from the clouds? Precipitation is one of the possible processes. Dry removal by sedimentation, on the other hand, is also a likely mechanism. During the

launch of the Titan rocket, only scattered stratus clouds formed near the top of the boundary layer, and no precipitation was observed, therefore, our study will be primarily concerned with dry removal.*

III ANALYSIS

(a) Aerosol particle size distribution

In the study of dry removal by sedimentation, the concentration and size distribution of particles are two important parameters. The University of Washington's B-23 aircraft made several penetrations of the Titan cloud. Measurements at 4 minutes after launch indicated that the aerosol particle diameters ranged from a few microns to a few hundred microns, and the number of particles per cm^3 ranged from 10^3 to 10^{-5} . For purposes of computation the whole distribution curve has to be put in mathematical form. To fit the distributions over each size domain, the simplest description is a two parameter function in the form of a power law as follows:

$$\frac{dN}{dD} = C_1 D^{-\alpha} \quad (\text{size regime 1}) \quad (1)$$

$$\frac{dN}{dD} = C_2 D^{-\beta} \quad (\text{size regime 2}) \quad (2)$$

$$\frac{dN}{dD} = C_3 D^{-\gamma} \quad (\text{size regime 3}) \quad (3)$$

where dN is the number of particles per cm^3 in the range of dD , D is the diameter (cm), and C_i are constants depending on the total number, N , of particles per cm^3 over each particular size range. The values of α , β , and γ have to be determined from curve fittings.

* See Lee and Barnes², for a model of effluent removal by precipitation.

For continuity,

$$C_1 = C_2 D_{\min}^{\alpha-\beta} \quad \text{and}$$

$$C_3 = C_2 D_{\max}^{\gamma-\beta}$$

where D_{\min} and D_{\max} are the minimum and maximum particle diameters, respectively, of the size distribution curve represented by Eq. (2).

Using a least squares procedure, the data plotted in Fig. 10 of Radke et al¹ can be approximated by these expressions. The numerical values of the parameters are:

$8 \times 10^{-4} < D(\text{cm}) < 2.7 \times 10^{-3}$	$C_1 = 1.06 \times 10^{-10} \text{ cm}$	$\alpha = 5$
$2.7 \times 10^{-3} < D < 2.7 \times 10^{-2}$	$C_2 = 1.45 \times 10^{-3} \text{ cm}^{-1}$	$\beta = 3$
$2.7 \times 10^{-2} < D < 0.1$	$C_3 = 2.08 \times 10^{-13} \text{ cm}^4$	$\gamma = 8$

For illustration the results of these computations are plotted in Fig. 1.

(b) Particulate mass

Knowing the size distributions and the volume of the ground cloud, we can estimate the mass distribution in each size regime. Observations indicated that the ground cloud was approximately disc, with an initial volume $V_0 = 1.76 \times 10^7 \text{ m}^3$.

An estimate of the particulate mass can be obtained by integrating

$$m = \frac{1}{6} \int_{D_{\min}}^{D_{\max}} \pi D^3 \rho_p V_0 dN \quad (4)$$

where ρ_p is the particle density for Al_2O_3 , i.e., $\rho_p = 2 \text{ gm/cm}^3$, and D_{\min} and D_{\max} are the minimum and maximum particle diameter, respectively, of each size range.

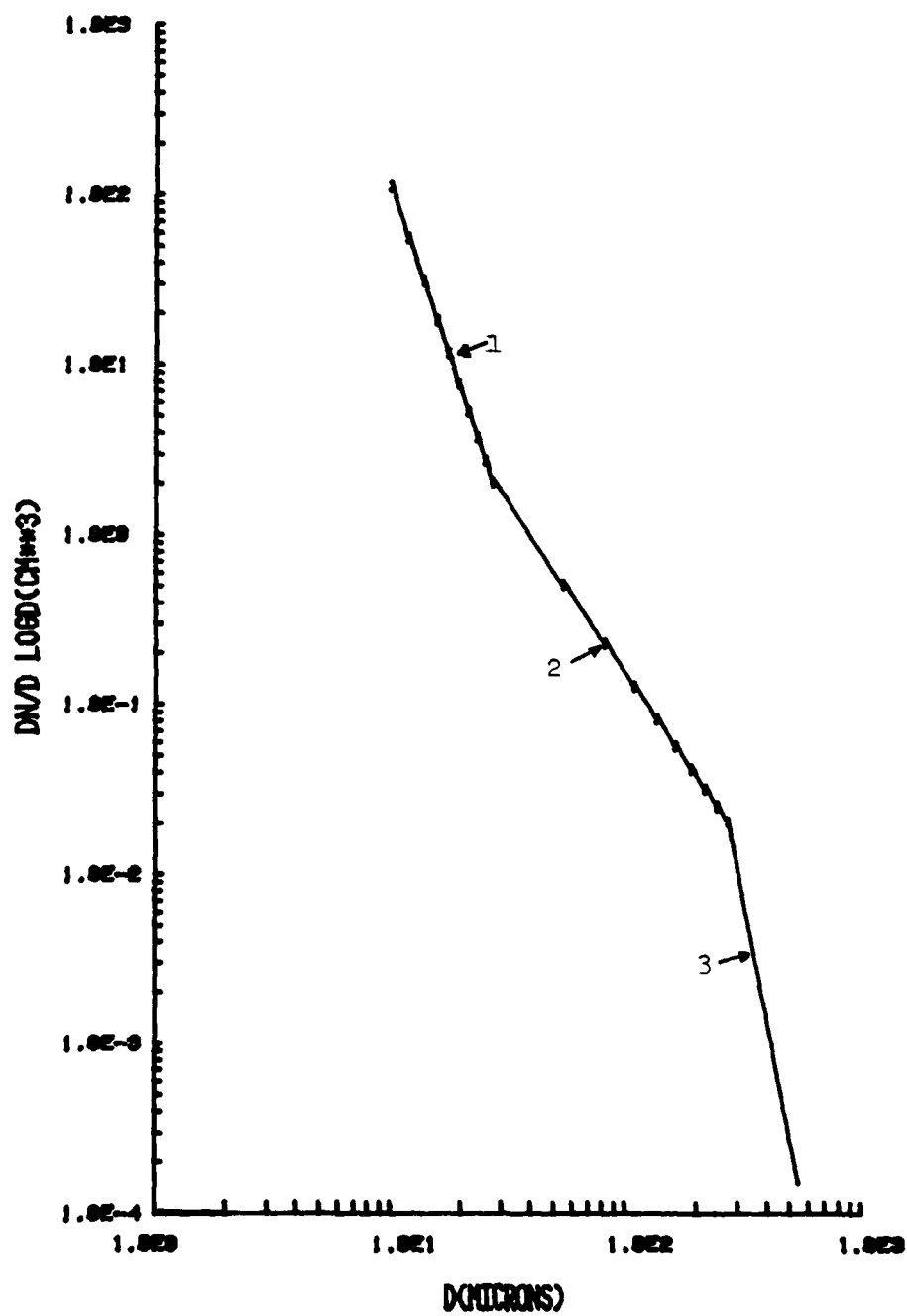


Fig. 1. Computed size distribution of aerosol in the TITAN ground cloud at $t=4$ min after launch.

Substitution of Eqs. (1)-(3) in Eq. (4) and integration over each size range as shown in section 2 results in the mass in each regime,

$$m_1 = 1.71 \times 10^3 \text{ kg}$$

$$m_2 = 6.50 \times 10^3 \text{ kg}$$

$$m_3 = 1.79 \times 10^3 \text{ kg}$$

$M = m_1 + m_2 + m_3 = 10^4 \text{ kg}$, which is the total mass of Al_2O_3 released by a Titan launch.

(c) Particle fall velocity

Particles larger than 40 micron diameter have very short residence time in the ground cloud because of their appreciable fall velocities. Terminal fall velocity V_t is a function of diameter and density of the particle, and of drag coefficient C_d , which in turn is a function of V_t . The complex relationships between parameters are beyond the scope of this study. The empirical expressions we used here are:

For size regime 3

$$V_t = -0.17895 + 44.895D + 16.372D^2 - 459.516D^3 \text{ (Dingle and Lee)}^3 \quad (5)$$

For size regime 2

$$V_t = 3 \times 10^3 D^2 \quad (6)$$

where V_t is in m sec^{-1} and D in cm.

Equations (5) and (6) are empirical relationships for water drops of unit density. For particles of density other than unity, we simply adjust the density difference by writing

$$V_{aj} = V_t \rho_p^{0.5} \quad (7)$$

In deriving Eq. (7), it was assumed that the particle is spherical and the drag coefficients are the same in both cases.

To reduce computations, we assume that all the particles in each size regime fall out of the ground cloud with a mean velocity, defined as

$$\bar{V} = \frac{\int_{D_{\min}}^{D_{\max}} V_{aj} dN}{\int_{D_{\min}}^{D_{\max}} dN} \quad (8)$$

Substituting V_t given in Eq. (7) and dN given in Eq. (3) along with the appropriate constants in section 2, after integrating, we have $\bar{V}_3 = 1.87 \text{ m sec}^{-1}$, for size regime 3. Following the same procedure, we obtain the mean velocity $\bar{V}_2 = 0.14 \text{ m sec}^{-1}$ for size regime 2. Particles in size regime 1 have negligible fall velocity.

III. THE MODEL

Airborne measurements indicated that the Titan ground cloud formed a roughly cylindrical disc with a fairly constant thickness of 70 m over the period of observations. Our analysis described in Section 2 shows that 83% of Al_2O_3 mass (that is, the sum of masses in size regime 2 and 3) embedded in the ground cloud consists of fairly large particles. Because of their appreciable fall velocities, these particles are expected to fall out of the shallow cloud in a short period of time. To determine quantitatively the amount of mass removed from the cloud through the process of gravitational settling, we propose here a simplified model. The following important assumptions and limitations are used in this model.

(1) The observed particle size distribution is divided into three domains. An analytical expression is proposed to describe the size distribution in each size domain.

(2) The particle spectra (that is the number density and the size) are assumed to be time-independent.

(3) To simplify computations, it is assumed that the depletion of particulate mass through the process of gravitational settling of large particles is such that particles in size regime 2 and 3 all fall at their mean velocity for that size regime.

(4) Gravitational settling of particles in size regime 1 is neglected. However, these particles are assumed to be continuously swept out of the cloud by large particles through impact collection.

(5) The net rate of loss of mass from the cloud is balanced by the deposition of particles.

(a) Particle deposition

By applying the above assumptions, the mass balance equation can be written as

$$\frac{d}{dt} (\pi R^2 H \chi) = -\bar{V} (\pi R^2 \chi) \quad (9)$$

where R is the radius of the cloud, χ is the concentration of particles, and H is the thickness of the cloud, $H = 70\text{m}$.

Equation (9) immediately integrates to give the result:

$$\chi = \chi_0 \left(\frac{R}{R_0} \right)^2 e^{-\frac{[60\bar{V}t]}{H}} \quad (10)$$

where the subscript 0 denotes the initial conditions at the time the ground cloud became stabilized, and t is the time in minutes. From their measurements (Radke et al¹), the volume of the cloud as a function of time (t in minutes) can be expressed as

$$V = V_0 t^n \quad (11)$$

with $V_0 = 1.76 \times 10^7 \text{ m}^3$, and $n = 0.94$.

Equation (11) can be rewritten as

$$\pi R^2 H = \pi R_0^2 t^n \quad (12)$$

or

$$\left(\frac{R}{R_0}\right)^2 = \frac{1}{t^n} \quad (13)$$

Substituting Eq. (13) in Eq. (10), we have

$$\chi = \frac{\chi_0}{t^n} e^{-\frac{(60 \bar{V} t)}{H}} \quad (14)$$

A physical interpretation of the simplified Eq. (14) is that the depletion of particulate concentration in the ground cloud results from cloud dispersion and particle deposition.

The particulate mass remaining in the cloud at time t as the particles fall out of the cloud at their mean velocity can be written directly as

$$\bar{m}_2 = m_2 e^{-\frac{(60 \bar{V}_2 t)}{H}} \quad (15)$$

for the particles in size regime 2, and

$$\bar{m}_3 = m_3 e^{-\frac{(60 \bar{V}_3 t)}{H}} \quad (16)$$

for the particles in size regime 3.

(b) Impact collection

The impact collection rate at which the capture of particles in size regime 1 by much larger particles (that is, particles in regimes 2 and 3) can be written as

$$\lambda = \int_{D_{\min}}^{D_{\max}} \pi D^2 v_{aj} E dN \quad (17)$$

where E is the collision efficiency and is taken as 1 in this study.

Substituting Eqs. (2) and (7) in Eq. (17), after integration, we have the impact collection rate of size regime 2, $\lambda_2 = 1.74 \times 10^{-3} \text{ sec}^{-1}$.

Following the same procedure for size regime 3, $\lambda_3 = 4.26 \times 10^{-4} \text{ sec}^{-1}$. The total mass collected by the falling large particles can then be written as

$$\bar{m}_1 = m_1 e^{-60(\lambda_2 + \lambda_3)t} \quad (18)$$

The summation, $\sum m = m_1 + m_2 + m_3$, gives the total particulate mass remaining in the cloud at time t . Results of the computations are plotted in Figs. 2 and 3.

IV. RESULTS AND DISCUSSION

In this study we have presented the model results of the mass concentration of particles (Fig. 2) and the total mass remaining in the cloud (Fig. 3) as a function of time. The model computations were extended to $t = 59 \text{ min}$, because the airborne measurements at $t = 59 \text{ min}$ were available for comparison. The results indicate that large particles in size regime 3 were almost completely removed from the Titan ground cloud in the first 10 minutes. This is not surprising because the mass concentration of particles (or total mass) decays exponentially with a decay factor, that is the ratio of particle mean fall velocity to cloud thickness. Obviously,

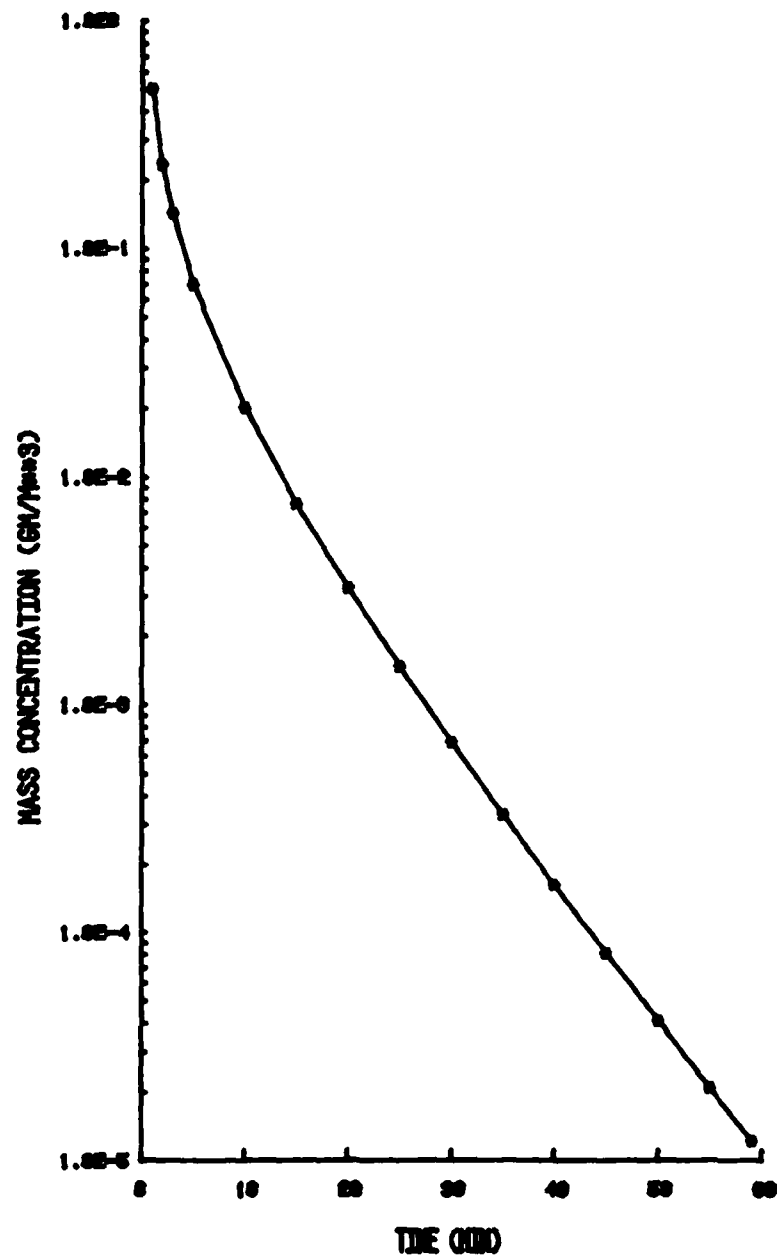


Fig. 2. Computed mass concentration in the TITAN ground cloud as a function of time after launch.

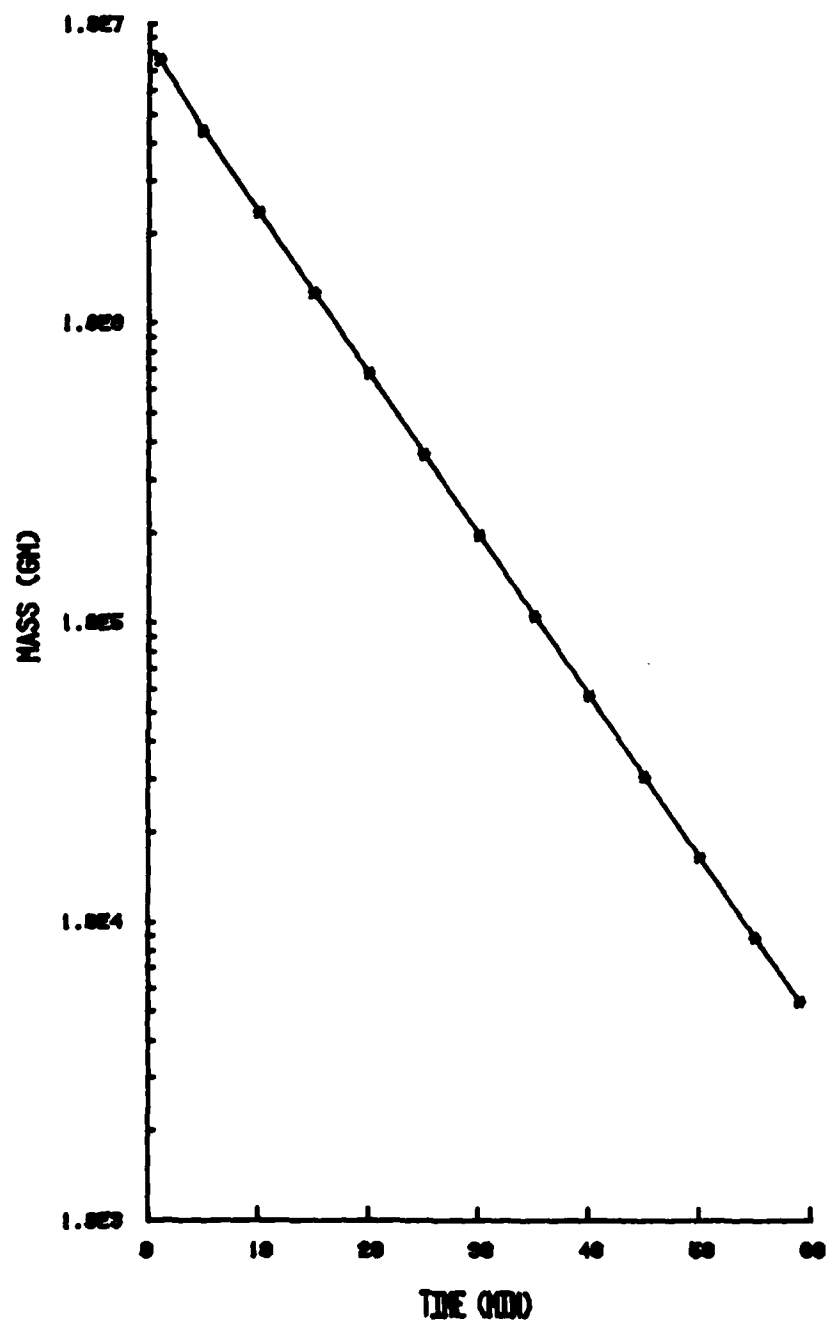


Fig. 3. Computed mass of material in the TITAN ground cloud as a function of time after launch.

a rather large \bar{V} causes the removal of mass very rapidly. Particles in size regime 2 were not removed as rapidly as the large particles, however, a substantial amount of the mass was removed by $t = 59$ min. Thus, by $t = 59$ min, large particles could be below measurable concentrations in the cloud. The observed size distributions confirm this finding. In addition, the model predicts that total mass remaining in the cloud at $t = 59$ min was about 5.4 kg. Observed data indicates that mass was 5 ~ 10 kg. It is clear that very close agreement between the predicted and observed values illustrate that the proposed model shows promise in predicting the quantities.

In conclusion it may be stated that, in spite of all the limitations, the simple analytical form of this model allows for easy estimates of the consequences when the physical parameters: particle fall velocity, cloud size, cloud height, cloud dispersion rate, and particle size spectrum are available. In addition, the results of this study suggest that substantial quantities of Al_2O_3 ejected in the Titan ground cloud are removed by sedimentation. Of course, in a more thorough analysis of this problem, one could formulate complex numerical models taking account of chemistry and variations of particle size distributions as the ground cloud evolves. Nevertheless, we thought it worthwhile at present to focus on developing a simple methodology and utilize it as an interpretive tools for the analysis of the most likely mechanism in removal behavior.

V. RECOMMENDATIONS

Listed below are a number of suggestions for future research, some of which are being considered for the next investigation period.

1. At present, only limited aircraft measurements are available for testing the model results. It is certainly desirable to obtain

as much additional data as possible for further verification of the model applicability.

2. Obtain detailed measurements on the spatial and temporal variation of (a) particle size spectra, (b) particle concentration, (c) cloud shape dispersion rate, and (d) liquid drop size distribution and concentration. These data will be valuable for model evaluation and improvement under both dry and wet (raining) conditions.
3. As an extension of the present study, it is suggested that a scavenging model be developed, incorporating cloud dynamics and microphysical processes.
4. Incorporate the microphysical processes into the cloud dynamics model to determine (a) the amount of materials removed by the precipitation generation system, and (b) the fate of materials within the cloud as a function of time and, (c) the spatial and temporal distribution of wet deposition on the earth's surface.

REFERENCES

1. Radke, Lawrence F., Peter V. Hobbs, and Dean A. Hegg, "Aerosols and trace gases in the effluents produced by the launch of large liquid- and solid-fueled rockets," J. Appl. Meteor., vol. 21, pp1332-1345, 1982.
2. Lee, Yean and Arnold A. Barnes, Jr., "An evaluation of scavenging of the rocket effluents," to be presented at the AIAA Shuttle Environment and Operations conference, Washington, DC. October 31-November 2, 1983.
3. Dingle, A.N. and Yean Lee, "Terminal fallspeeds of raindrops," J. Appl. Meteor., vol. 11, pp879-1972.

AN EVALUATION OF SCAVENGING OF ROCKET EFFLUENTS

Yean Lee

Air Force Geophysics Scholar Program, AFGL, Hanscom AFB, MA

Arnold A. Barnes, Jr.

Air Force Geophysics Laboratory, Hanscom AFB, MA

Abstract

This paper deals with the precipitation scavenging of the exhaust products produced by the launch of the Space Shuttle. The budget of airborne effluents is evaluated by means of three differential equations which express the overall mass conservation of effluents. The model incorporates the present state of the art of the physical processes; nucleation, Brownian and turbulent motion, phoretic effect, and inertial impaction. Each process is parameterized in terms of relatively easily measurable meteorological quantities. From the model one can infer the relative importance of each of the processes being parameterized. Two case studies are presented. The computation results provide new insights into the influence of such parameters as average droplet size, water content, rainfall rate, nucleating scavenging, and attachment mechanism in the scavenging effect. The model appears to be of general validity. Application of this model is suggested for use in the analysis of environmental impacts resulting from shuttle operations.

For older exhaust clouds, the major portion of the pollutant mass in the cloud water comes from the attachment process rather than from the nucleation process.

1. Introduction

During the normal launch of the space shuttle, a ground cloud is formed by the exhaust products from the solid rocket booster (SRB) and entrained in the sound suppression water. The sound suppression system strips out a large portion of HCl. The exhaust cloud contains a major component of Al_2O_3 particles along with HCl , H_2O and other gases. Because of its buoyancy, the cloud rises to a stabilization altitude which depends upon meteorological conditions. In Florida, the ground cloud usually settles at an altitude between 500 and 700 m where an inversion layer exists. The highly polluted ground cloud is transported by the prevailing winds and may drift for hours. Although it is unlikely that a launch will occur during a rainstorm, the exhaust cloud can encounter independently generated rain and can be entrained into a developing convective cloud system. The ultimate fate of the exhaust products however, remains the same; they are removed to the ground by precipitation.

Pertinent to the analysis of the depletion of the exhaust products, a mathematical model proposed by Dingle and Lee⁽¹⁾ is modified. This model views the in-cloud scavenging as a multi-rate process:

- a. Particles are depleted through various microphysical mechanisms.

- b. Cloud droplets become polluted as a result of nucleation and particle attachment. Cloud droplets are characterized by their small size, thus they have a negligible terminal fall-speed. Therefore, particles incorporated into cloud droplets would remain in the cloud and would not reach the ground unless it were to rain.

- c. Polluted cloud droplets and particles are finally removed to the earth surface by the precipitation elements.

2. A Mathematical Model of Scavenging Exhaust Cloud

The temporal variation of the pollutant mass concentration is expressed by means of three ordinary differential equations:

$$\frac{dM_a}{dt} = -(\alpha_c + \alpha_R + \beta_p)M_a \quad (1)$$

$$\frac{dM_c}{dt} = \alpha_c M_a - \beta_c M_c \quad (2)$$

$$\frac{dM_R}{dt} = (\alpha_R + \beta_p)M_a + \beta_c M_c \quad (3)$$

where M_a = particulate mass in the exhaust cloud air (g/m^3), M_c = particulate mass attached to cloud droplets (g/m^3), M_R = particulate mass removed by raindrops (g/m^3), α_c = total attachment rate between particles and cloud droplets (sec^{-1}), α_R = total attachment rate between particles and raindrops (sec^{-1}), β_p = impact collection rate of particles by raindrops (sec^{-1}), and β_c = rate of accretion of cloud droplets by raindrops (sec^{-1}).

Obviously, as long as α_c , α_R , β_p and β_c are considered as constants in a single time interval, the equations 1, 2 and 3 can be integrated with respect to time. As the exhaust cloud becomes stabilized and moves downwind, before encountering the rain storm, the particles interact with the cloud droplets for a time t_c , giving a particulate mass concentration which can be written directly as:

$$M_a(t_c) = M_a(0)e^{-u_c t_c} \quad (4)$$

where $M_a(0)$ is the initial mass in the exhaust cloud. The mass associated with the cloud droplets prior to the rain is

$$M_c(t) = M_c(0) + M_a(0) (1 - e^{-\alpha_c t}) \quad (5)$$

where $M_c(0)$ is the mass of the condensation nuclei on which the cloud forms.

After the rainstorm starts to cleanse the exhaust cloud, the particulate mass remaining in the cloud at time t , computed from the onset of rain, becomes

$$M_a(t) = M_a(0) e^{-\alpha_c t} e^{-(\alpha_c + \alpha_R + \beta_p)t} \quad (6)$$

The particulate mass associated with the remaining cloud droplets is then

$$M_c(t) = [M_c(0) + M_a(0)(1 - e^{-\alpha_c t})] e^{-\beta_c t} + \frac{\alpha_c M_a(0) e^{-\alpha_c t} [e^{-(\alpha_c + \alpha_R + \beta_p)t} - e^{-\beta_c t}]}{\beta_c - (\alpha_c + \alpha_R + \beta_p)} \quad (7)$$

and the particulate mass removed by raindrops can be written as

$$M_R(t) = [M_c(0) + M_a(0)] (1 - e^{-\beta_c t}) + \frac{M_a(0) e^{-\alpha_c t} [e^{-\beta_c t} - e^{-(\alpha_c + \alpha_R + \beta_p)t}] [\beta_c - (\beta_p + \alpha_R)]}{\beta_c - (\alpha_c + \alpha_R + \beta_p)} \quad (8)$$

3. Estimation of Parameters:

3a. Simplified Analysis of Total Nucleating Mass Incorporated Into Cloud Elements.

Previous researchers have suggested, that the consumption of condensation particles during the formation of cloud elements should play a most important role as a process of in-cloud scavenging when compared to other removal mechanism. In view of this, an attempt is made to provide a simplified methodology for predicting the possible amount of pollutant mass removed through nucleation.

As a starting point, we consider the simplified case of the equilibrium between an aqueous solution drop and humid air. If a solution drop containing a nucleating particle of mass M_p , is in equilibrium with the environmental humid air, and the solution is dilute, one may use (Fletcher (2)):

$$\frac{RH}{100} = 1 + \frac{A}{r} - \frac{B}{r^3} \quad (9)$$

where RH is the relative humidity, $A = 3.3 \times 10^{-7}/T$ and $B = 4.3 \times 10^{-6}$, M_p/M_w are constants for a given temperature T , M_p and M_w are the mass and the molecular weight of the particle, respectively, i is the van't Hoff factor ($i = 2$), and $r(m)$ is the cloud droplet radius in meters. Solving Eq (9) for M_p , we can obtain an expression which relates the mass of a single nucleating particle to a cloud droplet of radius (r) at a given ambient temperature (T) and relative humidity (RH).

$$M_p = (b_1 r^3 + b_2 r^2) M_w \quad (10)$$

where $s = 1 - RH/100$, $b_1 = 1.16 \times 10^5$ and $b_2 = 3.84 \times 10^{-2}/T$

Our primary interest is to derive an expression which will determine the total amount of pollutant mass incorporated into the cloud water during the formation of the cloud elements. We first assume that the cloud has formed with a certain size distribution according to the Khragian and Mazin (3) size relationship:

$$n(r) = ar^2 e^{-br} \quad (11)$$

Here $n(r)$ is the number of droplets per unit volume in the radius interval between r and $r + dr$, and

$$a = 1.45 \times 10^{-6} (\bar{r})^{-6} Q_c / \rho_l$$

$$b = 3/\bar{r}$$

where Q_c is the cloud water content, ρ_l the water density, and $\bar{r}(m)$ the average cloud droplet radius in meters. Estimates of the total particle mass contained in the entire cloud drop size spectrum can thus be obtained by integrating the product of Eq. (10) and Eq. (11) over all sizes. Combining Eq. (10) and Eq. (11), we obtain

$$M_c = \int_0^\infty M_w (b_1 r^3 + b_2 r^2) ar^2 e^{-br} dr \quad (12)$$

Integration of Eq (12) provides the desired expression:

$$M_c = (c_1 s + c_2/\bar{r}) M_w Q_c / \rho_l \text{ (gm/m}^3\text{)} \quad (13)$$

Where M_c is the total nucleating particle mass contained in the cloud elements, c_1 and c_2 are constants and equal to 2.77×10^{-2} and 5.48×10^{-9} respectively.

It is interesting to note that M_c is directly proportional to Q_c and inversely proportional to \bar{r} . Physically speaking, this is quite realistic; a large cloud water content implies a large population of cloud droplets which, in turn, implies a large consumption of condensation nuclei. On the other hand, if the average cloud droplet becomes large, the corresponding cloud droplet population should be reduced for a given cloud water content Q_c . Consequently, M_c is also reduced. For computation purpose, we adopt the concept of so-called potential radius, i.e., a solution droplet is in equilibrium with an environment of $RH = 100$.

3b. Parameterization of the Attachment Rate Between Cloud Droplets and Particles.

3b.1. Brownian Motion

The particles become attached to cloud elements as a result of Brownian and turbulent motion, each of which contributes to the removal of particles floating in the cloud air. Assuming that the cloud droplets act independently, the total attachment

for a given cloud droplet size spectrum can be expressed as

$$\alpha_B = \int_0^\infty \pi r^2 E_B(r, r_p) V_C(r) n(r) dr \quad (14)$$

where α_B is the attachment rate due to Brownian motion, $E_B(r, r_p)$ is the attachment efficiency for droplets of radius r collecting particles of radius r_p ; and $V_C(r)$ is the settling velocity of the droplets.

Using Stokes law for $V_C(r)$ and $E_B(r, r_p)$ suggested by Williams⁽⁴⁾ and integrating Eq. (14) over all droplet sizes results in

$$\alpha_B = \left(\frac{c_3}{r^2} + \frac{c_4}{r} \right) Q_C / \rho_L \quad (15)$$

where $c_3 = 1.44 \times 10^{-15} \text{ (m}^2/\text{sec)}$ and $c_4 = 5.98 \times 10^{-10} \text{ (m/sec)}$

3b.2 Turbulent Motion

Besides Brownian motion, Levich⁽⁵⁾ indicated that the attachment of particles is enhanced under the influence of air turbulence.

The attachment rate due to turbulent motion is given by Eq (14) when $E_T(r, r_p)$ the turbulent diffusion coefficient is substituted for $E_B(r, r_p)$. After integration, we obtain

$$\alpha_T = (c_5 + c_6 \bar{r}^{1/3}) Q_C / \rho_L \quad (16)$$

where $c_5 = 5.59 \times 10^{-6} \text{ (sec}^{-1}\text{)}$ and $c_6 = 1.79 \times 10^{-3} \text{ (sec}^{-1} \text{ m}^{1/3}\text{)}$.

3b.3 Diffusiophoresis and Thermophoresis

The expression that will be used here to describe the net phoretic contribution to the particle flux is that which has been derived by Slinn and Males⁽⁶⁾.

$$F = \frac{n^c}{r} (2 + 0.6 Re^{1/2} Pr^{1/3}), \quad (17)$$

where F is the phoretic flux and c is an expression given by Slinn and Males⁽⁶⁾.

The net phoretic attachment rate is estimated by integrating the product of the phoretic flux F and the surface area of the droplets over the entire droplet size spectrum.

Utilizing Eq. (11) and Eq. (17) and integrating gives

$$\alpha_P = \frac{c_7}{r^2} Q_C / \rho_L \quad (18)$$

where $c_7 = 1.55 \times 10^{-16} \text{ (m}^2/\text{sec)}$

Each of the potential attachment mechanisms has been evaluated separately, but these of course act simultaneously. In this study, we have combined mechanisms by adding the various contribution, and have written

$$\alpha_C = \alpha_B + \alpha_T + \alpha_P, \text{ (sec}^{-1}\text{)} \quad (19)$$

where α_C denotes the total attachment rate between cloud droplets and particles.

3c. Parameterization of the attachment rate between raindrops and particles.

The estimates of various attachment rates between rain drops and particles are generally similar to the treatments evaluated in section 3b. But the raindrops have a different size distribution and larger terminal velocities. In order to derive the integrated attachment rates for various processes, the raindrop size distribution $N(r)$, is approximated with a Marshall-Palmer⁽⁷⁾ distribution.

In addition, V_R , the terminal velocities of precipitation sized elements approximated by Kessler⁽⁸⁾ is used in this study. Similarly, the attachment rate α'_B (Brownian Motion) resulting from interaction between raindrops and particles can be written as

$$\alpha'_B = \int_0^\infty \pi R^2 E_B(R, r_p) V_R N dR \quad (20)$$

where $E_B(R, r_p)$ is given Williams⁽⁴⁾, when V_R is substituted for V_C , and R is substituted for r . Integration of Eq.(20) results in

$$\alpha'_B = a_1 J^{4/9} + a_2 J^{5/9} \text{ (sec}^{-1}\text{)} \quad (21)$$

where $a_1 = 3.27 \times 10^{-9}$, $a_2 = 1.6 \times 10^{-7}$ and J is rainfall rate (mm/hr).

Following the same procedures, the derived expression for α'_T (turbulent motion) can be written as

$$\alpha'_T = a_3 J^{8/9} + a_4 J^{23/27} \text{ (sec}^{-1}\text{)} \quad (22)$$

where $a_3 = 4.18 \times 10^{-7}$ and $a_4 = 4.53 \times 10^{-6}$.

To simplify further calculations, we assume that the raindrops falling from the overriding rainstorm are in thermal equilibrium with the exhaust cloud air temperature. Thus, the attachment between raindrops and particles resulting from phoretic effect is negligible. Summing the attachment rates resulting from these processes, Similarly, we write

$$\alpha_R = \alpha'_B + \alpha'_T \quad (23)$$

where α_R denotes the total rate at which the particles become attached to the raindrops.

3d. The removal of polluted cloud droplet by falling raindrops.

The rate at which the cloud droplets removed by raindrops distributed according to a Marshall-Palmer size distribution can thus be obtained from Eq. (20) by selecting $E(R, r) = 1$ for inertial impaction.

After integration, we obtain

$$\beta_c = 5.43 \times 10^{-4} J^{7/9} \text{ (sec}^{-1}\text{)} \quad (24)$$

3e. The removal of particles by falling rain drops

Following the same procedures, the rate of removal of particles by raindrops can be written as

$$\beta_p = 5.43 \times 10^{-4} E_p J^{7/9} \text{ (sec}^{-1}\text{)} \quad (25)$$

where E_p is the collection efficiency ($E_p = 0.3$).

4. Discussion

In section 3b, we adopt the theory of heterogeneous homomolecular nucleation of water-vapor condensation on a soluble particle (i.e. nucleation of a single gaseous species on to a foreign soluble body). Utilizing the generalized equation devised from that theory, we propose a simplified expression to estimate the total amount of particulate mass associated with the cloud water through the nucleation process. In doing so, several important assumptions are made. First, the Al_2O_3 particle, a major component of the exhaust cloud, is assumed to act as a soluble particle for nucleation. Second, it is assumed that the nucleating particle mass in each individual growing droplet remains constant. This assumption would hold for at least the early stage of cloud droplet formation; during the later stages of droplet growth, additional particulate mass will be added to it through the various microphysical processes mentioned in section 3. Third, another major component of the exhaust cloud is hydrogen chloride gas (HCl). Accordingly, a solution droplet is formed from two gaseous species (i.e. water vapor and hydrochloric acid). At present, there is no theory available for this particulate process to describe the Al_2O_3 - H_2O - HCl mutual interaction effects. The detailed study of this process is beyond the scope of this study. For our purpose, we follow a concept similar to that suggested by Hamill et al (9) and consider the formation of soluble droplets taking place in two discrete steps. In the first step, the soluble droplet reaches quasi-equilibrium with respect to the water vapor. Although the droplet is in equilibrium with respect to water vapor, it is not in equilibrium with hydrochloric acid vapor. Therefore, the second step is the additional absorption of HCl . Absorption of HCl lowers the vapor pressure of the droplet. This allows more water vapor to be absorbed, but has no effect on the particulate mass in each individual droplet. We propose the present approach with reservations and suggest that these restrictions imposed on this approach should be lifted when appropriate theories are developed. Generally, however, such a simplified approach will provide a first order approximation of the magnitude of the overall problem.

In the model computations, the parameter α_c must be adjusted for each time interval, because it is directly related to cloud water Q_c , which is depleted through the accretion of falling raindrops. The amount of cloud water depleted is calculated from

$$Q_c(t) = Q_c(0)e^{-\beta_c t}$$

where β_c is obtained from Eq. (24).

The parameter β_p , describing the impact collection of particles by raindrops, becomes insignificant if the particle size $r_p < 2\mu m$. This is reasonable since for sufficiently small particles, the motion is controlled by viscous force and thus the role of inertial impaction can then be neglected. The parameter α_p denoting the attachment rate between particles and raindrops is less important when compared to α_c because of the much larger raindrop sizes.

Case I: Rain begins immediately after the exhaust cloud has stabilized

$$(t_c = 0)$$

Initially, the overriding rain is not polluted, but it is polluted after traversing the cloud. As a rain of constant intensity falls through the cloud, each raindrop not only contributes to the removal of particulate mass, but also depletes the amount of cloud water. Results for this case indicated that about 21% (without nucleation) to 37% (with nucleation) of the particulate mass is scavenged.

Case II: Similar to case I except particles remain in the cloud for one hour prior to the onset of rain.

In this case, the in-cloud mixing has lasted for an hour before the cloud encounters the overriding rain. As soon as the rain falls into the cloud, scavenging begins. This case demonstrates the increased removal of particulate mass where preliminary interaction is allowed.

At this point, it is appropriate to further analyze the important aspect of the attachment rate α_c . Utilizing $Q_c = 1 \text{ gm/m}^3$ and r (average cloud droplet size = $6\mu m$), $\alpha_c = 1.82 \times 10^{-4} \text{ sec}^{-1}$. Setting $t_c = 3600 \text{ sec}$, from Eq. (3), we find $M_p(t_c = 3600 \text{ sec}) = 0.518 M_p(0)$. The result indicates that if the particles are allowed to interact with the cloud droplets for a period of an hour before the rain starts, that about 48% of the total particulate mass embedded in the cloud will have been removed from the cloud air through various attachment processes (assuming the particle sizes are distributed in a very narrow size range). On the other hand, from Eq. (4), we see that the fraction of mass removed by nucleation is $M_c(0) = 0.25$ (i.e. 25% of the total mass is initially incorporated into the cloud water). Now, the important question arises. Is the nucleation scavenging more important than other processes, or vice versa? Immediately, we realize it is unrealistic to state that one process is dominant over the other without carefully examining several other important aspects: rain origination, cloud dynamics, type of cloud, physical and chemical properties of particle, size spectra, etc. However, from the example cases presented here, we may state that for an aged, stabilized, and non-precipitating cloud, if the majority of the particles are of submicron sizes, various attachment processes may overtake the nucleation process and contribute significantly to the ultimate removal of pollutant from clouds.

5. Summary

The modified multi-rate model of in-cloud scavenging presented in this study has brought out these features:

1. The model explicitly incorporates the rates of progress of each process at each in-cloud scavenging stage.

2. The two most important parameters are α_c ; the attachment rate, and β_c ; the cloud water removal rate.

3. α_c is parameterized and is expressed as a function of cloud water Q_c and average cloud droplet size r . This parameterization approach provides a possible explanation of why and how α_c varies in the range between 10^{-5} to 10^{-4} sec^{-1} which is the order of magnitude obtained from many previous investigators.

4. The concept that nucleation is the most important process in precipitation scavenging is being challenged. Of course, nucleation process contributes significantly to the initial removal of pollutant during the early stages of cloud droplet formation, but as the clouds become stabilized (as in the case of exhaust cloud and perhaps stratiform clouds), their capability to remove pollutants by nucleation may become less significant due to the limited amount of water. Meanwhile attachment processes continue. Consequently, more and more particles accumulate on the cloud droplets. Thus, for older clouds, the major portion of pollutant mass contained in the cloud water comes from the attachment process. Case II in this study is a good example.

Finally, as stressed in section 3a, for the particular case of an exhaust cloud (including HCl), refinements to the approach suggested for evaluating the pollutant mass associated with cloud water should be made, when a more thorough theory becomes available. For the moment, we may consider it as a first approximation and use it with reservations.

Acknowledgements: This work was performed under research sponsored by the Air Force Office of Scientific Research/AFSC, United States Air Force, under contract F49620-82-C-0035. The United States Government is authorized to reproduce and distribute reprints for governmental purposes not withstanding any copyright notation hereon.

The first author would like to acknowledge the Air Force Geophysics Laboratory, in particular the Meteorology Division, for its assistance and excellent working conditions.

REFERENCES

1. Dingle, A.M., and Y. Lee, 1973: An analysis of in-cloud scavenging. J. Appl. Meteor., 12, 1295-1302.
2. Fletcher, N.H., 1962: The physics of rain-clouds. Cambridge University Press, 309 pp.
3. Khrgin, A. Kh., and I.P. Mazin, 1952: The size distribution of droplets in clouds. Tr. Tsent. Aerol. Observ., No. 7.
4. Williams, A.L., Analysis of in-cloud scavenging efficiencies. AEC Symposium Ser. Precipitation Scavenging (1970), 258-275. [NTIS No. Conf 700601].
5. Levich, V.A., 1962: Physico-chemical hydrodynamics. Englewood Cliffs, N.J., Prentice-Hall, 700pp.
6. Slinn, W.G.N., and J.M. Hales, 1971: A reevaluation of the role of thermophoresis as a mechanism of in-and below-cloud scavenging. J. Atmos. Sci., 28, 1465-1471.
7. Marshall, J.S., and W. McK. Palmer, 1948: The distribution of raindrops with size. J. Meteor., 5, 165-166.
8. Kessler, E., 1969: On the distribution and continuity of water substance in atmospheric circulation. Meteor. Mongor., No. 32, 84pp.
9. Hamill, P., C.S. Kiang and R.D. Cadle, 1976: The nucleation of H_2SO_4 - H_2O solution aerosol particles in the stratosphere. J. Atmos. Sci., 34, 150-162.

1982-83 AFGL-SCEEE GEOPHYSICS SCHOLAR PROGRAM

Sponsored by the

AIR FORCE OFFICE OF SCIENTIFIC RESEARCH

Conducted by the

SOUTHEASTERN CENTER FOR ELECTRICAL ENGINEERING EDUCATION

FINAL REPORT

AN EXPERIMENTAL METHOD FOR CALIBRATING ELECTRON DETECTORS

Prepared by:	Dr. Frederic J. Marshall
Research Location:	The Air Force Geophysics Laboratory Space Physics Division Space Particle Environment Branch
AFGL Research Contact:	Dr. David Hardy
Date:	December 29, 1983
Contract No:	F49620-82-0035

Acknowledgement

The author acknowledges support for this effort from the Air Force System Command, the Air Force Office of Scientific Research, the Air Force Office of Scientific Research, the Southeastern Center for Electrical Engineering Education and the Air Force Geophysics Laboratory. The design of the facility described in this report was really a collaboration of ideas from the author, D. Hardy, D. Winningham, A. Huber, J. Pantazio, W. Denig, K. Kalata and W. Huber. Support by the staff at AFGL, in particular R. Hubbard, J. Iodice, J. Larrabee, J. MacAdam, C. Mitropoulos, Airman D. Moon, A. Perkinson, D. Pendleton, G. Shea and B. Stromski. We thank Herb Cohen and his staff for technical assistance and the use of his vacuum chamber facility. We thank Joyce Maillett for typing this manuscript.

I. INTRODUCTION

A. Overview

The goal of this project was to design, construct and test an experimental facility which will be used to calibrate the detection efficiency of electrostatic analyzers. This report describes the design of this experiment and necessary considerations taken. The electron beam produced by the experiment was measured. The facility was then used to calibrate the Defense Meteorological Satellite Program (DMSP) F8 electrostatic analyzers.

The method employed for generating a electron beam is to liberate photoelectrons from a metallic surface by illuminating the surface with ultraviolet light. Typically a heated filament has been used in other such facilities (Sanderson and Henrion 1975, Arnoldy et al. 1973). The photoelectrons are accelerated to the desired energy by a negative voltage applied to the metallic surface. They pass through a wire screen, which is electrically grounded, forming a beam of electrons. Electron detectors are placed in the electron beam and their response is measured.

B. Experiment Design

A schematic diagram of the experiment is shown in figure 1. The experiment consists of an ultraviolet light and optical system used to provide ultraviolet illumination, a metallic coating which is the source of photoelectrons, high voltage power supplies used to accelerate the photoelectrons, a grounded screen which they pass through and a gimbal table used to translate or rotate detectors which are in the path of the electron beam.

The photoelectron emitting surface is a thin semi-transparent gold coating, 400 Å thick, deposited on the surface of a quartz flat. The gold layer is illuminated by shining ultraviolet light from a low pressure mercury vapor lamp onto the back or uncoated side of the quartz flat. High voltage supplies are used to apply a negative bias to the gold coating setting up an accelerating electric field between the

quartz flat frame and a grounded wire screen. The electron beam is measured by monitoring the total photoelectron current. Helmholtz coils (not shown) surround the beam and can be used to cancel the effect of the earth's magnetic field on the beam. Electron detectors are mounted on a gimbal table which is placed in the path of the beam. The gimbal table consists of two rotary tables configured to provide rotation about two axes perpendicular to the beam. Each rotary table has a linear table attached to it to allow the beam intensity versus position to be measured.

The experiment is computer controlled by a PDP11/34A. The PDP11 controls the positioning of the gimbal table, sets the high voltage, monitors the photoelectron current, receives counts from the electron detectors and monitors the light intensity. This is done in a timed sequence and the results are stored in binary files for later analysis.

C. The DMSP-F8 SSJ/4 electrostatic analyzer

The DMSP-F8 SSJ/4 detector consists of 4 cylindrical plate electrostatic analyzers (ESA's) two for electrons and two for ions, covering the energy range of 30 eV to 30 keV in 20 energy channels, 10 for each plate pair. The design is similar to that reported by Hardy et al. (1979). The flight operation mode consists of cycling the deflection plates through ten voltages corresponding to ten energies per each one second. The plate voltages are spaced to yield logarithmically spaced energy bands between 30 eV and 30 keV.

The electron ESA's of the SSJ/4 package were calibrated with the electron beam at individual plate voltages of the operating sequence. This was accomplished by setting the plate voltage to a given energy channel and then wobbling the detector in azimuth and elevation about the beam direction. This was then repeated for beam energies above and below the central energy of that band. The recorded count rates versus angle at the various energies were used to compute the geometric factor for each band measured as described in the following section.

D. The geometric factor

The key to deriving the absolute electron flux, $j(E)$, from the observed count rate, r , is knowledge of the detector area solid angle product or energy dependent geometric factor, $g(E)$. The observed count rate, r , is related to the differential electron flux $j(E, \theta, \phi)$ impinging on the detector by the equation,

$$r = \int j(E, \theta, \phi) A(E_i, \theta, \phi) \epsilon(E) \cos \alpha d\Omega \quad (1)$$

where $A(E_i, \theta, \phi)$ is the effective collecting area of the detector for the i th energy band E_i , $\epsilon(E)$ is the efficiency of the detector to electrons of energy E and α is the angle that the particle trajectories make with the normal to the entrance aperture. Typically in magnetospheric measurements one assumes that the flux is uniform over the solid angle in which electrons are detected. In that case r is given by

$$r = j(E_i) G(E_i) \quad (2)$$

where

$$G(E_i) = \int g(E, E_i) dE \quad (3)$$

$$g(E, E_i) = \int A(E_i, \theta, \phi) \epsilon(E) \cos \alpha d\Omega \quad (4)$$

Here $g(E, E_i)$ is the energy dependent geometric factor and $G(E_i)$ is the total geometric factor for the i th energy band setting of the detector, E_i .

In the laboratory measurement one employs a monoenergetic, unidirectional beam in which case

$$r(E, E_i, \theta, \phi) = j(E) A(E_i, \theta, \phi) \epsilon(E) \cos \alpha \quad (5)$$

Equation 5 can then be inverted to find $g(E)$ in terms of laboratory measurements.

$$g(E, E_1) = \frac{\int r(E, E_1, \theta, \phi) d\Omega}{j(E)} \quad (6)$$

We see that $g(E)$ can be computed from the observed count rates and the beam flux density, j_0 . The values found for $g(E)$ can then be used in equation 3 to compute the total geometric factor of the detector.

II. OBJECTIVES

The objective of this project was to build and test a device whereby the absolute properties of electron detectors of widely different design could be measured. This system had to have the following capabilities:

- 1) produce a beam of monoenergetic electrons with energy in the range 10 eV to 50 keV
- 2) The beam must be large in size and uniform in order to simultaneously impinge on a multiple apertures or other large apertured detectors.

III. INSTRUMENTATION

A. The illumination system

The ultraviolet illumination for the electron detector calibration experiment, (figure 2a,b), is provided by a low pressure mercury vapor lamp which emits ~ 92% of its total output at 2537 Å (Childs 1962). The lamp used was an 11 SC-2 PEN-RAY lamp manufactured by UltraViolet Products, Inc. The 2537 Å output of the pen ray lamp is 6×10^{-3} watts sr⁻¹. The lamp is supported in a housing (see figure 2b) containing a condensor and focusing lens both of fused silica. The condensor is an f/0.7 aspheric lens and the focusing lens has a 250 mm focal length. The combination of the two lens makes it possible to illuminate the entire gold coating with light emitted by the lamp into ~ 1 sr.

The light beam is focused and passes through a fused silica viewport in the vacuum chamber. The light is redirected by a large (50 cm X 50 cm) UV reflecting mirror so that the uncoated side of the gold coated quartz flat is illuminated. The mirror coating is 1800 Å of aluminum coated with MgF₂. The intensity of the light striking the quartz flat can be regulated by placing a neutral density filter in the path of the light before it diverges.

Illumination provided by the lamp and optics is monitored by a UV sensitive photodiode manufactured by Electronic Vision and Systems Division of Science Applications, Inc. The photodiode has a magnesium fluoride window with a cesium telluride photocathode.

B. The electron beam system

The gold coating which is the source of the photoelectrons used to produce the electron beam is a 400 Å layer deposited onto a bare fused silica, or quartz, flat. The flat is 13 inches in diameter, and 0.75 inches thick, the inner 12.5 inches is coated with gold leaving a 0.25 inches clear annulus left to provide electrical isolation. The gold coating was done by the Perkin Elmer Corporation coating facility in Wilton, Conn. where measurements were made of the actual thickness of test samples coated simultaneously with the gold photocathode. The mean coating thickness of the gold photocathode was so estimated to be 385 Å near the center and 388 Å near the edge. The close agreement is perhaps fortuitous since the measurements were made with an angstrometer with a measurement accuracy of 50 Å.

The gold photocathode is housed in an 18 inch square aluminum frame which is bored with a 12 inch diameter hole to allow the light to pass through and fall on a controlled area of the gold coating (729.6 cm²). The frame is counterbored on a 13.50 inch diameter which is 0.75 inches thick to accept the gold photocathode which is held in place by teflon spacers (figure 2a).

A negative voltage is applied to the gold coating and the frame by a high voltage line connected to high voltage power supplies via a

coaxial HV feed through. Both the gold coating and the frame are held at the same voltage so as to create a uniform electric field between the frame and the wire screen. Fringe field effects are minimized since the edge of the beam is not at the edge of the frame. The screen is actually two layers of crosswrapped .002 inch tungsten wire. The wire is spaced every 0.11 inch across the 18 inch screen frame. One vertical layer and one horizontal layer on each side of an 18 inch by 18 inch frame. The calculated transmission of the screen is 93%.

In operation the total photoelectron current needed to generate the electron beam is measured by a current monitor. The current monitor is a device which measures the current passing through it from the photocathode frame to the gold layer. The monitor is supported directly by the external coaxial connector on the high voltage feedthrough (figure 2a). The monitor is battery operated and isolation is maintained on data transmission by a fiber optic data link.

Connection to the negative high voltage applied to the gold coating is through the high voltage feed through which has a floating coaxial feedthrough providing isolation from ground up to 50 kV. The outer lead is connected to the gold photocathode frame. The inner lead penetrates the photocathode frame on the side opposite the gold coating. Electrical contact is made to the gold coating via a beryllium copper spring. The spring contacts the gold surface outside the 12 inch inner diameter coated area so as not to interfere with the production of photoelectrons. The circuit is completed by the current monitor which measures current supplied to the gold layer, compensating for the loss of photoelectrons. The current monitor is guarded from measuring current generated by leakage across the high voltage standoffs, which support the photocathode frame, and current generated by a loss of photoelectrons from the frame itself. The photocathode current is then a direct measure of the average beam current density times the beam area.

C. The gimbal table

The gimbal table consists of two rotary tables, manufactured by Daedal, Inc., mounted at right angles to each other. Each rotary table has a linear translation table mounted to its rotating platform. This allows for translation of a detector so that the aperture is located along the axis of rotation of each rotary table. The beam can be mapped out by rotating the base rotary table so that a monitor detector faces the beam. The tables are driven by stepper motors which are in turn controlled by the PDP11 via an HP6942A multiprogrammer and stepper motor driver cards. The stepper motors are manufactured by Dana Rapid Syn. They are variable reluctance type stepper motors which contain no permanent magnets, have 303 stainless steel housings, graphite bearings and are otherwise vacuum prepared. The tables are geared so that one step is 0.01 degree on the rotary tables and .0005 inches on the translation tables.

D. Computer Control

The experiment control is accomplished by a PDP11 which is interfaced to the electronics equipment rack by an IEEE-488 interface bus. The interface bus is connected to a Hewlett Packard 6942A multiprogrammer, a Keithley 480 picoammeter and three Bertan 205A high voltage power supplies. The HP6942A controls several parts of the experiment through its input/output cards. Those used and their functions are:

- (1) pulse output cards to move the stepper motors of the gimbal table;
- (2) relay cards to switch between HV power supplies; (3) counter cards to accumulate counts detected by the electron detectors and counts received by the fiber optics data link connected to the current monitor;
- (4) timer cards to start and stop accumulation of counts received by the counter cards.

Overall computer control is accomplished by program modules written in a modern high level language known as MAGIC/L (Epstien and Morris 1982). The structure of this language makes it possible to write 'primitives' which accomplish various tasks necessary to the computer control of this experiment. These primitives are then executed sequen-

tially in the process of running the experiment. As an example, the primitive which runs the stepping motor is executed followed by one which accumulates and reads out detector counts, and so on in a loop. Results are saved on magnetic disk storage and displayed for real time monitoring.

E. Calculated beam flux density

The photoelectric quantum yield of gold is $\sim 1.3 \times 10^{-5}$ electrons per photon at 2537 Å (Hughes and DuBridge 1932). Knowing the light intensity incident on the gold coating we can then calculate the rate with which photoelectrons are generated. We first need to consider the net efficiency of the optical system.

The transmission at each quartz-air or quartz-vacuum interface $\sim 96\%$ at 2537 Å. There are 13 of these which will lower the transmission to $\sim 60\%$. The transmission of UV grade fused silica is $\sim 90\%$ for a pathlength of 10mm at a wavelength of 2537 Å. The condensor thickness is ~ 20 mm, the focusing lens ~ 4 mm, the vacuum viewport 6mm, the gold substrate 19mm, for a total pathlength of ~ 50 mm and a net transmission of $\sim 60\%$. The front surface mirror has a reflectance of $\sim 90\%$. The net transmission of the illumination system up to the gold layer is $\sim 30\%$. The condensor lens subtends a solid angle of ~ 1 sr with respect to an object placed at the focal point.

Given the lamp intensity at 2537 Å of 6×10^{-3} watts sr^{-1} , the transmission of the optical system, .3, and the area of the gold surface, 730 cm^2 , the calculated photon flux density at the gold layer would be 3×10^{12} photons $\text{cm}^{-2} \text{ s}^{-1}$. Absorption by the gold layer is calculated to be $\sim 90\%$ utilizing the constants of Irani et al. (1971). The photoelectron flux density should be proportional to the absorbed light intensity with the proportionality constant being the photoelectric quantum yield, 1.3×10^{-5} . The expected beam flux density is then $j = 3 \times 10^7$ electrons $\text{cm}^{-2} \text{ s}^{-1}$. The actual yield for this experiment will be less since the gold coating is back illuminated.

IV. RESULTS

A. Measurement of the electron beam

The experiment was operated in a 6 foot diameter, 6 foot long stainless steel cryo-pumped vacuum system at or near a pressure of 1×10^{-6} Torr. The electron beam was measured by utilizing an aperatured channeltron and the EVSD UV-photodiode. The purpose of this was two-fold. First the relative intensity of the electron beam versus position was measured and compared with the relative light intensity versus position. Second, the total beam current was computed from the beam current density measurements versus position. We note that the lamp output was found to be stable after initial warm up of ~ 15 minutes. The accelerating voltage was 1 KV for this test. Results of this measurement are displayed in figure 3 which shows the measured channeltron count rate and photodiode intensity versus position.

The electron flux density near the center of the beam was 10% higher than the average flux density. This appears to be due to the nonuniformity of the light intensity. The average transmitted light intensity calculated from the observed photodiode current was 3.2×10^{10} photons $s^{-1} cm^{-2}$.

In the previous section we calculated that the light intensity transmitted by the gold layer should be $\sim 3 \times 10^{11}$ photons $s^{-1} cm^{-2}$ from the unfiltered pen-ray lamp. During this test a neutral density filter was used which reduced the intensity by $\sim 90\%$ at 2537 Å. The measured and calculated light intensity are seen to be in rough agreement.

The average electron flux density calculated from the observed channeltron count rate was 6.1×10^4 electrons $s^{-1} cm^{-2}$. The implied photoelectric quantum yield of the gold photocathode is then 2.1×10^{-7} electrons per photon of absorbed light. This compares to a value of 1.3×10^{-5} reported from measurements described in Hughes

and DuBridge (1932) and 1.2×10^{-6} reported by Childs (1961) for a partially transparent gold layer which was front illuminated.

The absolute beam current density was computed from the individual current density measurements by integrating over the measurements weighting each by the area between successive points measured. The channeltron was assumed to be 100% efficient at 1 keV (Kurz 1979). The total beam current as measured by the current monitor during this test was $(7.43 \pm .16) \times 10^{-12}$ amps while the total beam current calculated from integration was 7.53×10^{-12} . The two values agree, to within error, demonstrating the effectiveness and accuracy of this method of measuring the absolute beam current density.

B. Calibration of the DMSP F8 ESA

The DMSP-F8 ESA was mounted on the gimbal table and a series of calibration scans were performed. The calibration was performed in the following manner: The beam direction was located by performing a coarse angular scan in azimuth and elevation then the peak count rate and location of the peak count rate were noted. The beam intensity was adjusted if necessary by adjusting the UV light intensity with neutral density filters. The center of the scan was adjusted so that the peak count rate occurred at the center. The adjustment was performed at the energy corresponding to the peak response of that energy band. After this initial adjustment, scans were made of the detector response at energies above and below the peak response energy.

A representative scan of count rate versus azimuth and elevation is given in figure 4. In this figure we show an example of the response of the low energy detector, channel 11, and the nearly overlapping energy band of the high energy detector, channel 10. The differences in angular resolution are due to the differences in aperture sizes and length of the deflecting path.

AD-A144 144

UNITED STATES AIR FORCE GEOPHYSICS SCHOLAR PROGRAM
1982-1983(U) SOUTHEASTERN CENTER FOR ELECTRICAL
ENGINEERING EDUCATION INC S... W D PEELE ET AL. MAR 84
AFOSR-TR-84-0622 F49620-82-C-0035

3/3

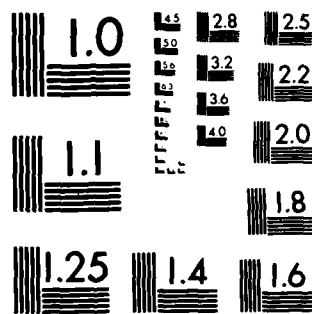
UNCLASSIFIED

F/G 5/1

NL



END
DATE
FILMED
9 84
DTIC



MICROCOPY RESOLUTION TEST CHART
NATIONAL BUREAU OF STANDARDS-1963-A

The results of the calibration are summarized in Table 1. The values given in Table 1 are: E_{peak} , the energy at which $g(E)$ is a maximum; ΔE , the full width at half maximum of $g(E)$; g_{peak} , the maximum value of $g(E)$ and $\int g(E)dE$, the total geometric factor.

Table 1. Calibration values for the DMSP-F8 electron ESA

<u>Channel</u>	<u>E_{peak}</u>	<u>ΔE</u>	<u>g_{peak}</u>	<u>$\int g(E)dE$</u>
1	30500eV	2900eV	$1.7 \times 10^{-4} \text{ cm}^2\text{-sr}$	$5.1 \times 10^{-1} \text{ cm}^2\text{-sr-eV}$
4	9500	840	3.4×10^{-4}	3.0×10^{-1}
10	905	74	9.0×10^{-4}	6.9×10^{-2}
11	960	100	2.3×10^{-4}	2.4×10^{-2}

These measurements show some interesting features about the high energy detector of which channels 1, 4 and 10 are three energy channels. When normalized by plotting $g(E)/g_{\text{peak}}$ and E/E_{peak} the curves are the same below the peak energy but are broader above the peak energy for the two higher energy channels (1 and 4). Channel 1 has the broadest response. This indicates a contribution to $g(E)$ from electrons scattered off the back cylindrical deflection plate. The scattering apparently increases with energy. This effect is also apparent upon inspection of the scans of count rate versus angle for channels 1 and 4.

The SSJ/4 detectors for DMSP-F6 and F7 were of the same design as for F8 but no calibration data exists for these detectors. However, a comparison was made of in-flight counting rates for channels 10 and 11 of these detectors. The ratios of rates were found to be 5.2 and 2.8 for F6 and F7 respectively. The rate data came from observations taken when the electron spectra were seen to be flat, i.e. not decreasing with energy. Consequently a prediction for this ratio can be made from the ratio of measured geometric factors. The value pre-

dicted for the F8 detector is therefore 2.9. This agrees well with the value found for F7 but not for F6. However, we, suspect that one of the two channeltrons in the low energy analyzer of the F6 instrument has ceased to function. This could explain why the ratio of count rates of channel 10, (high energy analyzer), to channel 11, (low energy analyzer), is high.

Another comparison that can be made is the relative change in g_{peak} versus energy. This gives a measure of the change in channeltron efficiency versus energy and avoids the previously mentioned problem of electron scattering. The ratio of g_{peak} at 9.5 keV to that at 905 eV was measured to be 0.38 for the F8 detector. The same ratio was found to be 0.57 for the F4 and F5 detectors, (Hardy et al. 1979), although not on the same calibration facility. The reason for this difference is not understood although it may simply be due to differences in the energy response of the channeltrons used in these detectors.

V. RECOMMENDATIONS

The results of implementing this method of calibrating electron detectors has been described in the previous section. However, several improvements have yet to be implemented and will be undertaken in further work on this project. The experiment itself worked remarkably well although due to lack of time not all of the energy channels of the F8 detector were measured. Also the beam itself should have been measured at the two extremes of the acceleration energy. The beam was measured at 1 keV but not at 30 keV. However, we have no reason to suspect that the beam flux density calculated from the total photocathode current should be inaccurate at 30 keV.

Several problems were encountered during operation which can be corrected. Computer crashes were apparently initiated by charging of wire insulation which was in the path of the electron beam. Freezing of the rotary tables occurred due to excess torque on the stepper motors. These and other mechanical problems will be corrected before future calibrations.

The goal of this project was to extend the operating range of this facility down to 10 volts. At this energy use of Helmholtz coils will be necessary to cancel the effect of the earth's magnetic field on the beam. Coils large enough to surround the 72 inch vacuum chamber are now built and will soon be in operation.

Another goal, that of the beam uniformity, needs to be improved upon. The transmitted light intensity was seen to vary by $\sim 1/3$ over the gold surface. This can be improved upon in future calibrations by realignment of the light source and remeasurement of the transmitted light intensity which is repeated until satisfactory uniformity is achieved.

REFERENCES

- R.L. Arnoldy, P.O. Isaacson, D.F. Gats, Rev. Sci. Instrum. 44, 172 (1973).
- C.B. Childs, J. Opt. Soc. Amer. 51, 583 (1961).
- C.B. Childs, Appl. Optics, 1, 711 (1962).
- P. Christophersen, Ark. Geofys. 5, 637 (1971).
- A. Epstien, J.D. Morris, Mini-Micro Systems, Sept. (1982).
- D.A. Hardy, M.S. Gussenhoven and A. Huber, AFGL-TR-79-0210 (1979).
- A. Huber, J. Pantazis, A.L. Besse, P.L. Rothwell, AFGL-TR-77-0202 (1977).
- A.L. Hughes and L.A. DuBridge, Photoelectric Phenomena, (McGraw Hill, New York, 1932) p. 42.
- G.B. Irani, T. Huen, F. Wooten, J. Opt. Soc. Amer. 61, 128 (1971).
- E.A. Kurz, Amer. Lab. March (1979).
- T.R. Sanderson, J. Henrion, Space Sci. Instrum. 1, 351 (1975).

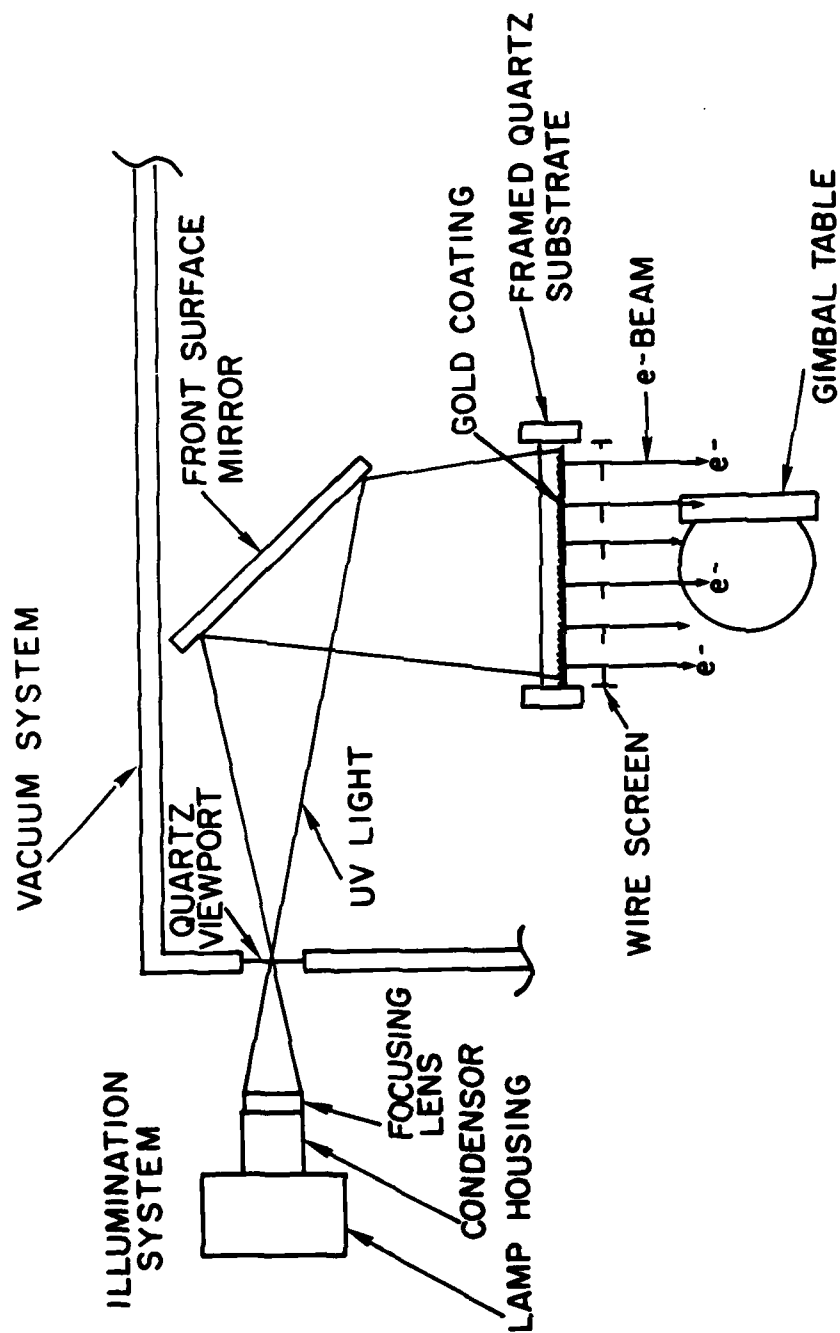


FIGURE 1: SCHEMATIC OF THE ELECTRON DETECTOR CALIBRATION FACILITY

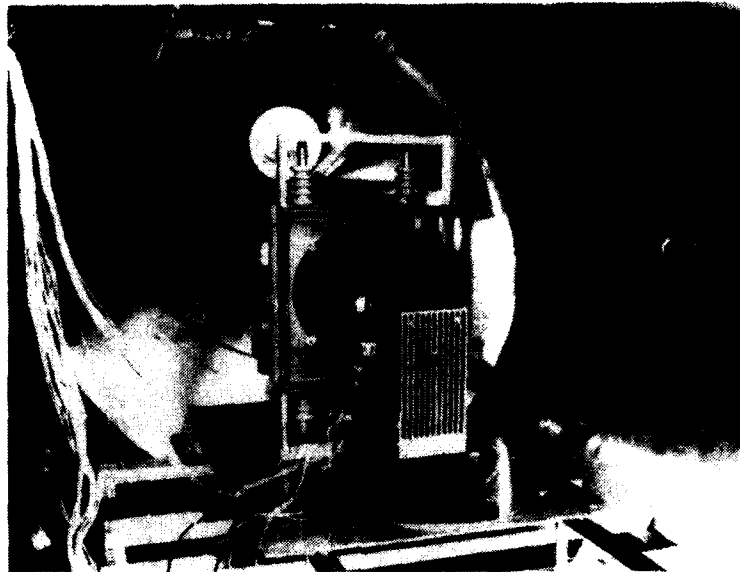


Figure 2a. Photograph of the electron beam system. The gold coated photocathode is in the center. The gimbal table is seen in the beam mapping orientation.



Figure 2b. Exterior view of the vacuum system. The electronics rack, lamp housing and high voltage feed through are visible.

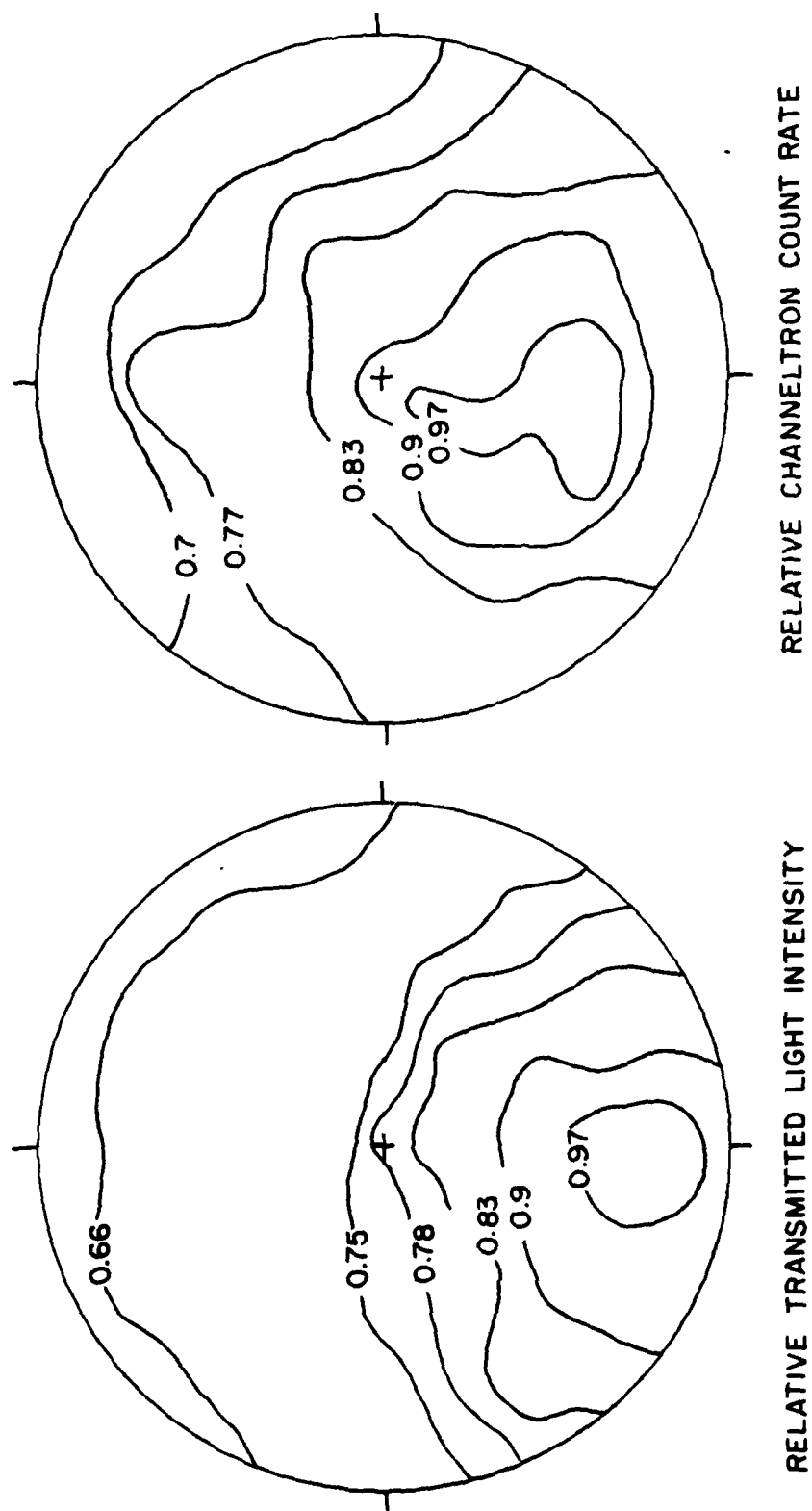


Figure 3: Measurements of the 12 inch electron beam system as viewed from the dectector.

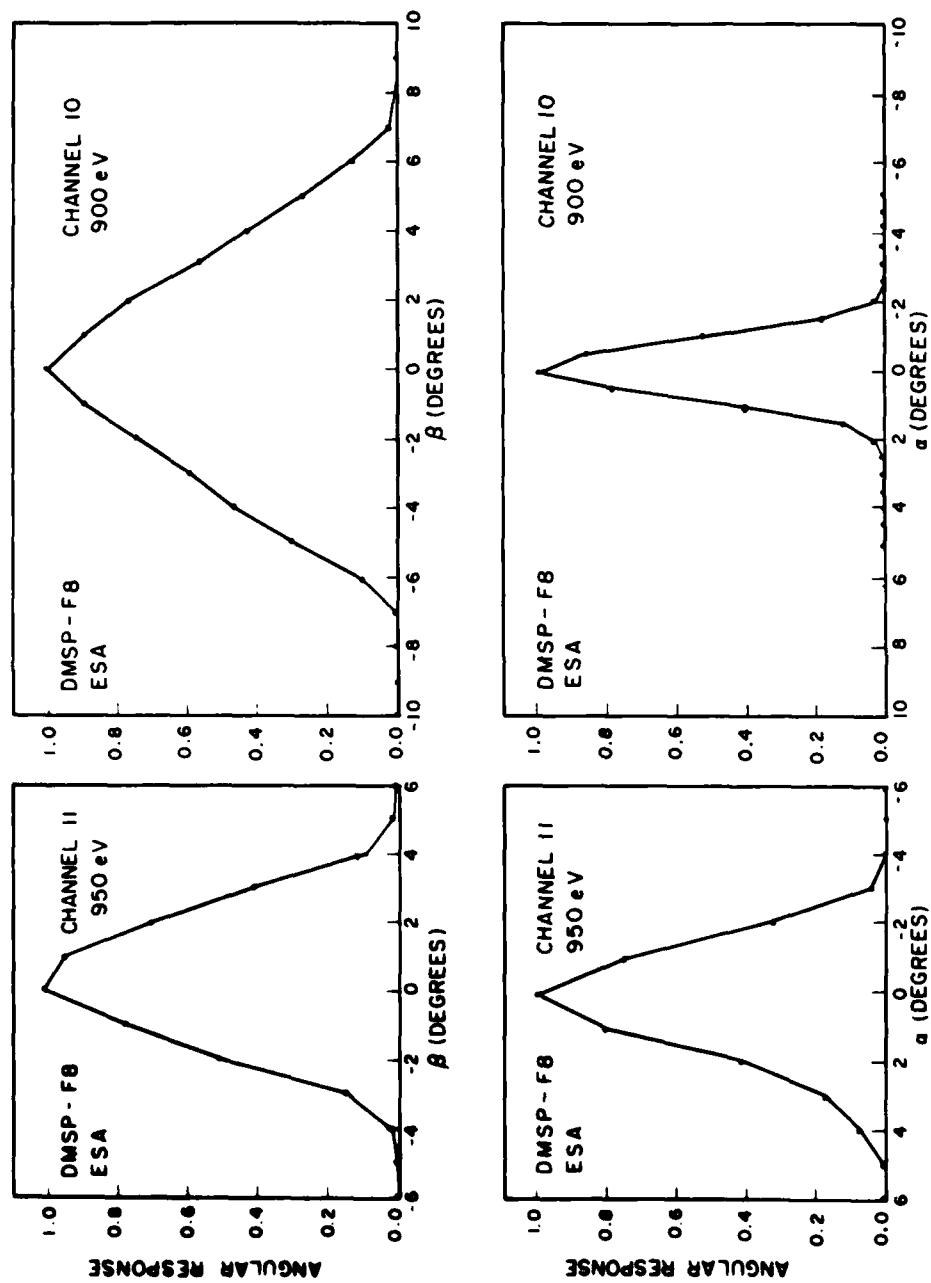


Figure 4: The angular response of the DMSP-F8 electron electrostatic analyzers as measured in the electron detector calibration facility.

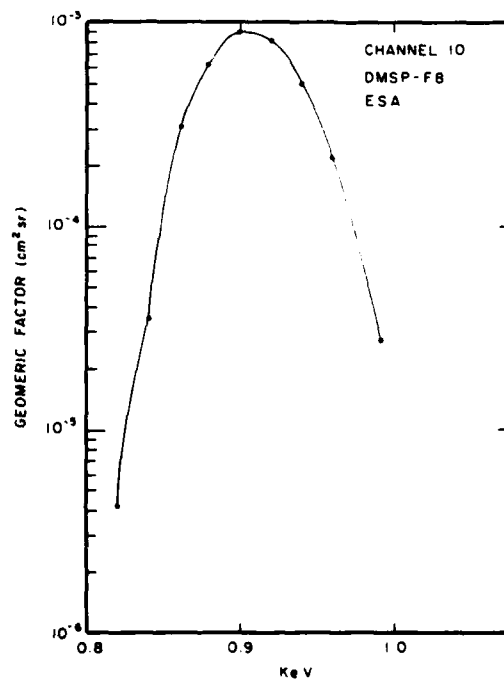
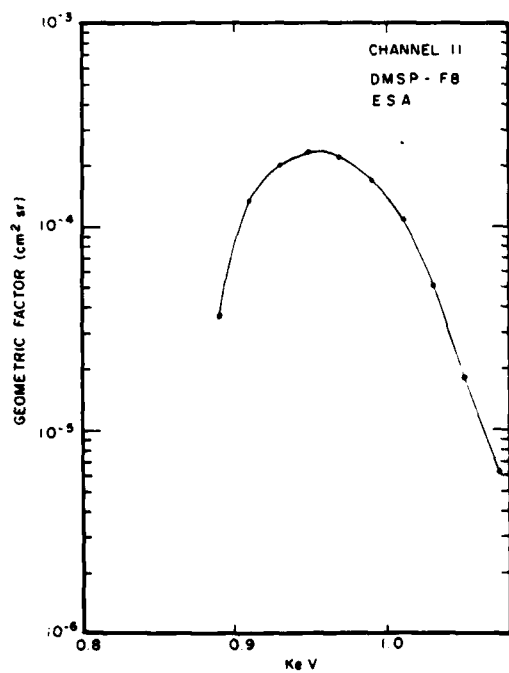
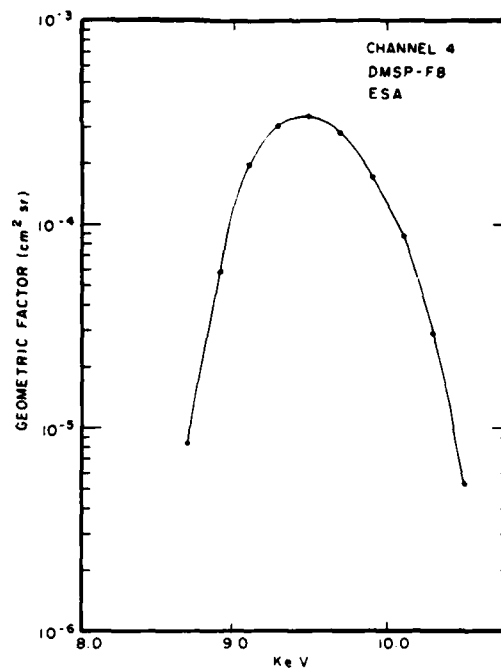
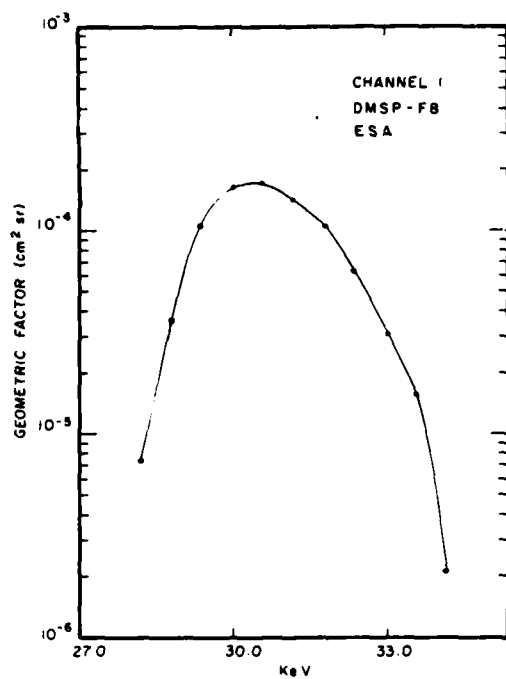


Figure 5: The energy dependent geometric factors calculated from the measurements taken in the electron detector calibration facility.

1982-1983 AFGL-SCEEE GEOPHYSICS SCHOLAR PROGRAM

Sponsored by the

AIR FORCE OFFICE OF SCIENTIFIC RESEARCH

Conducted by the

SOUTHEASTERN CENTER FOR ELECTRICAL ENGINEERING EDUCATION

FINAL REPORT

NUMERICAL SIMULATION OF THUNDERSTORM GUST FRONTS

INCLUDING AMBIENT SHEAR AND ARC CLOUD GENERATION

Prepared by:	Keith L. Seitter
Research Location:	Air Force Geophysics Laboratory Meteorology Division
AFGL Research Contact:	Donald A. Chisholm
Date:	August 31, 1983
Contract Number:	F49620-82-C-0035

I. INTRODUCTION

A relatively small but very important feature of thunderstorms is the gust front. The gust front is the leading edge of the cold downdraft air which spreads out upon reaching the ground. As shown in Figure 1, the gust front acts as a wedge which lifts low level air into the updraft of the thunderstorm. This maintains the thunderstorm by either supplying a continual inflow of potentially unstable air in the case of a supercell storm or initiating new updraft cells in the case of a multicell storm². Gust fronts which have propagated well away from their parent thunderstorms can be responsible for the initiation of new thunderstorm activity, especially at the intersection of the gust front and some other air mass boundary or front³. Recent studies have indicated that the gust front may also play a role in tornado genesis^{4,5}.

Observational studies have shown that the cold air outflow from the thunderstorm can be treated as density current^{6,7,8}. A schematic of an atmospheric density current is shown in Figure 2. The current is characterized by an elevated head region, an overhanging nose, and a turbulent wake at the rear of the head. The arc cloud shown in Figure 2 is a commonly observed feature which is the result of moist boundary layer air being lifted above its level of condensation during the passage of the current.

There have been many laboratory studies of density current motion⁹ and several numerical studies^{10,11,12}. While one of the laboratory studies dealt with the effect of ambient wind on the gust front motion⁹, none of these studies included the effect of the environmental shear commonly associated with severe storms or moist processes such as arc cloud formation. These studies also did not address the question of "gust front decoupling", the process by which the gust front separates from the parent storm and leads to the storm's rapid decay⁸.

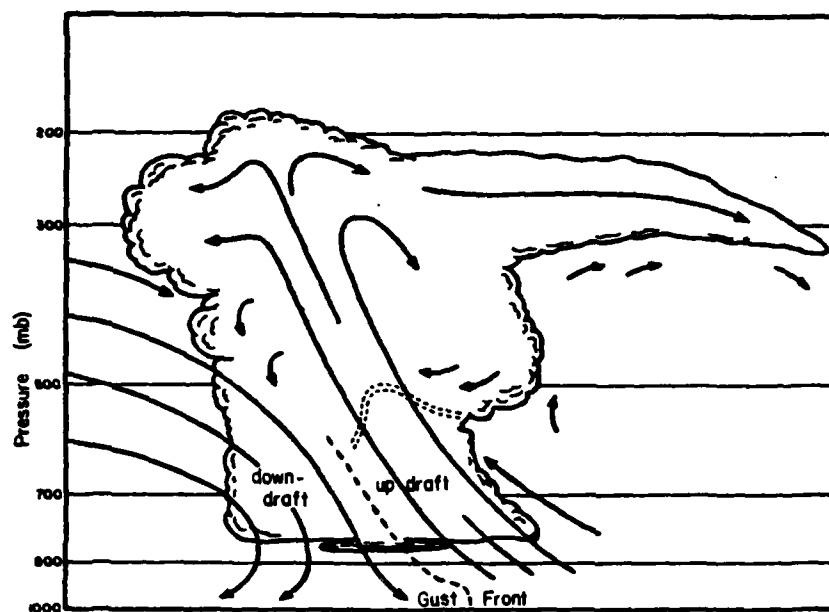


Figure 1. Cross section through a supercell type thunderstorm.
(After Fritsch¹.)

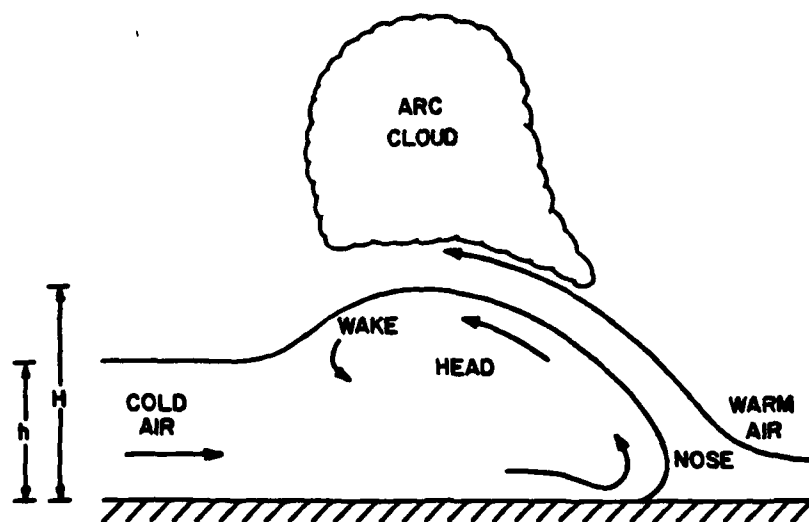


Figure 2. Schematic representation of atmospheric density current.
(After Goff⁷.)

II. OBJECTIVES OF THE RESEARCH PROJECT

This research is meant to extend the work of the previous numerical and laboratory studies through the use of a numerical model. Specifically, the objectives were:

- a) Determine the effect of the ambient winds on gust front motion;
- b) Examine the effect of arc cloud generation on the gust front speed and intensity;
- c) Investigate the decoupling phenomena associated with gust fronts;
- d) Determine the profile of lifting which is associated with gust frontal passage;
- e) Show that the gust front can be accurately represented in a numerical model which uses the same resolution as current thunderstorm models.

One aspect of the study pertaining to objectives a, b, and c was the development of a more general gust front speed equation than has been used in previous studies. This important result will be discussed in the following section.

III. THE GUST FRONT SPEED EQUATION

A major concern of many observational and laboratory studies of gust front and density current motion has been the determination of an equation relating the speed of the front to other measurable quantities^{6,7,8,9}. Most of these studies used an equation of the form¹³

$$V = k \left[g h \frac{\Delta \rho}{\rho} \right]^{1/2} \quad (1)$$

In (1), V is the velocity of the front, g the acceleration of gravity, h the height of the denser fluid outflow, $\Delta \rho$ the difference in density

between the current and the environment, and ρ the density of the environment. The constant, k^* , is the internal Froude number.

Benjamin¹³ showed that for two immiscible, inviscid fluids, $k^* = \sqrt{2}$.

In (1), the height, h , refers to the depth of the fluid behind the head. With a redefinition of the Froude number, however, the height of the head, H , can be used. For atmospheric density currents we can write

$$V = k \left[\frac{\Delta T}{T} g H \right]^{1/2}, \quad (2)$$

where ΔT is the temperature difference between the warm and cold air, T is the temperature of the warm air, and k is the redefined Froude number.

Although theoretically the value of $k^* = \sqrt{2}$ and $k \approx 1.0$, the measured values of these quantities in the atmosphere and laboratory are substantially smaller. This is because the actual flows occur in fluids in which viscous and surface drag effects are present. These effects tend to reduce the speed from the theoretical limit, and this is incorporated into the value of the Froude number. There has been a fairly wide range of k values obtained for atmospheric density currents and gust fronts running from $k = 0.70$ to $k = 1.08^8$.

The driving force of the density current is the pressure gradient force resulting from the increased hydrostatic pressure in the cold air. This is reflected in (1) and (2), which may be rewritten

$$V = k \left[\frac{\Delta p}{\rho} \right]^{1/2}, \quad (3)$$

where Δp is the difference in surface hydrostatic pressure between the density current head and the environment.

For the constant density fluids assumed in the derivation of (1), all three of these equations will give identical results. However, for atmospheric density currents, the results given by these three

equations will differ substantially. This is because (1) and (2) deal only with the density differences over the height of the outflow while (3) includes the integrated effect of the entire depth.

In applying (3) to observed atmospheric density currents, some assumptions must be made. The pressure difference, Δp , refers to the hydrostatic pressure in (3), but the measured pressure is the total surface pressure. Wakimoto⁸ has shown, however, that the maximum surface pressure increase measured during the passage of the head is primarily hydrostatic and can therefore be used directly in (3). The numerical results of Mitchell and Hovermale¹¹ also indicate this. The density, ρ , in (3) is the average density of the warm air over the depth of the current. For ease of application, however, the surface density may be used in (3) with virtually no error.

It is common for gust fronts to propagate through environments which have an ambient wind. The component of the wind parallel to the gust front motion will affect its speed according to⁹

$$V = k \left[\frac{\Delta p}{\rho} \right]^{1/2} + 0.62 \bar{U} \quad , \quad (4)$$

where \bar{U} is the average wind parallel to the gust front motion and positive in the direction of gust front motion.

In order to determine the value of k which applies to gust fronts when the pressure form of the equation is used, (3) and (4) were applied to 20 observed gust fronts. These included the case studied by Charba⁶, the three cases of Wakimoto⁸, and the type I, II, and III cases of Goff⁷. The data on these cases included the recorded surface pressure rise, the gust front speed, and information on the ambient winds. The surface value of the density in the warm air was used in all cases.

Figure 3 shows these observations plotted so that they should fall on a straight line with k as the slope. The best fit line through the origin gives $k = 0.79$. The correlation coefficient is 0.84. The numerical results of Mitchell and Hovermale¹¹ are also plotted in Figure 3 but were not used in determining the best fit line.

IV. THE NUMERICAL MODEL

The model used to obtain the numerical results reported in this paper is an improved version of the two-dimensional, Boussinesq, moist model developed by Seitter¹⁴. The domain is 40 km in the horizontal and 10 km in the vertical in the x - z plane with a grid spacing of 500 m in both directions. The equations governing the vorticity, η , temperature, T , water vapor mixing ratio, q , and liquid water mixing ratio, m , are, respectively,

$$\frac{\partial \eta}{\partial t} + u \frac{\partial \eta}{\partial x} + w \frac{\partial \eta}{\partial z} = -g \frac{1}{\theta_0} \frac{\partial T_v}{\partial x} + g \frac{\partial m}{\partial x} + KV^2 \eta, \quad (5)$$

$$\frac{\partial T}{\partial t} + u \frac{\partial T}{\partial x} + w \frac{\partial T}{\partial z} + w \Gamma_d = \frac{L}{c_p} G + KV^2 T, \quad (6)$$

$$\frac{\partial q}{\partial t} + u \frac{\partial q}{\partial x} + w \frac{\partial q}{\partial z} = -G + KV^2 q, \quad (7)$$

$$\frac{\partial m}{\partial t} + u \frac{\partial m}{\partial x} + w \frac{\partial m}{\partial z} + \frac{\partial}{\partial z} (V_t m) = G + KV^2 m. \quad (8)$$

The velocities, u and w , are written in terms of a streamfunction, ψ ,

$$u = \frac{\partial \psi}{\partial z}, \quad w = -\frac{\partial \psi}{\partial x}, \quad (9)$$

$$\eta = \frac{\partial u}{\partial z} - \frac{\partial w}{\partial x} = \nabla^2 \psi. \quad (10)$$

In the above, T_v is the virtual temperature, G is the liquid water generation term including evaporation and condensation¹⁴ and V_t is the mass-weighted

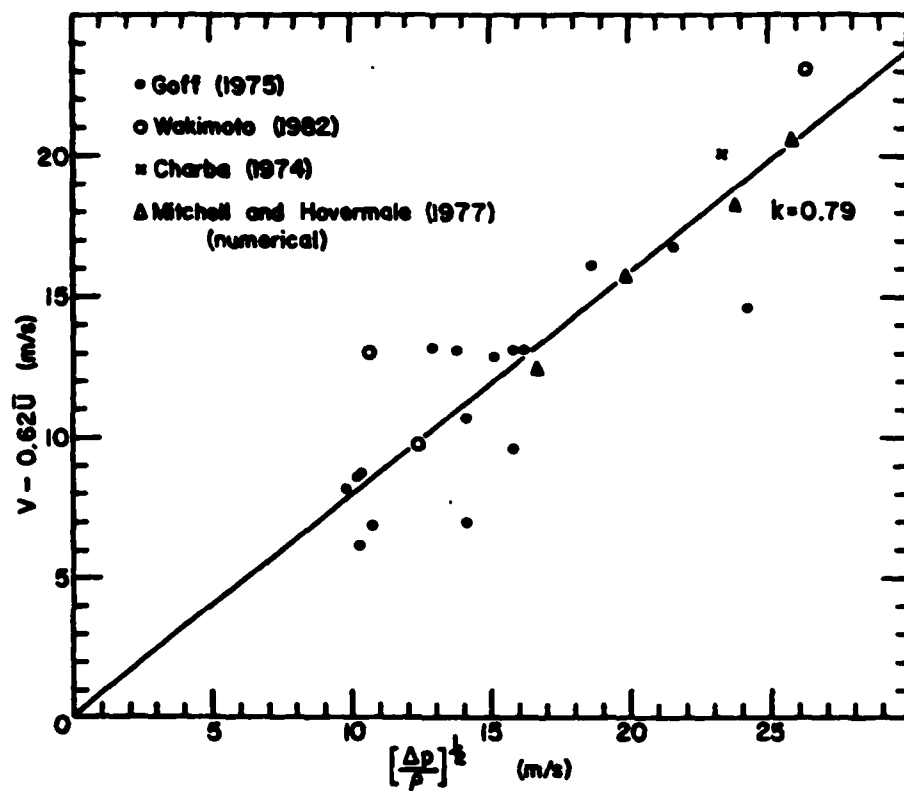


Figure 3. Observations of gust front speed vs. surface pressure rise.

fallspeed of the precipitation. Liquid water less than 1 g/kg is assumed to be cloud water and has zero fallspeed. K is the eddy viscosity.

The equations are integrated in time using the Adams-Bashforth method, with the advective terms represented by the Arakawa Jacobian and the other derivatives by the consistent 9-point form¹⁴. Eq. (10) is solved after each time step by a successive-over-relaxation scheme.

A bulk aerodynamic drag formulation is applied at the surface similar to that of Mitchell and Hovermale¹¹, although modified for application in a vorticity model. A two-dimensional radiation condition¹⁴ is applied on the vorticity at the lateral boundaries with the other variables being specified on inflow and advected on outflow.

The density current is initiated by a cold air source located near the left boundary. Two types of cold air sources were used. The first, referred to as M-type, is a fixed temperature source based on the work of Mitchell and Hovermale¹¹. For this source, the temperature in the source region is given by

$$T = T_{env.} - \Delta T [\cos(2\pi/L (z-z_0)) \cos(2\pi/L (x-x_0))], \quad (11)$$

for $|z - z_0| < L/4$ and $|x - x_0| < L/4$, where $L = 12$ km. $T_{env.}$ is the temperature of the undisturbed environment at that height. Once the integration is begun only the top half of this region is maintained at this temperature. While this source has the desirable property of providing cold air at a fixed temperature, it requires a large eddy viscosity, $K = 900 \text{ m}^2/\text{sec}$, to suppress noise which is generated near the source.

A second type of cold air generator used is based on the work of Thorpe et al.¹² and is referred to as the Q-type source. This source

applies a constant cooling rate of the form

$$\frac{\partial T}{\partial t} = -Q[\cos(2\pi/L (z-z_0)) \cos(2\pi/L (x-x_0))], \quad (12)$$

for $|z - z_0| < L/4$ and $|x - x_0| < L/4$. Q is the cooling rate in the generator region. This source allows the use of a flow-field dependent eddy viscosity which had a domain average of about $K = 190 \text{ m}^2/\text{sec}$. The density currents produced by this source in the present study were not as steady as those obtained with the M-type source since the flux of cold air tended to pulsate.

V. M-TYPE SOURCE RESULTS

A summary of the results of the simulations carried out using the M-type cold air source is given in Table 1. An example of one of these simulations, case MD9, is shown in Figure 4. Note the accurate representation of the shape of the density current head compared to Figure 2. An overhanging nose is not evident in this figure, but observational and laboratory studies indicate that the nose would be below 500 m and thus not resolvable in the model⁷. For cases with small environmental stability, such as MD2, the current is considerably deeper, in agreement with the findings of Mitchell and Hovermale¹¹. The smaller stability also results in a larger vertical velocity at the front since higher static stability inhibits vertical motion.

As the thunderstorm propagates, the downdraft represents a moving cold air source, so it is of interest to consider the effect that movement of the source has on the resulting density current. Numerically, it is much easier to subtract a velocity from the domain than to advect the source, so this is the approach taken.

Table 1. Results of M-Type Simulations

Case	Source ΔT ($^{\circ}\text{C}$)	Stability $(\partial\theta/\partial z)$ ($^{\circ}\text{C}/\text{km}$)	Source Velocity (m/s)	Ambient Shear ($\times 10^{-3} \text{ s}^{-1}$)	ΔT at Head ($^{\circ}\text{C}$)	H (km)	\bar{U} (m/s)	V (m/s)	Updraft at front (m/s)	Δp at Head (Pa)	k
MD1	4.0	0.2	0	0	2.0	3.2	0	11.9	5.7	357.0	0.70
MD2	8.0	0.2	0	0	4.7	3.3	0	17.3	10.1	706.6	0.72
MD3	8.0	0.2	5.0	0	5.0	3.7	0	18.3	11.4	835.7	0.70
MD4	8.0	0.2	10.0	0	4.8	4.4	0	18.8	12.0	991.0	0.66
MD5	8.0	0.2	0	0	4.5	4.2	-10.0	11.1	10.5	879.8	0.73
MD6	8.0	0.2	10.0	2.0	4.1	4.2	4.2	21.8	13.0	815.0	0.71
MD7	8.0	0.2	20.0	4.0	6.3	4.1	8.2	28.1	18.2	1020.7	0.73
MD8	4.0	1.46	0	0	1.7	1.3	0	11.8	1.7	369.6	0.68
MD9	8.0	1.46	0	0	3.9	2.1	0	17.7	5.0	877.0	0.70
MD10	8.0	1.46	10.0	0	4.3	2.4	0	19.6	6.1	1022.4	0.68
MM1	4.0	1.46	0	0	2.0	1.8	0	11.0	2.1	299.2	0.71
MM2	8.0	1.46	0	0	4.7	2.1	0	15.3	4.8	610.4	0.69
									Ave.		0.70

Table 2. Results of Q-type Simulations

Case	Source Cooling Rate ($^{\circ}\text{C}/\text{min}$)	Stability $(\partial\theta/\partial z)$ ($^{\circ}\text{C}/\text{km}$)	Low Level Humidity (%)	ΔT at Head ($^{\circ}\text{C}$)	H (km)	V (m/s)	Updraft at front (m/s)	k Eq. 2	Δp at Head (Pa)	k Eq. 3
QD1	1.0	0.2	dry	3.3	2.4	13.0	6.4	0.80	343	0.79
QD2	2.0	0.8	dry	5.3	1.9	16.4	6.8	0.91	585	0.77
QD3	1.0	1.46	dry	3.0	1.4	11.8	2.6	0.99	325	0.75
QD4	2.0	1.46	dry	4.1	1.7	15.3	4.1	1.01	530	0.76
QD5	3.0	1.46	dry	5.8	1.9	18.1	6.2	0.95	755	0.75
QM1	2.0	1.46	50	4.3	1.6	14.4	4.6	0.96	476	0.75
QM2	2.0	1.46	60	4.6	1.7	13.0	3.8	0.81	364	0.77
QM3	3.0	1.46	60	6.2	1.8	15.0	4.8	0.80	502	0.76
QM4	2.0	1.46	70	4.8	1.7	11.0	3.9	0.68	246	0.80
									Ave.	0.77

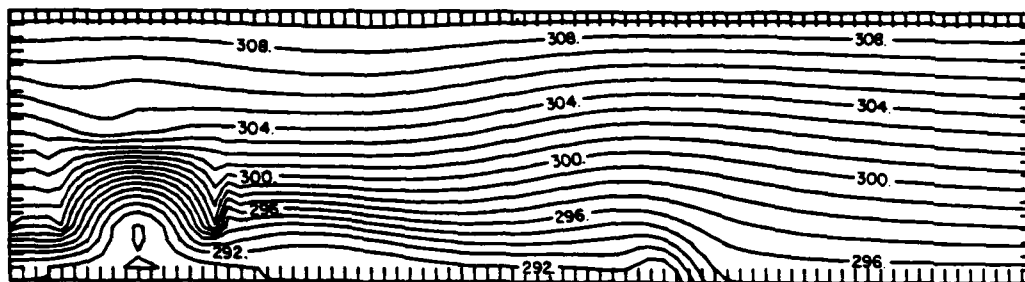


Figure 4. Potential temperature distribution for case MD9 at 20 min. Tick marks are at 500 m intervals.

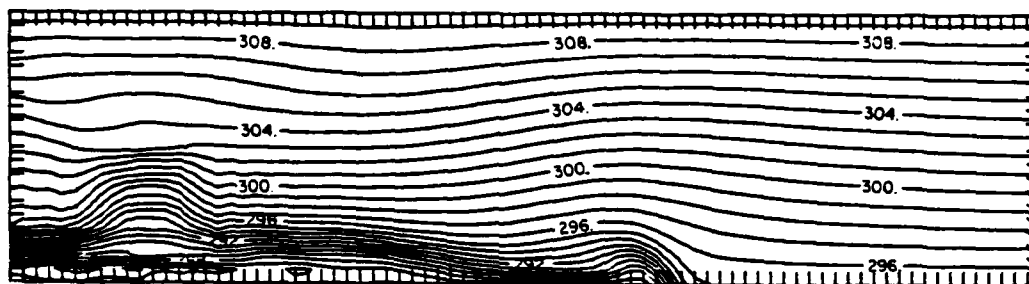


Figure 5. Potential temperature distribution for case QD5 at 20 min.

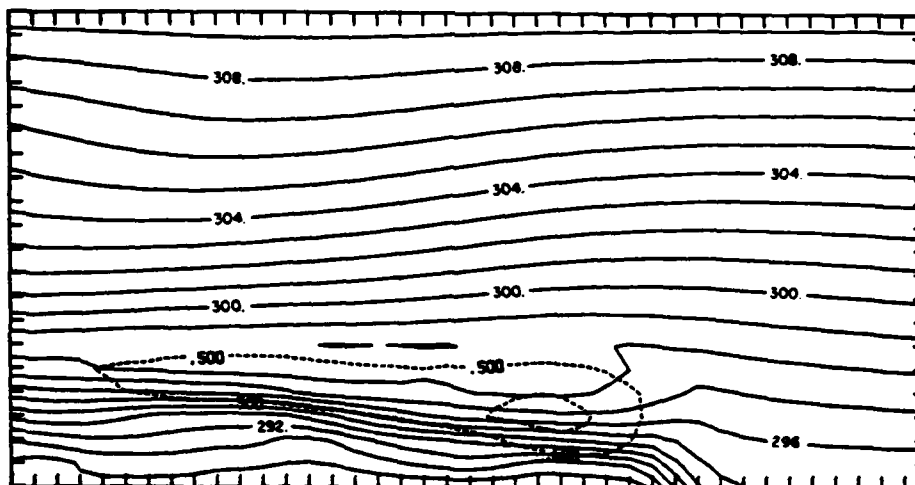


Figure 6. Potential temperature and liquid water fields for case QM2 at 25 min. Liquid water contour interval is 0.5 g/kg. Only center 20 km of domain is shown.

An interesting result pertains to the time at which the source is set in motion. If the density current is allowed to propagate on the order of 15 km away from the source while the source is stationary, and then the source is set in motion at a speed less than or equal to the density current speed, the resulting density current is indistinguishable from one in which the source is stationary for the entire integration. In fact, if the source is set in motion at the speed of the current, the source/current system remains nearly steady with the current showing virtually no propagation relative to the source. In this situation we may say that the gust front is "decoupled" from the source in the sense that its speed is determined by its local characteristics.

If the source is moving at the start of the integration, the resulting density current is modified relative to that given by a stationary source. This is illustrated by comparing the results in Table 1 of the moving source cases (MD3, MD4, and MD10) with the corresponding stationary source cases (MD2 or MD9). In the moving source simulations, cold air is "piled up" near the source during the early stages of the integration before the current propagates a sufficient distance to be decoupled. This greater depth results in a higher hydrostatic pressure and thus a greater speed.

Since most severe thunderstorms develop in environments exhibiting vertical shear, constant vertical shear was included in simulations MD6 and MD7. The source was set in motion at the mid-tropospheric wind-speed, which is approximately the speed a thunderstorm would move in such an environment¹⁴. Because of the shear, the frontal boundary tends to be retarded more near the surface than above so the frontal boundary becomes more vertical. The current shapes in these simulations

were very similar to the gust front observed by Charba⁶. Since the source was moving very fast in case MD7, the density current did not begin propagating away from the source until it had achieved a sufficient temperature difference and depth for its density current speed to be greater than the source speed. Its close proximity to the source for a considerable length of time resulted in substantially lower temperatures in the head.

The density currents in the simulations with shear are moving through an environment with an effective ambient wind equal to the average winds over the depth of the current. Therefore, (4) must be used to calculate the appropriate value of k . For cases MD6 and MD7, and for case MD5 which had a stationary source but constant ambient wind, it was found that the best agreement was obtained when $0.85 \bar{U}$ was used in (4) rather than $0.62 \bar{U}$. Therefore, the k values shown in Table 1 use this form. The other values of k shown in Table 1 were calculated using (3). The average k value for the M-type simulations was $k = 0.70$.

Two moist simulations were run with an M-type source. Both of these simulations, cases MM1 and MM2, had a low level humidity of 50%. The results of these simulations are shown in Table 1. The high diffusion required for the M-type source seemed to significantly affect the arc cloud water distribution in these simulations. Therefore, the Q-type source seemed more appropriate for moist simulations.

VI. Q-TYPE SOURCE RESULTS

The dry simulation results using the Q-type source were very similar to those with the M-type. Figure 5 shows the potential temper-

ature field for case QD5 at 20 min. Table 2 gives the results of the Q-type simulations. Comparison of the dry cases shows the effect of stability and source cooling rate. The average value of k for these simulations is $k = 0.77$ and is somewhat larger than the M-type value. This is probably a reflection of the smaller eddy viscosity used in the Q-type simulations.

The lifting experienced during gust frontal passage was determined by computing the trajectories of parcels originally in the calm air ahead of the front using the method of Schlesinger¹⁵. It was found that even though the density current is a shallow phenomenon, lifting is experienced by parcels throughout the depth of the troposphere with the amount of lifting decreasing linearly with height¹⁶.

A comparison of QD1 and QD3 can be used to explain why (3) is better than either (1) or (2). In the more stable environment, the lifting of air over the head of the current results in a cooling of this air which contributes to the surface hydrostatic pressure. Since (2) considers only the temperature difference between the low level environment and the current it gives quite different values of k for QD1 and QD3. Equation (3), on the other hand, incorporates the integrated effect of the lifting so the k values for the two cases are nearly the same.

Table 2 also shows the results of moist simulations with low level humidities varying from 50% to 70%. The result for case QM2 at 25 min is shown in Figure 6. The arc cloud is produced by the low level air being lifted by the current above its condensation level. The release of latent heat associated with this condensation produces a warm pocket at the top of the head which results in the isentropic structure shown in Figure 6. The air over the head has, in fact, been raised

above its level of free convection and is warmer than the environment. However, deep convection does not develop even in this conditionally very unstable atmosphere. It is felt that the convection is suppressed for two reasons. First, the air lifted by the current is quickly raised above the head and then, as the head passes, it subsides in the wake region. An individual parcel is only above its level of free convection for a short period of time before being forced downward. Secondly, the frontal boundary above the head is a region of strong shear which will inhibit convection. The lack of deep convection initiation is an interesting result. Satellite observations of gust fronts have shown them to propagate large distances producing shallow cumulus, but initiate deep convection only after they intersect with another outflow boundary which provides additional lifting³.

The production of the warm pocket above the head has a pronounced effect on the speed of the gust front. This warm air decreases the surface hydrostatic pressure under the head (although the weight of the liquid water provides a slight increase) and therefore reduces the pressure gradient force driving the current. Thus, the moist current propagates at a slower speed than would a dry current of the same depth and temperature difference. This fact is evident in Table 2 through the comparison of the dry and moist simulation results. For instance, comparing QD4 and QM2, we can see that although both are the same depth and QM2 has a larger temperature difference than QD4, QM2 propagates slower than QD4. This is in direct conflict with (2), but is easily explained through (3). The warm pocket above the head in QM2 results in a smaller surface pressure difference and therefore a slower speed of propagation.

Table 2 also lists the calculated updraft velocity at the front. These values compare very well with those obtained by Mitchell and Hovermale¹¹. This upward motion is primarily accomplished by mechanical lifting even in the moist cases. Because of this, for a given stability, the updraft speed is determined almost entirely by the speed and depth of the density current. The upward motion is suppressed in the more stable environments, as would be expected. If the release of latent heat is sufficient, the updraft in the moist cases will be augmented by the buoyancy of the parcels. This is evident in a comparison of Cases QM2 and QM4.

VII. RECOMMENDATIONS

This study has produced some very interesting results concerning the effects of ambient winds and moisture on density current motion. Many of these results have direct bearing on the speed, depth, and intensity of thunderstorm outflows and their associated gust fronts. Further work is required, however, to truly quantify these effects. The result that the lifting is experienced throughout the depth of the troposphere indicates that results from an anelastic model should be included in this study. Further, a more complete series of moving source and sheared environment studies should be carried out in a more stable environment where the density current would have a more realistic depth. This shallower depth would require a higher resolution in the vertical (say, 200 m) in order to allow the proper interaction of the current with the shear. The effects of the shear may be considerably reduced for shallow currents. These further simulations would require considerable further model development and were therefore not possible in the time period of this appointment.

ACKNOWLEDGMENTS

The author acknowledges the support of the Air Force Systems Command, the Air Force Office of Scientific Research and the Southeastern Center for Electrical Engineering Education during his appointment as an Air Force Geophysics Scholar. The staff of the Air Force Geophysics Laboratory, especially the LYP Branch and the AFGL Computer Center, were very helpful throughout this project. Special thanks are due Dr. Kenneth Mitchell for many helpful discussions and Mr. Donald Chisholm for continual support. The author also thanks Ms. Betty Blanchard for typing this report.

All computations were performed on the AFGL CDC 6600 computer. Computer plots were made using the NCAR graphics software library translated for use on the AFGL system by P. Fougere.

REFERENCES

1. Fritsch, J.M., 1975: Cumulus dynamics: Local compensating subsidence and its implications for cumulus parameterizations. Pure Appl. Geophys., 113, 851-867.
2. Browning, K.A., 1977: The structure and mechanisms of hailstorms. Meteor. Mono., 16, No. 38, 1-43.
3. Purdom, J.F.W., 1976: Some uses of high-resolution GOES imagery in the mesoscale forecasting of convection and its behavior. Mon. Wea. Rev., 104, 1474-1483.
4. Klemp, J.B., and R. Rotunno, 1983: A study of the tornadic region within a supercell thunderstorm. J. Atmos. Sci., 40, 359-377.
5. Weaver, J.F., and S.P. Nelson, 1982: Multiscale aspects of thunderstorm gust fronts and their effects on subsequent storm development. Mon. Wea. Rev., 110, 707-718.
6. Charba, J., 1974: Application of gravity current model to analysis of squall-line gust front. Mon. Wea. Rev., 102, 140-156.
7. Goff, R.C. 1975: Thunderstorm outflow kinematics and dynamics. NOAA Tech. Memo, ERL NSSL-75, National Severe Storms Laboratory. Norman, OK, 63 pp.
8. Wakimoto, R.M., 1982: The life cycle of thunderstorm gust fronts as viewed with Doppler radar and rawinsonde data. Mon. Wea. Rev., 110, 1050-1082.
9. Simpson, J.E., and R.E. Britter, 1980: A Laboratory model of an atmospheric mesofront. Quart. J. Roy. Met. Soc., 106, 485-500.
10. Daly, B.J., and W.E. Pracht, 1968: Numerical study of density current surges. Phys. Fluids, 10, 15-30.
11. Mitchell, K.E., and J.B. Hovermale, 1977: A numerical investigation of the severe thunderstorm gust front. Mon. Wea. Rev., 105, 657-675.
12. Thorpe, A.J., M.J. Miller, and M.W. Moncrieff, 1980: Dynamical two-dimensional downdraughts. Quart. J. Roy. Met. Soc., 106, 463-484.
13. Benjamin, J.B., 1968: Gravity current and related phenomena. J. Fluid Mech., 31, 209-248.
14. Seitter, K.L., 1982: The dynamical structure of squall-line type thunderstorms. Ph.D. thesis, Dept. Geophys. Sci., Univ. of Chicago, 139 pp.
15. Schlesinger, R.E., 1973: A numerical model of deep moist convection: Part A prototype experiment and variations upon it. J. Atmos. Sci., 30, 1374-1391.
16. Seitter, K.L., 1983: The effect of arc cloud generation on thunderstorm gust front motion. Preprints, 13th Conference on Severe Local Storms. Oct. 17-20, 1983, Amer. Meteor. Soc.

1982-1983 AFGL-SCEEE GEOPHYSICAL SCHOLAR PROGRAM

Sponsored by the

AIR FORCE OFFICE OF SCIENTIFIC RESEARCH

Conducted by the

SOUTHEASTERN CENTER FOR ELECTRICAL ENGINEERING EDUCATION

FINAL REPORT

REACTIONS OF NEGATIVE IONS

Prepared by: Albert A. Viggiano
Research Location: Air Force Geophysics Laboratory/LID
AFGL Research Contact: John F. Paulson
Date: December 30, 1983
Contract Number: F49620-82-C-0035

Reactions of Negative Ions
Albert A. Viggiano* and John F. Paulson
Air Force Geophysics Laboratory
Hanscom AFB, Massachusetts 01731

*Air Force Geophysics Scholar

Acknowledgements

I would like to thank the Air Force System Command, the Air Force Office of Scientific Research and the Air Force Geophysics Laboratory for support during this year. I also want to thank Fred Dale for his technical support and John Paulson for many helpful discussions.

Objectives

Negative ion-molecule reactions play an important role in controlling the electrical properties of the earth's atmosphere as well as other plasmas. In particular, associative detachment plays a major role in controlling the electron density of the earth's mesosphere. No previous studies of these reactions had been made as a function of temperature, and therefore, the present study was made to remedy this. Reactions were chosen that were expected to have large temperature effects in either the rate coefficient or the branching ratios. The results of such experiments would then be compared with theory. Two additional reactions, one insertion reaction and two reactions with multiple reaction pathways were chosen.

The second part of this report involves a review of the negative ion-molecule reactions carried out in swarm experiments in the last five years. During this time new techniques have developed in order to study a wide variety of negative ion processes. A compilation of the results was, therefore, called for and a review chapter written for the book "Swarms of Ions and Electrons in Gases."

A. Introduction

Traditionally, negative ion-molecule reactions have been much less studied than those of positive ions. This is due to the fact that the most popular type of ion source, electron impact, produces a much greater variety of positive ions than negative ions and usually in greater abundances. Thus, in order to make workable signals of many types of negative ions, ion sources in which ion-molecule reactions take place have to be used.

The flowing afterglow has been ideally suited to the study of negative ion reactions since in it there exists a region where primary ions can be converted easily into secondary ions /1/. More recently, relatively gas tight electron impact sources, in which the pressure can be a few torr, have been used in selected ion flow tubes (SIFTS) to generate a variety of negative ions. In addition, ion beam experiments, /2/, /3/ and ion cyclotron resonance mass spectrometers, /4/, /5/ have been used to study a number of negative ion-molecule reactions. The latter instrument has been used to a great degree to establish a scale of gas phase acidities /6/. In this review we will cover the research on negative ion reactions performed using swarm experiments in the last five years. The emphasis will be on giving a broad overview of the most recent work in order to show the variety of measurements that can be made with these systems. The work presented covers a wide spectrum of results, including studies of vibrational product distributions and temperature dependences of associative detachment reactions, many studies involving atmospheric species, as well as those relating to electron affinity determinations and isotope exchange. The work involving H_3O^- shows that by choosing conditions carefully one can study species that are difficult to produce. Two main areas are left out of this review: the effects of solvation and the reactions of organic anions. The former topic has recently been reviewed by Bohme /7/ and the latter by DePuy and Bierbaum /8/.

B. Associative Detachment

Associative detachment is an important process in controlling the electron density in a variety of natural plasmas, such as the earth's ionosphere and interstellar space, and has been a much studied process for many years. In spite of this, much new information has become available recently. This new information involves the first studies of the temperature dependence of the rate coefficients of these reactions /9/ and of the infrared emissions from the neutral products of the reactions /10/-/14/. These studies have yielded new insights into the reaction mechanisms as well as details of the kinematics involved. In addition, much recent work has been done on the theoretical aspect of these reactions /15/.

The reactions whose temperature dependences were studied fell into two classes, those which were slow and those for which associative detachment was only one of several channels. These reactions could then be expected to have a significant dependence on temperature in either the rate coefficient or branching ratio. Table 1 lists the results of this study. The temperature dependences are the results of least squares calculations to power law dependences.

For the reactions involving only associative detachment, the temperature dependence was found to be $T(-0.75 \pm 0.1)$ in all three cases. The authors /9/ concluded that this represented mainly the temperature dependence of the lifetime of the collision complex with respect to dissociation back into reactants. This result should be compared with the theories of Bates /16/ and Herbst /17/, which predict a complex lifetime varying as $T^{-0.5}$ for atomic-diatom systems.

Among these associative detachment reactions, a particularly interesting one is that of S^- with O_2 . This is an example of an insertion reaction, in which one of the reactants must insert itself between two atoms already bonded together. The standard model for an insertion reaction was thought to be a two step process /18/ which is written for this reaction as,



where the products of the first step never separate. The criterion for this to be allowed is that the first step is exothermic. In this example, step 1 is endothermic by 8.7 kcal mole⁻¹ and therefore might not be expected to occur. An alternate explanation of this process as an addition reaction to form an isomer of SO_2 also fails, as this is endothermic.

Table 1. Rate Coefficients for Associative Detachment Reactions /9/

Reaction	$k(T)(\text{cm}^3 \text{ s}^{-1})$
$O^- + NO \rightarrow NO_2 + e$	$3.1(-10) * (300/T)^{0.83}$
$S^- + CO \rightarrow COS + e$	$2.3(-10)(300/T)^{0.64}$
$S^- + O_2 \rightarrow SO_2 + e$	$4.6(-11)(300/T)^{0.72}$
$O^- + C_2H_2 \rightarrow C_2H_2O + e$	$1.1(-9)(300/T)^{0.39}$
$O^- + C_2H_2 \rightarrow \text{products}$	$1.94(-9)$
$O^- + C_2H_4 \rightarrow C_2H_4O + e$	$5.7(-10)(300/T)^{0.53}$
$O^- + C_2H_4 \rightarrow \text{products}$	$9.0(-10)(300/T)^{0.43}$
*3.1 (-10) means 3.1×10^{-10}	

The authors /9/ then proposed that the reaction could be explained in terms of the insertion model if the kinetic energy gained during the collision was taken into account. In order

the low mass of the outgoing electron, essentially all of the incoming orbital angular momentum must end up in the product neutral. This leads to the unique case in which the entrance channel impact parameter maps directly into the rotational quantum number of the diatomic product. The maximum allowed J then depends on the vibrational level in question and the overall energetics of the reaction. As stated above, Smith and Leone /14/ have qualitatively observed this high level of rotational excitation for the F^- reaction with D in an argon buffer. The observed falloff in population at the highest vibrational level in both the H and D reactions is then explained by the fact that the highest rotational levels are not energetically accessible for states with a large amount of vibrational excitation, and consequently collisions with large impact parameters (large orbital angular momentum) cannot form the product neutral in a high vibrational level and still conserve angular momentum.

Table 2. Relative Product Vibrational Populations from the $F^- + H, D$ Reactions /14/

$F^- + H \rightarrow HF(v) + e$		$F^- + D \rightarrow FD(v) + e$	
v	nascent distribution	v	nascent distribution
1	0.00 ± 0.06	1	$0.08 - 0.07$
2	0.09 ± 0.01	2	0.09 ± 0.01
3	0.21 ± 0.01	3	0.15 ± 0.02
4	0.41 ± 0.02	4	0.11 ± 0.02
5	0.30 ± 0.02	5	0.15 ± 0.01
		6	0.24 ± 0.03
		7	0.18 ± 0.02

In contrast to the fact that the high level of rotational excitation can be explained classically, the high degree of vibrational excitation must be explained quantum dynamically. Smith and Leone /14/ argue that the $F^- + H(D)$ reaction can best be explained by the virtual state model rather than the resonant state model because there exists an open s-wave electron detachment exit channel. In the former model, transitions are facilitated due to a breakdown in the Born-Oppenheimer approximation. The increased nuclear velocity associated with higher vibrational levels then aids the Born-Oppenheimer breakdown, and qualitatively one can expect an increase in the transition rate for this state. Model calculations by Gauyacq /15/ support these arguments. At present, however, there is no explanation for the differences in the product vibrational distributions for H and D.

C. Atmospheric Negative Ion Chemistry

In the past several years a large effort has gone into understanding the ion chemistry of the atmosphere, especially the stratosphere. This interest has been fueled by the advent of balloon-borne mass spectrometers that have yielded the first

detailed height profiles of both positive and negative ions in the stratosphere /19/, /20/. In order to explain the results, many of which were unexpected, laboratory measurements had to be performed. This section will deal with the most recent laboratory measurements that pertain to negative ions of atmospheric interest.

The first in-situ measurements of stratospheric negative ions revealed the presence of a series of ions that could be best fit as $R^-(HR)_m(HNO_3)_n$, where HR had a mass of 98 ± 2 amu /21/. Arnold and Henschen /21/ speculated that HR was sulfuric acid. In order to test this hypothesis, Viggiano et al./22/ studied a number of positive and negative ion reactions with H_2SO_4 . In order to get sulfuric acid into the gas phase in a controlled manner, they used a furnace in which dry nitrogen was passed through glass wool covered with several drops of concentrated H_2SO_4 . The flow conditions were set such that the flow was viscous, and the H_2SO_4 flow was then proportional to the square root of the N_2 flow. In this manner, they were able to measure the relative rates of the reactions but were unable to set absolute values, since the absolute concentration of sulfuric acid in the flow tube was not known. However, they noted that the ratio of the rate coefficients for the fastest reactions was the same as would be expected for the collision rates based on the masses of the respective reactant ions. By then setting the fastest rate equal to the collision rate, the rate coefficients were put on an absolute basis. Since the time of publication of the results, the dipole moment of H_2SO_4 has been measured, and the rate coefficients have been revised accordingly /23/. The revised results are listed in Table 3.

Table 3. Reaction Rate Coefficients for H_2SO_4 Reactions at 343K /23/

Reaction	$k(\text{cm}^3 \text{ s}^{-1}) \times 10^9$	$\frac{k_{\text{meas}}}{k_{\text{theor}}}$
1. $O^- + H_2SO_4 \rightarrow HSO_4^- + OH$	4.2	(1)*
2. $Cl^- + H_2SO_4 \rightarrow HSO_4^- + HCl$	2.7	0.9
3. $NO_3^- + H_2SO_4 \rightarrow HSO_4^- + HNO_3$	2.6	1.0
4. $I^- + H_2SO_4 \rightarrow HSO_4^- + HI$	1.9	0.9
5. $NO_3^-(HNO_3) + H_2SO_4 \rightarrow HSO_4^-(HNO_3) + HNO_3$	2.3	1.1
6. $NO_3^-(HNO_3)_2 + H_2SO_4 \rightarrow HSO_4^-(HNO_3)_2 + HNO_3$	1.1	0.6
* defined as 1		

The most important results from an atmospheric viewpoint are the reactions of H_2SO_4 with $NO_3^-(HNO_3)_n$ ions. The latter ions had previously been thought to be the terminal negative ions in the stratosphere, and the fast reactions of these ions with sulfuric acid indicated that HR was correctly identified by Arnold and Henschen /21/. In fact, these measurements have provided the only means at present for determining the gaseous sulfuric acid concentration in the stratosphere /24/.

The laboratory studies indicated that sulfuric acid should not play a role in the positive ion chemistry of the stratosphere, and this conclusion is supported by more recent in-situ results. In addition to the atmospheric implications, the reaction of I^- with H_2SO_4 puts a lower limit to the electron affinity of HSO_4 at 4.5 eV.

Another important species in the stratosphere is N_2O_5 . Two studies were made of the reactions of atmospheric ions with N_2O_5 /25/, /26/. The results of the negative ion reactions in these studies are listed in Table 4. All the reactions were found to be fast to produce NO_3^- except those involving hydrates of NO_3^- . These results imply that N_2O_5 will speed the conversion rate of primary negative ions in the stratosphere to NO_3^- core ions. The important reactions from this point of view are those of CO_3^- , O_2^- and its hydrates, and NO_2^- and its hydrates, all of which are precursors to NO_3^- in the stratosphere. Particularly interesting is the reaction with CO_3^- since in the mesosphere the conversion of CO_3^- to NO_3^- is slow. The rapidity of this reaction as well as that of the reaction of CO_3^- with HNO_3 ensures rapid production of NO_3^- core ions in the stratosphere. The lack of reaction of the hydrates of NO_3^- with N_2O_5 indicates that the barrier in the reaction of N_2O_5 with H_2O is not overcome in the presence of the NO_3^- core. This last result also holds for positive ion hydrates.

Table 4. Rate Coefficients of Negative Ions Reacting with N_2O_5

Reaction	$k(cm^3s^{-1})$	Ref
$F^- + N_2O_5 \rightarrow NO_3^- + FNO_2$	$1.1(-9)$	25
$Cl^- + N_2O_5 \rightarrow NO_3^- + ClNO_2$	$9.4(-10)$	25
$Br^- + N_2O_5 \rightarrow NO_3^- + BrNO_2$	$5.9(-10)$	25
$I^- + N_2O_5 \rightarrow NO_3^- + INO_2$	$5.9(-10)$	25
$CO_3^- + N_2O_5 \rightarrow NO_3^- + NO_3 + CO_2$	$2.8(-10)$	25
$\quad \quad \quad \rightarrow NO_3^- + NO_2 + CO_3$		
$NO_2^- + N_2O_5 \rightarrow NO_3^- + 2NO_2$	$7.0(-10)$	25
$Cl^- + N_2O_5 \rightarrow NO_3^- + ClNO_2$	$9.3(-10)$	26
$Cl^-(H_2O) + N_2O_5 \rightarrow \text{products}$	$8.2(-10)$	26
$O_2^- + N_2O_5 \rightarrow \text{products}$	$1.1(-9)$	26
$O_2(H_2O) + N_2O_5 \rightarrow \text{products}$	$1.0(-9)$	26
$O_2(H_2O)_2 + N_2O_5 \rightarrow \text{products}$	$9(-10)$	26
$NO_2^- + N_2O_5 \rightarrow NO_3^- + 2NO_2$	$6(-10)$	26
$NO_2(H_2O) + N_2O_5 \rightarrow \text{products}$	$5(-10)$	26
$NO_3(H_2O) + N_2O_5 \rightarrow \text{products}$	$<1(-11)$	26
$NO_3(H_2O)_2 + N_2O_5 \rightarrow \text{products}$	$<1(-11)$	26

Another interesting subset of the N_2O_5 reactions are those with the halide ions. These are all fast and produce NO_3^- and the nitryl halide. The fast reaction of I^- with N_2O_5 has been exploited in order to study the thermal decomposition rate of N_2O_5 /27/. In this study, the flowing afterglow was used in a novel way as a detector for neutral kinetics. Em-

playing this technique of selective chemical ionization, Viggiano et al./27/ studied the thermal decomposition of N_2O_5 over a pressure range of 10 to 800 torr and a temperature range of 285 to 384K. The results of this study and that by Connell and Johnston /28/ have been combined by Malko and Troe /29/ and compared to the latest theories on unimolecular decomposition.

CH_3CN has been found to play an important role in the positive ion chemistry of the stratosphere. A study was made by Paulson and Dale /30/ using a SIFT in order to see if CH_3CN could also enter into the negative ion chemistry of the stratosphere. The results of this work are shown in Table 5.

Table 5. Rate Coefficients for Reactions of CN Containing Compounds at 297 K /30/

Reaction	$k(\text{cm}^3\text{s}^{-1})$
$O^- + CH_3CN \rightarrow CH_2CN^- + OH + 0.54 \text{ eV}$	3.5(-9)
$\rightarrow OH^- + CH_2CN + 0.85$	<5(-12)
$OH^- + CH_3CN \rightarrow CH_2CN^- + H_2O + 0.89$	3.3(-9)
$\rightarrow CN^- + CH_3OH + 1.00$	<5(-12)
$OH^-(H_2O) + CH_3CN \rightarrow CH_2CN^- + 2H_2O - 0.19$	3.1(-9)
$\rightarrow CH_2CN^-(H_2O) + H_2O$	2.6(-9)
$OH^-(H_2O)_2 + CH_3CN \rightarrow \text{products}$	slow
$CH_2CN^-(H_2O) + CH_3CN \rightarrow CH_2CN^-(CH_3CN) + H_2O$	>5(-10)
$CN^- + CH_3CN + He \rightarrow CN^-(CH_3CN) + He$	3.5(-12)*
$Cl^- + CH_3CN + He \rightarrow Cl^-(CH_3CN) + He$	2.5(-12)*
$O_2^- + CH_3CN + He \rightarrow O_2^-(CH_3CN) + He$	3.7(-11)*
$CH_2CN^- + CH_3CN + He \rightarrow CH_2CN^-(CH_3CN) + He$	1.3(-12)*
$NO_2^- + CH_3CN + He \rightarrow NO_2^-(CH_3CN) + He$	8.5(-12)*
$NO_3^- + CH_3CN + He \rightarrow NO_3^-(CH_3CN) + He$	7.8(-12)*
$CO_3^- + CH_3CN + He \rightarrow CO_3^-(CH_3CN) + He$	1.1(-12)*
$CN^- + HNO_3 \rightarrow NO_3^- + HCN$	2.0(-9)
$CH_2CN^- + HNO_3 \rightarrow NO_3^- + CH_3CN$	1.4(-9)
$CH_2CN^- + NO_2 \rightarrow NO_2^- + CH_2CN$	1.0(-9)
*Two-body rate coefficients at a He pressure of 0.4 torr ($1.3 \times 10^{16} \text{ cm}^{-3}$).	

In the reactions of acetonitrile with both O^- and OH^- , only the proton transfer channel was observed, although hydrogen atom transfer in the reaction with O^- and nucleophilic dis-

placement in the reaction with OH^- are also exothermic. The latter reaction would lead to $\text{CH}_3\text{OH} + \text{CN}^-$. Reaction with $\text{OH}^-(\text{H}_2\text{O})$ produced both m/e 40 i.e., CH_2CN^- and m/e 58, written here as $\text{CH}_2\text{CN}^-(\text{H}_2\text{O})$. The ratio of these product ions in the limit of zero reactant flow is 1.22. Production of CH_2CN^- is slightly endothermic, based upon current thermochemical information. Production of m/e 58 might be regarded as nucleophilic displacement if, as suggested by Caldwell et al./31/, the m/e 58 ion product is written not as $\text{CH}_2\text{CN}^-(\text{H}_2\text{O})$ but as $\text{CN}^-(\text{CH}_3\text{OH})$. With further addition of CH_3CN to the flow tube, however, the m/e 58 species reacts further and is replaced with m/e 81, $\text{CH}_2\text{CN}^-(\text{CH}_3\text{CN})$. This suggests that m/e 58 is $\text{CH}_2\text{CN}^-(\text{H}_2\text{O})$ which then undergoes a solvent switching reaction with further addition of CH_3CN . Reaction of $\text{OH}^-(\text{H}_2\text{O})_2$ with CH_3CN is slow. The other reactions of CH_3CN listed in Table 5 are three-body association processes. The fate of CH_2CN^- and of CN^- in the stratosphere is determined by the rapid reactions of both of these species with HNO_3 and by the reaction of CH_2CN^- with NO_2 . Based upon the rate coefficients for these reactions and upon recent measurements of stratospheric number densities for HNO_3 and NO_2 , the lifetimes of CH_2CN^- and CN^- are about 3 seconds at 35 km, compared to ion lifetimes of thousands of seconds, indicating that these should be minor species, as has been observed /19/, /20/.

Two recent studies pertain to the ion chemistry of the mesosphere. The first of these was made to determine the role of chlorine-containing species in this region /32/. The results are listed in Table 6. HCl was found to react rapidly with O^- , O_2^- , NO_2^- and CO_4^- producing Cl^- (or ClHO_2^- in the latter case). This indicates that these reactions are likely to be the source of Cl^- in the 60-80 km region of the atmosphere. The reaction of CO_3^- with HCl was found to be slow, presumably because the reaction is endothermic. In contrast, ClO^- was predicted not to be an important species in the atmosphere. This is due to the fact that the rate constant for ClO^- production from the reaction of Cl^- with O_3 has a small upper limit and that ClO^- was found to react rapidly with NO , NO_2 , and O_3 . The electron affinity of ClO was found to be 1.95 ± 0.25 eV in the same study.

Table 6. Reactions of Chlorine Containing Species at 300K
/32/

Reaction	$k(\text{cm}^3 \text{ s}^{-1})$
$\text{O}^- + \text{CCl}_4 \rightarrow \text{ClO}^- + \text{CCl}_3$	$(1.4 \pm 0.4) \times 10^{-9}$
$\text{O}^- + \text{HCl} \rightarrow \text{Cl}^- + \text{OH}$	$(2.0 \pm 0.6) \times 10^{-9}$
$\text{O}_2^- + \text{HCl} \rightarrow \text{Cl}^- + \text{HO}_2$	$(1.6 \pm 0.5) \times 10^{-9}$
$\text{NO}_2^- + \text{HCl} \rightarrow \text{Cl}^- + \text{HNO}_2$	$(1.4 \pm 0.4) \times 10^{-9}$
$\text{CO}_2^- + \text{HCl} \rightarrow \text{ClHO}_2^- + \text{CO}_2$	$(1.2 \pm 0.4) \times 10^{-9}$
$\text{CO}_3^- + \text{HCl} \rightarrow \text{products}$	$< 3 \times 10^{-11}$
$\text{ClO}^- + \text{NO} \rightarrow \text{NO}_2^- + \text{Cl}$	$(2.9 \pm 0.9) \times 10^{-11}$
$\text{ClO}^- + \text{NO}_2 \rightarrow \text{NO}_2^- + \text{ClO}$	
$\quad \quad \quad \rightarrow \text{Cl}^- + \text{NO}_3$	$(3.2 \pm 1.6) \times 10^{-10}$
$\quad \quad \quad \rightarrow \text{NO}_3^- + \text{Cl}$	
$\text{ClO}^- + \text{SO}_2 \rightarrow \text{Cl}^- + \text{SO}_3$	$(1.3 \pm 0.4) \times 10^{-9}$
$\text{ClO}^- + \text{CO}_2 \rightarrow \text{products}$	$< 1 \times 10^{-13}$
$\text{ClO}^- + \text{O}_3 \rightarrow \text{Cl}^- + 2\text{O}_2$	$(7 \pm 3.5) \times 10^{-11}$
$\quad \quad \quad \rightarrow \text{O}_3^- + \text{ClO}$	
$\text{Cl}^- + \text{O}_3 \rightarrow \text{ClO}^- + \text{O}_2$	$\leq 5 \times 10^{-13}$

The other study pertaining to mesospheric negative ion chemistry involves silicon-containing species. These measurements were made after a rocket-borne mass spectrometer found an ion at mass 76 that could not be identified with any conventional ions. The results of the rocket flight and the laboratory results are reported by Viggiano et al./33/. An important conclusion was that O_3^- and CO_3^- react rapidly with SiO to produce SiO_3^- . The absolute values of the rate coefficients could not be determined because the flow of SiO could not be measured. The other important laboratory result was that SiO_3^- did not react with NO , NO_2 , CO , CO_2 , O , O_3 , or Cl_2 , the most important trace species that could be expected to react with SiO_3^- in the mesosphere. The absence of reaction with these neutrals suggests that they are endothermic and places a lower limit of 4.7 eV on the dissociation energy of the bond between O^- and SiO_2 . The authors concluded that the mass 76 ion was probably SiO_3^- and went on to speculate that very heavy ions found in the same flight may be ions of the type SiO_3^- (SiO_2)_m (MgO)_n (FeO)_o...formed by electron attachment to particles resulting from meteor ablation. This hypothesis is based on the large stability found for SiO_3^- .

Recently, there has been a study by Fahey et al. /34/ that has looked at the largely unexplored area of tropospheric ion chemistry. This research involves the reactions of $O_2^-(H_2O)_n$ with $n = 0$ to 4. The study was carried out in a variable temperature flowing afterglow modified so that the reactant ions were created in a high pressure region (27 torr) which was separated from the main flow tube by a membrane having an aperture 0.4 cm in diameter. In this manner, the cluster ions could be produced with a minimum amount of H_2O , which minimized the effects of secondary reactions. The technique had the additional advantage of ensuring that the reactant ions were formed in the source region and not in the reaction region. The results of this study are listed in Table 7.

Table 7. Reaction Rate Coefficients for $O_2^-(H_2O)_n$ Reactions /34/

Reaction	$k(cm^3s^{-1})$	Temp.(K)
$O_2^- + O_3 \rightarrow O_3^- + O_2$	$7.8(-10)$	335
$O_2^-(H_2O) + O_3 \rightarrow O_3^- + O_2 + H_2O$	$8.0(-10)$	292-335
$O_2^-(H_2O)_2 + O_3 \rightarrow O_3^- + O_2 + 2H_2O$	$7.8(-10)$	235-292
$O_2^-(H_2O)_3 + O_3 \rightarrow O_3^- + O_2 + 3H_2O$	$\sim 6.4(-10)$	181-235
$O_2^-(H_2O)_4 + O_3 \rightarrow O_3^- + O_2 + 4H_2O$	$\sim 4.6(-10)$	181
$O_2^-(H_2O) + NO \rightarrow O_2^-(NO) + H_2O$	$2(-10)$	211-300
$O_2^-(H_2O)_2 + NO \rightarrow O_2^-(NO)(H_2O) + H_2O$	$1.5(-10)$	176-300
$O_2^-(H_2O)_3 + NO \rightarrow O_2^-(NO)(H_2O)_2 + H_2O$	$1.5(-10)$	176-211
$O_2^-(H_2O)_4 + NO \rightarrow O_2^-(NO)(H_2O)_3 + H_2O$	$1.2(-10)$	176-184
$O_2^-(H_2O)_5 + NO \rightarrow O_2^-(NO)(H_2O)_4 + H_2O$	$1.2(-10)$	184
$O_2^- + SO_2 \rightarrow SO_2^- + O_2$	$1.9(-9)$	303
$O_2^-(H_2O) + SO_2 \rightarrow SO_2^- + H_2O$	$1.8(-9)$	303-304
$O_2^-(H_2O)_2 + SO_2 \rightarrow$ products	$1.7(-9)$	207-304
$O_2^-(H_2O)_3 + SO_2 \rightarrow$ products	$1.7(-9)$	207-210
$O_2^-(H_2O)_4 + SO_2 \rightarrow$ products	$1.6(-9)$	207
$O_2^-(H_2O) + CO_2 \rightarrow CO_2^- + H_2O$	$>5.2(-10)$	295
$O_2^-(H_2O)_2 + CO_2 \rightarrow$ products	$7(-11)$	292
$O_2^-(H_2O)_3 + CO_2 \rightarrow$ products	$<1(-12)$	187-213
$O_2^-(H_2O)_4 + CO_2 \rightarrow$ products	$<1(-12)$	187-213

In the cases in which there is an exothermic exchange of ligands (NO, SO₂, or CO₂ for H₂O), the reactions were all fast, even for the higher hydrates. This could be expected since there are no steric barriers for ligand exchange. The identity of the ion formed in the O₂⁻ (H₂O)_n reaction with NO is probably the peroxy isomer of NO₃⁻, although rearrangement into the more stable form could not be ruled out. The most surprising result of this study was that O₂⁻ (H₂O)_n ions reacted rapidly with O₃ to produce O₃⁻ with one less water molecule attached. This process might involve either the transfer of an oxygen atom or the simultaneous transfer of both charge and one or more water molecules. Studies using ¹⁸O labeling in the reactant ion showed that only the latter process occurred. The speed of these ligand exchange and charge exchange reactions at large degrees of hydration is in contrast to similar studies involving ion-atom exchange. In the latter case reactivity typically decreased significantly with increased hydration /7/. The findings in this study ensure that the primary O₂⁻ (H₂O)_n ions expected in the earth's troposphere will quickly react to form more evolved ions and that O₂⁻ hydrates will not be a major species when ambient tropospheric ions are measured.

D. Electron Affinity Determination

One of the major applications of negative ion-molecule reactions is for electron affinity determination. In the last several years, a number of swarm studies have involved the determination of electron affinities. The determination of electron affinities in a swarm experiment can be done in a variety of ways. A direct method is that of bracketing. This involves studying a number of charge exchange reactions with compounds of known electron affinities. The reactions involved are



and



A fast reaction implies the reactant neutral has the higher electron affinity. By studying a number of such reactions for both A^- and A one can then bracket the electron affinity of species A if the electron affinities of the other species are known. A less direct form of bracketing involves studying more complex reactions than charge exchange, and then by knowing the thermochemistry of the other species involved, one can again put limits on the electron affinity.

An alternative to this method is to study an equilibrium process and derive the electron affinity of one of the negative species from the measured thermochemistry. One may study the equilibrium directly or determine the equilibrium constant by measuring both the forward and reverse rate coefficients independently.

In this manner a number of studies in recent years have yielded electron affinity determinations. In some of the studies the determination of an electron affinity (or limit to it) was an added bonus, as in the studies involving sulfuric acid /22/ and ClO_2 /32/ mentioned in the atmospheric section of this paper. In addition, there have been several studies where the determination of the electron affinity was the prime purpose /35/-/38/. The most recent electron affinity determinations in swarm experiments are listed in Table 8 along with the technique. In some cases, such as HSO_4 and UF_6 , only lower limits could be placed. Rather tight limits, as low as 0.1 eV, can be obtained in favorable cases, such as SF_4 , with careful attention given to the reactions studied.

Table 8. Recent Electron Affinity (EA) Determinations

Molecule	EA (eV)	Method	Reference
SF_6	1.0 ± 0.2	bracketing	37
SF_4	2.35 ± 0.1	bracketing	36
UF_6	>3.61	bracketing	35
HO_2	1.16 ± 0.15	equilibrium constant	38
HSO_4	>4.5	bracketing	22
ClO	1.95 ± 0.25	bracketing	32

to overcome the endothermicity, the reactants must come within 1.94\AA of each other. This leads to a reaction efficiency of 8.4%, which compares well with the measured value of 6.2%, lending credence to this explanation. The temperature dependence of this reaction can then still be explained by a change in the complex lifetime.

The reactions of O^- with C_2H_2 and C_2H_4 are fast and have the associative detachment channel as a main channel. The overall rate of the reaction with C_2H_2 was found to be independent of temperature, although the branching ratio was found to have a significant temperature dependence. The reaction of O^- with C_2H_4 was found to have a slight temperature dependence, but the branching ratio was found not to change significantly with temperature. The rate coefficient for the associative detachment channel for each of these reactions was found to vary as $T^{(-0.45 \pm 0.06)}$.

Over the past several years the flowing afterglow has been used to study the chemiluminescence associated with a number of reactions, many of which were associative detachment reactions. Included in the associative detachment reactions are the reactions of O^- with CO /10/ and of the halide negative ions with hydrogen and deuterium atoms /11/-/14/. The most complete study to date is that of Smith and Leone on the reactions of F^- with H and D /14/, and the present discussion will emphasize these results. The reaction of F^- with H is sufficiently exothermic to produce HF with up to 5 quanta of vibrational energy, and the reaction of F^- with D can produce DF with up to 7 vibrational quanta. The nascent vibrational energy product distributions found for these reactions are shown in Table 2. For the H reaction, it was found that the population in each vibrational level increased up to $v = 4$ and then decreased for $v = 5$. The F^- reaction with D also showed a large amount of product vibrational excitation, although more uniformly distributed as a function of v than the H analog. Smith and Leone /14/ were also able to get some information on the rotational energy distribution of the DF product by studying this reaction in an argon buffer, where the rotational energy quenching rate was slower than in helium. They found a large amount of rotational excitation, equal to about 13% of the available energy.

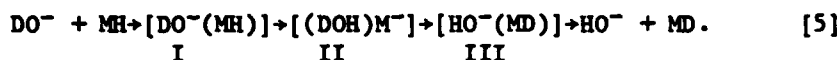
Associative detachment reactions are an extreme example of a reaction in which there is a large difference in the reduced mass of the products and reactants. Smith and Leone /14/ have pointed out that many aspects of the product distributions can be explained by classical kinematics. Due to

One particularly interesting aspect of the above studies not related to electron affinity determinations warrants further discussion. It is usually assumed in flowing afterglow studies that the ambipolar diffusion coefficient is a constant independent of degree of reaction. Streit and Newton /35/, /39/ have found that this is not the case for UF_6 reactions. UF_6^- probably has a much smaller free diffusion coefficient than the lighter reactants used in the study. As the reaction proceeds, the ambipolar diffusion coefficient of the reactant ion in the flowing afterglow increases as the reactant ion is replaced by the slower diffusing UF_6^- /39/. Thus as the flow of UF_6 increases, the decline in the primary signal deviates from linearity in the normal plot of the logarithm of the ion signal versus reactant neutral flow. The effect is that, upon addition of small amounts of UF_6 , the decline in the primary signal is more than if only reaction occurred because the ambipolar diffusion coefficient is increasing. Upon large additions of UF_6 , the ambipolar diffusion coefficients reach constant values, and the decline in the primary is a straight line. This problem does not occur in a SIFT as charged particles of only one sign are present.

E. Isotope Effects Involving Proton Transfer

Proton transfer is one of the most basic types of ion-molecule reactions. Many studies of proton transfer reactions have been used to establish tables of gas phase acidities and proton affinities /6/, /40/. In this section two studies involving the basic nature of proton transfer will be discussed. Both of these involve the use of isotopically labelled species to help elucidate the reaction mechanism.

The first study to be discussed involves the measurements of the rate coefficients for hydrogen-deuterium exchange between HO^- (and DO^-) with a variety of weakly acidic neutrals, MD (and MH) /41/. The results of this study are listed in Table 9. Grabowski et al. /41/ have pointed out that there is only a weak correlation of the H-D exchange rate with the relative acidity of the exchange reagent. The mechanism used to explain these data is



The rate of the H-D exchange is then determined by several factors. Molecules with either large dipole moments or large polarizabilities will generally form longer lived ion-molecule complexes and, therefore, will have a better chance for reaction. The slowness of the DO^- reaction with ethylene is an example where the low initial bond strength of the complex causes the reaction to be slow, the reaction efficiency being less than 0.02 percent. In contrast, the analogous reaction with ammonia leads to a complex with large initial bond strength and to a reaction efficiency of 18 percent.

Table 9. Rate Coefficients for H-D Exchange Reactions at 299K /41/

Reaction	$k \times 10^{10}$ ($\text{cm}^3 \text{s}^{-1}$)	k/k_c^*	Reaction	$k \times 10^{10}$ ($\text{cm}^3 \text{s}^{-1}$)	k/k_c^*
$\text{HO}^- + \text{D}_2$	0.68	0.060	$\text{HO}^- + \text{C}_6\text{D}_6$	7.5	0.38
$\text{DO}^- + \text{H}_2$	0.38	0.024	$\text{DO}^- + \text{C}_6\text{H}_6$	6.6	0.34
$\text{HO}^- + \text{HD}$	0.35	0.027	$\text{DO}^- + \text{CH}_4$	<0.002	<0.0002
$\text{DO}^- + \text{HD}$	0.15	0.012	$\text{DO}^- + \text{C}_2\text{H}_4$	<0.002	<0.0002
$\text{HO}^- + \text{ND}_3$	2.7	0.13	$\text{DO}^- + \text{CH}_3\text{NH}_2$	5.7	0.28
$\text{DO}^- + \text{NH}_3$	3.8	0.18	$\text{DO}^- + (\text{CH}_3)_2\text{NH}$	7.5	0.38
$\text{HO}^- + \text{D}_2\text{O}$	12	0.50	$\text{DO}^- + \text{H}_2\text{CO}$	exchange observed	
$\text{DO}^- + \text{H}_2\text{O}$	18	0.74			

* k_c means the collision rate

Once a long lived complex is formed, the reaction rate is determined by the rate of intramolecular proton transfer. This rate is determined primarily by two factors, the relative basicity of OD^- and M^- and the relative bond strength of HOD to M^- and that of OD^- to MH (the bond strengths of complex I and II, respectively). These two factors then determine the relative energies of the $\text{OD}^- (\text{MH})$ and $\text{M}^- (\text{HOD})$ complexes which play a major role in determining the rate of the reaction. Faster rates result when OD^- is the stronger base and the $\text{M}^- (\text{HOD})$ complex has the stronger bond. Both effects facilitate proton transfer.

Another effect that has an influence on the reaction efficiency is multiple proton transfer within the collision complex. This problem of intramolecular proton transfer is treated in another study from the same laboratory /42/. This study involved the reactions of amide and hydroxyl with SO_2 , CO_2 , N_2O and CS_2 . The results are listed in Table 10. The observation of unlabeled hydroxide products in the reactions involving H^{18}O^- reactants shows that an intramolecular proton transfer is occurring.

Table 10. Reactions of OH^- and NH_2^- /42/

Reaction	$k(\text{cm}^3 \text{ s}^{-1})$
$\text{NH}_2^- + \text{SO}_2 \rightarrow (66.5\%) \text{SO}_2^- + \text{H}_2\text{N}$ $\quad \quad \quad \rightarrow (26.0\%) \text{NSO}^- + \text{H}_2\text{O}$ $\quad \quad \quad \rightarrow (7.5\%) \text{HO}^- + \text{HNSO}$	2.94(-9)
$\text{NH}_2^- + \text{CO}_2 \rightarrow \text{NCO}^- + \text{H}_2\text{O}$	9.29(-10)
$\text{NH}_2^- + \text{N}_2\text{O} \rightarrow (72.1\%) \text{N}_2^- + \text{H}_2\text{O}$ $\quad \quad \quad \rightarrow (27.9\%) \text{HO}^- + \text{HN}_3$	2.88(-10)
$\text{NH}_2^- + \text{CS}_2 \rightarrow (54\%) \text{NCS}^- + \text{H}_2\text{S}$ $\quad \quad \quad \rightarrow (46\%) \text{HS}^- + \text{HNCS}$	1.8(-9)
$\text{H}^{18}\text{O}^- + \text{S}^{16}\text{O}_2 \rightarrow \text{H}^{16}\text{O}^- + \text{S}^{16}\text{O}^{18}\text{O}$	1.25(-9)
$\text{H}^{18}\text{O}^- + \text{C}^{16}\text{O}_2 \rightarrow \text{H}^{16}\text{O}^- + \text{C}^{16}\text{O}^{18}\text{O}$	5.69 (-10)
$\text{D}^{18}\text{O}^- + \text{C}^{16}\text{O}_2 \rightarrow \text{D}^{16}\text{O}^- + \text{C}^{16}\text{O}^{18}\text{O}$	6.33 (-10)
$\text{H}^{18}\text{O}^- + \text{N}_2^{16}\text{O} \rightarrow \text{H}^{16}\text{O}^- + \text{N}_2^{18}\text{O}$	1.16 (-11)
$\text{H}^{34}\text{S}^- + \text{C}^{32}\text{S}_2 \rightarrow \text{H}^{32}\text{S}^- + \text{C}^{32}\text{S}^{34}\text{S}$	1.53 (-11)

Grabowski /42/ has set up a simple statistical model to help elucidate some of the mechanistic detail of the reactions involving H^{18}O^- and H^{34}S^- . In this model, once a complex is formed it can either undergo an intramolecular proton transfer or dissociate into products which may or may not be the initial reactants. The model can then be used to predict the reaction efficiency as a function of the ratio of the proton transfer rate to the dissociation rate. The results of this calculation pertaining to the situation where there are three equivalent heavy atoms (e.g., $\text{H}^{18}\text{O}^- + \text{CO}_2$) are shown in Figure 1. The maximum reaction efficiency is 2/3 since two of the heavy atoms are equivalent. Using this graph one finds that on the average 2 to 3 proton transfers occur in the reaction of H^{18}O^- with CO_2 and 11 to 12 in the reaction with SO_2 . The fact that more proton transfers occur in the case of SO_2 is due to the fact that the CO_2 bond energy is less than the SO_2 bond energy. This leads to a reduced reaction efficiency as explained above. By doing experiments in

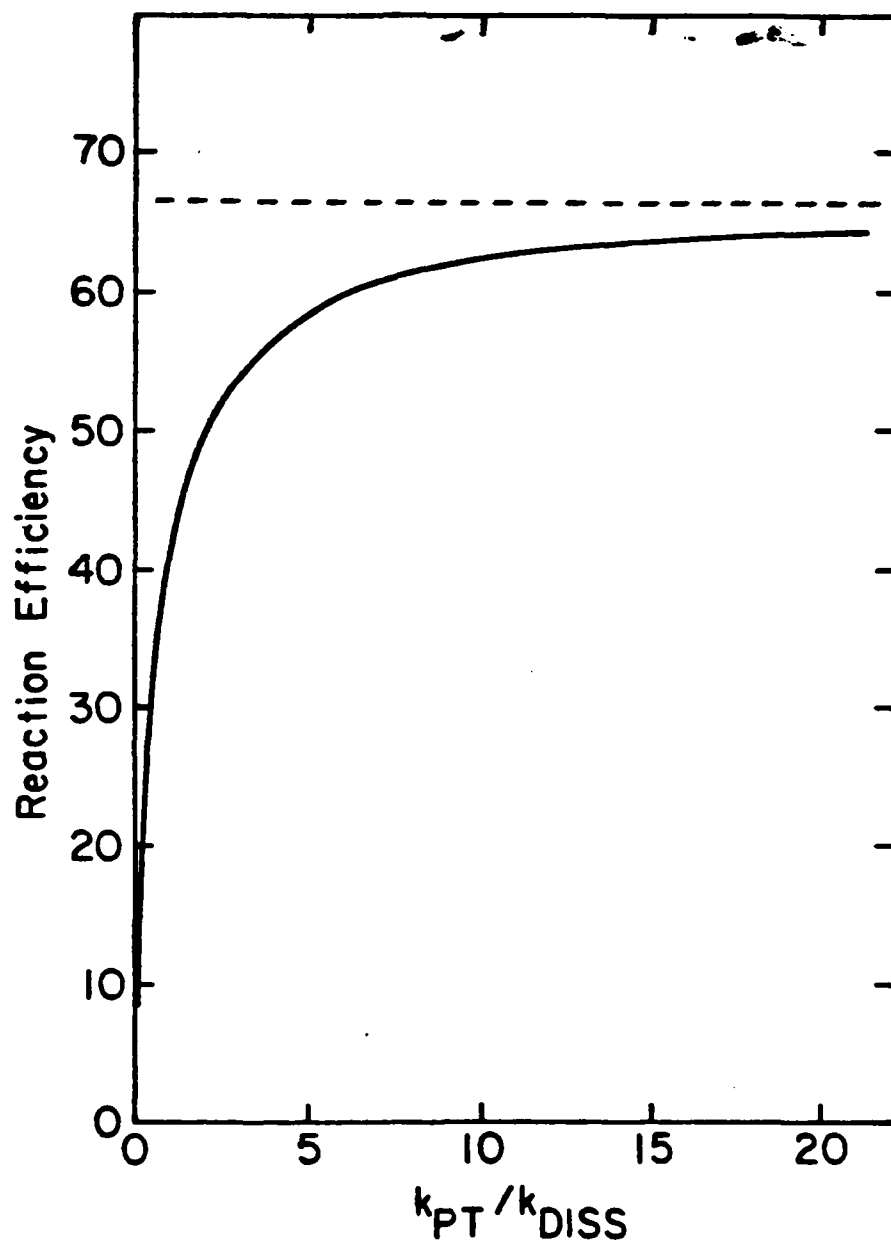


Fig. 1. A plot of the calculated reaction efficiency as a function of the ratio of proton transfer to dissociation rate coefficients for the reactions of $H^{18}O^-$ with SO_2 and CO_2 and the reaction of $H^{34}S^-$ with CS_2 . The dashed line is the statistical limit for the reaction efficiency in the event of complete randomization of the proton. Reprinted by permission /42/.

which the hydrogen was replaced by deuterium, the author concluded that the lifetime of the complexes with respect to dissociation, rather than the proton transfer rate, controlled the exchange, since this substitution neither slowed the reaction nor changed the reaction efficiency.

F. Reaction of H_3O^-

The ion H_3O^- has been observed in ion beam experiments /43/ where it is formed in the endothermic reaction



and in an ion cyclotron resonance (ICR) apparatus /5/ from the exothermic reaction



The dissociation energy $D(\text{H}^--\text{H}_2\text{O})$ is known to be about 17 ± 3 kcal mol⁻¹ from the beam experiments and from molecular orbital calculations /44/. An attempt to observe H_3O^- produced in the reaction between OH^- and H_2CO in a SIFT was unsuccessful /45/. The ions H_3CO^- and H_3CO_2^- were observed, however, and are thought to result from the reactions



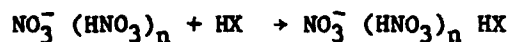
which have also been observed in the ICR /5/. When $\text{OD}^-(\text{D}_2\text{O})$ reacted with H_2CO , no evidence was obtained for the formation of H_2DO^- , and the only ion product was H_2DCO_2^- , which corresponds to a solvent switching reaction.

G. Conclusions

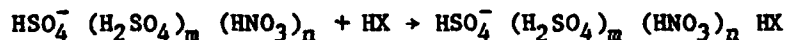
In the past several years, a wide range of experimental work has been done on negative ion-molecule reactions. The development of the SIFT apparatus for use with negative ions has greatly expanded the type of experiments that can be performed, as it has for positive ions. As many of the more straight-forward reactions have been studied, experimenters have turned to novel techniques to perform their experiments. Those reported here include the study of vibrational product distributions, use of a membrane ion source region to study large cluster ions, and the study of neutrals difficult to work with, such as H_2SO_4 and N_2O_5 . Information has even been obtained on undetected ions such as H_3O^- . All this information has given new insights into the basic mechanisms of ion-molecule reactions as exemplified by the work on proton transfer reactions and associative detachment.

Recommendations

The temperature dependences of negative ion-molecule reactions have received little attention. In particular, not much is known about the rates of three body association reactions as a function of temperature and especially as a function of ligand number. These reactions are important in the stratosphere and troposphere. Knowledge of the rates of reactions such as



and



where HX is HCl, H₂O₂, HNO₃ and HNO₂ is needed to help understand the chemistry of the lower atmosphere. These rates may then be used to derive the concentration of some of the clustering neutrals from results of in-situ ion composition measurements.

References

1. Ferguson, E.E., Fehsenfeld, F.C., Schmeltekopf, A.L.: Flowing Afterglow Measurements of Ion-Neutral Reactions. *Adv. At. Molec. Phys.* 5, 1-55 (1969).
2. Paulson, J.F., Dale, F.: Reactions of $\text{OH}^- \cdot \text{H}_2\text{O}$ with NO_2 . *J. Chem. Phys.* 77, 4006-4008 (1982).
3. Wu, R.L.C., Tiernan, T.O.: Evidence for Excited States of CO_3^* and NO_3^* from Collisional Dissociation Processes. *Planet. Space. Sci.* 29, 735-739 (1981).
4. Kleingeld, J.C., Ingemann, S., Jalonen, J.E., Nibbering, N.M.M.: Formation of NH_4^- Ion in the Gas Phase. *J. Am. Chem. Soc.* 105, 2474-2475 (1983).
5. Kleingeld, J.C., Nibbering, N.M.M.: The Long Lived H_2O^- Ion in the Gas Phase: Its Formation, Structure, and Reactions. *Int. J. Mass Spectrom. Ion Phys.* 49, 311-318 (1983).
6. Bartmess, J.E.: Compilation of Gas Phase Anion Thermochemistry. *J. Phys. Chem. Ref. Data* (in press).
7. Bohme, D.K.: Gas Phase Studies of the Influence of Solvation on Ion Reactivity. In: *Nato Advanced Study Institute Volume on Chemistry of Ions in the Gas Phase*. Holland. D. Reidel Publishing (in press).
8. DePuy, C.H., Bierbaum, V.M.: Gas Phase Reaction of Organic Ions as Studied by the Flowing Afterglow Technique. *Accts. Chem. Res.* 14, 146-153 (1981).
9. Viggiano, A.A., Paulson, J.F.: Temperature Dependence of Associative Detachment Reactions. *J. Chem. Phys.* 79, 2241-2245 (1983).
10. Bierbaum, V.M., Ellison, G.B., Futrell, J.H., Leone, S.R.: Vibrational Chemiluminescence from Ion-Molecule Reactions: $\text{O}^- + \text{CO} \rightarrow \text{CO}_2^* + \text{e}^-$. *J. Chem. Phys.* 67, 2375-2376 (1977).
11. Zwier, T.S., Maricq, M.M., Simpson, C.J.S.M., Bierbaum, V.M., Ellison, G.B., Leone, S.R.: Direct Detection of the Product Vibrational-State Distribution in the Associative Detachment Reaction $\text{Cl}^- + \text{H} \cdot \text{HCl}(\text{v}) + \text{e}^-$. *Phys. Rev. Lett.* 44, 1050-1053 (1980).
12. Maricq, M.M., Smith, M.A., Simpson, C.J.S.M., Ellison, G.B.: Vibrational Product States from Reactions of CN^- with the Hydrogen Halides and Hydrogen Atoms. *J. Chem. Phys.* 74, 6154-6170 (1981).

13. Zwiier, T.S., Weisshaar, J.C., Leone, S.R.: Nascent Product Vibrational State Distributions of Ion-Molecule Reactions: The $\text{H} + \text{F}^- \rightarrow \text{HF}(\text{v}) + \text{e}$ Associative Detachment Reaction, *J. Chem. Phys.* 75, 4885-4892 (1981).
14. Smith, M.A., Leone, S.R.: Product Nascent State Distributions in Thermal Energy Associative Detachment Reactions: $\text{F}^- + \text{H}, \text{D} \rightarrow \text{HF}(\text{v}), \text{DF}(\text{v}) + \text{e}$. *J. Chem. Phys.* 78, 1325-1334 (1983).
15. Gauyacq, J.P.: Associative Detachment in Collisions Between Negative Halogen Ions and Hydrogen Atoms. *J. Phys. B.* 15, 2721-2739 (1982).
16. Bates, D.R.: Temperature Dependence of Ion-Molecule Association. *J. Chem. Phys.* 71, 2318-2319 (1979).
17. Herbst, E.: Refined Calculated Ion-Molecule Association Rates. *J. Chem. Phys.* 72, 5284-5285 (1980).
18. Fehsenfeld, F.C.: Associative Detachment. In: *Interactions Between Ions and Molecules*. (Ausloos, P., ed.), p. 387-412. New York: Plenum Publishing Corp. 1974.
19. Arnold, F.: Physics and Chemistry of Atmospheric Ions. In: *Atmospheric Chemistry*. (Goldberg, E.D., ed.) p. 273-300. Berlin: Springer Verlag, 1982 and references therein.
20. Arijs, E.: Positive and Negative Ions in the Stratosphere. *Ann. Geophys.* 1, 149-160 (1983) and references therein.
21. Arnold, F., Henschen, G.: First Mass Analysis of Stratospheric Negative Ions. *Nature*. 257, 521-522 (1978).
22. Viggiano, A.A., Perry, R.A., Albritton, D.L., Ferguson, E.E., Fehsenfeld, F.C.: The Role of H_2SO_4 in Stratospheric Negative-Ion Chemistry. *J. Geophys. Res.* 85, 4551-4555 (1980).
23. Viggiano, A.A., Perry, R.A., Albritton, D.L., Ferguson, E.E., Fehsenfeld, F.C.: Stratospheric Negative Ion Reaction Rates with H_2SO_4 in the Stratosphere. *J. Geophys. Res.* 87, 7340-7342 (1982).
24. Viggiano, A.A., Arnold, F.: Stratospheric Sulfuric Acid Vapor - New and Updated Results. *J. Geophys. Res.* 88, 1457-1462 (1983) and references therein.
25. Davidson, J.A., Viggiano, A.A., Howard, C.J., Fehsenfeld, F.C., Albritton, D.L., Ferguson, E.E.: Rate Constants for the Reactions of O_2^+ , NO_2^+ , NO^+ , H_3O^+ , CO_3^- , NO_2^- and Halide Ions with N_2O_5 at 300K. *J. Chem. Phys.* 68, 2085-2087 (1978).

26. Bohringer, H., Fahey, D.W., Fehsenfeld, F.C., Ferguson, E.E.: The Role of Ion-Molecule Reactions in the Conversion of N_2O_5 to HNO_3 in the Stratosphere. *Planet. Space Sci.* **31**, 185-191 (1983).
27. Viggiano, A.A., Davidson, J.A., Fehsenfeld, F.C., Ferguson, E.E.: Rate Constants for the Collisional Dissociation of N_2O_5 by N_2 . *J. Chem. Phys.* **74**, 6113-6125 (1981).
28. Connell, P., Johnston, H.S.: The Thermal Decomposition of N_2O_5 in N_2 . *Geophys. Res. Lett.* **6**, 553-556 (1979).
29. Malko, M.W., Troe, J.: Analysis of the Unimolecular Reaction $N_2O_5 + M \rightarrow NO_2 + NO_3 + M$. *Int. J. Chem. Kin.* **14**, 399-416 (1982).
30. Paulson, J.F., Dale, F.: unpublished results.
31. Caldwell, G., Rozeboom, M.D., Kiplinger, J.P., Bartmess, J.E.: Displacement, Proton Transfer or Hydrolysis? Mechanistic Control of Acetonitrile Reactivity by Stepwise Solvation of Reactants. *J. Am. Chem. Soc.* (in press).
32. Dotan, I., Albritton, D.L., Fehsenfeld, F.C., Streit, G.E., Ferguson, E.E.: Rate Constants for the Reactions of O^- , O_2^- , NO_2^- , CO_3^- and CO_4^- with HCl and ClO with NO, NO_2 , SO_2 and CO_2 at 300K. *J. Chem. Phys.* **68**, 5414-5416 (1978).
33. Viggiano, A.A., Arnold, F., Fahey, D.W., Fehsenfeld, F.C., Ferguson, E.E.: Silicon Negative Ion Chemistry in the Atmosphere - In Situ and Laboratory Measurements. *Planet. Space Sci.* **30**, 499-509 (1982).
34. Fahey, D.W., Bohringer, H., Fehsenfeld, F.C., Ferguson, E.E.: Reaction Rates Constants for $O_2^-(H_2O)_n$ Ions with $n=0$ to 4 with O_3 , NO, SO_2 and CO_2 . *J. Chem. Phys.* **76**, 1799-1805 (1982).
35. Streit, G.E., Newton, T.W.: Negative Ion-Uranium Hexafluoride Charge Transfer Reactions. *J. Chem. Phys.* **73**, 3178-3182 (1980).
36. Streit, G.E., Babcock, L.M.: Negative Ion-Molecule Reactions of SF_4 . *J. Chem. Phys.* **75**, 3864-3870 (1981).
37. Streit, G.E.: Negative Ion Chemistry and the Electron Affinity of SF_6 . *J. Chem. Phys.* **77**, 826-833 (1982).
38. Bierbaum, V.M., Schmitt, R.J., DePuy, C.H., Mead, R.D., Schulz, P.A., Lineberger, W.C.: Experimental Measurement of the Electron Affinity of the Hydroperoxy Radical. *J. Am. Chem. Soc.* **103**, 6262-6263 (1981).
39. Streit, G.E., Newton, T.W.: The Effect of Chemical Reaction on Diffusive Ion Loss Processes in a Flowing Afterglow. *Int. J. Mass Spectrom. Ion Phys.* **38**, 105-126 (1981).
40. Lias, S.G., Liebman, J.F., Levin, R.D.: An Evaluated Compilation of Gas Phase Basicities and Proton Affinities of Molecules: Heats of Formation of Protonated Molecules. *J. Phys. Chem. Ref. Data* (in press).
41. Grabowski, J.J., DePuy, C.H., Bierbaum, V.M.: Gas Phase Hydrogen-Deuterium Exchange Reactions of HO^- and DO^- with Weakly Acidic Neutrals. *J. Am. Chem. Soc.* **105**, 2565-2571 (1983).

42. Grabowski, J.J.: Studies of Gas Phase Ion-Molecule Reactions Using a Selected Ion Flow Tube. Doctoral Thesis.
43. Paulson, J.F., Henschman, M.J.: On the Formation of H_3O^+ in an Ion-Molecule Reaction. In: NATO Advanced Study Institute Volume on Chemistry of Ions in the Gas Phase. Holland. D. Reidel Publishing Co. (in press).
44. Squires, R.R.: Ab Initio Studies of the Structures and Energies of Some Anion-Molecule Complexes. In: NATO Advanced Study Institute Volume on Chemistry of Ions in the Gas Phase. Holland. D. Reidel Publishing Co. (in press).
45. Paulson, J.F., Viggiano, A.A.: unpublished results.

Temperature dependence of associative detachment reactions

A. A. Viggiano^{a)} and John F. Paulson

Air Force Geophysics Laboratory, Hanscom AFB, Massachusetts 01731
(Received 25 April 1983; accepted 19 May 1983)

The temperature dependences of the rate coefficients for the associative detachment reactions $O^- + NO$, $S^- + CO$, and $S^- + O_2$ have been measured. All rate coefficients varied as $T^{-0.74 \pm 0.1}$. In addition, the rate coefficients and branching ratios for the reactions $O^- + C_2H_2$ and $O^- + C_2H_4$ have also been studied as a function of temperature. Both reactions were found to have a large associative detachment channel over the entire temperature range 140–494 K.

I. INTRODUCTION

Laboratory studies of associative detachment reactions have now been made for nearly 20 years. The first measurements were made in a flowing afterglow apparatus at the NOAA laboratory (then ESSA) in Boulder.^{1,2} Since these measurements, many aspects of this class of reaction have been studied by a variety of techniques including the flowing afterglow,^{1–12} flow drift tube,^{13,14} drift tubes,¹⁵ ion beams,^{16–18} and time of flight mass spectrometry.¹⁹ A review of the earlier work is given by Fehsenfeld.²⁰ These studies have yielded results on a wide variety of ions and neutrals, including unstable neutrals such as O, N, H, and $O_2^+(A^1\Delta_g)$.

In addition to the experimental work, many theoretical studies have also been made on associative detachment reactions^{21–24} and the closely linked reverse process, dissociative electron attachment.^{25,26} The earlier theories all centered on the formation of a resonance state $(AB)^*$ after the collision of A^- and B or e^- and AB . More recently, however, an alternate theory based on the concept of virtual states has been successful in explaining many aspects of these two processes.^{24,26}

In the last several years, interest in associative detachment reactions has been rekindled, mainly due to the work done at the University of Colorado on the vibrational product distribution of reactions between O^- and CO ²⁷ and between the halide ions and atomic hydrogen.^{28–31} These results have yielded important results on the dynamics of this class of reaction and have prompted much of the recent theoretical work as well.

In spite of all the work done on associative detachment reactions, no studies on the temperature dependence of these reactions have been made. The present work reports the first such study, in which the temperature dependence of five associative detachment reactions has been investigated over the temperature range 88–494 K. The reactions investigated have been chosen as those whose rate coefficients at room temperature are less than the Langevin collision limit, i.e.,



^{a)} Air Force Geophysics Scholar.

and



or those with multiple pathways, i.e.,



and



Both of these classes of reaction might be expected to have a significant temperature dependence in either the rate coefficient or branching ratio.

II. EXPERIMENTAL DETAILS

The apparatus used for these experiments is the selected ion flow tube (SIFT). A similar apparatus has been described in detail elsewhere,³² so only a brief description will be given here. Ions are created in an electron impact ion source. After formation, the ions are drawn into a quadrupole mass filter and mass selected. The mass selected ions then pass through a set of focusing lenses, through an inlet orifice and into a flow tube. In order to aid in getting the ions from the low pressure mass filter into the flow tube region (~ 0.5 Torr), a venturi inlet is used. This enables the ions to be injected at lower energy and reduces the probability of collisional detachment of electrons from the negative ions. A helium carrier gas flow of approximately 0.2 standard $l\ s^{-1}$ is passed through the venturi inlet and carries the ions downstream at a velocity on the order of $10^4\ cm\ s^{-1}$. The neutral reactant gases were added at any of three ports along the length of the flow tube. Finally, the ions were sampled through a 0.3 mm orifice leading to a second quadrupole mass filter. The ions were counted with the aid of a Channeltron electron multiplier. The bulk of the carrier gas was pumped by a Roots blower.

The flow tube could be heated or cooled. The cooling was accomplished by passing liquid nitrogen through two loops going in opposite directions along the flow tube. A series of six platinum resistance thermometers measured the temperature along the flow tube and controlled the servo valves which supplied the liquid nitrogen to the cooling loops. The heating was accomplished with resistance heaters. Both the heaters and the cooling circuits were attached to a copper heat sink which was

placed in close contact with the flow tube.

The gases used were all commercially available. The O_2 , CO, C_2H_4 , SF_6 , and N_2O were used without further purification. The NO was passed through a trap cooled to dry ice temperature in order to remove NO_2 and HNO_3 . Acetylene was purified by passage through a liquid nitrogen/dichloromethane slush bath ($-97^\circ C$). The primary ions O^- and S^- were made by dissociative electron attachment in N_2O and CS_2 , respectively.

Rate coefficients were derived by monitoring the primary ion signal as a function of the flow rate of reactant gas. The flow rate was measured by monitoring the inlet pressure and pressure differential along a capillary which had been calibrated by monitoring the pressure drop vs time from a known volume. The helium flow was measured by a mass flow meter, and all pressures were measured by capacitance manometers.

III. RESULTS AND DISCUSSION

The reactions studied can be divided into two groups. The first can be classified as slow reactions (those which proceed more slowly than the Langevin collision rate) between an atomic ion and diatomic neutral. These reactions have only associative detachment channels. The second group includes reactions of O^- with the two lightest unsaturated hydrocarbons. These reactions have numerous reaction pathways of which associative detachment is only one.

Figure 1 shows a logarithmic plot of the measured rate coefficients vs temperature for the atomic ion reactions with diatomic neutrals. The triangles, pluses, and circles represent the reactions, $O^- + NO$, $S^- + CO$, and $S^- + O_2$, respectively. All three rate coefficients decrease by approximately a factor of three or four as the temperature rises from 88–468 K.

Table I lists the reactions, collision rate coefficients, least squares fits to T^{-n} temperature dependences, and other values of the rate coefficients measured at room temperature, along with the associated references. The error limits for this study are $\pm 30\%$, the same as that quoted for the other references, which refer to the flowing afterglow work of the NOAA group in Boulder. Considering these error limits, all the results are in good agreement.

The results of the least square results are also shown in Fig. 1. For the reaction $O^- + NO$, we can compare the temperature dependence found in this work to that derived from the kinetic energy dependence found in

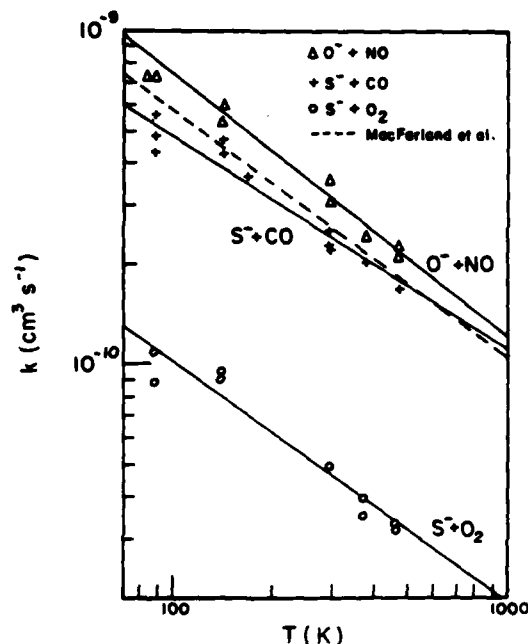


FIG. 1. Rate coefficients for the atomic ion–diatomic neutral associative detachment reactions as a function of temperature. The triangles, pluses, and circles represent the reactions $O^- + NO$, $S^- + CO$, and $S^- + O_2$, respectively. The solid lines represent the results of least squares fits to the data. The dash line represents the results of McFarland *et al.* (Ref. 13) on the $O^- + NO$ reaction.

the flow drift tube work of McFarland *et al.*¹³ These data are shown as a dashed line in Fig. 1. The temperature dependence is quite similar ($T^{-0.83}$ vs $T^{-0.75}$), although the absolute values differ by about 25%, well within the combined error limits of the measurements. The fact that the results are in good agreement indicates that it is kinetic energy rather than internal energy that accounts for the temperature dependence, since in the work of McFarland *et al.* it was kinetic energy that was varied rather than temperature.

In order to check that associative detachment was actually taking place, in some of the experiments SF_6 was added upstream of the neutral reactant inlet port. SF_6 was chosen because it rapidly attaches electrons to form SF_6^- and does not charge transfer with O^- or S^- . SF_6^- was observed in all cases, but the increase in the SF_6^- ion signal did not balance the decrease in primary ion signal, probably due to the mass discrimination

TABLE I. Rate coefficients for the atomic ion–diatomic neutral reactions.

Reaction	$k(T)(cm^3 s^{-1})$	Previous results (300 K)($cm^3 s^{-1}$)	Reference	$k_{coll}(cm^3 s^{-1})$
$O^- + NO \rightarrow NO_2 + e$	$3.1(-10)(300/T)^{0.83}$	$2.1(-10) \pm 30\%$ $2.8(-10) \pm 30\%$	13 1	$1.0(-9)$
$S^- + CO \rightarrow COS + e$	$2.3(-10)(300/T)^{0.44}$	$3.1(-10) \pm 30\%$	8	$8.5(-10)$
$S^- + O_2 \rightarrow SO_2 + e$	$4.6(-11)(300/T)^{0.72}$	$3(-11) \pm 30\%$	5	$7.4(-10)$

associated with the large mass difference between SF_6 and O^+ or S^+ .

A careful search for the occurrence of an association reaction, in addition to associative detachment, was made in all cases at the low temperatures. In no instance was an association product observed, and upper limits to the association rate coefficients of 10^{-29} to $10^{-30} \text{ cm}^3 \text{ s}^{-1}$ could be made at 88 K.

The rate coefficients for the reactions $\text{O}^+ + \text{NO}$ and $\text{S}^+ + \text{CO}$ approach the collision limit at 88 K ($h/k_B = 0.8$ and 0.5 , respectively). This fact taken together with the observed temperature dependence leads us to conclude that at 88 K the lifetime of the collision complex with respect to autodetachment is comparable with the lifetime with respect to dissociation back to reactants. One may expect the autodetachment lifetime to be influenced much more by reaction exothermicity and shape of the potential curves than by temperature. We therefore propose that the decrease in the rate coefficient with increasing temperature reflects a decrease in the lifetime with respect to dissociation into reactants. This is supported by the fact that temperature and kinetic energy have the same effect. Fehsenfeld²⁰ has pointed out that the $\text{O}^+ - \text{NO}$ complex has a long lifetime, presumably due to a relatively long-lived Feshbach resonance in the formation of the compound state.³³

The $\text{S}^+ + \text{O}_2$ reaction has been thought to be an example of an insertion reaction, in contrast to the addition reactions discussed above. A model for associative detachment insertion reactions has been proposed by Fehsenfeld and Ferguson.⁵ They postulate a criterion for an activation barrier in insertion reactions to be $\Delta E_{\text{ad}} > \Delta E_r$, where ΔE_r is the exothermicity of the reaction and ΔE_{ad} is the energy change in stretching the reactant bond distance to that found in the product of the associative detachment reaction. In the case of $\text{S}^+ + \text{O}_2$, this requires stretching the $\text{O}-\text{O}$ length of 1.2 \AA in O_2 to the $\text{O}-\text{O}$ distance of 2.48 \AA in SO_2 . The energies³ are $\Delta E_{\text{ad}} = 5.1 \text{ eV}$ and $\Delta E_r = 3.8 \text{ eV}$. Based on these numbers, one would then expect an activation barrier. This is not consistent with the present data. What we observe is a temperature dependence similar to that for the addition reactions discussed above, a negative dependence rather than the positive temperature dependence one would expect for insertion reactions from the above considerations.

Fehsenfeld also has postulated that insertion reactions take place by a two step mechanism.²⁰ For the $\text{S}^+ + \text{O}_2$ reaction, this mechanism is



or



where the products from the first reaction, i.e., reactions (6) or (8), never separate. The criterion for reaction is that the first step is exothermic. In this case, reactions (6) and (8) are endothermic by 16.5

and $8.7 \text{ kcal mol}^{-1}$, respectively. Again, the criterion for an insertion reaction is violated.

Alternatively, one may consider that it is not an insertion reaction that is taking place but rather an addition reaction leading to a less stable neutral, i.e., either $\text{S}-\text{O}-\text{O}$ or cyclic SO_2 . In order for the reaction,



to be exothermic, the $\text{S}-\text{O}$ bond strength must be greater than 49 kcal mol^{-1} . Dunning and Raffanetti³⁴ have calculated this bond strength to be only 38 kcal mol^{-1} . They also calculated the energies for the ring isomer of SO_2 , and the reaction of $\text{S}^+ + \text{O}_2$ to produce this isomer is endothermic by 6 kcal mol^{-1} . Considering free energies, the endoergicities are even larger, 25 kcal mol^{-1} for $\text{S}-\text{O}-\text{O}$ formation and 13 kcal mol^{-1} for cyclic SO_2 formation. We can therefore rule out reactions producing these isomeric forms of SO_2 . Thus, we must assume that the reaction is an insertion reaction.

There remains a possibility to explain this reaction as an insertion reaction following the two step mechanism proposed above, if one takes into account the kinetic energy gained during the collision. During the collision between S^+ and O_2 , electrostatic potential energy is converted into kinetic energy. If this kinetic energy is greater than the endothermicity of reaction (8) ($8.7 \text{ kcal mol}^{-1}$) then this reaction may proceed, but the products would remain trapped. Reaction (9) can then follow, leading to normal SO_2 and an electron. One may make an estimate of the likelihood of this process taking place. To gain the kinetic energy necessary to overcome the endothermicity of reaction (8), S^+ and O_2 must come within 1.94 \AA of each other. The maximum impact parameter, according to the Langevin theory, that leads to a "collision" is 6.7 \AA , assuming an average velocity at 300 K . The fraction of collisions that can overcome the barrier is then given by the square of the ratio of these numbers or 0.084 . This corresponds to an upper limit to the rate coefficient of $6.2 \times 10^{-11} \text{ cm}^3 \text{ s}^{-1}$. Our measured value is $4.6 \times 10^{-11} \text{ cm}^3 \text{ s}^{-1}$, consistent with this limit. A mechanism similar to this has been used to explain the rapidity of the association of Si^+ with O_2 .³⁵ The observed temperature dependence can then still be explained by a change in the lifetime of the collision complex, as suggested above.

Table II presents the results of the work on C_2H_2 reacting with O^+ . The measured total rate coefficients are accurate to 30%. The rate coefficients for the major channels ($\geq 10\%$) are accurate to about 40% and for the minor channels to a factor of 2. These additional uncertainties are due to mass discrimination effects and to small signals for the minor channels. The presence of associative detachment channels was detected by adding SF_6 and observing SF_6^+ formed by electron attachment. We could not rule out that some of the SF_6^+ came from charge transfer reactions with the other products but could be certain that most of it came from electron attachment. The branching ratios were determined by assuming the associative detachment channel to account for the loss of the primary ion signal that could not be accounted for by the increase in the other

TABLE II. Rate coefficients and branching ratios for the reactions of O^- with C_2H_2 and C_2H_4 .

Reaction	Rate coefficients ($cm^3 s^{-1} \times 10^{10}$)				
	T = 140	T = 294	T = 494	Bohme <i>et al.</i> ^a (296 K)	Parkes ^b (0.04)
$O^- + C_2H_2 \rightarrow C_2H_2O + e$	15.2	11.0	9.3	12.0	13
$\rightarrow C_2^- + H_2O$	0.19	0.76	0.62	1.0	0
$\rightarrow C_2H^- + OH$	2.2	6.84	9.52	6.0	8
$\rightarrow C_2HO^- + H$	0.93	0.38	1.2	1.0	0.8
\rightarrow products	18.5	19.0	20.7	20.0	21.8
$O^- + C_2H_4 \rightarrow C_2H_4O + e$	7.9	6.9	3.9		4.4
$\rightarrow C_2H_2^- + H_2O$	4.1	3.0	2.7		2.1
$\rightarrow C_2HO^- + 3H$	0	0	0		0.1
$\rightarrow C_2H_2O^- + H$	0.12	0.31	0.20		0.13
\rightarrow products	12.0	10.2	6.8		6.5

^aReference 11.^bReference 15.

products. This procedure was favored over using the SF_6^- peak as a monitor because of the mass discrimination at the large SF_6^- mass and possible complications due to reactions of SF_6^- with the other ionic products.

For the reaction of O^- with C_2H_2 , the total rate coefficients remained essentially constant over the entire temperature range. However, the two major product channels exhibited a marked temperature dependence. The associative detachment channel decreased from $15.2 \times 10^{-10} cm^3 s^{-1}$ at 140 K to $9.3 \times 10^{-10} cm^3 s^{-1}$ at 494 K. The temperature dependence for this channel can be written as $1.1 \times 10^{-9} (300/T)^{0.39} cm^3 s^{-1}$. The channel going to C_2H^- increased by an amount similar to the decrease in the associative detachment channel, and this temperature dependence can be best written as $1.76 \times 10^{-9} e^{-349/T} cm^3 s^{-1}$.

Interpretation of the temperature dependences is difficult due to the competitive nature of the reaction channels. The fact that the associative detachment channel decreases with increasing temperature may either reflect a change in lifetimes, similar to that observed for the other associative detachment reactions, or may result from the increased likelihood of the proton transfer reaction (leading to C_2H^-). The increase in the latter channel with temperature may be due to a slight energy barrier.

There have been numerous other studies of the $O^- + C_2H_2$ reaction. The results from the two studies that observed the associative detachment channel are listed in Table II. The reaction was studied by Bohme¹¹ *et al.* at room temperature in a flowing afterglow system and by Parkes¹⁵ in a drift tube. The present results are generally in good agreement with these two studies. However, we see considerably less C_2HO^- production at 294 K. Due to the larger error limits for the minor channels, this is not a serious discrepancy. Parkes saw no production of C_2^- . Bohme *et al.* have attributed this to a possible reaction of C_2^- with O_2 in Parkes' system. The results of other workers are in reasonable agreement for the channels they have seen and are reviewed by Bohme *et al.*¹¹

The total rate coefficient for the reaction of $O^- + C_2H_4$ as well as that for each of the major products dropped with increasing temperature. Obscured in presenting

the data this way is the fact that the branching ratio for the various channels remained constant with temperature within the experimental uncertainty. The associative detachment channel accounted for about 65% of the products and the $C_2H_2^-$ channel for about 35%. The $C_2H_2O^-$ channel varied between 1% and 3%. A small drop in the percentage of the associative detachment channel relative to the $C_2H_2^-$ channel may have occurred at 494 K but is within the error limitations.

The temperature dependence of the total rate coefficient for reaction of O^- with C_2H_4 can be written as $9.0 \times 10^{-10} (300/T)^{0.43} cm^3 s^{-1}$ and that for the associative detachment channel as $5.7 \times 10^{-10} (300/T)^{0.53} cm^3 s^{-1}$. At 140 K, the total rate coefficient for this reaction approaches 75% of the Langevin collision limit of $1.6 \times 10^{-9} cm^3 s^{-1}$. In the case of the reaction of O^- with C_2H_2 , the measured rate coefficient exceeded the Langevin collisional rate coefficient of $1.4 \times 10^{-9} cm^3 s^{-1}$ at all temperatures. Parkes suggested that this is due to the long-range potential being more attractive than that from a charge-induced dipole interaction for this reaction (i.e., charge quadrupole). Summarizing, all reactions which reacted at less than the collision rate showed negative temperature dependences between $T^{-0.4}$ and $T^{-0.53}$ and the one reaction that proceeded at the collision rate showed no temperature dependence. This is the normal behavior for exothermic ion-molecule reactions.

The reaction of $O^- + C_2H_4$ has also been studied by a variety of investigators and techniques. Parkes¹⁵ was the only investigator to give complete branching ratios, and these results are listed in Table II. Our values for the total rate coefficient is higher than that of Parkes and other investigators by about 30%, within the combined error limits of the results. In addition to the channels observed in this study, Parkes also observed minor channels producing C_2HO^- and OH^- , the magnitude of which were just below our detection limit. Parkes observed no change in rate coefficient with increasing electric field in his drift tube. However, Lindinger *et al.*¹⁴ found the total rate coefficient to decrease with increasing kinetic energy, in agreement with the temperature dependence found here. Lindinger *et al.* have summarized previous work on this reaction. The branching ratio observed in the present work is in

agreement with Parkes *et al.* and Lindinger *et al.* for the channels they observed. The drift tube studies^{14,15} showed that at higher energies, the OH⁻ channel started to increase dramatically and was the major product channel at energies on the order of 1 eV.

IV. SUMMARY

We have presented here the first measurements of associative detachment reactions as a function of temperature. The reactions O⁻ + NO and S⁻ + CO have similar temperature dependences of $T^{-0.53}$ and $T^{-0.44}$, respectively. Both reaction rate coefficients approach the collision limit at low temperature. No association products were observed at low temperature. The reaction S⁻ + O₂ is slower but exhibits a similar temperature dependence ($T^{-0.73}$). However, there are problems in explaining the temperature dependence in terms of either an insertion reaction or an addition reaction to form some isomer of SO₂. The reaction of O⁻ + C₂H₂ proceeds extremely quickly over the temperature range 140–494 K, and the total rate coefficient remains constant. The branching ratio of this reaction, however, was found to vary with temperature. The O⁻ + C₂H₄ reaction showed a weak temperature dependence in the total rate coefficient, but the branching ratio was found to remain constant.

ACKNOWLEDGMENTS

The authors wish to acknowledge the technical support of Fred Dale. This work has been supported in part by the Defense Nuclear Agency.

- ¹F. C. Fehsenfeld, E. E. Ferguson, and A. L. Schmeltekopf, *J. Chem. Phys.* **45**, 1844 (1966).
- ²F. C. Fehsenfeld, A. L. Schmeltekopf, H. I. Schiff, and E. E. Ferguson, *Planet. Space Sci.* **15**, 373 (1967).
- ³A. L. Schmeltekopf, F. C. Fehsenfeld, and E. E. Ferguson, *Astrophys. J.* **148**, L155 (1967).
- ⁴F. C. Fehsenfeld, D. L. Albritton, J. A. Burt, and H. I. Schiff, *Can. J. Chem.* **47**, 1793 (1969).
- ⁵F. C. Fehsenfeld and E. E. Ferguson, *J. Chem. Phys.* **51**, 3512 (1969).
- ⁶F. C. Fehsenfeld and E. E. Ferguson, *J. Chem. Phys.* **53**, 2614 (1970).
- ⁷D. B. Dunkin, F. C. Fehsenfeld, and E. E. Ferguson, *J. Chem. Phys.* **53**, 987 (1970).
- ⁸E. E. Ferguson, *Acc. Chem. Res.* **3**, 402 (1970).
- ⁹F. C. Fehsenfeld, C. J. Howard, and E. E. Ferguson, *J. Chem. Phys.* **58**, 5841 (1973).
- ¹⁰C. J. Howard, F. C. Fehsenfeld, and M. McFarland, *J. Chem. Phys.* **60**, 5086 (1974).
- ¹¹D. K. Bohme, G. I. Mackay, H. I. Schiff, and R. S. Hemsworth, *J. Chem. Phys.* **61**, 2175 (1974).
- ¹²H. I. Schiff and D. K. Bohme, *Int. J. Mass Spectrom. Ion Phys.* **16**, 167 (1975).
- ¹³M. McFarland, D. L. Albritton, F. C. Fehsenfeld, E. E. Ferguson, and A. L. Schmeltekopf, *J. Chem. Phys.* **59**, 6629 (1973).
- ¹⁴W. Lindinger, D. L. Albritton, F. C. Fehsenfeld, and E. E. Ferguson, *J. Chem. Phys.* **63**, 3239 (1975).
- ¹⁵D. A. Parkes, *J. Chem. Soc. Faraday Trans. 1* **68**, 613 (1972).
- ¹⁶J. L. Mauer and G. J. Schulz, *Phys. Rev. A* **1**, 593 (1973).
- ¹⁷J. Comer and G. J. Schulz, *J. Phys. B* **7**, L249 (1974).
- ¹⁸J. Comer and G. J. Schulz, *Phys. Rev. A* **10**, 2100 (1974).
- ¹⁹J. A. D. Stockdale, R. N. Compton, and P. W. Reinhardt, *Int. J. Mass Spectrom. Ion Phys.* **4**, 401 (1970).
- ²⁰F. C. Fehsenfeld, in *Interactions between Ions and Molecules*, edited by P. Ausloos (Plenum, New York, 1975).
- ²¹J. C. Y. Chen, *Phys. Rev.* **156**, 12 (1967).
- ²²A. Herzenberg, *Phys. Rev.* **160**, 80 (1967).
- ²³R. J. Bieniek and A. Dalgarno, *Astrophys. J.* **228**, 635 (1979).
- ²⁴J. P. Gauyacq, *J. Phys. B* **15**, 2721 (1982), and references within.
- ²⁵T. F. O'Malley, *Phys. Rev.* **150**, 14 (1966).
- ²⁶L. Dubé and A. Herzenberg, *Phys. Rev. Lett.* **38**, 820 (1977).
- ²⁷V. M. Bierbaum, G. B. Ellison, J. H. Futrell, and S. R. Leone, *J. Chem. Phys.* **67**, 2375 (1977).
- ²⁸T. S. Zwier, V. M. Bierbaum, G. B. Ellison, and S. R. Leone, *J. Chem. Phys.* **72**, 5426 (1980).
- ²⁹T. S. Zwier, M. M. Maricq, C. J. S. M. Simpson, V. M. Bierbaum, G. B. Ellison, and S. R. Leone, *Phys. Rev. Lett.* **44**, 1050 (1980).
- ³⁰T. S. Zwier, J. C. Weisshaar, and S. R. Leone, *J. Chem. Phys.* **75**, 4885 (1981).
- ³¹M. A. Smith and S. R. Leone, *J. Chem. Phys.* **78**, 1325 (1983).
- ³²N. G. Adams and D. Smith, *Int. J. Mass Spectrom. Ion Phys.* **21**, 349 (1976).
- ³³L. Sanche and G. J. Schulz, *J. Chem. Phys.* **58**, 479 (1973).
- ³⁴T. H. Dunning, Jr. and R. C. Raffanetti, *J. Phys. Chem.* **85**, 1350 (1981).
- ³⁵E. E. Ferguson (private communication).

DATE
LME